



Computer-Guided Design of Photocatalyst for PET-RAFT Polymerisation

Author:

Wu, Chenyu

Publication Date:

2020

DOI:

<https://doi.org/10.26190/unsworks/3949>

License:

<https://creativecommons.org/licenses/by-nc-nd/3.0/au/>

Link to license to see what you are allowed to do with this resource.

Downloaded from <http://hdl.handle.net/1959.4/68278> in <https://unsworks.unsw.edu.au> on 2024-04-26



THE UNIVERSITY OF
NEW SOUTH WALES
SYDNEY • AUSTRALIA

**Computer-Guided Design of Photocatalyst for
PET-RAFT Polymerisation**

by

Chenyu Wu

*A thesis submitted in fulfilment of the requirements for the degree of
Doctor of Philosophy*

School of Chemical Engineering
Faculty of Engineering
University of New South Wales, Australia

June 2020

Thesis/Dissertation Sheet

Surname/Family Name	: Wu
Given Name/s	: Chenyu
Abbreviation for degree as give in the University calendar	: PhD
Faculty	: Engineering
School	: Chemical Engineering
Thesis Title	: Computer-Guided Design of Photocatalyst for PET-RAFT Polymerisation

Abstract 350 words maximum: (PLEASE TYPE)

Photo-controlled polymerisation uses a photo-excited photocatalyst (PC) to reversibly active and deactivate the propagating species. Under regulation by light, photo-controlled polymerisation features temporal control, spatial control, sequence control and high level of selectivity/orthogonality between different systems, leading to a range of applications in advanced macromolecular synthesis such as surface patterning, 3D/4D printing, polymeric micelles, multiblock antimicrobial polymers with precise sequences and architectures. All these unique features of photo-controlled polymerisation are largely dependent on properties and functionalities of PCs. Traditionally, the selection and discovery of appropriate PCs rely heavily on a trail-and-error approach, where extensive experimental screening is needed to identify desired candidates. To reduce costs and circumvent the challenges in laborious experimental work, a rational design strategy emerged where a new PC in application to a photo-controlled polymerisation system can be designed based on understanding of the structure-property-performance relationships.

This dissertation aims to enable and streamline a general fully computer-guided rational strategy of designing an efficient and functional PC for a commonly used photo-controlled polymerisation technique, namely photoinduced electron/energy reversible addition-fragmentation chain transfer (PET-RAFT) polymerisation. This thesis starts from using naturally evolved Chl a with various functional substituents and investigating its photocatalytic performance and functionalities in PET-RAFT polymerisation. General orientations for the design of PET-RAFT PCs were inspired from this natural design. On top of this, comprehensive structure-property-performance relationships were established at the quantum chemical level as guiding principles for rational PC design of PET-RAFT polymerisation, by combining experimental and computational studies on a library of halogenated xanthene dyes. Finally, by implementing the most cutting-edged quantum chemical software packages, the fully computer-guided strategy of functional PC design for PET-RAFT polymerisation was enabled based on broadened structure-property-performance relationships. As an example, an efficient pH-switchable organic PC was designed. Application of this rationally designed PC in PET-RAFT polymerisation resulted in the first organocatalysed pH and light dual-gated controlled polymerisation.

Declaration relating to disposition of project thesis/dissertation

I hereby grant to the University of New South Wales or its agents a non-exclusive licence to archive and to make available (including to members of the public) my thesis or dissertation in whole or in part in the University libraries in all forms of media, now or here after known. I acknowledge that I retain all intellectual property rights which subsist in my thesis or dissertation, such as copyright and patent rights, subject to applicable law. I also retain the right to use all or part of my thesis or dissertation in future works (such as articles or books).

.....
Signature

.....
Date

The University recognises that there may be exceptional circumstances requiring restrictions on copying or conditions on use. Requests for restriction for a period of up to 2 years can be made when submitting the final copies of your thesis to the UNSW Library. Requests for a longer period of restriction may be considered in exceptional circumstances and require the approval of the Dean of Graduate Research.

ORIGINALITY STATEMENT

'I hereby declare that this submission is my own work and to the best of my knowledge it contains no materials previously published or written by another person, or substantial proportions of material which have been accepted for the award of any other degree or diploma at UNSW or any other educational institution, except where due acknowledgement is made in the thesis. Any contribution made to the research by others, with whom I have worked at UNSW or elsewhere, is explicitly acknowledged in the thesis. I also declare that the intellectual content of this thesis is the product of my own work, except to the extent that assistance from others in the project's design and conception or in style, presentation and linguistic expression is acknowledged.'

Signed

Date

INCLUSION OF PUBLICATIONS STATEMENT

UNSW is supportive of candidates publishing their research results during their candidature as detailed in the UNSW Thesis Examination Procedure.

Publications can be used in their thesis in lieu of a Chapter if:

- The candidate contributed greater than 50% of the content in the publication and is the “primary author”, ie. the candidate was responsible primarily for the planning, execution and preparation of the work for publication
- The candidate has approval to include the publication in their thesis in lieu of a Chapter from their supervisor and Postgraduate Coordinator.
- The publication is not subject to any obligations or contractual agreements with a third party that would constrain its inclusion in the thesis

Please indicate whether this thesis contains published material or not:

- This thesis contains no publications, either published or submitted for publication
- Some of the work described in this thesis has been published and it has been documented in the relevant Chapters with acknowledgement
- This thesis has publications (either published or submitted for publication) incorporated into it in lieu of a chapter and the details are presented below

CANDIDATE’S DECLARATION

I declare that:

- I have complied with the UNSW Thesis Examination Procedure
- where I have used a publication in lieu of a Chapter, the listed publication(s) below meet(s) the requirements to be included in the thesis.

Candidate’s Name	Signature	Date (dd/mm/yy)

COPYRIGHT STATEMENT

'I hereby grant the University of New South Wales or its agents a non-exclusive licence to archive and to make available (including to members of the public) my thesis or dissertation in whole or part in the University libraries in all forms of media, now or here after known. I acknowledge that I retain all intellectual property rights which subsist in my thesis or dissertation, such as copyright and patent rights, subject to applicable law. I also retain the right to use all or part of my thesis or dissertation in future works (such as articles or books).'

'For any substantial portions of copyright material used in this thesis, written permission for use has been obtained, or the copyright material is removed from the final public version of the thesis.'

Signed

Date

AUTHENTICITY STATEMENT

'I certify that the Library deposit digital copy is a direct equivalent of the final officially approved version of my thesis.'

Signed

Date

Abstract

Photo-controlled polymerisation uses a photo-excited photocatalyst (PC) to reversibly activate and deactivate the propagating species. Under regulation by light, photo-controlled polymerisation features temporal control, spatial control, sequence control and high level of selectivity/orthogonality between different systems, leading to a range of applications in advanced macromolecular synthesis such as surface patterning, 3D/4D printing, polymeric micelles, multiblock antimicrobial polymers with precise sequences and architectures. All these unique features of photo-controlled polymerisation are largely dependent on properties and functionalities of PCs. Traditionally, the selection and discovery of appropriate PCs rely heavily on a trial-and-error approach, where extensive experimental screening is needed to identify desired candidates. To reduce costs and circumvent the challenges in laborious experimental work, a rational design strategy emerged where a new PC in application to a photo-controlled polymerisation system can be designed based on understanding of the structure-property-performance relationships.

This dissertation aims to enable and streamline a general fully computer-guided rational strategy of designing an efficient and functional PC for a commonly used photo-controlled polymerisation technique, namely photoinduced electron/energy reversible addition-fragmentation chain transfer (PET-RAFT) polymerisation. This thesis starts from using naturally evolved Chl a with various functional substituents and investigating its photocatalytic performance and functionalities in PET-RAFT polymerisation. General orientations for the design of PET-RAFT PCs were inspired from this natural design. On top of this, comprehensive structure-property-performance relationships were established at the quantum chemical level as guiding principles for rational PC design of PET-RAFT polymerisation, by combining experimental and computational studies on a library of halogenated xanthene dyes. Finally, by implementing the most cutting-edged quantum chemical software packages, the fully computer-guided strategy of functional PC design for PET-RAFT polymerisation was enabled based on broadened structure-property-performance relationships. As an example, an efficient pH-switchable organic PC was designed. Application of this rationally designed PC in PET-RAFT polymerisation resulted in the first organocatalysed pH and light dual-gated controlled polymerisation.

Acknowledgement

My foremost gratitude goes to my respectful supervisor Prof. Cyrille Andre Jean Marie Boyer. His big enlightenments and encouragements throughout my entire doctoral research duration have greatly developed my interests in academia, shaped my views of science and broadened my visions. He is strongly supportive, always showing passions, supports and much care in our frequent conversations. In multiple critical periods and turning points of my doctoral research, his visionary and farsighted advice constantly keep me on a right track, resulting in smooth and fruitful three years in a row more than I could have imagined. His professional and great expertise in polymer and materials science has deeply inspired me and guided me through the appealing world of applied science.

I am also thankful for my co-supervisor Dr. Jiangtao Xu, who has given me much constructive and insightful advice for different projects especially in early times of my doctoral researches. Special thanks go to our lab manager Eu Hau Pan, who is also a friend of mine and has been taking care of me in laboratories and kindly helping me with numerous laboratory activities.

I would also like to thank my colleagues Dr. Sivaprakash Shanmugam, Dr. Jordan Theriot, Dr. Nathaniel Corrigan and Dr. Kenward Jung, who has provided me with a lot of insightful advice in a great number of in-depth conversations. I thank my former coursework students Tong Zhang, Huijie Zhu, Qianlan Lin, Hengqi Chen and Junchen He for their assistance and supportive coworking in a number of projects.

Prof. Garret Miyake and Dr. Chern-Hooi Lim from Colorado State University have given me much advice, guidance and initial inspirations on quantum chemical calculations and the topic of photocatalyst design. Prof. Wenjian Liu from Peking University and Shandong University has further provided insightful advice on computation and helped me go deep into quantum chemical calculations and the practical uses of different computational tools. Prof. Jian Zhu and Dr. Jiandong Zhang from Soochow University also provided guidance on my quantum chemical calculations in early times of my doctoral research.

I would like to thank the UNSW Bioanalytical Mass Spectrometry Facility (BMSF) team, the UNSW Nuclear Magnetic Resonance (NMR) team, the UNSW Katana High Performance Computing (HPC) team, the Beijing Density Functional (BDF) team from Peking University, and the Molecular Materials Property Prediction Package (MOMAP) team from Tsinghua University, Chinese Academy of Sciences and the Hzwtech Company, for their kind assistance and guidance on various technical aspects of my doctoral research.

It is a great pleasure to work alongside my colleagues at the Centre for Advanced Macromolecular Design (CAMD) codirected by Prof. Per Zetterlund and Prof. Martina Stenzel, who have given me a lot of support in past years. I would like to thank Prof. Per Zetterlund, Dr. Peter Richard Wich, A/Prof Frank Lucien and A/Prof. Patrick Spicer for their encouraging words at different stages of my doctoral research. I thank my colleagues Dr. Sivaprakash Shanmugam, Dr. Nathaniel Corrigan, Dr. Kenward Jung, Peter R. Judzewitsch, Rashin Namivandi-zangeneh, Gervase Ng, Sihao Xu, Yasemin Fadil, Dr. Susan Oliver, Dr. Haiqiao Wang, Dr. Dewen Zhou, Yingying Chu, Zixuan Huang and Dr. Guofeng Li for their support.

I sincerely acknowledge my mother Prof. Yueqin Yu, my father Prof. Yumin Wu, Uncle Jianjun Kan and Aunt Hongmei Zhang for their everyday support, advice and company. I express my gratitude to Prof. Yingjie Zhao and Prof. Zhibo Li as friends of my family and my supervisor Cyrille, for their advice.

I acknowledge Rui Guo for being alongside during writing of this dissertation.

Publication Arising from this Thesis

1. **Wu, C.**; Shanmugam, S.; Xu, J.; Zhu, J.; Boyer, C., Chlorophyll a Crude Extract: Efficient Photo-Degradable Photocatalyst for PET-RAFT Polymerisation. *Chemical Communications* **2017**, 53 (93), 12560-12563 (DOI: 10.1039/C7CC07663K).
2. **Wu, C.**; Corrigan, N.; Lim, C; Jung, K.; Zhu, J.; Miyake, G; Xu, J.; Boyer, C., Guiding the Design of Organic Photocatalyst for PET-RAFT Polymerisation: Halogenated Xanthene Dyes. *Macromolecules* **2018**, 52 (1), 236-248 (DOI: 10.1021/acs.macromol.8b02517).
3. **Wu, C.**; Chen, H.; Corrigan, N.; Jung, K.; Kan, X.; Li, Z.; Liu, W.; Xu, J.; Boyer, C., Computer-Guided Discovery of a pH-Responsive Organic Photocatalyst and Application for pH and Light Dual-Gated Polymerisation. *Journal of the American Chemical Society* **2019**, 141 (20), 8207-8220 (DOI: 10.1021/jacs.9b01096).

Table of Contents

Abstract	i
Acknowledgement	ii
Publication Arising from this Thesis	iv
Table of Contents	v
List of Figures	x
List of Tables	xxiii
List of Schemes	xxv
List of Equations	xxx
List of Abbreviations	xxxi
Chapter 1 Introduction	1
1.1 Current state-of-the-art of photo-controlled polymerisation.....	1
1.2 Thesis motivation	3
1.3 Thesis outline	5
1.4 References	8
Chapter 2 Literature Review: Computer-Aided Photocatalyst Design for Photo- Controlled Polymerisation: Theories, Guidelines, Methodologies and Applications.....	10
2.1 Introduction	10
2.1.1 Scope of the review	10
2.1.2 Inspiration from PC “design” strategies implemented by natural evolution..	13
2.1.3 Rational design of PCs for photo-controlled polymerisation.....	14
2.2 Overview of PCs in photo-controlled polymerisation	15
2.2.1 First photo-ATRP systems with transition-metal-based PCs.....	15
2.2.2 First PET-RAFT systems with transition-metal-based PCs.....	18
2.2.3 Metal-free photo-ATRP (O-ATRP) with organic PCs.....	21
2.2.4 PET-RAFT polymerisation with organic PCs	29
2.2.5 Photo-RDRP with organic PCs via a reductive quenching pathway	32

2.2.6 Photo-LCP with organic and transition-metal-based PCs.....	34
2.2.7 Photo-ROMP with organic PCs	36
2.3 Setting the frame	38
2.3.1 Structure-property-performance relationships (SPPRs).....	38
2.3.2 Photon absorption: molar extinction coefficients and absorption wavelengths	39
2.3.3 Electronic transitions: rate constants and quantum yields	40
2.3.4 Activation and deactivation of photo-controlled polymerisation: redox properties.....	40
2.4 Spectral properties: bathochromic shift and hyperchromic effect	41
2.4.1 Theories and structure-property relationships.....	41
2.4.2 Computational methodologies	41
2.4.3 Bathochromic shift and hyperchromic effect by heavy halogen substituents	42
2.4.4 Bathochromic shift by chromophore core-twisting.....	44
2.4.5 Bathochromic shift by introduction of alkyl/aryl oxide or sulfide substituents	46
2.4.6 Bathochromic shift and hyperchromic effect by extended π -conjugation	49
2.5 Electronic transitions: enhanced triplet quantum yield.....	52
2.5.1 Theories and structure-property relationships.....	52
2.5.2 Computational methodologies	54
2.5.3 Enhanced triplet quantum yield by excited state charge transfer.....	56
2.5.4 Enhanced triplet quantum yield by heavy atom effect.....	60
2.5.5 Enhanced triplet quantum yield by chromophore core-twisting.....	61
2.6 Redox properties: the catalytic role of PCs in quenching pathways.....	64
2.6.1 Theories and structure-property relationships.....	64
2.6.2 Photo-ATRP via the oxidative quenching pathway	66
2.6.3 PET-RAFT via the oxidative quenching pathway	73
2.6.4 Photo-LCP via the reductive quenching pathway.....	76

2.7 References	77
Chapter 3 Learning from Natural Photocatalyst Design: Chlorophyll a and its Crude Extract as Efficient Photocatalyst for PET-RAFT Polymerisation with Oxygen Tolerance and Post-Decolourisation Functionalities	84
3.1 Introduction	85
3.2 Experimental section	87
3.2.1 Monitoring PET-RAFT polymerisation catalysed by Chl a	87
3.2.2 General procedures for observation of singlet oxygen in solution	87
3.2.3 Catalyst removal after polymerisation	88
3.2.4 Characterisation of end-group fidelity	88
3.3 Results and discussion	89
3.3.1 Kinetic studies of PET-RAFT polymerisation catalysed by Chl a	89
3.3.2 Oxygen tolerance in PET-RAFT polymerisation catalysed by Chl a	93
3.3.3 Post-decolourisation of Chl a after polymerisation	97
3.4 Conclusions	100
3.5 References	100
Chapter 4 Guiding the Design of Organic Photocatalyst for PET-RAFT Polymerisation: Halogenated Xanthene Dyes	103
4.1 Introduction	104
4.2 Experimental section	106
4.2.1 General procedures for kinetic study of PET-RAFT polymerisation in the presence/absence of oxygen	106
4.3 Results and discussion	107
4.3.1 Kinetics and oxygen tolerance studies	107
4.3.2 Property-performance relationship: correlating PET-RAFT performance with PC properties	120
4.3.3 Structure-property relationship: effect of halogen substitution on photophysical properties	126

4.3.4 Structure-property relationship: effect of halogen substitution on electrochemical properties	130
4.3.5 Employing the structure-property-performance relationship for on-demand design of PC in PET-RAFT	131
4.3.6 An extension of the structure-property-performance relationship	136
4.4 Conclusions	138
4.5 References	138
Chapter 5 Fully Computer-Guided Rational Design of a pH-Responsive Organic Photocatalyst and Application for pH and Light Dual-Gated Polymerisation.....	143
5.1 Introduction	144
5.2 Experimental section	147
5.2.1 Synthesis of the RAFT agent: BTPA-M	147
5.2.2 General procedures for PET-RAFT polymerisation	149
5.2.3 Polymer purification.....	150
5.3 Results and discussion	150
5.3.1 Establishing structure-property relationships for functional OPC design....	150
5.3.2 Structure-property relationship: electrostatic studies of pH-responsive xanthene dyes	151
5.3.3 Structure-property relationship: photophysical and electrochemical studies of OPCs	155
5.3.4 Quantum chemical calculations	156
5.3.5 Computer-guided design of highly pH-responsive OPC and theoretical predictions	160
5.3.6 Synthesis and characterisation of the designed OPC	163
5.3.7 Application of the designed OPC for dual-switchable PET-RAFT polymerisation.....	181
5.4 Conclusion	191
5.5 References	192
Chapter 6 Conclusions and Future Work.....	197

TABLE OF CONTENTS

6.1 Conclusions	197
6.2 Future work	198
6.3 References	200
Chapter 7 Appendix	201
7.1 Materials.....	201
7.2 Instrumentation	201

List of Figures

- Figure 2.1** FMOs and their energy levels of S_0 state (A) Erythrosine B (64), (B) Eosin Y (63), (C) Rose Bengal (65), and (D) Phloxine B (66). q : percentage of the MO localised on the specified element.44
- Figure 2.2** (a) The planar, bent, and twisted conformations of two adjacent p-orbitals. (b) Calculated HOMO and LUMO energy levels of anthracene (as a simplified example of twisted acene derivatives) with different twist angles.45
- Figure 2.3** Chemical structures, molecular geometries and visualized FMOs (isovalue = 0.03) of PDI derivatives PDI-1, PDI-2, PDI-3, PDI-4, PDI-5 and PDI-6.47
- Figure 2.4** Chemical structures and molecular geometries of the free-base phthalocyanine 85, the free-base β -alkyloxy-substituted phthalocyanine 86, the free-base α -alkyloxy-substituted phthalocyanine 87, the zinc(II) phthalocyanine 88, the zinc(II) β -alkyloxy-substituted phthalocyanine 89, the zinc(II) α -alkyloxy-substituted phthalocyanine 90..49
- Figure 2.5** Chemical structures and HOMOs/LUMOs (and corresponding energy levels) of polynaphthalenetetracarboxylic dianhydride diimide dyes 91, 92 and 93.51
- Figure 2.6** Left: molecular geometries of 30 and 40, with Φ_{ISC} (Φ_T) denoted below. Right: diagram of excited and ground state energy levels with alternative ISC pathways presented for 30 and 40. Less likely pathways are indicated in dashed lines.57
- Figure 2.7** Top: chemical structures of 96, 34 and 35. Bottom: energy level diagram of 96, 34 and 35 showing dominant decay pathways of excited states.59
- Figure 2.8** Top: chemical structures of twisted acene derivatives Ant- C_n ($n = 3-6$) tethered with alkyl bridges ($n =$ propyl bridge to hexyl bridge). Bottom: transient EPR spectra for Ant- C_n and the open (no alkyl bridges) reference compound.63
- Figure 2.9** (A) Chemical structures of 22 and 23, with $E_{ox}^*(PC^{*+}/^3PC^*)$ denoted below the label. (B) T_1 FMOs of 22 and 23 visualising the higher-lying SOMO (top) and the lower lying SOMO (bottom).69

- Figure 2.10** (A) Chemical structures, geometric reorganisation energies and reduction potentials (vs. SCE) for the three original chromophore core structures (phenoxazine 27, dihydrophenazine 18 and phenothiazine 12). 70
- Figure 2.11** (A) Chemical structures of 27-30, with $E_{ox}^*(PC^{•+}/^3PC^*)$ denoted below the label. (B) T_1 FMOs of 27-30 visualising the higher-lying SOMO (top) and the lower lying SOMO (bottom). 71
- Figure 3.1** Kinetic studies of PET-RAFT polymerisation of DMA with BTPA as the RAFT agent, catalysed by pure Chl a (blue line in (A) and blue square in (B)) or a crude extract with identical Chl a concentration (red line in (A) and red triangle in (B)) under red light irradiation, using a molar ratio of [DMA]:[BTPA]:[Chl a (pure or in crude extract)] = 200:1:0.0025, in degassed systems. (A) Plot of $\ln([M]_0/[M]_t)$ against reaction time and (B) M_n and M_w/M_n (polydispersity PDI) versus monomer conversion. 91
- Figure 3.2** Molecular weight distributions at different time points for DMA polymerisation with BTPA (under red light irradiation, using a molar ratio of [DMA]:[BTPA] = 200:1) in nitrogen degassed systems (A) catalysed by 12.5 ppm Chl a (with respect to the monomer concentration) and (B) catalysed by a crude extract containing 12.5 ppm Chl a. 92
- Figure 3.3** Plot of $\ln([M]_0/[M]_t)$ against reaction time measured by online FTNIR for DMA polymerisation with 1.25 ppm β -carotene (with respect to the monomer concentration) added at the beginning (blue curve) and in the middle (red curve) of polymerisation, under red light and deoxygenated conditions. The molar ratio: [DMA]:[BTPA]:[Chl a (pure)] = 200:1:0.0025. 93
- Figure 3.4** Kinetic studies of PET-RAFT polymerisations of DMA using BTPA as RAFT agent and pure Chl a (A and B) or crude extract (C and D) as photo-catalyst under red light irradiation, in degassed systems (blue line in A and C; blue square in B and D) and non-degassed systems (red line in A and C; red triangle in C and D) with a molar ratio of [DMA]:[BTPA]:[Chl a (pure or in crude extract)] = 200:1:0.0025. (A and C) $\ln([M]_0/[M]_t)$ versus reaction time of polymerisation. (B and D) M_n and M_w/M_n (polydispersity PDI) versus monomer conversion. 94

Figure 3.5 (A, B, D and E) Plot of $\ln([M]_0/[M]_t)$ against time with on/off properties measured by online FTNIR for DMA polymerisation with BTPA (under red light irradiation, using a molar ratio of $[DMA]:[BTPA] = 200:1$); (C and F) molecular weight distributions at different time points; (A) catalysed by 12.5 ppm Chl a in the degassed system, (B and C) catalysed by 12.5 ppm Chl a in the non-degassed system (D) catalysed by a crude extract containing 12.5 ppm Chl a in the degassed system and (E and F) catalysed by a crude extract containing 12.5 ppm Chl a in the non-degassed system. ..95

Figure 3.6 ^1H NMR spectrum (300 MHz, CDCl_3) for purified PDMA synthesised in the presence of 12.5 ppm pure Chl a (with respect to the monomer concentration), red LED light and oxygen ($M_{n,\text{GPC}} = 15\,400$ g/mol, $M_{n,\text{th}} = 17\,300$ g/mol, monomer conversion = 86%), obtained from a different experiment from that in Table 3.1, #3 under identical conditions.96

Figure 3.7 ^1H NMR spectrum (300 MHz, CDCl_3) of purified PDMA synthesised in the presence of 12.5 ppm Chl a (crude), red LED light and oxygen ($M_{n,\text{GPC}} = 14\,000$ g/mol, $M_{n,\text{th}} = 14\,700$ g/mol, monomer conversion = 72%), obtained from a different experiment from that in Table 3.1, #4 under identical conditions.97

Figure 3.8 Evolution of the absorbance of dimethylantracene in the presence of Chl a overtime in CH_3CN (red line) and DMSO (blue line) under red light irradiation without degassing.97

Figure 3.9 UV-Vis spectra before (red curve in A and B) and after (blue curve in A and B) PET-RAFT polymerisations in non-degassed systems (A) catalysed by pure Chl a and (B) catalysed by crude extract using a molar ratio of $[DMA]:[BTPA]:[\text{Chl a (pure or in the crude extract)}] = 200:1:0.0025$98

Figure 3.10 (A) Photograph and (B) UV-Vis spectra of pure Chl a solutions in DMSO before and after 12 h red light irradiation ($[\text{Chl a}] = 4$ ppm).98

Figure 3.11 Photographs of MA polymerisation using pure Chl a under air with a molar ratio of $[\text{MA}]:[\text{BTPA}]:[\text{Chl a}] = 200:1:0.0025$ at the beginning and after polymerisation under red light irradiation and the corresponding UV-vis spectrum after polymerisation.99

- Figure 3.12** Chl a degradation and catalyst removal. (A) photographs of the polymer solution before and after 10 h of catalyst degradation under open air and red light irradiation and their corresponding UV-vis spectra; (B) GPC traces for PMA obtained after polymerisation (red line) and catalyst degradation (blue dashed line) as well as the diblock copolymer synthesised by chain extension of PMA macroRAFT agent with pure Chl a as the photoredox catalyst in the absence of oxygen ([DMA]:[macroPMA]:[Chl a] = 1000:1:0.0025) (green line). 99
- Figure 4.1** (A) Structural variation of halogenated xanthene dyes investigated in this work; (B) properties of PCs and halogen substituents; (C) UV-vis spectra of dyes determined in model DMSO solution of a typical PET-RAFT system (top) and the corresponding λ_{\max} (bottom). 108
- Figure 4.2** $\ln([M]_0/[M]_t)$ versus irradiation time under 2 mW/cm² 530 nm and 2 mW/cm² 560 nm in an EB-catalysed PET-RAFT polymerisation. 109
- Figure 4.3** Kinetics studies of degassed PET-RAFT polymerisations of DMA catalysed by (A, E and I) EB, (B, F and J) EY, (C, G and K) RB and (D, H and L) PB. (A-D) plot of $\ln([M]_0/[M]_t)$ versus time to reveal k_p^{app} and temporal control; (E-F) M_n and M_w/M_n versus monomer conversion; (I-L) molecular weight distributions of four GPC aliquots taken during polymerisation, denoted as S1, S2, S3, S4, which corresponds to blue arrows in (A-D) following the time order. 110
- Figure 4.4** Oxygen tolerance studies of PET-RAFT polymerisations of DMA catalysed by (A, E and I) EB, (B, F and J) EY, (C, G and K) RB and (D, H and L) PB. (A-D) Evolution of $\ln([M]_0/[M]_t)$ versus time; (E-F) Evolution of M_n and M_w/M_n versus monomer conversion; (I-L) molecular weight distributions taken during polymerisation, denoted as S1, S2, S3, S4, which correspond to red arrows in (A-D) following the time order. 111
- Figure 4.5** MALDI-TOF MS of a PDMA sample synthesised by PET-RAFT polymerisation (A) in the absence of oxygen (degassed polymerisation) and (B) in the presence of oxygen (non-degassed polymerisation) with EB as PC. By zooming into the molecular weights range of 2200-2400 g/mol, we observed that major peaks (a and c) excellently agree with the theoretical values of PDMA with BTPA chain-end group plus Na⁺ whereas minor peaks (b and d) can be assigned to PDMA with BTPA chain-end

group plus K^+ , all within experimental error (< 1 m/z). For peaks a and b, number of monomer insertion (n) is determined to be 20, whereas for peaks c and d, it is determined to be 21. 113

Figure 4.6 MALDI-TOF MS of a PDMA sample synthesised by PET-RAFT polymerisation in the absence of oxygen (degassed polymerisation) with EY as catalyst. By zooming into the molecular weight range of 2200-2400 g/mol, we observed that major peaks (a and c) excellently matches theoretical predication of PDMA with BTPA chain-end group plus Na^+ while minor peaks can be assigned to PDMA with BTPA chain-end group plus K^+ , all within experimental error (< 1 g/mol). For peaks a and c, number of monomer insertion (n) is determined to be 20, whereas for peaks c and d, it is determined to be 21. $M_{n,GPC} = 2,300$ g/mol; PDI = 1.11. 113

Figure 4.7 MALDI-TOF MS of a PDMA sample synthesised by PET-RAFT polymerisation in the presence of oxygen (non-degassed polymerisation) with EY as catalyst. By zooming into the molecular weight range of 2200-2400 g/mol, we observed that major peaks (a and c) excellently matches theoretical predication of PDMA with BTPA chain-end group plus Na^+ while minor peaks can be assigned to PDMA with BTPA chain-end group plus K^+ , all within experimental error (< 1 g/mol). For peaks a and c, number of monomer insertion (n) is determined to be 20, whereas for peaks c and d, it is determined to be 21. $M_{n,GPC} = 2,300$ g/mol; PDI = 1.11. 114

Figure 4.8 MALDI-TOF MS of a PDMA sample synthesised by PET-RAFT polymerisation in the absence of oxygen (degassed polymerisation) with RB as catalyst. By zooming into the molecular weight range of 2200-2400 g/mol, we observed that major peaks (a and c) excellently matches theoretical predication of PDMA with BTPA chain-end group plus Na^+ while minor peaks can be assigned to PDMA with BTPA chain-end group plus K^+ , all within experimental error (< 1 g/mol). For peaks a and c, number of monomer insertion (n) is determined to be 20, whereas for peaks c and d, it is determined to be 21. $M_{n,GPC} = 2,400$ g/mol; PDI = 1.11. 115

Figure 4.9 MALDI-TOF MS of a PDMA sample synthesised by PET-RAFT polymerisation in the presence of oxygen (non-degassed polymerisation) with RB as catalyst. By zooming into the molecular weight range of 2200-2400 g/mol, we observed that major peaks (a and c) excellently matches theoretical predication of PDMA with

BTPA chain-end group plus Na^+ while minor peaks can be assigned to PDMA with BTPA chain-end group plus K^+ , all within experimental error (< 1 g/mol). For peaks a and c, number of monomer insertion (n) is determined to be 20, whereas for peaks c and d, it is determined to be 21. $M_{n,\text{GPC}} = 2,500$ g/mol; PDI = 1.11. 115

Figure 4.10 MALDI-TOF MS of a PDMA sample synthesised by PET-RAFT polymerisation in the absence of oxygen (degassed polymerisation) with PB as catalyst. By zooming into the molecular weight range of 2200-2400 g/mol, we observed that major peaks (a and c) excellently matches theoretical predication of PDMA with BTPA chain-end group plus Na^+ while minor peaks can be assigned to PDMA with BTPA chain-end group plus K^+ , all within experimental error (< 1 g/mol). For peaks a and c, number of monomer insertion (n) is determined to be 20, whereas for peaks c and d, it is determined to be 21. $M_{n,\text{GPC}} = 2,300$ g/mol; PDI = 1.11. 116

Figure 4.11 MALDI-TOF MS of a PDMA sample synthesised by PET-RAFT polymerisation in the presence of oxygen (non-degassed polymerisation) with PB as catalyst. By zooming into the molecular weight range of 2200-2400 g/mol, we observed that major peaks (a and c) excellently matches theoretical predication of PDMA with BTPA chain-end group plus Na^+ while minor peaks can be assigned to PDMA with BTPA chain-end group plus K^+ , all within experimental error (< 1 g/mol). For peaks a and c, number of monomer insertion (n) is determined to be 20, whereas for peaks c and d, it is determined to be 21. $M_{n,\text{GPC}} = 2,500$ g/mol; PDI = 1.11. 117

Figure 4.12 (A) ^1H NMR spectrum (400 MHz, CDCl_3) for purified PDMA synthesised through EB-catalysed PET-RAFT polymerisation in the presence of oxygen. (B) Molecular weight distributions for PDMA in (A) before (blue line) and after (red line) chain extension; (C) corresponding M_n and M_w/M_n versus degree of polymerisation. M_n determined by NMR spectrum in (A) in blue square, as well as M_n determined by GPC for the same polymer before and after chain extension in red square, were all in excellent agreement with theoretical values (in dashed line). 117

Figure 4.13 Molecular weight distribution of the non-deoxygenated PET-RAFT polymerisation (A) with head space and (B) without head space catalysed by EB, targeting high molecular weights. $[\text{DMA}]:[\text{BTPA}] = 1400:1$; the concentration of EB is 20 ppm with respect to DMA. (A) with head space: $M_{n,\text{GPC}} = 61,000$ g/mol, $M_{n,\text{theoretical}} =$

76,000 g/mol, $M_w/M_n = 1.18$; (B) without head space: $M_{n, \text{GPC}} = 65,000$ g/mol, $M_{n, \text{theoretical}} = 73,000$ g/mol, $M_w/M_n = 1.10$ 119

Figure 4.14 Frontier orbitals, energy levels, their gaps and orbital composition on X-position halogens of the ground state (A) EB, (B) EY, (C) RB and (D) PB. Top: LUMO; bottom: HOMO. Contribution of HOMO→LUMO transitions to S_1 is denoted under the dye label. DFT calculations for frontier orbitals and TD-DFT calculations for excited state contribution were employed with B3LYP (6-31+G** basis set for C H O and LANL2DZ basis set for heavy atoms Cl Br I) level of theory and the CPCM-DMSO solvation model. Atom colour: C in yellow, H in white, O in red, Cl in green, Br in blue and I in purple. q: the portion of the corresponding molecular orbital located on the enclosed element, in percentage. 127

Figure 4.15 Upper and lower SOMOs, their energy levels and gaps between upper SOMO and lower SOMO of the T_1 state of (A) EB, (B) EY, (C) RB and (D) PB. Top: upper SOMO; bottom: lower SOMO. Unrestricted DFT calculations for T_1 frontier orbitals and TD-DFT calculations for excited state contribution were employed with B3LYP (6-31+G** basis set for C H O and LANL2DZ basis set for heavy atoms Cl Br I) level of theory and the CPCM-DMSO solvation model. 131

Figure 4.16 ^1H NMR spectrum (400 MHz, DMSO-d₆) of synthesised tetrabromofluorescein. 132

Figure 4.17 ^1H NMR spectrum (400 MHz, DMSO-d₆) of synthesised H1. 133

Figure 4.18 (A) Dye structure of the synthesised dye H1 and its (B) UV-vis spectrum determined in model DMSO solution of a typical PET-RAFT system. (C) evolution of $\ln([M]_0/[M]_t)$ versus time, (D) M_n and M_w/M_n versus monomer conversion, (E-F) molecular weight distributions taken during polymerisation in the presence (E) and absence (F) of oxygen, denoted as S1, S2, S3, S4, which corresponds to blue arrows in (D) following the time order of H1-catalysed PET-RAFT polymerisation. (G) HOMO, LOMO and their energy levels and (H) upper SOMO, lower SOMOs and their energy levels of H1. (I) Table summarizing property-performance evaluation of four commercial xanthene dyes and the synthesised H1; the quantum yield range of H1 was estimated from the first-order approximation fitting of the reported data for EY, EB, PB and RB (SI,

Figure S14), based on the oxygen inhibition time of 14 min for H1-catalysed PET-RAFT polymerisation in the presence of oxygen.	134
Figure 4.19 Deriving the estimated range of Φ_T and Φ_Δ of H1 by respectively fitting the lower limits and higher limits of the reported values of EB, EY, RB and PB, employing first-order approximation.	135
Figure 4.20 (A) EOB chemical structure, (B) UV-vis spectrum determined in DMSO using a typical PET-RAFT concentration, (C) evolution of $\ln([M]_0/[M]_t)$ versus time, (D) evolution of M_n and M_w/M_n versus monomer conversion of the EOB-catalysed PET-RAFT polymerisation. (E) EOB HOMO, LOMO and their energy levels and (F) EOB upper SOMO, lower SOMOs and their energy levels.	137
Figure 4.21 Oxygen tolerance study of PET-RAFT polymerisation catalysed by EOB. (A) plot of $\ln([M]_0/[M]_t)$ versus time to reveal k_p^{app} and temporal control; (B) M_n and PDI versus conversion; (C-D) molecular weight distribution of four GPC aliquots taken during polymerisation, denoted as S1, S2, S3, S4, which corresponds to blue arrows in (B) for polymerisation in the absence of oxygen (C) and red arrows in (B) in the presence of oxygen (D) according to time order.	137
Figure 5.1 ^1H NMR spectrum (400 MHz, CDCl_3) of the synthesised BTPA-M.	148
Figure 5.2 ^{13}C NMR spectrum (400 MHz, CDCl_3) of the synthesised BTPA-M.	149
Figure 5.3 (A) Mechanism of the structural transition with response to specific pH (indicated below the corresponding dye structure at that pH) for EY (left), PB (middle), and the designed tetrabrominated benzoic acid group substituted-fluorescein (TBrFL, right). ¹⁰⁶ (B) Electrostatic potential (ESP) maps (presented as molecular surface coloured by ESP) calculated at the mono-protonated “intermediate” state structure of EY (left), PB (middle), and TBrFL (right) with the extreme points of interest indicated, correlating with their colourless transition pH (bottom). DFT calculations were performed at the BLY3P level of theory with the 6-31+G** basis set for C H O and the LanL2DZ basis set for heavy atoms Cl and Br under the SMD-water solvation model.	153
Figure 5.4 Computationally derived ground and excited state transition map of TBrFL.	160

- Figure 5.5** (A) Chemical structures of the active state (TBrFL²⁻, top) and the inactive/colourless state (TBrFLH₂, bottom) of TBrFL and their transition mechanism. (B) Frontier orbitals, energy levels (and their gaps) of the ground state TBrFL²⁻ (left) and the T₁ state TBrFL²⁻ (right). (C) Frontier orbitals, energy levels and their gaps of the ground state TBrFLH₂. Top: LUMO; bottom: HOMO. Contribution of HOMO→LUMO transitions to S₁ is denoted under the dye label. DFT calculations for frontier orbitals and TD-DFT calculations for orbital transition to S₁ were employed with B3LYP (6-31+G** basis set for C H O and LanL2DZ basis set for Br) level of theory and the SMD-water solvation model. Atom colour: C in yellow, H in white, O in red and Br in blue. 161
- Figure 5.6** pH-UV-vis kinetics of a RB aqueous solution (1.01×10⁻⁴ mol/L) demonstrating the spectral transition of RB with pH change. 163
- Figure 5.7** ¹H NMR spectrum (400 MHz, DMSO-d₆) of the synthesised TBrFL. 165
- Figure 5.8** ¹³C NMR spectrum (400 MHz, DMSO-d₆) of the synthesised TBrFL. 166
- Figure 5.9** pH-UV-vis kinetics of a TBrFL aqueous solution (1.68×10⁻⁴ mol/L) demonstrating the spectral transition of TBrFL with pH change. 166
- Figure 5.10** ¹H NMR spectrum (400 MHz, DMSO-d₆) of TBrFL²⁻ in a solution containing 5 mg TBrFL and ~2 mg NaHCO₃. 168
- Figure 5.11** ¹H NMR spectrum (400 MHz, DMSO-d₆) of TBrFLH₂ in a solution containing 5 mg TBrFL and bubbled with HCl/N₂ fume for 10 s. The split character in peaks for the four protons most adjacent to hydroxyl groups (denoted as “b” and “c”) confirmed the double presence of protons on the hydroxyl groups of the colourless ring-closed TBrFLH₂. 169
- Figure 5.12** Kinetic studies of TBrFL-catalysed PET-RAFT polymerisation of DMA in the presence or absence of oxygen. (A-C) Plot of ln([M]₀/[M]_t) versus time revealing (A) *k*_p^{app} and oxygen inhibition time, (B) temporal control in the absence of oxygen and (C) temporal control in the presence of oxygen; (D) *M*_n and *M*_w/*M*_n versus conversion, and (E-F) normalized molecular weight distribution of four GPC aliquots taken during polymerisation, denoted as S1, S2, S3, S4, (E) in the absence of oxygen corresponding to

blue arrows in (A) and (F) in the presence of oxygen corresponding to red arrows in (A), following the time order.	170
Figure 5.13 ^1H - ^{13}C HSQC NMR (CDCl_3 , 400 MHz, ^1H : δ 0~10 ppm; ^{13}C : δ 0~90 ppm) spectrum of the PDMA oligomers.	171
Figure 5.14 ^1H NMR spectrum (400 MHz, CDCl_3) of a mixture of 63.8% PDMA-BTPA-M oligomers and 36.2% BTPA-M as determined by specific proton signals.	172
Figure 5.15 ^1H NMR spectrum (400 MHz, CDCl_3) of an unpurified mixture of a DMA polymerisation aliquot from the batch in Table 2, entry 11. As this sample has a degree of polymerisation as low as ~20, the typical shape of proton signals as is in a polymer can be clearly identified.	173
Figure 5.16 ^1H NMR spectrum (400 MHz, CDCl_3) of purified PDMA synthesised through TBrFL-catalysed PET-RAFT polymerisation in the absence of oxygen (degassed).	174
Figure 5.17 ^1H NMR spectrum (400 MHz, CDCl_3) of purified PDMA synthesised through TBrFL-catalysed PET-RAFT polymerisation in the presence of oxygen (non-degassed).	175
Figure 5.18 Molecular weight distributions for the synthesised PDMA after TBrFL-catalysed PET-RAFT polymerisation in the absence of oxygen (red line) and the chain-extended PDMA- <i>b</i> -PDMA after chain extension EB-catalysed PET-RAFT polymerisation (blue line). Complete shift of molecular weight distributions to higher molecular weights confirmed the high retention of the trithiocarbonate chain end group.	175
Figure 5.19 Molecular weight distributions for the synthesised PDMA after TBrFL-catalysed PET-RAFT polymerisation in the presence of oxygen (red line) and the chain-extended PDMA- <i>b</i> -PDMA after chain extension EB-catalysed PET-RAFT polymerisation (blue line). Complete shift of molecular weight distributions to higher molecular weights confirmed the high retention of the trithiocarbonate chain end group.	176

Figure 5.20 MALDI-TOF MS of a PDMA sample synthesised by TBrFL-catalysed PET-RAFT polymerisation in the absence of oxygen (degassed). By zooming into the molecular weight range of 2500-2700 g/mol, we observed that major peaks (inset a) excellently matches theoretical predication of PDMA with BTPA chain-end group plus Na^+ (indicated on the left of the full spectrum), within experimental error (< 1 g/mol). For the left peaks in the inset a, the number of monomer insertion (n) is determined to be 23, whereas for the right peaks in the inset a, it is determined to be 24. $M_{n,\text{GPC}} = 3,300$ g/mol; $\text{PDI} = 1.21$ 177

Figure 5.21 MALDI-TOF MS of a PDMA sample synthesised by TBrFL-catalysed PET-RAFT polymerisation in the absence of oxygen (degassed). By zooming into the molecular weight range of 2500-2700 g/mol, we observed that major peaks (inset a) excellently matches theoretical predication of PDMA with BTPA chain-end group plus Na^+ (indicated on the left of the full spectrum), while minor peaks (inset b) can be assigned to PDMA with BTPA chain-end group plus K^+ (indicated on the left of the full spectrum), all within experimental error (< 1 g/mol). For the left peaks in the inset a and b, the number of monomer insertion (n) is determined to be 23, whereas for the right peaks in the inset a and b, it is determined to be 24. $M_{n,\text{GPC}} = 2,700$ g/mol; $\text{PDI} = 1.21$ 178

Figure 5.22 Molecular weight distributions for PDMA before chain extension (red) and PDMA-*b*-PDEA after chain extension (blue), Table 5.2, entry 10. 181

Figure 5.23 (A) Plot of $\ln([M]_0/[M]_t)$ versus time of TBrFL-catalysed PET-RAFT polymerisation of DMA in water in the presence of oxygen under green light using a few bubbles (~ 1 mL) of gaseous HCl/N_2 to generate pH-“OFF” state and small amount of NaHCO_3 powder (~ 0.5 mg) to generate pH-“ON” state. (B) Corresponding UV-vis spectra of different states in (A). (C) Plot of $\ln([M]_0/[M]_t)$ versus time of TBrFL-catalysed PET-RAFT polymerisation of DMA in water with two 3 h periods of pH-“OFF” and one 8 h-period of light-“OFF”. (D) Molecular weight distribution of five GPC aliquots taken during polymerisation in (C), denoted as S1, S2, S3, S4 and S5. 182

Figure 5.24 ^1H NMR spectrum (400 MHz, CDCl_3) of purified PDMA synthesised through non-degassed TBrFL-catalysed PET-RAFT polymerisation where HCl/N_2 and NaHCO_3 mediated pH manipulation was introduced. 183

- Figure 5.25** Molecular weight distributions for the synthesised PDMA after non-degassed TBrFL-catalysed PET-RAFT polymerisation where HCl/N₂ and NaHCO₃ mediated pH manipulation was introduced (red line) and the chain-extended PDMA-*b*-PDMA after chain extension EB-catalysed PET-RAFT polymerisation (blue line). Complete shift of molecular weight distributions to higher molecular weights confirmed the high retention of the trithiocarbonate chain end group. 183
- Figure 5.26** Plot of $\ln([M]_0/[M]_t)$ versus time of TBrFL-catalysed PET-RAFT polymerisation of DMA in water ([DMA]:[BTPA-M]:[TBrFL] = 200:1:0.01) under 5 mW/cm² 530 nm irradiation with a 90 min prolonged pH-“OFF” period and 10 min light-“OFF” period. 185
- Figure 5.27** Plot of $\ln([M]_0/[M]_t)$ versus time of TBrFL-catalysed PET-RAFT polymerisation of DMA in water at pH 5.0 ([DMA]:[BTPA-M]:[TBrFL] = 200:1:0.01) under 5 mW/cm² 530 nm irradiation. No polymerisation was observed over 4 h irradiation. 185
- Figure 5.28** (A) Plot of $\ln([M]_0/[M]_t)$ versus time of TBrFL-catalysed PET-RAFT polymerisation of MA in DMSO ([MA]:[BTPA-M]:[TBrFL] = 200:1:0.01, MA to DMSO 1:1 v/v) under 5 mW/cm² 530 nm irradiation with a 3 h period of pH-“OFF”. (B) Molecular weight distribution of GPC aliquots taken during polymerisation, denoted as S1, S2 and S3. 186
- Figure 5.29** (A) Chemical structure of NAM. (B) Plot of $\ln([M]_0/[M]_t)$ versus time of TBrFL-catalysed PET-RAFT polymerisation of NAM in water ([NAM]:[BTPA-M]:[TBrFL] = 200:1:0.01, NAM to water 1:1 v/v) under 5 mW/cm² 530 nm irradiation with a 3 h period of pH-“OFF” (pH =5.0) and a 3 h period of light-“OFF”. (C) Molecular weight distributions of GPC aliquots taken during polymerisation, denoted as S1, S2, S3 and S4. 188
- Figure 5.30** (A) Plot of $\ln([M]_0/[M]_t)$ versus time of TBrFL-catalysed PET-RAFT polymerisation in the presence of oxygen under green light using 1 min CO₂ purging to generate gas-quasi-“OFF” state and 10 min N₂ purging to generate gas-on state. (B) Corresponding UV-vis spectra of different states in (A). 190

Figure 5.31 ^1H NMR spectrum (400 MHz, CDCl_3) of purified PDMA synthesised through non-degassed TBrFL-catalysed PET-RAFT polymerisation where CO_2 and N_2 were used to manipulate the polymerisation rate. 190

Figure 5.32 Molecular weight distributions for the synthesised PDMA after non-degassed TBrFL-catalysed PET-RAFT polymerisation where CO_2 and N_2 mediated pH manipulation was introduced (red line) and the chain-extended PDMA-*b*-PDMA after chain extension EB-catalysed PET-RAFT polymerisation (blue line). Complete shift of molecular weight distributions to higher molecular weights confirmed the high retention of the trithiocarbonate chain end group. 191

List of Tables

Table 2.1 Spectral Properties of Halogenated Xanthene Dyes.	44
Table 2.2 Observed and calculated absorption spectra of polynaphthalenetetracarboxylic dianhydride diimide dyes 91, 92 and 93.	51
Table 2.3 Photophysical properties of 96, 34 and 35.	59
Table 2.4 Photophysical properties of halogenated xanthene dyes 64, 63, 65 and 66.	60
Table 3.1 PET-RAFT polymerisation of DMA with BTPA using crude and pure Chl a ([DMA]: [RAFT]: [Chl a] = 200: 1: 2.5×10^{-3}) as photoredox catalysts ([Chl a]/[DMA] = 12.5 ppm) under red light irradiation ($\lambda_{\max} = 635$ nm, light intensity = 2.55 mW/cm ²) in DMSO.	91
Table 4.1 Photophysical properties of halogenated xanthene dyes.	107
Table 4.2 PET-RAFT polymerisation catalysed by EB in different solvents ([DMA]:[BTPA]:[EB] = 200:1:0.004, monomer/solvent, 1/1 (v/v)).	120
Table 4.3 k_p^{app} of PET-RAFT polymerisation in comparison with photophysical and electrochemical properties of the photocatalysts.	124
Table 4.4 Inhibition periods of PET-RAFT in the presence of oxygen and photocatalyst properties.	125
Table 5.1 Electrostatic, electrochemical, photophysical and pH responsive properties of dyes mentioned in this work in comparison.	162
Table 5.2 Details for polymerisation with different monomers, RAFT agents, solvents, and ratios.	179
Table 5.3 GPC characterisation of S1, S2, S3 ,S4 and S5 in pH and light dual-controlled DMA polymerisation in the kinetic study shown as Figure 5.23.	184
Table 5.4 GPC characterisation of S1, S2 and S3 in pH-gated MA polymerisation in the kinetic study shown as Figure 5.28.	186

Table 5.5 GPC characterisation of S1, S2 ,S3 and S4 in pH and light dual-controlled DMA polymerisation in the kinetic study shown as Figure 5.29.	188
---	-----

List of Schemes

Scheme 2.1 Left: the proposed mechanism for photo-ATRP via the oxidative quenching pathway. Right: chemical structures of ATRP initiators commonly used in photo-ATRP (EBPA, ECIPA, EBiB and BnBiB). ISC: intersystem crossing; M: monomer.	16
Scheme 2.2 Chemical structures of transition-metal-based complexes 1-7 used as PCs for photo-ATRP.	17
Scheme 2.3 Left: the proposed mechanisms for PET-RAFT polymerisation via the oxidative quenching pathway. Left top: PET-RAFT polymerisation via the oxidative quenching pathway by photoinduced electron transfer (PET). Left bottom: PET-RAFT polymerisation via the oxidative quenching pathway by photoinduced Dexter/triplet energy transfer (P3T). Right: chemical structures of thiocarbonylthio RAFT agents commonly used in PET-RAFT polymerisations (trithiocarbonates: BTPA, BSTP, CDTPA and CPDTC; dithiobenzoates: CPADB and CDB; xanthate). ISC: intersystem crossing; M: monomer. Z: the Z group of the RAFT agent.	19
Scheme 2.4 Chemical structures of transition-metal-based complexes 1 and 8-10 used as PCs for PET-RAFT polymerisation.	20
Scheme 2.5 Chemical structures of perylene 11 and phenothiazine derivatives 12-17 used as PCs for metal-free photo-ATRP.	22
Scheme 2.6 Chemical structures of dihydrophenazine derivatives 18-26 used as PCs for O-ATRP.	23
Scheme 2.7 Chemical structures of phenoxazine derivatives 27-37 used as PCs for O-ATRP.	25
Scheme 2.8 Chemical structures of phenoxazine derivatives 38-45 with extended π -conjugation used as PCs for O-ATRP.	26
Scheme 2.9 Chemical structures of dimethyl-dihydroacridine derivatives 46-52 used as PCs for O-ATRP.	27

Scheme 2.10 Chemical structures of representative examples 53 and 54 of highly efficient organic PCs for O-ATRP designed with D-A scaffolds via a computer-aided molecular design/screening platform. ³⁸	28
Scheme 2.11 Chemical structures of highly conjugated thienothiophene derivatives 55-58 for O-ATRP. ⁸⁶	29
Scheme 2.12 Chemical structures of metal-free porphyrin derivatives 59, 60 and 61 used as organic PCs for PET-RAFT polymerisation.....	30
Scheme 2.13 Chemical structures of fluorescein derivatives 62-68 used as organic PCs for PET-RAFT polymerisation.	31
Scheme 2.14 Chemical structures of PCs emerged from studies on photo-ATRP (68-70 and 53-54) used as organic PCs for PET-RAFT polymerisation.	32
Scheme 2.15 Left: the proposed mechanisms for photo-RDRP via the reductive quenching pathway. Left top: photo-ATRP via the oxidative reductive pathway. Left bottom: PET-RAFT polymerisation via the reductive quenching pathway. Right: chemical structures of representative tertiary amines (TAs) for photo-RDRP via the reductive quenching pathway (TEA, TEOA, TBA, MDEA, DMAP and EDB). ISC: intersystem crossing; M: monomer. TA: tertiary amine.	33
Scheme 2.16 Left: the proposed mechanism for photo-LCP via the reductive quenching pathway. Right: chemical structures of RAFT agents proven effective for photo-LCP, i.e., IBDTC (<i>S</i> -1-isobutoxyethyl <i>N,N</i> -diethyl dithiocarbamate) and IBTTC (<i>S</i> -1-isobutoxyethyl <i>S'</i> -ethyl trithiocarbonate). ISC: intersystem crossing; M: monomer. Z: the Z group of the RAFT agent.	34
Scheme 2.17 Chemical structures of pyrylium derivatives (72-76) and Ir-based complexes (77-79) used as PCs for photo-LCP.	36
Scheme 2.18 Left: the proposed mechanism for photo-ROMP via the reductive quenching pathway. Right: chemical structures of the initiators (right top) and monomers (right bottom) used in photo-ROMP. ISC: intersystem crossing. R and R' in left: the substitution groups on both sides of the initiator.	36

Scheme 2.19 Chemical structures of pyrylium derivatives (72-74 and 82) and thiopyrylium derivatives (80, 81, 76 and 83) used as PCs for photo-ROMP.	37
Scheme 2.20 The general mechanism of photo-controlled polymerisation catalysed by a PC. Left: the oxidative quenching pathway. Right: the reductive quenching pathway.	39
Scheme 2.21 Chemical structures of halogenated xanthene dyes 64, 63, 65 and 66.	43
Scheme 2.22 Chemical structures of 9 and 84.	45
Scheme 2.23 Chemical structures of a phthalocyanine derivative 94 and the corresponding naphthalocyanine derivative 95.	52
Scheme 2.24 (a) Jablonski diagram. (b) El-Sayed's rules. (c) Rotational property of the orbital angular momentum.	53
Scheme 2.25 Computationally derived Jablonski diagram of a synthesised halogenated xanthene dye and its derivation of Φ_T from different excited state decay constants.	56
Scheme 2.26 Chemical structures of 62 and 68, with k_f , k_{ic} , k_{isc} and Φ_T denoted below.	60
Scheme 2.27 Chemical structures and representation of molecular geometries of 97, 98, 99, with Φ_T and k_{isc} denoted below the dye labels.	62
Scheme 2.28 The oxidative quenching pathway (left) and the reductive quenching pathway (right) of a PC. "cat" represents PC and "sub" represents the substrate.	65
Scheme 2.29 Redox potentials for the PET process depicted in the oxidative quenching pathway (left) and the reductive quenching pathway (right) of a PC. "sub" stands for the substrate.	65
Scheme 2.30 Left: chemical structures of 1 <i>fac</i> -[Ir(ppy) ₃] and 12 Ph-PTZ with $E_{ox}^*(PC^{*+}/^3PC^*)$ and $E_{ox}(PC^{*+}/PC)$ denoted below the dye label. Right: Simplified scheme for the activation/deactivation mechanism of photo-ATRP.	66
Scheme 2.31 Top: chemical structures of dihydrophenazine derivatives 19, 18, 20 and 21, with $E_{ox}^*(PC^{*+}/^3PC^*)$ denoted below the label. Bottom: the proposed mechanism for O-ATRP.	68

- Scheme 2.32** (A) Chemical structures of 27, 29-45 and 100, arranged by $E_{\text{ox}}^*(\text{PC}^{*\cdot}/^3\text{PC}^*)$, with $E_{\text{ox}}^*(\text{PC}^{*\cdot}/^3\text{PC}^*)$, $E_{\text{ox}}(\text{PC}^{*\cdot}/\text{PC})$ and E_{T} denoted below the label. $E^{0*\cdot}_{\text{T1,calc}}$: the calculated $E_{\text{ox}}^*(\text{PC}^{*\cdot}/^3\text{PC}^*)$. E^0_{ox} : $E_{\text{ox}}(\text{PC}^{*\cdot}/\text{PC})$. E_{T} : the T₁ excitation energy. 72
- Scheme 2.33** (A) Chemical structures of 46-52, arranged by $E_{\text{ox}}^*(\text{PC}^{*\cdot}/^3\text{PC}^*)$, with $E_{\text{ox}}^*(\text{PC}^{*\cdot}/^3\text{PC}^*)$, $E_{\text{ox}}(\text{PC}^{*\cdot}/\text{PC})$ below the label. $E^{0*\cdot}_{\text{T1,exp}}$: the experimental $E_{\text{ox}}^*(\text{PC}^{*\cdot}/^3\text{PC}^*)$. $E_{1/2}$: $E_{\text{ox}}(\text{PC}^{*\cdot}/\text{PC})$ 73
- Scheme 2.34** Top: the proposed mechanism of PET-RAFT polymerisation with *fac*-[Ir(ppy)₃] 1 as PC. Bottom: chemical structures of RAFT agents CPADB, BTPA, BSTP and Xanthate. 74
- Scheme 2.35** Chemical structures of ZnTPP 9 and TPP 58. 75
- Scheme 2.36** Chemical structures of 64, 63, 65, 66, 62 and 68 with their $E_{\text{ox}}^*(\text{PC}^{*\cdot}/^3\text{PC}^*)$ denoted below the label. Bottom right: electronegativity of the substituent halogens and $E_{\text{ox}}^*(\text{PC}^{*\cdot}/^3\text{PC}^*)$ of the PCs in comparison. 76
- Scheme 2.37** Top: the proposed mechanism of photo-LCP regulated by a RAFT agent. Bottom: chemical structures of 72-76 with $E_{\text{red}}^*(\text{PC}^*/\text{PC}^{\cdot-})$ and $E_{\text{red}}(\text{PC}/\text{PC}^{\cdot-})$ vs. SCE denoted below the label. 77
- Scheme 3.1** (A) Proposed mechanism of PET-RAFT polymerisation catalysed by Chl a and post-polymerisation catalyst degradation; (B) the chemical structure of Chl a. 90
- Scheme 4.1** (A) Proposed mechanism of oxygen-tolerant PET-RAFT polymerisation. TTA: triplet-triplet annihilation for oxygen elimination; $^3\Sigma$: molecular oxygen; $^1\Delta$: singlet oxygen; (B) Chemical structures of commercial halogenated xanthene dyes; and (C) the model RAFT agent and monomer for investigation of PC structure-property-performance relationships in this work. 106
- Scheme 5.1** (A) Comparison of the current work with our previous work.⁹⁰ Whereas the previous work revealed the foundations for structure-property-performance (SPP) relationships of OPCs in the scope of PET-RAFT polymerisation, the current work expands upon the SPP relationships to physical and photophysical properties by predicting quantum yields and excited state transition rate constants. Additionally, this work demonstrates a fully computer-guided catalyst design (TBrFL) for application in

the first reported example of pH/light dual-gated organic catalysis. (B) Flow chart of application-directed OPC design fully guided by computational predictions. 147

Scheme 5.2 (A) pH dependence of fluorescein derivative equilibria.¹⁰⁶⁻¹⁰⁷ Structure *I* is the major and most stable light-absorbing species whereas structure *V* is the major and most stable ring-closed colourless species. pK_2 is the key pK_a equilibrium constant that describes the critical point for the change between a light-absorbing-species-dominant condition and a colourless-species-dominant condition. According to the rule of thumb in pH indicators, dye solutions visually turn colourless at the colourless $pH \approx pK_2 - 1$.¹⁰⁸ (B) Summary of structure-property relationships investigated in this work to guide OPC design. Structure of FL, EY, PB, and the designed TBrFL with substituent variations (left); colourless pH (physical property, middle left bottom); electronegativity and atomic number of the substituents in comparison (middle right); electrochemical and photophysical properties (determining photocatalysis efficacy) of FL, EY, PB, and the designed TBrFL (right). 151

Scheme 5.3 Chemical structures of (A) monomers, (B) RAFT agents, and (C) solvents used. 179

List of Equations

Equation 4.1 Relation between ΔG_{red} and $E^0(\text{PC}^{*+}/{}^3\text{PC}^*)$	121
Equation 4.2 The PET reaction in the PET-RAFT polymerisation.	121
Equation 4.3 Expression of ΔG	121
Equation 4.4 Basic equation of the Marcus Theory.	121
Equation 4.5 The electron transfer rate equation for activation-controlled reactions expressed by the Gibbs free energy change of the formation of the transition state. ..	122
Equation 4.6 The experimental empirical expression of ΔG^\ddagger for intermolecular electron transfer in solvents according to the Rehm-Weller behaviour.	122
Equation 4.7 In PET-RAFT polymerisation, because k_{et} should be positively related to the propagation radical concentration $[\text{R}^*]$ (k_{et} defines the rate of electron transfer and each electron transfer should generate a propagating radical which enters the activation-deactivation equilibrium), the apparent propagation rate $k_{\text{p}}^{\text{app}}$ should thus also be positively related to k_{et}	122
Equation 5.1 Calculation of Φ_{T} based on electronic transition decay constants.	159

List of Abbreviations

$^1\text{O}_2$	singlet oxygen
AdNDP	Adaptive Natural Density Partitioning
ATRP	atom transfer radical polymerisation
BA	<i>n</i> -butyl acrylate
BDF	Beijing Density Functional
BET	back electron transfer
BnBiB	benzyl α -bromoisobutyrate
Br	bromine
BSTP	3-benzylsulfanylthiocarbonylsulfanyl propionic acid
BTPA	2-(<i>n</i> -butyltrithiocarbonate)-propionic acid
CDB	2-phenyl-2-propyl benzodithioate
CDTPA	4-cyano-4-[(dodecylsulfanylthiocarbonyl)sulfanyl]pentanoic acid
Chl a	chlorophyll a
Cl	chlorine
CLRP	controlled/"living" radical polymerisation
CMPR	cobalt-mediated radical polymerisation
CPADB	4-cyano-4-(phenylcarbonothioylthio)pentanoic acid
CPDTC	2-cyano-2-propyl dodecyl trithiocarbonate
CT	charge transfer
D-A	donor-acceptor
DCC	1,3-dicyclohexylcarbodiimide
DCM	dichloromethane
DEA	diethyl acrylamide
DEGEEA	di(ethylene glycol) ethyl ether acrylate
DFT	density functional theory
DMA	<i>N,N'</i> -dimethylacrylamide
DMAc	<i>N,N'</i> -dimethylacetamide
DMAEMA	2-(dimethylamino)ethyl methacrylate
DMAP	dimethyl aminopyridine
DMAP	4-Dimethylaminopyridine
DMF	<i>N,N'</i> -dimethylformamide
DMSO	dimethyl sulfoxide
DMSO ₂	dimethyl sulfone
DP	degree of polymerisation
DVP	dimethyl vinylphosphonate
E ₀	standard redox potential
EB	erythrosin B
EBiB	ethyl α -bromoisobutyrate
EBPA	ethyl- α -bromophenylacetate
ECIPA	ethyl- α -chlorophenylacetate
EDB	ethyl dimethyl aminobenzoate

LIST OF ABBREVIATIONS

EDMA	electronic transition dipole moment absorption
EDME	electronic transition dipole moment emission
ELF	electron localization function
EOB	eosin B
ESP	electrostatic potential
EtOAc	ethyl acetate
EtOH	ethanol
EY	eosin Y
f	oscillator strength
FMO	frontier molecular orbital
FTNIR	Fourier transform near-infrared
G	Gibbs free energy change
GPC	gel permeation chromatography
HAE	heavy atom effect
HEAAm	hydroxylethyl acrylamide
HOMO	highest occupied molecular orbital
HOMO-1	second highest occupied molecular orbital
I	iodine
IBDTC	<i>S</i> -1-isobutoxyethyl <i>N,N</i> -diethyl dithiocarbamate
IBTTC	<i>S</i> -1-isobutoxyethyl <i>S'</i> -ethyl trithiocarbonate
IC	internal conversion
IFCT	inter-fragment charge transfer
Ir	iridium
ISC	intersystem crossing
ISC	intersystem crossing
ITP	iodine transfer polymerisation
k_f	fluorescence decay constant
k_{ic}	internal conversion decay constant
k_{isc}	intersystem crossing decay constant
k_{nr}	non-radiative decay constant
k_p^{app}	apparent propagation rate constant
k_r	radiative decay constant
LCP	living cationic polymerisation
LED	light emitting diode
LOL	localized-orbital locator
LUMO	lowest unoccupied molecular orbital
LUMO-1	second lowest unoccupied molecular orbital
μs	microsecond
M	monomer
MA	methyl acrylate
MALDI-TOF	matrix-assisted laser desorption ionization time-of-flight
MDEA	methyl diethanolamine
MeCN	acetonitrile

MeOH	methanol
MLCT	metal-to-ligand charge transfer
MMA	methyl methacrylate
M_n	number average molecular weights
MO	molecular orbital
MOMAP	Molecular Materials Property Prediction Package
ms	millisecond
MS	mass spectrometry
Multiwfn	Multifunctional Wavefunction Analyzer
M_w/M_n	molecular weight dispersity
NAM	4-acryloylmorpholine
NBO	Natural Transition Orbital
NIR	near-infrared
NMP	nitroxide-mediated radical polymerisation
NMR	nuclear magnetic resonance
NVP	<i>N</i> -vinyl pyrrolidinone
O-ATRP	organocatalysed atom transfer radical polymerisation
OEGMA	oligoethylene glycol methacrylate
OPC	organic photocatalyst
P3T	photoinduced Dexter/triplet energy transfer
PB	phloxine B
PC	photocatalyst
PDI	perylene diimide
PDI	polydispersity
PDMA	poly- <i>N,N'</i> -dimethylacrylamide
PET	photoinduced electron transfer photoinduced electron/energy transfer reversible addition- fragmentation chain transfer
PET-RAFT	photo-controlled atom transfer radical polymerisation
photo-ATRP	photo-controlled cobalt-mediated radical polymerisation
photo-CMPR	photo-controlled iodine transfer polymerisation
photo-ITP	photo-controlled living cationic polymerisation
photo-LCP	photo-controlled nitroxide-mediated radical polymerisation
photo-NMP	photo-controlled reversible deactivation radical polymerisation
photo-RDRP	photo-controlled ring-opening metathesis polymerisation
photo-ROMP	photo-controlled organotellurium-mediated radical polymerisation
photo-TERP	photo-controlled organotellurium-mediated radical polymerisation
PMA	poly-methyl acrylate
ps	picosecond
PTH	10-phenylphenothiazine
RAFT	reversible addition-fragmentation chain transfer
RB	rose Bengal
RDRP	reversible deactivation radical polymerisation
ROMP	ring-opening metathesis polymerisation
RTPP	reduced tetraphenyl porphyrin

S	second
S ₀	singlet ground state
S ₁	lowest singlet excited state
S _{deloc}	delocalised singlet excited state
SET	single electron transfer
S _{FC}	Frank-Condon excited state
sf-X2C	spin-free part of the exact two-component Hamiltonian
SG	singlet generator
SOC	spin orbit coupling
SOC	spin-orbit coupling
SOMO	singly occupied molecular orbital
SPP	structure-property-performance
SPPR	structure-property-performance relationship
St	styrene
S-TD-DFT	spin-adapted time-dependent density functional theory
T ₁	lowest triplet excited state
TA	tertiary amine
TBA	tributyl amine
<i>t</i> BuA	<i>tert</i> -butyl acrylate
TD-DFT	time-dependent density functional theory
TEA	triethylamine
TEOA	triethanolamine
TERP	organotellurium-mediated radical polymerisation
THF	tetrahydrofuran
TPP	tetraphenyl porphyrin
TTA	triplet-triplet annihilation
UV-Vis	ultraviolet-visible
VAc	vinyl acetate
VP	vinyl pivalate
X2C	exact two component Hamiltonian
Zn	zinc
ZnTPP	zinc(II) tetraphenyl porphyrin
ZnTPPS ⁴⁻	zinc meso-tetra (4-sulfonatophenyl) porphyrin
δ	chemical shift
ΔE _{st}	singlet-triplet energy gap
ΔG	Gibbs free energy change
ε	molar extinction coefficient
ε _{max}	maximum molar extinction coefficient
λ _{max}	maximum absorption wavelength
τ _{ph}	phosphorescence lift time
τ _T	triplet lifetime
Φ _F	fluorescence quantum yield

LIST OF ABBREVIATIONS

Φ_{ph}	phosphorescence quantum yield
Φ_{T}	triplet quantum yield
Φ_{Δ}	singlet oxygen quantum yield

Chapter 1 Introduction

1.1 Current state-of-the-art of photo-controlled polymerisation

Over the past 3.4 billion years, chlorophylls and bacteriochlorophylls evolved in plants and cyanobacteria have kept on very efficiently harvesting visible light to catalyse biosynthesis, which sustains life on the earth. Since 1912 when Ciamician proposed artificial use of visible light to mimic photosynthesis in plants and mediate complex chemical reactions,¹ myriads of man-made photocatalysts (PCs) have emerged to drive diverse organic transformations.²⁻⁴ In the past decade, photoredox catalysis was then introduced to controlled/living polymerisation systems.⁵ The advent of conventional controlled/living polymerisations since the turn of this century has revolutionised macromolecular synthesis, bearing effective regulation over molecular weights, molecular weight dispersities as well as predefined number, composition and architecture of polymer chains.⁶ However, these techniques usually initiated by heat, light or other stimuli cannot afford control over the chain growth step, and thus cannot be reversibly ceased and restarted in the course of polymerisation, which restricts their implementation in more complex macromolecular synthesis. The incorporation of photoredox catalysis into controlled/living polymerisation, which results in photo-controlled polymerisation, was initially brought by Hawker,⁷⁻⁹ Matyjaszewski¹⁰⁻¹¹ and coworkers and proven very successful in expanding the application of advanced macromolecular synthesis.

Photo-controlled polymerisation requires the presence of a PC, in its excited states, to reversibly active and deactivate the propagating species and thereby afford regulation of polymerisation by light, preferably visible light. Due to the instant on/off switching capabilities and orthogonal properties of light, photo-controlled polymerisation features temporal control, spatial control, sequence control and high level of selectivity/orthogonality between different systems. These unique features see tremendous potential in rapid synthesis of advanced polymeric materials, such as surface patterning,¹²⁻¹³ 3D/4D printing,¹⁴ polymeric micelles,¹⁵⁻¹⁶ multiblock antimicrobial polymers with precise sequences and architectures.¹⁷

All these unique features of photo-controlled polymerisation rely heavily on the properties of PCs. On one hand, the absorption spectra of PCs determine the activation wavelengths of photo-controlled polymerisation. On the other hand, depending on the

redox potentials of an excited PC versus those of the initiators, it can selectively activate one or more photo-controlled polymerisation techniques via different quenching pathways. Different combinations of PCs and photosystems can thus result in numerous possibilities of selectivity and orthogonality to enable precise control over complex hybrid polymerisation systems. Therefore, rational design of PCs with specialised properties is the key in developing advanced polymerisation systems with unique functionalities.

The development of photo-controlled polymerisation catalysed by a PC have been expanded to multiple mechanisms and quenching pathways. Current well-established systems include photo-controlled atom transfer radical polymerisation (photo-ATRP), photoinduced electron/energy transfer reversible addition-fragmentation chain transfer (PET-RAFT) polymerisation, photo-controlled living cationic polymerisation (photo-LCP) and photo-controlled ring-opening metathesis polymerisation (photo-ROMP). In particular, photo-ATRP and PET-RAFT fall in the scope of photo-controlled reversible deactivation radical polymerisation (photo-RDRP) and can operate intrinsically via an oxidative quenching pathway but can also operate via a reductive quenching pathway in the presence of an additional reducing agent. In contrast, photo-LCP and photo-ROMP are known to operate via a reductive quenching pathway. Normally, oxidative quenching requires PCs with sufficiently reducing excited states and by contrast, the reductive quenching needs PCs with oxidising excited states.

Because a PC is composed of a chromophore core and substituents. Modifying substitution of the chromophore can achieve precise tuning of PC properties based on the benchmark properties of the chromophore core. Hence, simple by judicious tuning of the PC structure, desirable properties for selectively activate a certain polymerisation mechanism can be obtained. As an typical example, Fors and coworkers demonstrated that, in the presence of the same RAFT agent, a PC with highly reducing excited states can reduce the RAFT agent and activate radical polymerisation of acrylate monomers, whereas another PC with highly oxidising excited states can oxidise the same chain and active cationic polymerisation of vinyl ethers.¹⁸ Consequently, these PCs can be selectively photoexcited depending on their absorption wavelengths in an orthogonal manner, which resulted in alternating sequence control of the same polymer chain by light wavelengths.¹⁸

1.2 Thesis motivation

Despite the success of photo-controlled polymerisation in application to advanced synthesis of polymeric materials, the selection and discovery of appropriate PCs rely heavily on a trial-and-error approach, where massive experimental screening is needed to identify desired candidates.¹⁹ This approach was once in a while effective at the initial stage of developing photo-controlled polymerisation techniques. Indeed, at the early time, little was known about the mechanistic interplay between PCs and the polymerisation techniques; most importantly, requirements and standards for a PC to be effective for a specific system are quite ambiguous. This lack of fundamental knowledge in photo-controlled polymerisation had driven researchers to widely search for new chromophore classes as possible PCs. Indeed, almost all the initial discoveries of new chromophore cores were based on experimental findings, such as transition-metal based complexes,^{7,20} xanthene dyes,²¹⁻²² polycyclic aromatic hydrocarbons,²³ porphyrin dyes,²⁴ phthalocyanine dyes,²⁵ phenothiazine derivatives,^{9, 11} dihydrophenazines,²⁶ phenoxazines,²⁷ dimethyl-dihydroacridines,²⁸ pyrylium derivatives²⁹⁻³⁰ and acridinium derivatives.³¹

PCs constructed by these basic chromophore cores were experimentally proven to be effective for specific photo-controlled polymerisation techniques, owing to the appropriate benchmark properties of the chromophore cores themselves. However, with the advances in photo-controlled polymerisation, modern manufacturing of sophisticated polymeric materials requires higher efficiency, more selectivity and even orthogonality from the PCs, which demands customisability of PCs with precisely desired properties to satisfy different specific needs. In this regard, the traditional trial-and-error approach falls short of the customisability in PCs, and a rational strategy is needed to design a PC that precisely reflects the demand.

Rational design of a new PC in application to a photo-controlled polymerisation system has to be based on understanding of the requirements for PC properties and how structural modification can lead to such requirements. On top of this understanding, relevant structure-property-performance relationships that reflects how the variation of PC structures would contribute to more desirable properties and thereby better performance of a photo-controlled polymerisation system. The emergence of various chromophore cores with diverse benchmark properties has provided sufficient selections opportunities

to precisely customise the properties of the PCs to achieve specific performance of the photo-controlled polymerisation.

PET-RAFT polymerisation is one of the most commonly used techniques in photo-controlled polymerisation, because of its robustness, good oxygen tolerance and easy control in molecular weight distribution. However, despite the recent progresses in developing structure-property relationships and property-performance relationships for PC design of the organocatalysed ATRP (O-ATRP) systems, such knowledge is still very limited. Indeed, the large differences in the intrinsic mechanisms between O-ATRP and PET-RAFT polymerisation, has led to many variations in requirements for an efficient/functional PC of PET-RAFT systems. Most importantly, there has been no efforts made in rational PC design for PET-RAFT polymerisation, with a huge lack in knowledge relating to structure-property-performance relationships. More generally speaking, fully computer-guided design of a functional PC in application to a specific photo-controlled polymerisation system, in which the real potential of rational PC design lies, has not been achieved.

Hence, the overarching goal of this thesis is to start from understanding the natural evolution “strategies” of PC as the general orientation, comprehensively establishing the guiding principles (structure-property-performance relationships) in PC design, and eventually achieve fully computer-guided design of a functional PC in application to PET-RAFT polymerisation with desired functionalities. Thereby, the traditional trial-and-error strategy can be replaced by a much more efficient and cost-effective computer-guided rational strategy for PC design.

Specifically, the goals of this dissertation are as follows:

1. The naturally occurring Chl a bears multiple functional substituents or structural modifications arising from natural evolution. These evolved desirable properties result in its strong visible light absorption at long wavelengths, high triplet quantum yield Φ_T , and unique redox properties. On account of these advantages, it is envisaged to exhibit much potential as an efficient multifunctional PC for PET-RAFT polymerisation. Thereby, this thesis firstly testifies and demonstrates the comprehensive performance and functionalities of PET-RAFT polymerisation catalysed by Chl a. Through these initial explorations, the general orientation of a

rational PC design strategy is roughly learned from nature, by preliminarily clarifying the typical characters of Chl a that makes it superior as a multifunctional PET-RAFT PC.

2. Considering that rational PC design requires explicit understanding of the structure-property-performance relationships (SPPRs) at the quantum chemical level, this thesis further utilise the classic halogenated xanthene dyes as the studying materials to comprehensively establish the SPPRs for functional PET-RAFT polymerisation. On top of the guiding principles generated, an initial trial in rational design of a functional PC for PET-RAFT polymerisation is demonstrated.
3. To finally enable the first computer-guided rational design of a PC for PET-RAFT polymerisation with unique functionalities, this thesis enriches the established SPPRs as guiding principles and collect the most cutting-edged quantum chemical tools as the design platform. With regard to the rising demand in orthogonal control of polymerisation by multiple stimuli, the first fully computer-guided rational approach is exemplified by designing a PC not only contributes to high photocatalytic efficiency and oxygen tolerance in PET-RAFT polymerisation, but also designed to exhibits remarkably sensitive pH response that enables the first organocatalysed pH and light dual-controlled polymerisation.

1.3 Thesis outline

Since the emergence of visible-light-controlled polymerisation in 2012, it is increasingly demanding for a rational PC design approach to circumvent the experimental efforts and costs in the traditional trial-and-error approach. This dissertation aims to enable and streamline a fully computer-guided rational strategy of designing an efficient PC with desired functionalities in application to a particular PET-RAFT polymerisation system. At the beginning of this thesis project, there has not been any clearly concluded requirements for a PET-RAFT PC. To start with, the best shortcut is to learn from nature, where the naturally occurring Chl a has been evolved to bear uniquely decorated structure and thus exhibit highly desirable properties for photocatalysis. By studying the comprehensive performance of Chl a as a PC in PET-RAFT polymerisation, general orientations for rational PC design in PET-RAFT systems can be roughly extracted. On top of the initial inspiration, more explicit understanding of SPPRs as guiding principles for PET-RAFT PC design can be established by detailed experimental and computational

investigations. Based on these achievements, the overall aim of this dissertation can be realised.

The milestones for enabling and streamlining a fully computer-guided rational strategy of designing an efficient and functional PC for PET-RAFT polymerisation, are briefly overviewed in this chapter and will be explicitly covered in the following chapters.

A comprehensive collection of the state-of-the-art theories, guidelines, methodologies and applications in the computer-guided rational strategy of PC design for photo-controlled polymerisation systems, is summarised in **Chapter 2**, including the major contributions from this thesis. In the first place, all of the key PCs discovered for photo-controlled polymerisation is listed and overviewed, highlighting their specialties, functionalities and importance for different photo-controlled polymerisation techniques. The structure-property relationships in pursuit of desired performance in photo-controlled polymerisation systems are outlined in detail, with a broad coverage of electronic-spectral, photophysical and electrochemical properties. The most cutting-edged quantum chemical tools that can be implemented in computer-guided PC design and their usage are introduced. Lastly, current progresses and examples in rational and computer-guided PC design are summarised.

The naturally derived Chl a has been evolved to bear a highly decorated porphyrin-based structure where excellent properties arise for efficient photocatalysis. Hence, this provides a best shortcut to derive the general orientations for rational PC design in PET-RAFT polymerisation, by studying Chl a and relating its superior properties and behaviour to the performance of PET-RAFT systems. **Chapter 3** comprehensively investigated the use of Chl a and its spinach extract as an efficient functional PC for PET-RAFT polymerisation. The remarkable visible-light absorption at long-wavelengths arising from the symmetry-breaking modifications to the porphyrin chromophore, high Φ_T that generates sufficient long-live triplet states and appropriate redox properties have resulted in remarkable catalytic efficiency in PET-RAFT polymerisation catalysed by Chl a. Given that Chl a is reported capable of singlet oxygen generation suggesting sufficient triplet energy, because of its high Φ_T , photoexcited Chl a efficiently produce singlet oxygen via triplet-triplet annihilation and eliminate molecular oxygen, which brings excellent oxygen tolerance to PET-RAFT polymerisation. Interestingly, owing to the uniquely evolved structure of Chl a initially designed for rapid metabolism in plants, it

can be completely decomposed to colourless small molecules upon exposure to ambient air and light. By making use of this functionality of Chl a for post-decolouration after polymerisation, it circumvents the difficulties in removing colours of the synthesised polymers from PET-RAFT polymerisation. From the practices in this work, we learned from the nature and initially obtained the general orientations for rational PC design of PET-RAFT polymerisation. This work has been published as a research article: Wu et al., Chlorophyll a crude extract: efficient photo-degradable photocatalyst for PET-RAFT polymerisation. *Chemical Communications* **2017**, 53 (93), 12560-12563 (DOI: 10.1039/C7CC07663K).

Acknowledging the general orientations, detailed understanding of the structure-property-performance relationships as guiding principles of rational PC design for PET-RAFT polymerisation at the quantum chemical level must precede any possible computer-guided design. By relating experimental observations to quantum chemical calculations, **Chapter 4** uses the halogenated xanthene dyes as an example to tease out the effect of substituents of the xanthene chromophore on the electronic-spectral, photophysical and electrochemical properties of these dyes; subsequently, the effect of these properties on the performance of PET-RAFT polymerisation like photocatalytic efficiency, activation wavelengths and oxygen tolerance were explicitly evaluated. Thereby, the full scope of structure-property-performance relationships were comprehensively established and generalised for PET-RAFT systems. Accordingly, judicious design of a new PC was exemplified, which can yield efficient PET-RAFT photocatalysis while affording the best ever oxygen tolerance in organocatalysed PET-RAFT polymerisation. This work serves as a theoretical framework in broadly guiding the design of high performance photocatalysts for organic photocatalysis. It has been published as a research article: Wu et al., Guiding the Design of Organic Photocatalyst for PET-RAFT Polymerisation: Halogenated Xanthene Dyes. *Macromolecules* **2018**, 52 (1), 236-248 (DOI: 10.1021/acs.macromol.8b02517).

With the solid foundation of the established theoretical framework, in **Chapter 5**, a fully computer-guided rational strategy for PC design was for the first time established. To achieve this, the structure-property-performance relationships were further greatly enriched, and a collection of the most cutting-edged quantum chemical tools were implemented. Specifically, this fully computer-guided strategy was adopted in rationally designing an efficient pH-switchable organic PC, unprecedentedly turning colourless at

pH 5 and recovering strong visible-light absorption and photoactivity at pH 7. This is the first example of a PC design fully guided by comprehensive quantum chemical studies covering electrostatic, electrochemical, and photophysical predictions. After the fully computer-guided rational design, the proposed PC was synthesised and characterised with a range of expected properties that confirmed the design based on computational predictions. Thereby, the first pH and light dual-gated controlled polymerisation was enabled by using this new PC. This work has been published as a research article: Wu et al., Computer-Guided Discovery of a pH-Responsive Organic Photocatalyst and Application for pH and Light Dual-Gated Polymerisation, *Journal of the American Chemical Society* **2019**, 141 (20), 8207-8220 (DOI: 10.1021/jacs.9b01096).

Finally, a brief outlook regarding the current challenges, future developments, potential future directions and important potential applications of computer-guided PC design in photo-controlled polymerisation is overviewed in **Chapter 6**.

1.4 References

- (1) Ciamician, G., *Science* **1912**, 36, 385.
- (2) Narayanam, J. M. R.; Stephenson, C. R. J., *Chemical Society Reviews* **2011**, 40, 102.
- (3) Prier, C. K.; Rankic, D. A.; MacMillan, D. W., *Chemical Reviews* **2013**, 113, 5322.
- (4) Romero, N. A.; Nicewicz, D. A., *Chemical Reviews* **2016**, 116, 10075.
- (5) Dadashi-Silab, S.; Doran, S.; Yagci, Y., *Chemical Reviews* **2016**, 116, 10212.
- (6) Braunecker, W. A.; Matyjaszewski, K., *Progress in Polymer Science* **2007**, 32, 93.
- (7) Fors, B. P.; Hawker, C. J., *Angewandte Chemie International Edition English* **2012**, 51, 8850.
- (8) Treat, N. J.; Fors, B. P.; Kramer, J. W.; Christianson, M.; Chiu, C. Y.; de Alaniz, J. R.; Hawker, C. J., *ACS Macro Letters* **2014**, 3, 580.
- (9) Treat, N. J.; Sprafke, H.; Kramer, J. W.; Clark, P. G.; Barton, B. E.; Read de Alaniz, J.; Fors, B. P.; Hawker, C. J., *Journal of the American Chemical Society* **2014**, 136, 16096.
- (10) Pan, X. C.; Lamson, M.; Yan, J. J.; Matyjaszewski, K., *ACS Macro Letters* **2015**, 4, 192.
- (11) Pan, X.; Fang, C.; Fantin, M.; Malhotra, N.; So, W. Y.; Peteanu, L. A.; Isse, A. A.; Gennaro, A.; Liu, P.; Matyjaszewski, K., *Journal of the American Chemical Society* **2016**, 138, 2411.
- (12) Pester, C. W.; Narupai, B.; Mattson, K. M.; Bothman, D. P.; Klinger, D.; Lee, K. W.; Discekici, E. H.; Hawker, C. J., *Advanced Materials* **2016**, 28, 9292.
- (13) Telitel, S.; Dumur, F.; Campolo, D.; Poly, J.; Gimes, D.; Fouassier, J. P.; Lalevee, J., *Journal of Polymer Science Part a-Polymer Chemistry* **2016**, 54, 702.
- (14) Zhang, Z.; Corrigan, N.; Bagheri, A.; Jin, J.; Boyer, C., *Angewandte Chemie International Edition English* **2019**, 58, 17954.

- (15) Tan, J. B.; Sun, H.; Yu, M. G.; Sumerlin, B. S.; Zhang, L., *ACS Macro Letters* **2015**, *4*, 1249.
- (16) Yeow, J.; Xu, J.; Boyer, C., *J Vis Exp* **2016**, e54269.
- (17) Judzewitsch, P. R.; Nguyen, T. K.; Shanmugam, S.; Wong, E. H. H.; Boyer, C., *Angewandte Chemie International Edition English* **2018**, *57*, 4559.
- (18) Kottisch, V.; Michaudel, Q.; Fors, B. P., *Journal of the American Chemical Society* **2017**, *139*, 10665.
- (19) Orr-Ewing, A. J., *Struct Dyn* **2019**, *6*, 010901.
- (20) Xu, J.; Jung, K.; Atme, A.; Shanmugam, S.; Boyer, C., *Journal of the American Chemical Society* **2014**, *136*, 5508.
- (21) Xu, J. T.; Shanmugam, S.; Duong, H. T.; Boyer, C., *Polymer Chemistry* **2015**, *6*, 5615.
- (22) Liu, X. D.; Zhang, L. F.; Cheng, Z. P.; Zhu, X. L., *Polymer Chemistry* **2016**, *7*, 689.
- (23) Miyake, G. M.; Theriot, J. C., *Macromolecules* **2014**, *47*, 8255.
- (24) Shanmugam, S.; Xu, J.; Boyer, C., *Journal of the American Chemical Society* **2015**, *137*, 9174.
- (25) Wu, Z.; Jung, K.; Boyer, C., *Angewandte Chemie International Edition English* **2020**, *59*, 2013.
- (26) Theriot, J. C.; Lim, C. H.; Yang, H.; Ryan, M. D.; Musgrave, C. B.; Miyake, G. M., *Science* **2016**, *352*, 1082.
- (27) Pearson, R. M.; Lim, C. H.; McCarthy, B. G.; Musgrave, C. B.; Miyake, G. M., *Journal of the American Chemical Society* **2016**, *138*, 11399.
- (28) Buss, B. L.; Lim, C. H.; Miyake, G. M., *Angewandte Chemie International Edition English* **2019**, *n/a*.
- (29) Pascual, L. M. M.; Dunford, D. G.; Goetz, A. E.; Ogawa, K. A.; Boydston, A. J., *Synlett* **2016**, *27*, 759.
- (30) Kottisch, V.; Michaudel, Q.; Fors, B. P., *Journal of the American Chemical Society* **2016**, *138*, 15535.
- (31) Joshi-Pangu, A.; Levesque, F.; Roth, H. G.; Oliver, S. F.; Campeau, L. C.; Nicewicz, D.; DiRocco, D. A., *Journal of Organic Chemistry* **2016**, *81*, 7244.

Chapter 2 Literature Review: Computer-Aided Photocatalyst Design for Photo-Controlled Polymerisation: Theories, Guidelines, Methodologies and Applications

The incorporation of photoredox catalysis into controlled polymerisation techniques has brought tremendous new opportunities into macromolecular synthesis, making precise synthesis of polymers with defined sequences and complex architectures possible. Depending on the physical nature of the core chromophore and substituents, a photocatalyst (PC) with a specific chemical structure and molecular geometry exhibits a range of electronic states with particular wavefunctions, from which the unique electronic-spectral, photophysical and electrochemical properties of the PC arise. Different properties of a PC with respect to a certain photo-controlled polymerisation system can end up with diverse performance and functionalities of the system. Hence, rational design of structures of a PC by studying the evolution in its properties with the aid of quantum chemical calculations, can judiciously generate or optimise a photocatalysed controlled polymerisation system with designed performance for a particular application scenario. This chapter reviews the theories, guidelines and methodologies in rational design of PCs for photo-controlled polymerisation techniques developed in recent years. In particular, various strategies in tuning the electronic-spectral, photophysical and electrochemical properties of a PC for optimised performance in photo-controlled polymerisation are comprehensively concluded and overviewed. Successful examples in implementing computer-guided rational PC design for functional photo-controlled polymerisation systems are summarised.

2.1 Introduction

2.1.1 Scope of the review

Photocatalysts (PCs) are chromophores modified by substituents that can hugely accelerate a photoreaction upon excitation by absorbing one or more photons. Chemical substituents can donate, withdraw or delocalise electrons to the chromophore core and exert additional effects on its wavefunction.¹ Consequently, the modified chromophore is tuned to display a series of specialised electronic-spectral, photophysical and

electrochemical properties and thus leading to specialised catalytic capabilities and functionalities.²⁻³

An excited state of a PC is both a better oxidant and a better reductant than the ground state.⁴⁻⁵ Hence, depending on the relative redox properties between an excited PC and a substrate, the excited PC can readily donate an electron to or abstract an electron from a substrate, provided the reaction is thermodynamically favourable.⁵ This feature is especially useful in organic transformations driven by electron transfer. As sunlight is the cleanest and most abundant energy source on the earth, PCs that can harness the visible light energy and drive organic transformations are highly desirable for chemical synthesis. Indeed, since last century, a myriad of PCs with diverse properties have been discovered to fulfill a broad range of applications in organic synthesis.⁵⁻⁸

Following the great success of photocatalysed organic reactions by the use of PCs, researcher found substantial merits of implementing photoredox catalysis to improve the control of macromolecular synthesis by controlled/“living” polymerisation over the past decade.⁹⁻¹¹ Controlled/“living” polymerisation, which is initiated by an activated initiator splitting into a propagating radical/cation/anion with monomer additions and a leaving end group, can be terminated by recapping the end group to the polymer chain and can be repetitively reinitiated. This has allowed an equilibrium to be established between active propagating chains and dormant chains in the course of the controlled/“living” polymerisation, which consequently leads to the control in molecular weights and molecular weight distributions of the synthesised polymers. However, traditional controlled polymerisations induced by thermo-initiation or photo-initiation cannot provide temporal control in the chain growth processes, which impeded the application of such techniques into precise synthesis of polymeric materials with well-defined compositions, block sequences and complex architectures. Inspired by the photocatalytic processes in organic transformations, researchers realised that, upon irradiation, a PC appropriately selected/ designed with specific redox properties complying a initiator, can activate the initiator by donating/abstracting an electron (or transferring energy) forming a propagating species to initiate polymerisation and a leaving chain end group to initiate the polymerisation and subsequently deactivate the propagating species with the end group recapped to the polymer chain. As this process is fully reversible and can be regulated by turning on and off the light, temporal control, spatial control and sequence control were made possible to allow for synthesising advanced polymeric materials.¹⁰

Indeed, visible-light-controlled polymerisation catalysed by a PC have provided a versatile toolbox for polymer materials manufacturing and found broad applications in producing antimicrobial polymers,¹²⁻¹³ decorating bio-substances or organisms with functional polymers,¹⁴⁻¹⁵ synthesising polymeric micelles with complex architectures,¹⁶⁻²⁰ surface patterning²¹⁻²⁴ and 3D/4D additive manufacturing.²⁵⁻²⁷ The great merits of photo-controlled polymerisation systems lie in their instant temporal and spatial control regulated by light,¹⁰ orthogonality arising from discrete excitation wavelength²⁸⁻³⁴ as well as high level of molecular weight control in polymerisation.¹¹ Trivial amount of a particular PC efficiently converts the low-cost and ubiquitous light into chemical energies that facilitate the proceeding and precise regulation of controlled polymerisation processes.

Traditionally, the discovery of PCs for photo-controlled polymerisation or organic transformations relies on an experimental trial-and-error approach. This approach has generated a large library of PCs capable of mediating specific photo-controlled polymerisation systems,⁹⁻¹⁰ but it requires laborious synthetic workup and therefore lack efficiency. With the development of new computational tools, rational design approaches have emerged, which can allow rapid discovery of new PCs.^{2, 4, 35-39}

As the modification of chemical functionality in PCs affect their photophysical and electrochemical properties, computational tools can be used to rapidly elucidate structure-property relationships by probing changes in their wavefunctions. Therefore, by using large libraries of synthesised PCs, it is possible to establish correlations between structures and photocatalytic activities in photo-RDRP systems.^{38, 40-41} Thanks to fast-growing quantum chemical methods, especially density functional theory (DFT) and (relativistic) time-dependent (TD) DFT⁴² in recent years, a variety of emerging programs have emerged. By combined use of these programs, it is now possible to precisely predict the properties of PCs, which enables a fully computer-guided PC design strategy and thus circumvents laborious experimental screening processes. Moreover, wave function analyses provide an opportunity to comprehensively investigate and quantitatively analyse the physics of the established structure-property-performance relationships (SPPRs) for photo-controlled polymerisation systems,^{2, 38, 40-41, 43-46} thereby enabling direct evaluation of rational PC structural design. These computational tools can be implemented for phenothiazine, phenoxazine, dihydrophenazine, dimethyl-dihydroacridine, xanthene, porphyrin, tetraazaporphyrin, phthalocyanine chromophores

and resulted in up to a hundred rationally designed PCs with various ligands/substituents, exhibiting unique functionalities. Most importantly, rational design of PCs by the aid of computational methods allows direct customisation of the photocatalytic systems deployed to specific application scenarios.² Although joint efforts from different research areas have contributed to the emergence of a great variety of computational tools and guiding principles for rational PC design, these recent efforts and new knowledge have not been systematised and reviewed to be available for most researchers. Therefore, it is very timely to systematise the large amount of isolated knowledge, guiding principles (i.e. SPPRs) and computational methodologies in rational PC design to set solid foundation for future development of new functional photo-controlled polymerisation systems.

This chapter aims to be a comprehensive and accessible overview in the SPPRs of PCs. This chapter highlights theories and methodologies which can be applied in judicious design of PCs and serves as a guide to researchers who seek to rapidly select/design a PC with desired absorbance and photocatalytic activity. More specially, I focus my attention on the design of PCs which can be applied in photo-controlled polymerisation techniques, mostly the photo-controlled reversible deactivation radical polymerisation (photo-RDRP) and also the photo-controlled living cationic polymerisation (photo-LCP). Accordingly, this review does not aim to make an exhaustive list of existing PCs, but instead, will provide tools, methodologies and knowledges that allow the rational design of PCs.

2.1.2 Inspiration from PC “design” strategies implemented by natural evolution

Considering the limited amount of sunlight that can be utilised by organisms or green plants, natural PCs in a photosynthetic system tend to be evolved to more efficiently absorb accessible solar energy and more efficiently catalyse biosynthesis. This evolution has resulted in the functionalisation of the porphyrin chromophore with multiple substituents, which led to the emergence of chlorophylls 3.4-4 billion years ago.⁴⁷⁻⁴⁸ Chlorophylls, predominantly chlorophyll a (Chl a), are Mg porphyrin derivatives modified with one reduced pyrrole ring (namely chlorin derivatives) and various functional peripheral substituents. These structural modifications have endowed Chl a with Q-band absorption of 600-700 nm light which is an important component of visible light.

Indeed, the balance between low energy excitation (strong lower Q band absorption at ~660 nm) and excellent excited state oxidation potentials has also made Chl a especially

attractive in photo-RDRP systems.⁴⁹⁻⁵¹ For example, Boyer *et al* reported the use of Chl a to highly efficiently catalyse a photo-RDRP system with a dose as low as 4 ppm relative to the monomer under mild irradiation by a 5 W red light-emitting diode (LED) lamp.⁴⁹ Compared to Chl a, the original Mg porphyrin exhibits no Q band absorption because of symmetry-induced cancellation of excitation modes.^{3, 52} Through hundreds of million years of evolution, reduction of one pyrrole ring and installation of various peripheral substituents in the original porphyrin core chromophore largely break the porphyrin symmetry, leading to significantly enhanced lower Q band absorption and large bathochromic effect.³ This has greatly increased the light absorptivity of Chl a. Four electron-donating alkyl groups further strengthen its excited state oxidation potentials for efficient photo-RDRP.⁵³ Moreover, Chl a is prone to fast degradation under irradiation and air for metabolism in nature.⁵⁴⁻⁵⁵ This has made it an excellent degradable PC which can turn completely colourless after photo-RDRP by purging with air under irradiation.⁵³

The natural evolution of Chl a by functionalising the Mg porphyrin chromophore and the superiority of Chl a as a PC for chemical transformations including photo-RDRP have inspired chemists to seek for a rational strategy to functionalise a chromophore and design a desirable PC for a photo-RDRP system with specific functionalities.

2.1.3 Rational design of PCs for photo-controlled polymerisation

Photo-controlled polymerisation can be mainly classified as photo-RDRP, photo-controlled living cationic polymerisation (photo-LCP)⁵⁶ and photo-controlled ring-opening metathesis polymerisation (photo-ROMP).⁵⁷ Major types of photo-RDRP techniques include photo-controlled atom transfer radical polymerisation (photo-ATRP)^{36, 58} and photoinduced reversible addition-fragmentation chain transfer (PET-RAFT) polymerisation;⁵⁹ other types include photo-controlled nitroxide-mediated radical polymerisation (photo-NMP),⁶⁰ photo-controlled cobalt-mediated radical polymerisation (photo-CMPR),⁶¹ photo-controlled iodine transfer polymerisation (photo-ITP)⁶² and photo-controlled organotellurium-mediated radical polymerisation (photo-TERP).⁶³

Miyake and coworkers implemented computationally directed discovery to design a class of *N,N*-diaryl dihydrophenazine derivatives with strongly reducing lowest triplet excited (T_1) states and enhanced triplet quantum yields (Φ_T) by the excited-state charge transfer (CT) characters for visible-light-controlled organic photo-ATRP (O-ATRP).³⁶ Similarly, they continued to implement this computationally directed discovery strategy for PC

design of O-ATRP and further introduced *N*-aryl phenoxazine derivatives³⁷ and dimethyl dihydroacridine derivatives³⁵ which also exhibit highly reducing T₁ states with CT characters. On the one hand, Kwon and coworkers used computational tools to establish a rapid molecular design platform and successfully discovered highly efficient organic PCs based on donor-acceptor (D-A) scaffolds for O-ATRP.³⁸ They further used the same computer-aided molecular design strategy to identify organic PC candidates bearing D-A scaffolds for PET-RAFT polymerisation with excellent oxygen tolerance.⁴⁶ Our group investigated the SPPRs in PET-RAFT polymerisation by the aid of computational tools and designed a highly efficient xanthene PC from a series of halogenated xanthene dyes.⁴⁰ On top of that, we enabled a fully computer-guided approach to design the first pH and light dual-responsive organic PC for the first pH and light dual-controlled RDRP system.² It provides the first example and methodological framework for rational design of functional PCs systematically performed by computer-guided strategies with physical, electrochemical and photophysical properties all predicted by a combination of DFT, TD-DFT and relativistic TD-DFT calculations. Additionally, with respect to photo-LCP, Fors and coworkers investigated the impact of redox potentials and photophysical properties of PCs on the catalytic performance and the temporal control of photo-LCP.⁶⁴⁻⁶⁵

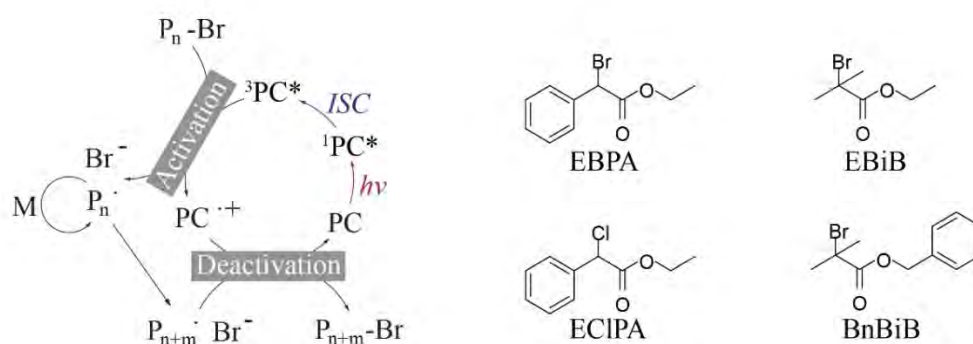
Through these joint contributions across different groups, the computer-guided discovery strategy has shown tremendous potentials for the next few decades in rational design of functional PCs complying with various photo-controlled polymerisation application scenarios.

2.2 Overview of PCs in photo-controlled polymerisation

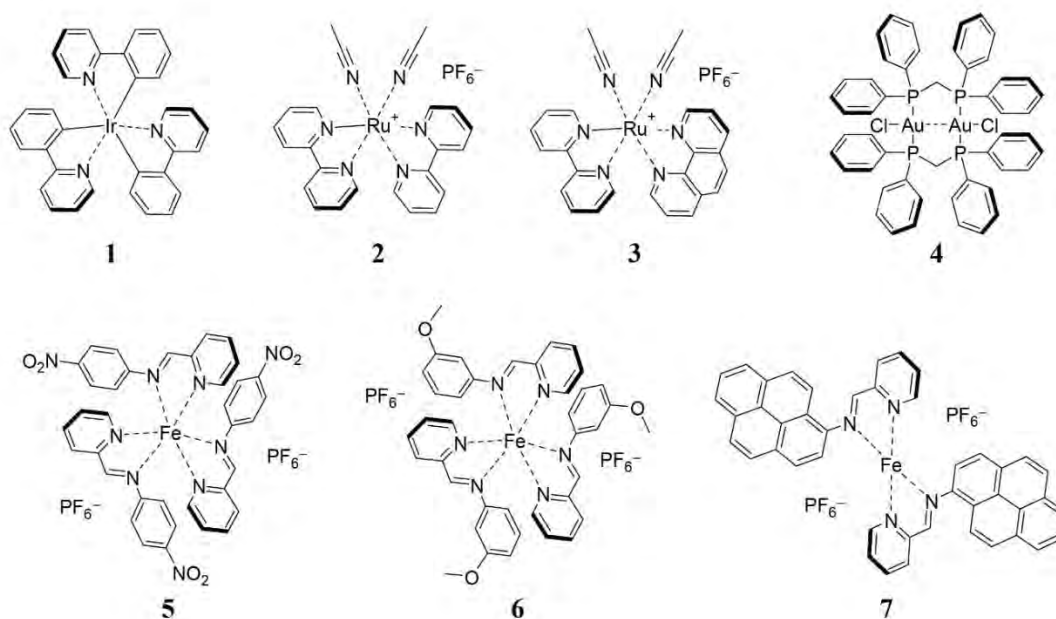
2.2.1 First photo-ATRP systems with transition-metal-based PCs

Since the first decade of this century, controlled radical polymerisations including ATRP,⁶⁶ RAFT⁶⁷⁻⁶⁸ and NMP⁶⁹⁻⁷⁰ have made revolutionary contributions to polymer chemistry, which enabled the synthesis of functional polymeric materials characteristic of well-defined molecular weights and molecular weight distributions. In the second decade of this century, the development of photo-RDRP techniques using PCs further allowed for the additional regulation over the chain growth processes affording excellent temporal, spatial and sequence control by light.¹⁰

The first example of a photo-RDRP catalysed by a PC is photo-ATRP reported by Fors and Hawker (**Scheme 2.1**, left),⁵⁸ where they utilised **1** (*fac*-[Ir(ppy)₃], **Scheme 2.2**) as a PC to reversibly activate and deactivate the ATRP process. As shown in **Scheme 2.1**, left, the ground state PC is anticipated to be excited to the lowest singlet excited ¹PC* by absorption of a photon and subsequently reaching a long-lived lowest triplet excited ³PC*. ³PC* can then reduce the ATRP initiator (activation of photo-ATRP) to yield the propagating carbon radical to initiate radical polymerisation (monomer propagation), a bromine ion (Br⁻, or a chlorine ion Cl⁻) and the cation radical PC^{•+}. After a certain number of monomer additions, PC^{•+} would occasionally encounter the propagating radical (or the radical/Br⁻) to oxidise the radical affording a dormant polymer chain and the regenerated ground state PC. Because of the presence of a Br end group, the polymer chain can be repetitively reactivated by ³PC* for continued monomer additions followed by recapping of the Br end group. The greatest advantage of this photo-ATRP system over the traditional Cu-mediated ATRP is its ability to reversibly activate and deactivate the ATRP process by visible light with controlled chain growth. The resultant temporal/spatial control benefits from the merits of using a PC with favourable photoredox properties versus ATRP initiators. As presented in **Scheme 2.1**, right, Common initiators proven suitable for photo-ATRP include ethyl- α -bromophenylacetate (EBPA), ethyl- α -chlorophenylacetate (ECIPA), ethyl α -bromoisobutyrate (EBiB) and benzyl α -bromoisobutyrate (BnBiB).



Scheme 2.1 Left: the proposed mechanism for photo-ATRP via the oxidative quenching pathway. Right: chemical structures of ATRP initiators commonly used in photo-ATRP (EBPA, ECIPA, EBiB and BnBiB). ISC: intersystem crossing; M: monomer.



Scheme 2.2 Chemical structures of transition-metal-based complexes **1-7** used as PCs for photo-ATRP.

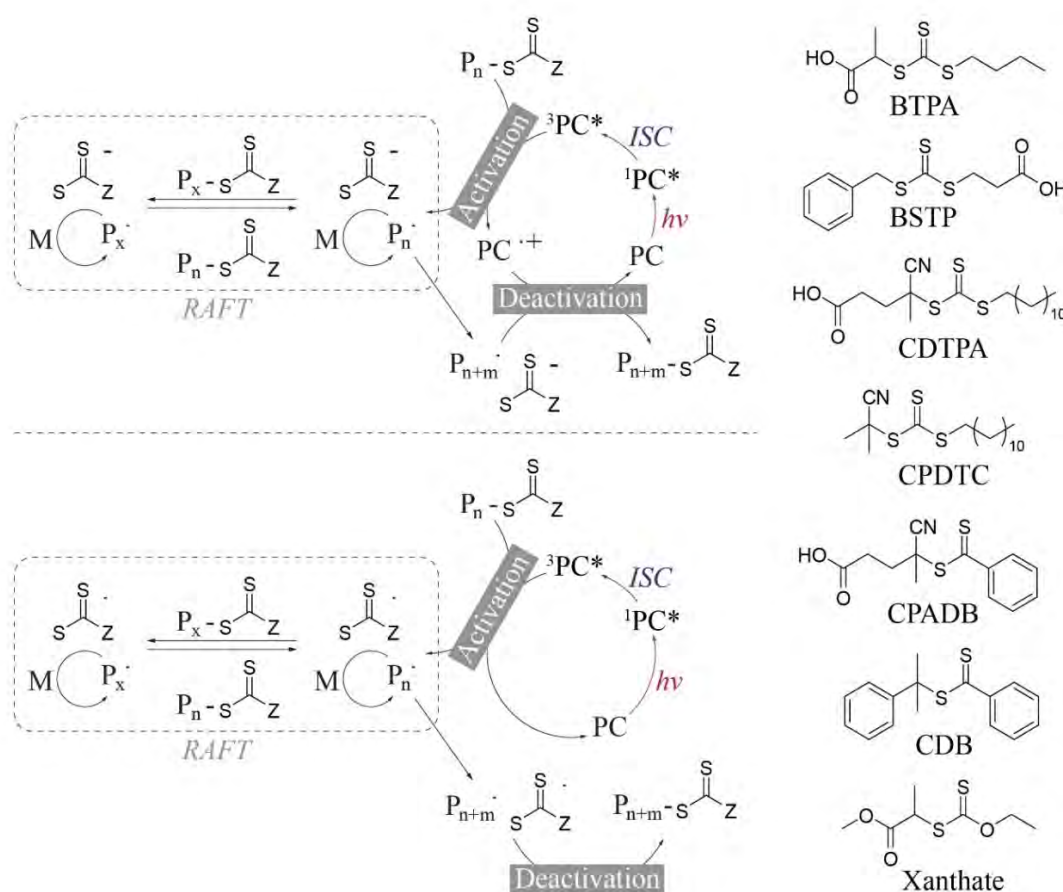
The key in selecting appropriate PCs for photo-ATRP lies in two electrochemical criteria, i.e. the ability of ${}^3\text{PC}^*$ to reduce the initiator (activating ATRP) described by the reduction potential of ${}^3\text{PC}^*$ as $E_{\text{ox}}^*(\text{PC}^{*+}/{}^3\text{PC}^*)$, and the ability of PC^{*+} to oxidise the propagating radical (deactivating ATRP) described by the oxidation potential of PC^{*+} as $E_{\text{ox}}(\text{PC}^{*+}/\text{PC})$. Technically, more negative (stronger) $E_{\text{ox}}^*(\text{PC}^{*+}/{}^3\text{PC}^*)$ demonstrates higher reducing power of the ${}^3\text{PC}^*$ and it should be more negative than the reduction potential of the initiator as substrate $E_{\text{red}}(\text{sub}/\text{sub}^{\bullet-})$ to enable successful activation of ATRP. On the other hand, more positive (higher) $E_{\text{ox}}(\text{PC}^{*+}/\text{PC})$ representing higher oxidising ability of PC^{*+} , which is in most cases more positive than $E_{\text{red}}(\text{sub}/\text{sub}^{\bullet-})$ of the initiator, leads to successful deactivation of ATRP. Combining both criteria, Hawker and coworkers identified **1**, previously implemented as a transition-metal-based PC for organic transformations,⁷¹ with both strong $E_{\text{ox}}^*(\text{PC}^{*+}/{}^3\text{PC}^*) = -1.73$ V vs. SCE and high $E_{\text{ox}}(\text{PC}^{*+}/\text{PC}) = 0.77$ V vs. SCE, for efficient photo-ATRP of both methacrylates⁵⁸ and acrylates.⁷² The great merits of transition-metal-based PCs include their excellent excited state redox properties, high triplet formation ability (high triplet quantum yield Φ_{T}) and enormous absorbance (large molar extinction coefficient ϵ), which result from the unique metal-to-ligand charge transfer (MLCT) characters of their excited states.

Therefore, following the initial work on photo-ATRP, more transition-metal based PCs were exploited. For example, Lagadec, Alexandrova and coworkers explored the use of Ru-based complexes **2** and **3** (**Scheme 2.2**) to effectively catalyse photo-ATRP of methyl methacrylate (MMA), *n*-butyl acrylate (BA) and styrene (St) under visible light in the presence of EBiB as the initiator.⁷³ Lalevée, Fensterbank, Goddard, Ollivier and coworkers discovered a novel Au-based complex **4** ($E_{\text{ox}}^*(\text{PC}^{*+}/^3\text{PC}^*) = -1.6 \text{ V vs. SCE}$, **Scheme 2.2**) as PC for photo-ATRP of various methacrylates with EBPA as the initiator, under sunlight or visible light.⁷⁴ Similarly, Lalevée and coworkers further demonstrated a class of Fe-based PCs **5**, **6** and **7** (**Scheme 2.2**) for photo-ATRP of MMA and BA initiated by EBPA; notably, compared to **1**, $E_{\text{ox}}^*(\text{PC}^{*+}/^3\text{PC}^*)$ vs. SCE of **5** (-2.35 V), **6** (-2.16 V) and **7** (-2.74 V) represent highly reducing $^3\text{PC}^*$ resulting from their unique chemical structures.⁷⁵

2.2.2 First PET-RAFT systems with transition-metal-based PCs

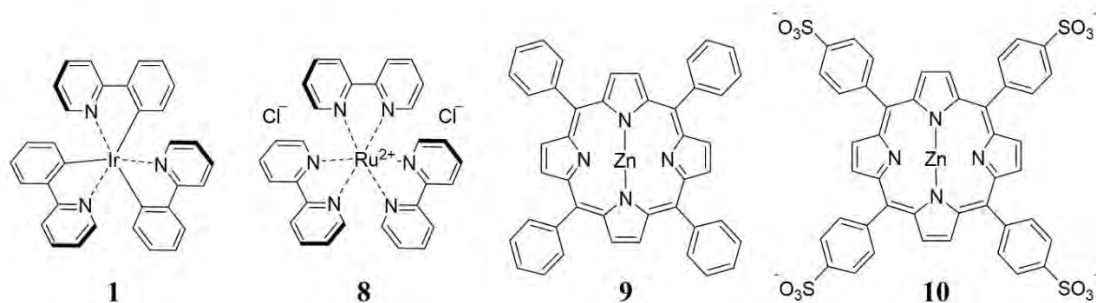
Inspired by the successful implementation of photoredox catalysis into ATRP, Boyer and coworkers similarly introduced PCs to RAFT polymerisation (namely PET-RAFT polymerisation, **Scheme 2.3**, left)⁵⁹ and used Ir-based PC **1** and a different Ru-based PC **8** (**Scheme 2.4**), in combination of representative trithiocarbonate RAFT agents BTPA and BSTP (**Scheme 2.3**, right) for polymerisation of acrylates, acrylamides, St and isoprene, a representative dithiobenzoate RAFT agent CPADB (**Scheme 2.3**, right) for polymerisation of methacrylates and methacrylamides, and a representative xanthate RAFT agent (**Scheme 2.3**, right) for polymerisation of unconjugated monomers like vinyl acetate (VAc), vinyl pivalate (VP), *N*-vinyl pyrrolidinone (NVP) and dimethyl vinylphosphonate (DVP). As shown in **Scheme 2.3**, left, there can be two main possible mechanisms of activating RAFT, i.e., photoinduced electron transfer^{59, 76} (PET, **Scheme 2.3**, left top) and photoinduced Dexter/triplet energy transfer⁷⁷ (P3T, **Scheme 2.3**, left bottom). Despite that PET-RAFT polymerisation is initially proposed to work via the PET mechanism,⁵⁹ in certain cases, it can be via the P3T mechanism. P3T is commonly known as electron exchange energy transfer, which involves $^3\text{PC}^*$ donating its excited electron while simultaneously accepting a valence electron from the ground state substrate forming PC and triplet excited substrate. For example, Allonas, Boyer and coworkers revisited PET-RAFT polymerisation catalysed by **1** and **8** and discovered that these two PCs are favourable for the P3T mechanism in activating RAFT agents like BTPA, BSTP, CDTPA, CPADB and others.⁷⁷ As shown in **Scheme 2.3**, left bottom, as the first step of

photoactivation via P3T, the PC **1** or **2** is photoexcited to $^1\text{PC}^*$ and reaches $^3\text{PC}^*$ through ISC. Subsequently, P3T can occur by transferring the comparable triplet excitation energy of $^3\text{PC}^*$ to the RAFT agent, which is then decomposed to the carbon propagating radical and the RAFT end group radical. following certain number of occasional monomer additions, deactivation can occur by recombination of both radicals forming the dormant polymer chain with a corresponding RAFT end group. Up to now, **1** and **2** are the only PCs known possible to proceed photocatalysis through a P3T mechanism in PET-RAFT polymerisation, due to their triplet excitation energies comparable to the RAFT agents themselves.



Scheme 2.3 Left: the proposed mechanisms for PET-RAFT polymerisation via the oxidative quenching pathway. Left top: PET-RAFT polymerisation via the oxidative quenching pathway by photoinduced electron transfer (PET). Left bottom: PET-RAFT polymerisation via the oxidative quenching pathway by photoinduced Dexter/triplet energy transfer (P3T). Right: chemical structures of thiocarbonylthio RAFT agents commonly used in PET-RAFT polymerisations (trithiocarbonates: BTPA, BSTP,

CDTPA and CPDTC; dithiobenzoates: CPADB and CDB; xanthate). ISC: intersystem crossing; M: monomer. Z: the Z group of the RAFT agent.



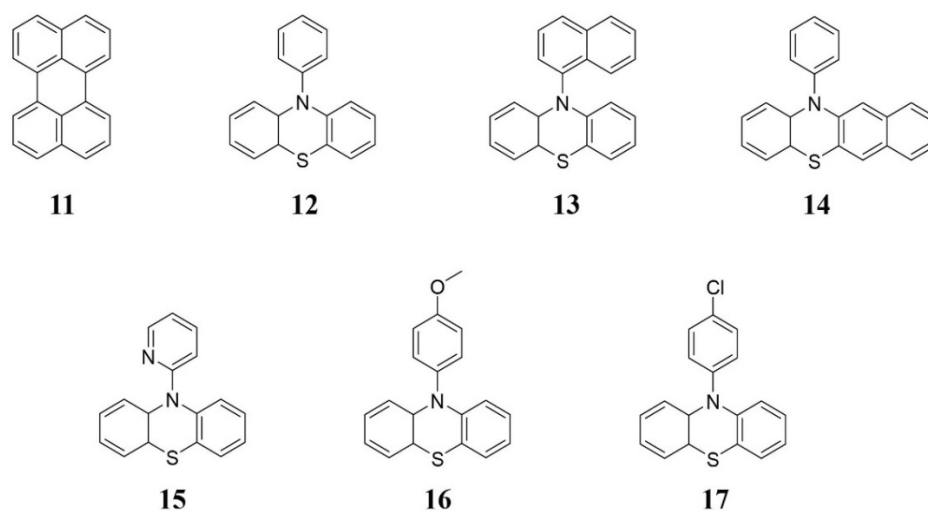
Scheme 2.4 Chemical structures of transition-metal-based complexes **1** and **8-10** used as PCs for PET-RAFT polymerisation.

However, for longer-wavelength-absorbing PCs with much lower triplet excitation energies compared to the blue-light-absorbing RAFT agents, P3T is believed to be unfavourable but PET should dominate the mechanism in PET-RAFT polymerisation. For example, Seal, Boyer, Smith and coworkers investigated the use of Zn(II) tetraphenyl porphyrin (ZnTPP, **9**, **Scheme 2.4**) in PET-RAFT polymerisation and found strong evidence that none of the common energy transfer mechanisms such as Förster resonance energy transfer, Dexter electron exchange (i.e., P3T) or internal conversion followed by vibrational energy transfer is possible for PET-RAFT polymerisation catalysed by **9**.⁷⁶ Instead, the PET mechanism is strongly supported by extensive quantum chemical characterisations.⁷⁶ Boyer and coworkers systematically explored **9** as a new PC for PET-RAFT polymerisation of acrylates, acrylamides and St regulated by trithiocarbonates, and methacrylates regulated by dithiobenzoates.⁷⁸ Notably, although the Zn-based **9** can be regarded as a transition-metal-based complex, it does not exhibit any MLCT character in excited states because of the inert nature of Zn, but instead, it is mainly characteristic of local excitation upon exposure to light.⁷⁶ Similar to the photo-ATRP system, PET-RAFT polymerisation catalysed by **9** via an oxidative quenching pathway and a PET mechanism has to meet the photochemical criteria. Specifically, **9** was reported to bear an $E_{\text{ox}}^*(\text{PC}^{+\cdot}/\text{PC}^*) = -1.3$ V vs. SCE, which is considered sufficiently more negative than the reduction potentials of representative RAFT agents BTPA (-0.6 V) and CPADB (-0.4 V).⁷⁸ Indeed, unlike photo-ATRP, PET-RAFT processes exhibit chain transfer features between dormant chains and active propagating chains, which leads to looser criteria for PET-RAFT polymerisation to yield well-defined polymers. Additional merits of using **9**

as a PC for PET-RAFT polymerisation not only include its excellent capability of light absorption over a broad range of wavelengths (435-600 nm), but also include its high Φ_T for singlet oxygen (1O_2) photosensitisation to provide strong oxygen tolerance to the PET-RAFT polymerisation system.⁷⁹ Boyer and coworkers further reported a water soluble alternative to **9** (i.e., **10**, **Scheme 2.4**) for aqueous PET-RAFT polymerisation.⁸⁰

2.2.3 Metal-free photo-ATRP (O-ATRP) with organic PCs

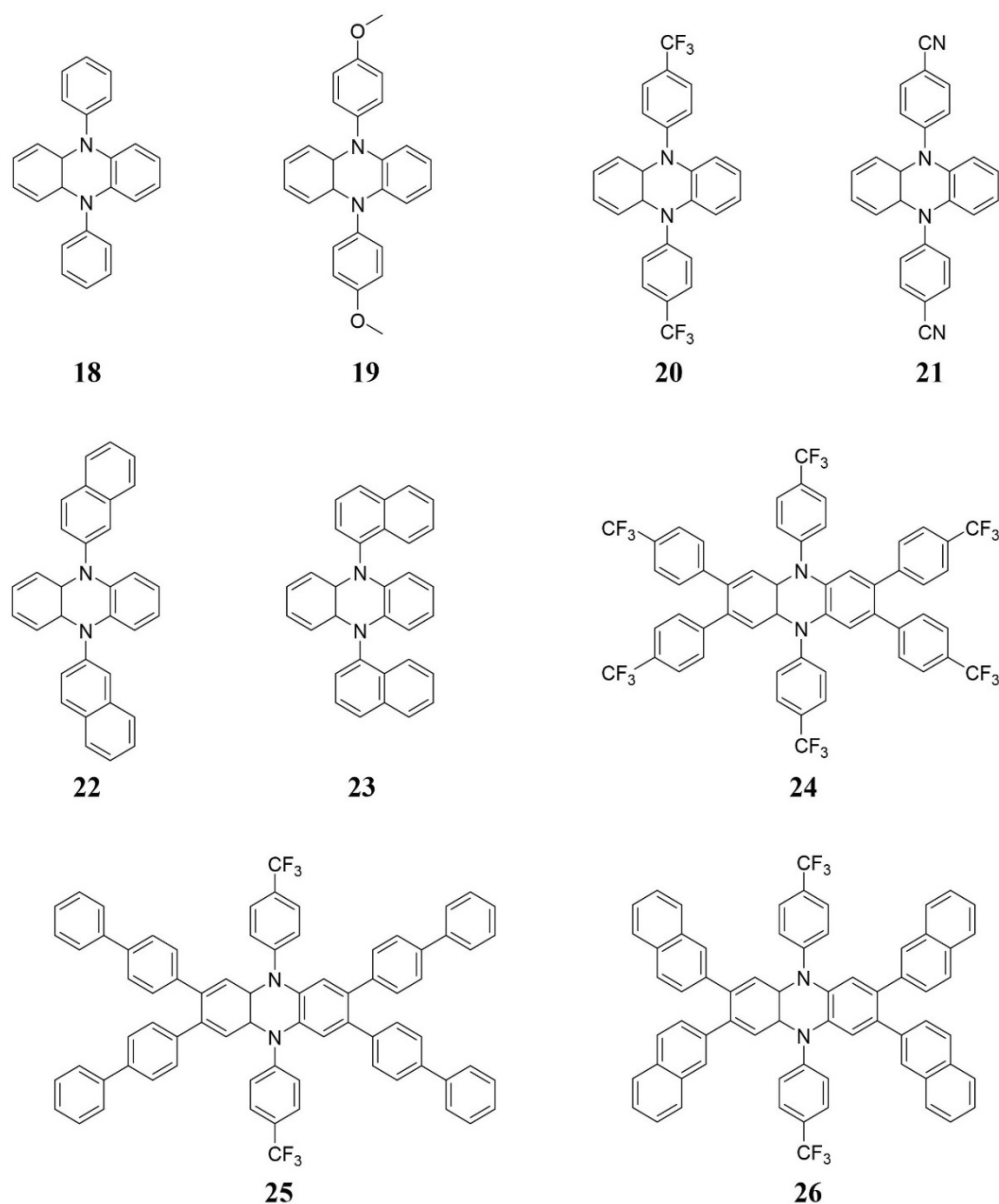
Pioneered by the successful disclosure of photo-ATRP catalysed by the transition-metal-based PC **1**, researchers started to seek for metal-free alternatives to catalyse photo-ATRP, in an effort to eliminate the need for removing the transition metal residues and pursue cleaner synthesis of polymer products to expand practical application of photo-ATRP. In this consideration, Fors, Hawker and coworkers demonstrated the use of an organic PC *N*-phenyl phenothiazine **12** (**Scheme 2.5**) for effectively catalysing metal-free photo-ATRP of methacrylates with EBPA as the initiator via an oxidative quenching pathway.⁸¹ Matyjaszewski and coworkers further expand the monomer scope of **12**-catalysed photo-ATRP to acrylonitrile.⁸² Remarkably, because **12** exhibits a highly negative $E_{ox}^*(PC^{+/\cdot}PC^*) = -2.1$ V vs. SCE, even better than **1** (-1.73 V), the authors decided to utilise this feature of **12** to expand the monomer scope to tolerate more functional groups. As an example, 2-(dimethylamino)ethyl methacrylate (DMAEMA), a monomer cannot be polymerised by **1**-catalysed photo-ATRP in a well-controlled manner, was found to yield excellently controlled polymerisation through **12**-catalysed metal-free photo-ATRP. At the same time, independently, Miyake and Theriot demonstrated successful implementation of perylene **11** to catalyse metal-free photo-ATRP of MMA with EBPA as the initiator in a controlled manner.⁸³



Scheme 2.5 Chemical structures of perylene **11** and phenothiazine derivatives **12-17** used as PCs for metal-free photo-ATRP.

Matyjaszewski and coworkers detailedly revisited and experimentally proved the proposed mechanism behind **12**-catalysed photo-ATRP (**Scheme 2.1**, left) and expand the scope of organic PCs to more phenothiazine derivatives **13-17** (**Scheme 2.5**). The authors further demonstrated the superiority of *N*-aryl phenothiazine derivatives and its π -extended derivatives in catalysing photo-ATRP in well controlled manner, whereas none of the other structurally similar dyes studied in their work can perform in a similar level of control.⁸⁴

Inspired by computationally directed discovery, Miyake and coworkers developed a library of dihydrophenazine derivatives **18-23** (**Scheme 2.6**) as efficient organic PCs with highly reducing ${}^3\text{PC}^*$ ($E_{\text{ox}}^*(\text{PC}^{+/\beta}\text{PC}^*) = -2.0\sim-2.4$ V vs. SCE) for O-ATRP of methacrylates and acrylates with EBPA as the initiator.³⁶ In particular, **3-6** exhibits excited state CT characters, which makes them even more efficient for O-ATRP (high initiator efficiency) compared to **1** and **2**. The introduction of excited state CT characters in these PCs is reasoned by the presence of lower-lying π -orbitals in the aryl groups of **3-6** as the acceptor moieties. The effect of CT T_1 states in promoted the performance of O-ATRP was later proven attributed to enhanced Φ_T (vide infra).^{43, 45} Because the introduction of CT characters in their T_1 states does not notably sacrifice their $E_{\text{ox}}^*(\text{PC}^{+/\beta}\text{PC}^*)$, it is believed to be a generally applicable strategy to construct highly efficient organic PCs for O-ATRP.

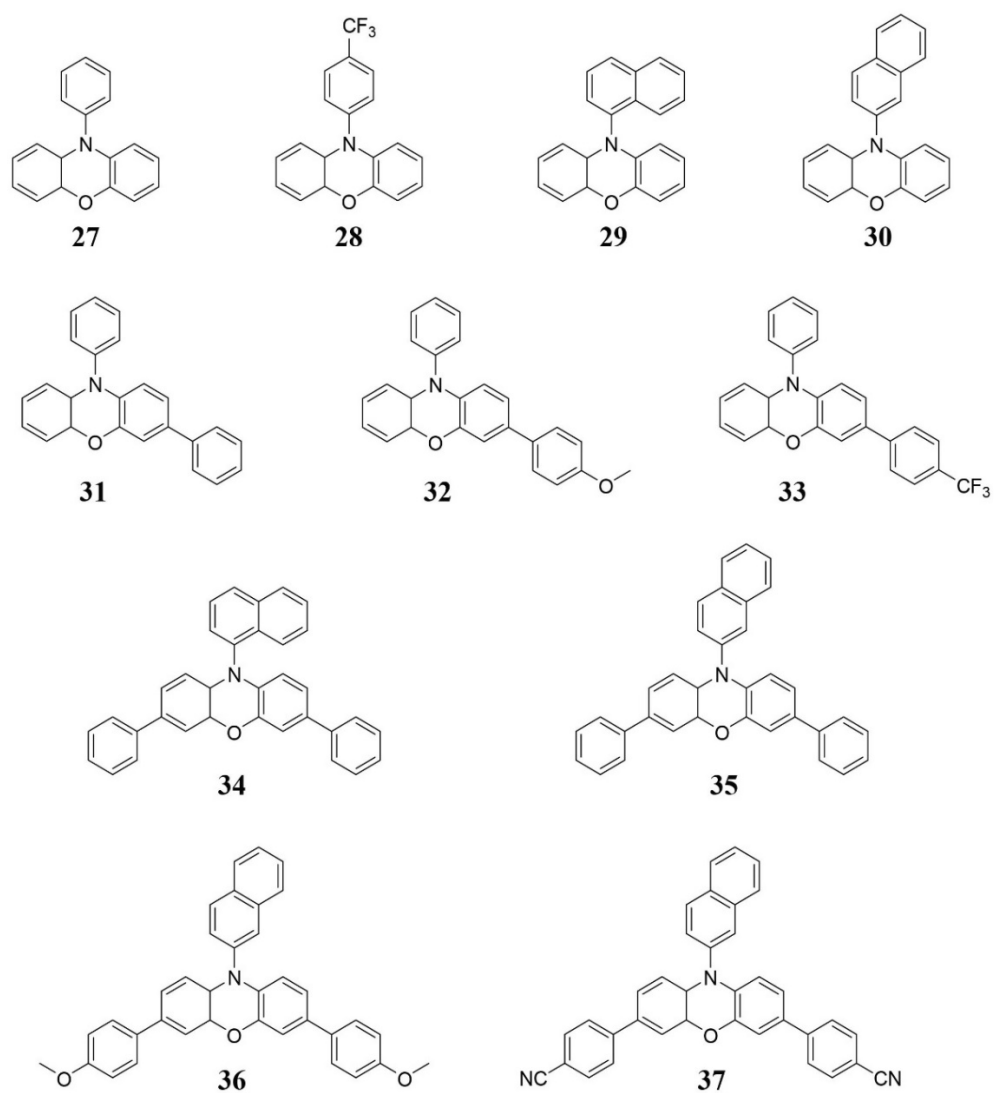


Scheme 2.6 Chemical structures of dihydrophenazine derivatives **18-26** used as PCs for O-ATRP.

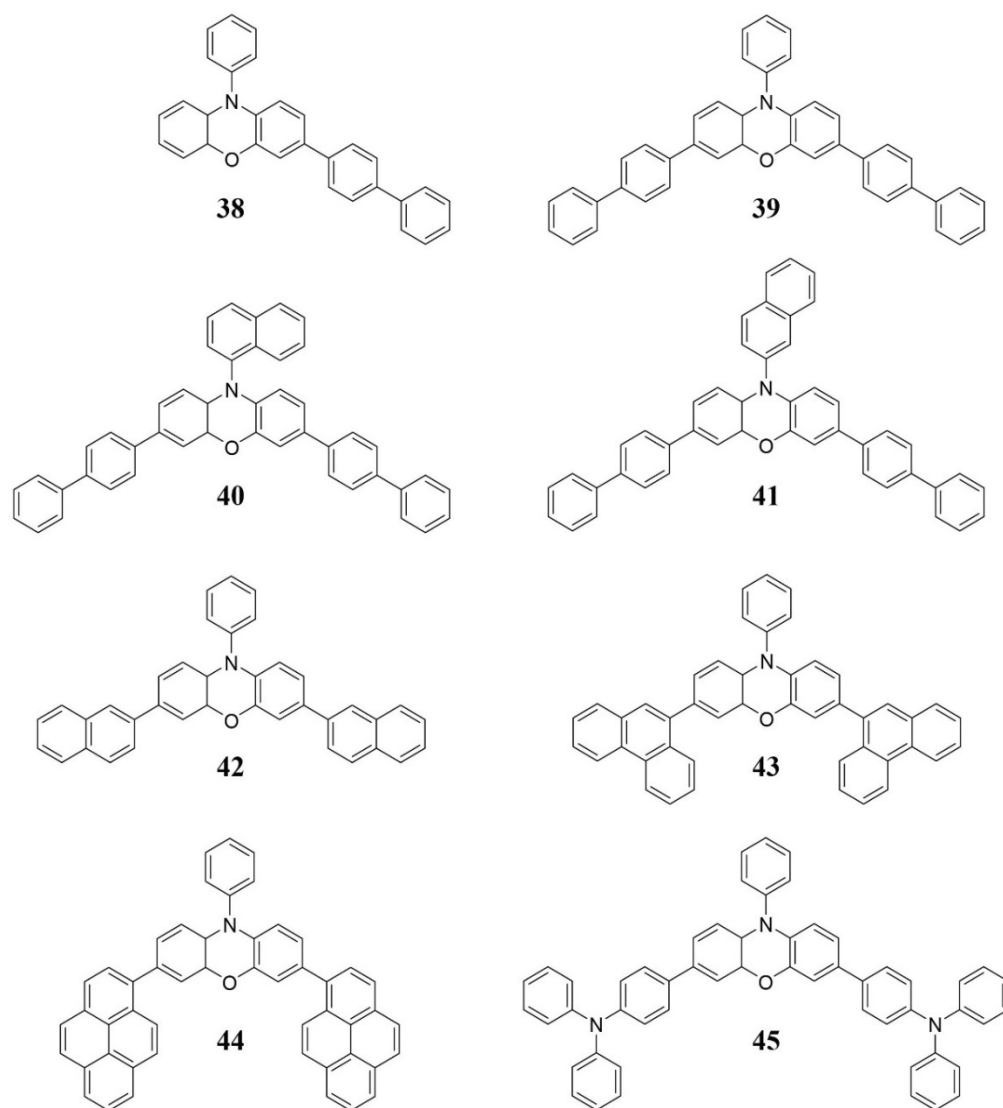
Accordingly, in an effort to pursue much reduced catalyst loading in O-ATRP, Miyake and coworkers synthesised new core-extended dihydrophenazine derivatives **24-26** (**Figure 2.6**) designed with functional substitutions to help introduce complex CT characters in T_1 states and promoting the O-ATRP performance.⁸⁵ For example, the successful implementation of **26** in O-ATRP has led to significant reduction in catalyst loading required by efficient O-ATRP from 1000 ppm of **3** (initiator efficiency < 75% and molecular weight dispersity > 1.30) down to 5~100 ppm of **26** (initiator efficiency =

93.2~106% and molecular weight dispersity 1.09~1.42), which is a remarkable improvement in the control of O-ATRP.

Similarly, Miyake and coworkers made continued progress in discovering a new library of phenoxazine derivatives **27-45** (**Scheme 2.7** and **Scheme 2.8**). Except for **27** and **28** characteristic of local excitation in excited states, **29-45** almost all exhibit CT characters in their T₁ states and a wide range of $E_{ox}^*(PC^{+}/{}^3PC^*)$ expanding from -1.40 to -2.00 V vs. SCE depending on the nature of their substituents.^{37, 41} Most importantly, core extension of the PCs leading to extended π -conjugation (e.g. some of **38-45**, **Scheme 2.8**) was reported to afford much enhanced visible light absorption, which is favourable for more efficient utilisation of visible light for O-ATRP.^{37, 41} One additional merit of CT characters in excited PCs is their broadened absorption peaks, which also helps to expand the visible light absorption of these PCs to longer wavelengths.³⁷

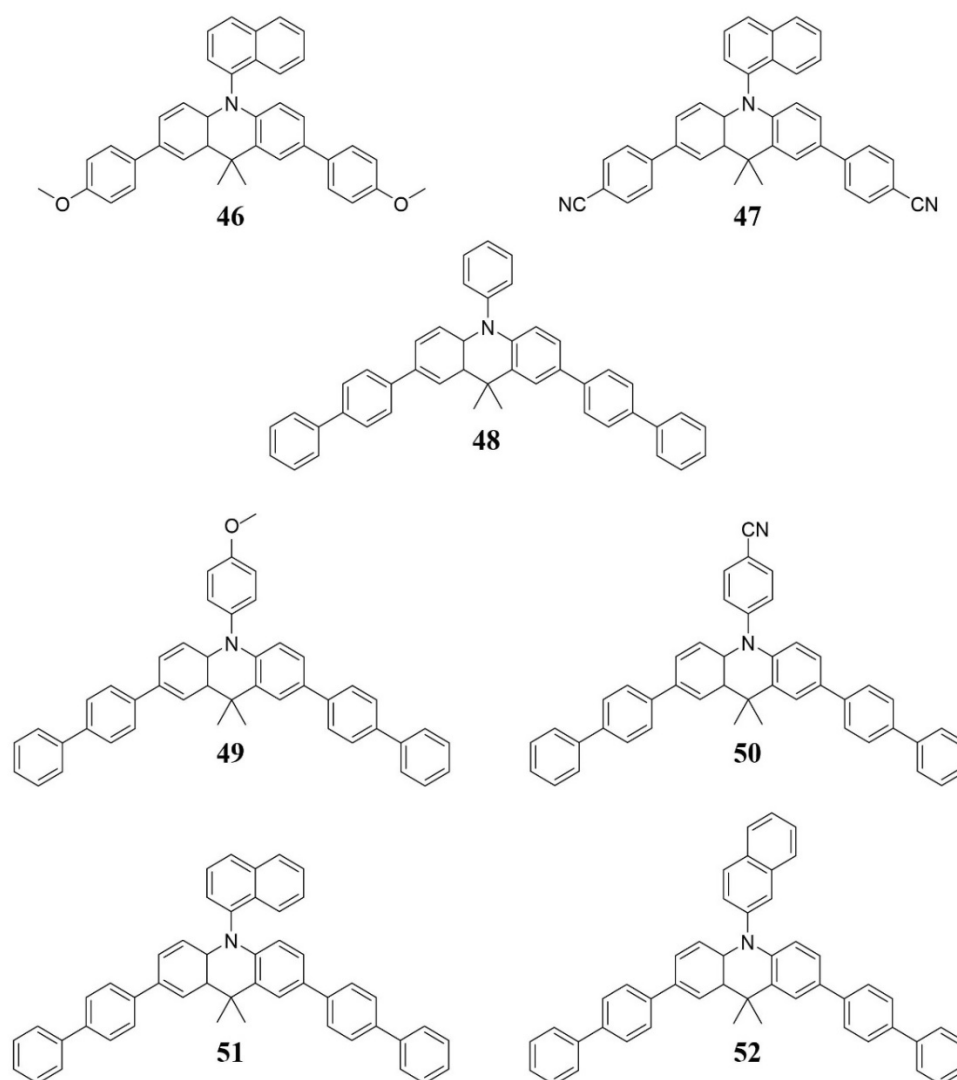


Scheme 2.7 Chemical structures of phenoxazine derivatives **27-37** used as PCs for O-ATRP.



Scheme 2.8 Chemical structures of phenoxazine derivatives **38-45** with extended π -conjugation used as PCs for O-ATRP.

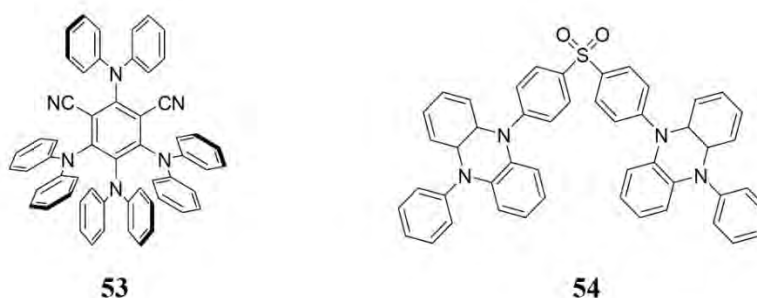
Dimethyl-dihydroacridine derivatives **46-52** (**Scheme 2.9**) with different CT characters in T_1 were also developed by Miyake and coworkers as PCs for O-ATRP.³⁵ This class of PCs features $E_{ox}^*(PC^{*+}/^3PC^*) = -1.45 \sim -1.70$ V vs. SCE and very high $E_{ox}(PC^{*+}/PC)$ of 0.71~0.90 V. Consequently, these dimethyl-dihydroacridine-based PCs can not only yield well-controlled O-ATRP of methacrylates, but also can be expanded to excellently control O-ATRP of acrylates, which are previously considered challenging in O-ATRP.³⁵



Scheme 2.9 Chemical structures of dimethyl-dihydroacridine derivatives **46-52** used as PCs for O-ATRP.

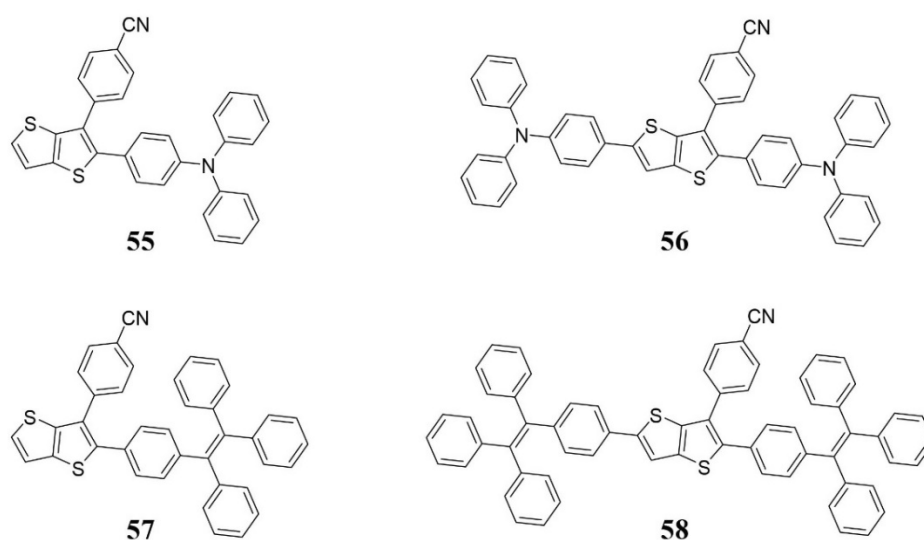
Following the pioneering work by Miyake *et al* in O-ATRP promoted by PCs with CT excited states, Kim, Gierschner, Kwon and coworkers reported a computer-aided molecular design/screening strategy to directly construct organic PCs with D-A scaffolds from a large library of common organic donor and acceptor moieties.³⁸ Dozens of organic PCs were proposed by this strategy. The authors successfully identified **53** (**Scheme 2.10**) as a highly efficient PC for O-ATRP with a requirement of less than 1 ppm catalyst loading to yield good control in O-ATRP, because of very strong visible light absorption, suitable redox properties ($E_{\text{ox}}^*(\text{PC}^{*\cdot}/\text{PC}^*) = -1.40$ V vs. SCE and $E_{\text{ox}}(\text{PC}^{*\cdot}/\text{PC}) = 1.04$ V vs. SCE) and a highly stable $\text{PC}^{*\cdot}$. Moreover, **54** (**Scheme 2.10**) is identified as a PC for

O-ATRP with a highly reducing ${}^3\text{PC}^*$ and sufficiently oxidising PC^{*+} ($E_{\text{ox}}^*(\text{PC}^{*+}/{}^3\text{PC}^*) = -2.30 \text{ V vs. SCE}$ and $E_{\text{ox}}(\text{PC}^{*+}/\text{PC}) = 0.26 \text{ V vs. SCE}$). **54** displayed a remarkably long lifetime of T_1 in excess of 1 ms and significant triplet generation ability, favourable for O-ATRP.³⁸



Scheme 2.10 Chemical structures of representative examples **53** and **54** of highly efficient organic PCs for O-ATRP designed with D-A scaffolds via a computer-aided molecular design/screening platform.³⁸

In addition, highly conjugated thienothiophene derivatives **55-58** were investigated by Yagci and coworkers as PCs in application for metal-free photo-ATRP (or O-ATRP), considering their competent role in PET reactions.⁸⁶ These highly conjugated dyes display broad absorption peaks and strong visible light absorption covering up to 500 nm of the visible spectral region, especially for **56**. In the presence of EBiB as the initiator, **55** can efficiently catalyse photo-ATRP of MMA with good control in molecular weights, excellent temporal control and high efficiency in initiation, however, **57-58** can only result in sluggish polymerisation lack of desirable control features.

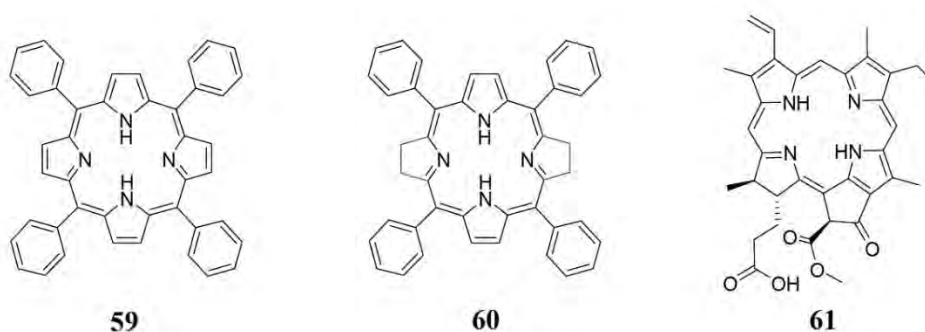


Scheme 2.11 Chemical structures of highly conjugated thienothiophene derivatives **55-58** for O-ATRP.⁸⁶

2.2.4 PET-RAFT polymerisation with organic PCs

Inspired by successful implementation of photoredox catalysis into RAFT polymerisation and the discovery of PET-RAFT polymerisation catalysed by transition-metal-based PCs, Boyer and coworkers further demonstrated efficient PET-RAFT polymerisation with the naturally derived Chl and BChl as PCs.^{49, 87} Like Zn in ZnTPP (**9**), the Mg metal centre in Chl and BChl also does not perform any role in generating MLCT characters in excited states, but instead, they only serve as an electron-donating substituent in the porphyrin macrocyclic chromophore. Hence, the success of these PCs inspired researchers that metal-free porphyrin derivatives should also likely to exhibit catalytic activities in PET-RAFT polymerisation. In light of this postulation, Boyer *et al* managed to use the metal-free tetraphenyl porphyrin (TPP, **59**) as a red-light-absorbing organic PC for PET-RAFT polymerisation of MMA in the presence of CPADB as the RAFT agent.⁷⁸ On the other hand, **59** is found to be incapable of activating trithiocarbonates like BTPA (because of the higher reduction potential) and unsuitable for polymerisation of acrylates. To circumvent this deficiency of **59**, Boyer, Xu and coworkers exploited a novel strategy by linking **59** with BSTP affording a donor-acceptor PC for efficient PET-RAFT polymerisation of MA in the presence of BTPA as the RAFT agent.⁸⁸ Similarly, the metal-free derivative of Chl without a hydrophobic carbon tail, i. e., pheophorbide a (**61**) was also investigated as a red-light-absorbing PC similar to **59**, which can selectively catalyse

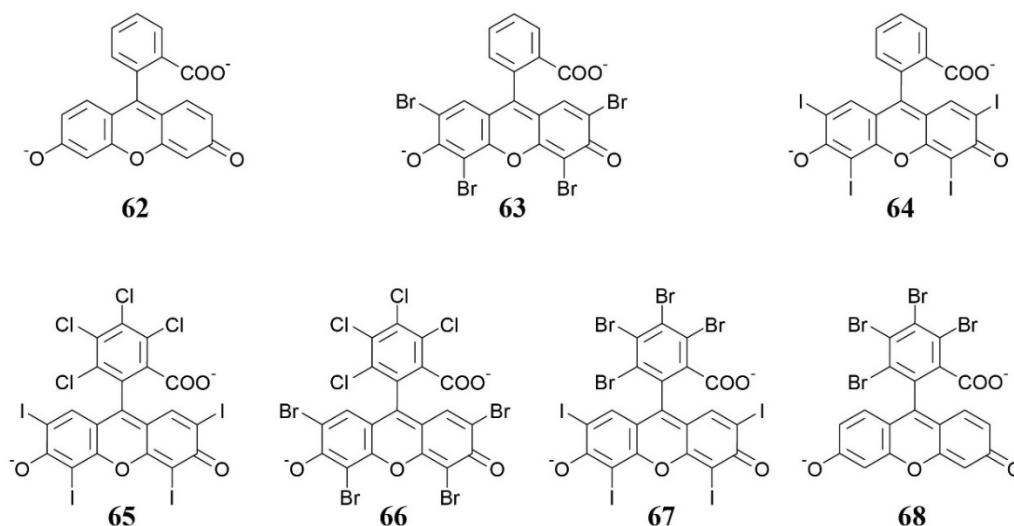
PET-RAFT polymerisation of MMA with CPADB as the RAFT agent.⁸⁹ Inspired by the success in BChl as a PET-RAFT PC, Zhang and coworkers discovered a reduced TPP with a bacteriochlorin core (RTPP, **60**) as an effective organic PC for PET-RAFT polymerisation of both acrylates and methacrylates in the presence of CDTPA or CDB as RAFT agents.⁹⁰ Most encouragingly, **60** has strong absorption in the far-red to near-infrared (NIR) range of the absorption spectrum, which makes it an unprecedented NIR-absorbing organic PC for efficient PET-RAFT polymerisation.



Scheme 2.12 Chemical structures of metal-free porphyrin derivatives **59**, **60** and **61** used as organic PCs for PET-RAFT polymerisation.

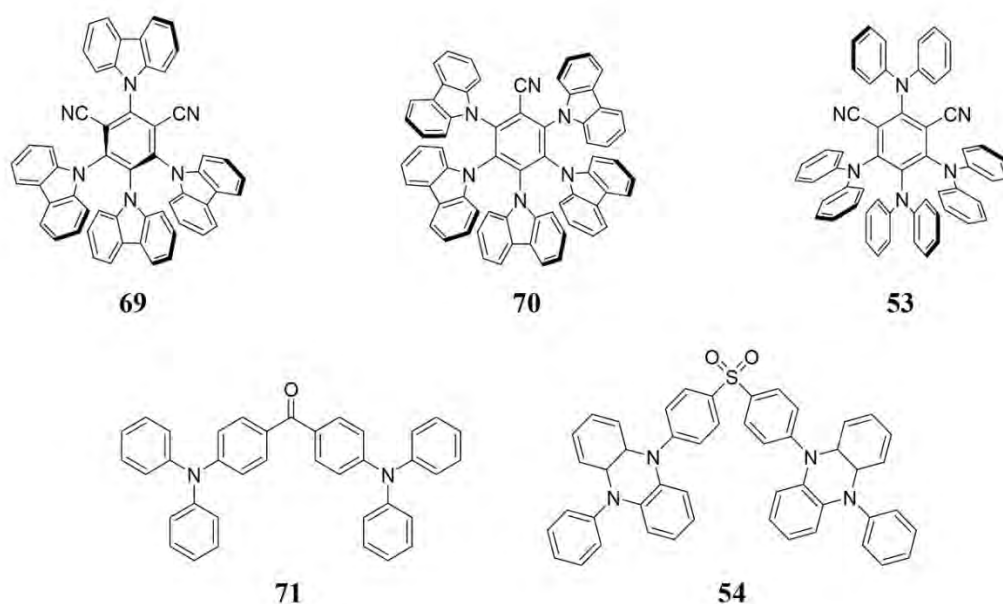
To explore more candidates as organic PCs of PET-RAFT polymerisation, Boyer, Xu and coworkers screened a couple of common organic dyes and identified fluorescein (**62**, **Scheme 2.13**) and its Br-substituted derivative Eosin Y (**63**, **Scheme 2.13**) as effective PCs for PET-RAFT polymerisation of MMA in the presence of CPADB as the RAFT agent.⁹¹ The efficacy of **62** and **63** is attributed to their sufficiently reducing T_1 ($E_{ox}^*(PC^{•+}/^3PC^*) = -1.22$ V vs. SCE of **62** and -1.10 V of **63**).⁹¹ However, **63** worked more efficiently than **62** in PET-RAFT polymerisation because of its much higher Φ_T .² We then demonstrated the use of other halogenated derivatives of this dye class **64-68** (**Scheme 2.13**) as efficient PET-RAFT PCs and compared their performance in PET-RAFT polymerisation in relation to their structure and properties.^{2, 40} In particular, the newly synthesised Br-substituted **68** was discovered as a highly sensitive and efficient pH/light dual-responsive organic PC for PET-RAFT polymerisation of acrylates, acrylamides, methacrylates and methacrylamides in the presence of BTPA, CPADB and CPDTC.² The great merits of the halogenated xanthene dyes **63-67** are that they bear exceptionally strong green-to orange light absorption, high $\Phi_T > 0.3$ and suitable $E_{ox}^*(PC^{•+}/^3PC^*) = -0.91 \sim -1.34$ V vs. SCE, which makes them ideal organic PCs for PET-

RAFT polymerisation requiring only ~20 ppm catalyst loading to yield an excellent efficiency.⁴⁰ Good oxygen tolerance was also achieved in these dye-catalysed systems due to high Φ_T . To maximise the oxygen tolerance performance in organic PET-RAFT polymerisation, **67** is judiciously designed and synthesised, exhibiting the best oxygen tolerance among organic PCs for PET-RAFT polymerisation.⁴⁰



Scheme 2.13 Chemical structures of fluorescein derivatives **62-68** used as organic PCs for PET-RAFT polymerisation.

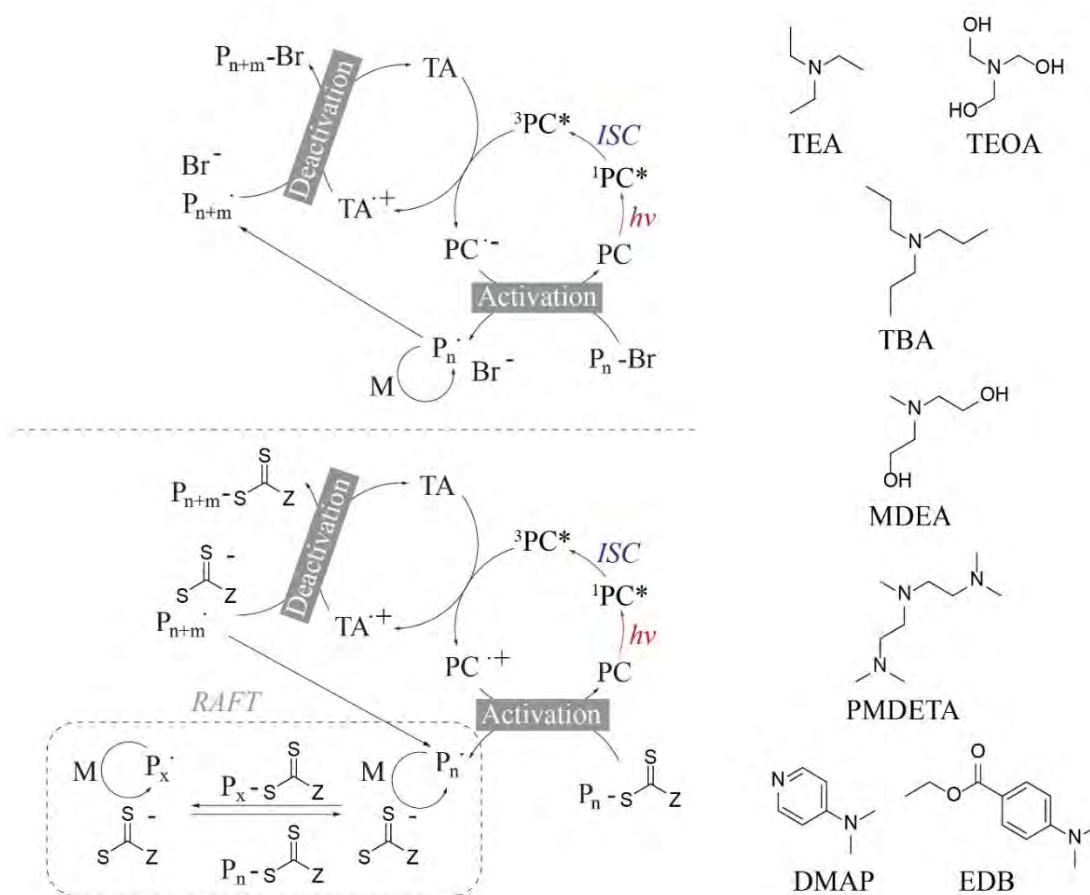
In course of the development of metal-free photo-ATRP (or O-ATRP), a few of effective candidates (**69-71** and **53-54**) were selected and implemented for PET-RAFT polymerisation, which were proven successful.^{46, 92}



Scheme 2.14 Chemical structures of PCs emerged from studies on photo-ATRP (**68-70** and **53-54**) used as organic PCs for PET-RAFT polymerisation.

2.2.5 Photo-RDRP with organic PCs via a reductive quenching pathway

Apart from the usually preferred oxidative quenching cycle (because of minimum use of catalytic species and hence less unwanted side reactions), photo-RDRP was also reported capable of mechanistically operating through a reductive quenching cycle.¹¹ This capability originates from the fact that PCs in their excited states are both a better reductant and a better oxidant compared to their ground states.^{4-5, 93} In the reductive quenching pathway (**Scheme 2.15**, left), a strong reducing agent, typically tertiary amines (TAs) can work as the electron donor and donate an electron to $^3\text{PC}^*$ forming PC^- , which can subsequently activate the ATRP process by reducing the alkyl halide (photo-ATRP via the reductive quenching pathway, **Scheme 2.15**, left top) or the RAFT process by reducing the thiocarbonylthio compound (PET-RAFT polymerisation via the reductive quenching pathway, **Scheme 2.15**, left bottom). Therefore, the presence of TAs in a proper content is the key of enabling a reductive quenching pathway for photo-RDRP. As shown in **Scheme 2.15**, right, common TAs used for reductive quenching photo-ATRP or PET-RAFT include triethylamine (TEA), triethanolamine (TEOA), tributyl amine (TBA), methyl diethanolamine (MDEA), dimethyl aminopyridine (DMAP) and ethyl dimethyl aminobenzoate (EDB).^{75, 94}



Scheme 2.15 Left: the proposed mechanisms for photo-RDRP via the reductive quenching pathway. Left top: photo-ATRP via the oxidative reductive pathway. Left bottom: PET-RAFT polymerisation via the reductive quenching pathway. Right: chemical structures of representative tertiary amines (TAs) for photo-RDRP via the reductive quenching pathway (TEA, TEOA, TBA, MDEA, DMAP and EDB). ISC: intersystem crossing; M: monomer. TA: tertiary amine.

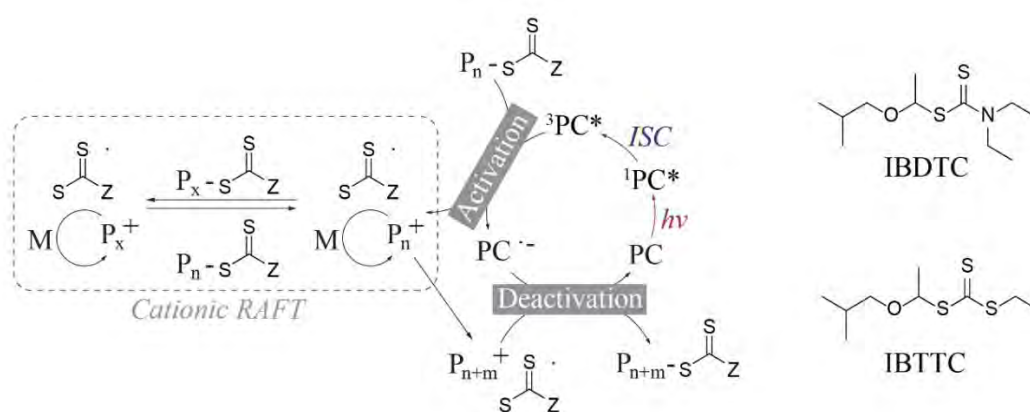
In reductive quenching photo-ATRP, fluorescein (**62**),⁹⁵ Eosin Y (**63**)⁹⁶ and Erythrosine B (**64**)⁹⁶ in conjunction with TAs were demonstrated as effective PC couples to produce monodisperse polymers.⁹⁷ Moreover, other photoactive compounds like camphor quinone, thioxanthone, benzophenone and isopropyl thioxanthone were also implemented for photo-ATRP via the reductive quenching pathway.⁹⁷⁻⁹⁸

Similarly, Eosin Y (**63**) were used as a typical example for researchers to comprehensively investigate the kinetics,⁹¹ mechanism⁹⁹ and TA scope⁹⁴ of reductive quenching PET-RAFT polymerisation. In particular, Ferji and coworkers performed a detailed investigation over the effect of the structure of the TA on the efficiency of

reductive quenching PET-RAFT polymerisation and its oxygen tolerance.⁹⁴ The authors discovered that enhanced amine radical stability by increased length of the alkyl substituents or increased conjugation of the TA structure leads to more efficient PET-RAFT polymerisation and better oxygen tolerance, with TBA and DMAP (**Scheme 2.15**, right) identified as the best TA candidates.

2.2.6 Photo-LCP with organic and transition-metal-based PCs

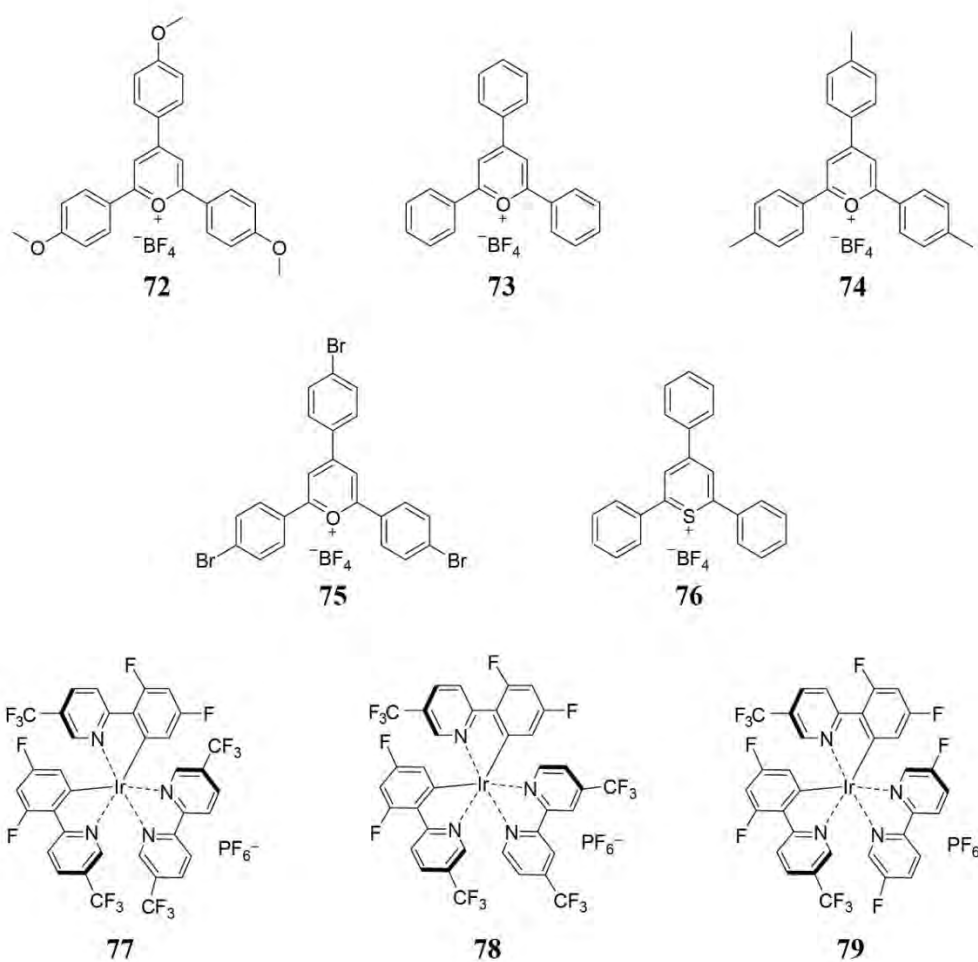
Herein, photo-LCP exclusively refers to photo-controlled cationic RAFT polymerisation developed by Fors *et al*, which is currently the only photo-LCP system.⁵⁶ In contrast to PET-RAFT polymerisation where the excited PC donates an electron to the RAFT agent forming a propagating radical and a leaving thiocarbonylthio anion, photo-LCP is activated by a photo-excited PC abstracting an electron from the RAFT agent IBDTTC or IBTTC, forming a propagating cation and a leaving thiocarbonylthio anion (**Scheme 2.16**). The formed propagating cation can then undergo the cationic RAFT process to polymerise vinyl ether monomers in a controlled manner. By occasional diffusive collision, the negatively charged PC⁻ can then reduce the propagating cation to restore the quenching cycle to dormant states of the PC and the polymer chain with a RAFT end group (deactivation). Although in **Scheme 2.16**, we denoted ³PC* as the active species for the subsequent reductive quenching PET, it still remains unclear whether ³PC* or ¹PC* or both should be the dominant active excited state for photo-LCP.⁶⁵



Scheme 2.16 Left: the proposed mechanism for photo-LCP via the reductive quenching pathway. Right: chemical structures of RAFT agents proven effective for photo-LCP, i.e., IBDTTC (*S*-1-isobutoxyethyl *N,N*-diethyl dithiocarbamate) and IBTTC (*S*-1-

isobutoxylethyl *S'*-ethyl trithiocarbonate). ISC: intersystem crossing; M: monomer. Z: the Z group of the RAFT agent.

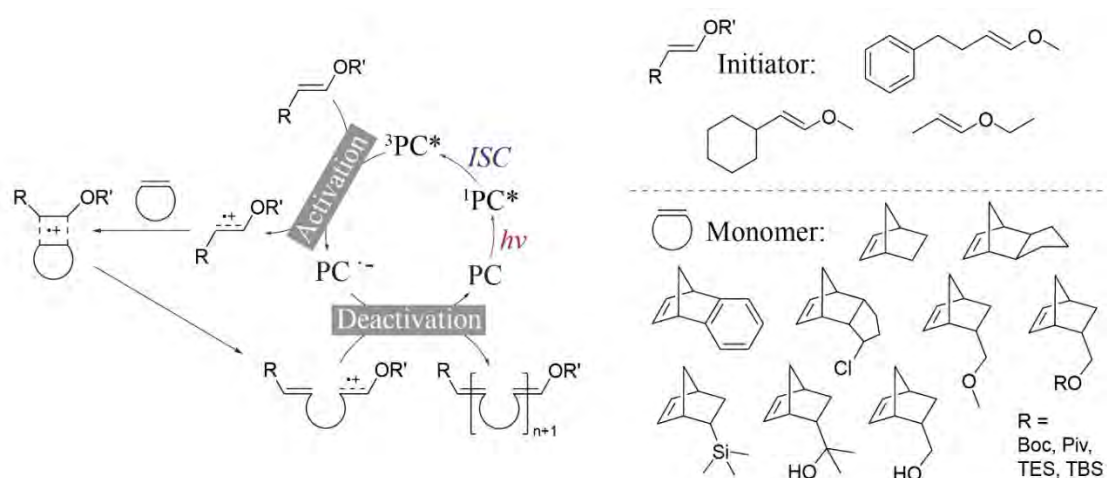
The first class of PCs that were proven to be effective for photo-LCP is pyrylium derivatives including **72-76** (Scheme 2.17). In particular, **72** can afford the best temporal control, presumably because of suitable redox properties, especially compared to **73** whose catalysis for photo-LCP nearly results in no temporal control.⁶⁵ However, these organic dye-catalysed photo-LCP systems still shows some dark polymerisation even for **72**.^{56, 65} To circumvent this problem and obtain ideal temporal control for photo-LCP, Fors and coworkers further introduced a series of modified Ir-based complexes **77-79** (Scheme 2.17), which has resulted in hugely improved temporal control for photo-LCP despite some slowing down in polymerisation rates, seemingly due to their stronger ground state reduction capability (more rapidly recapping the propagating cations), i.e., more negative $E_{ox}^*(PC^{+}/{}^3PC^*)$.⁶⁴



Scheme 2.17 Chemical structures of pyrylium derivatives (**72-76**) and Ir-based complexes (**77-79**) used as PCs for photo-LCP.

2.2.7 Photo-ROMP with organic PCs

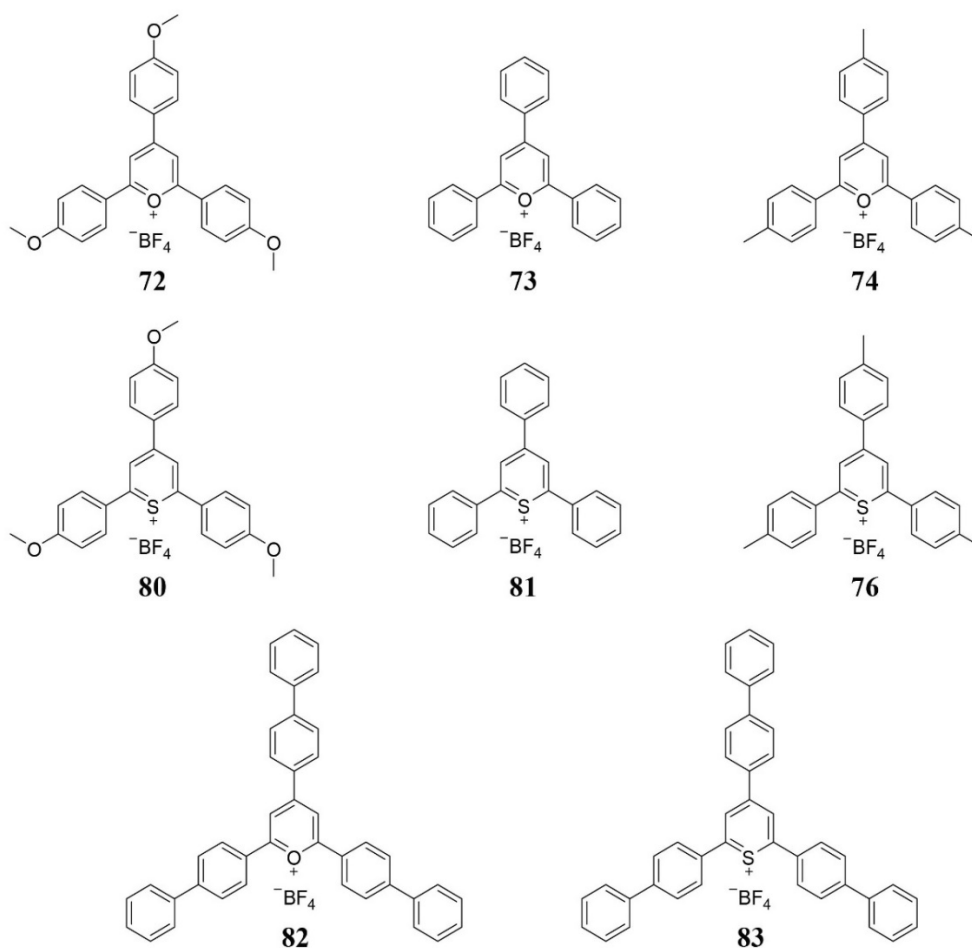
Boydston and coworkers developed a metal-free method to mediate the ring-opening metathesis polymerisation (ROMP) by introducing photoredox catalysis in the presence of organic initiators (**Scheme 2.18**, right top).⁵⁷ Because of the cationic nature of photo-ROMP, it also operates through a reductive quenching pathway (**Scheme 2.18**, left) similar to photo-LCP. As shown in **Scheme 2.18**, left, the authors mechanistically envisioned that the vinyl ether initiator is activated by donating an electron to the excited PC, to yield the vinyl ether radical cation. Subsequently, propagation of the vinyl ether radical cation proceeds the polymerisation by monomer (listed in **Scheme 2.18**, right bottom) additions.¹⁰⁰ Finally, occasional diffusive collisions between the vinyl ether radical cation and PC•- would restore them all to ground states for reinitiation, which clearly manifested the reversibility of the photo-ROMP system.^{57, 101}



Scheme 2.18 Left: the proposed mechanism for photo-ROMP via the reductive quenching pathway. Right: chemical structures of the initiators (right top) and monomers (right bottom) used in photo-ROMP. ISC: intersystem crossing. R and R' in left: the substitution groups on both sides of the initiator.

Photo-ROMP shares a similar library of PCs with photo-LCP, mainly including pyrylium derivatives (**72-74** and **82**) and thiopyrylium derivatives (**80**, **81**, **76** and **83**, **Scheme 2.19**).¹⁰² By systematically studying these varied pyrylium and thiopyrylium PCs, Boydston *et al* observed higher efficiency of thiopyrylium derivatives **80**, **81**, **76** and **83**

over their corresponding pyrylium counterparts.¹⁰² We postulated that this could be because of the heavy atom effect of S in thiopyrylium derivatives which promotes ΦT and increased their efficiency, which could indicate that $^3PC^*$ is the active state for the process of photo-ROMP. However, likewise in photo-LCP, this perspective (whether $^3PC^*$ or $^1PC^*$ or both are the major active states) has not been well established. Additionally, less oxidising (more electron-rich) PCs with lower excited state oxidation potential $E_{red}^*(PC^*/PC^{*+})$ vs. SCE (1.86 V for **70**, 1.89 V for **72**, 2.02 V for **82** and **83**, 2.20 V for **76**, 2.23 V for **74**, 2.41 V for **81** and 2.46 V for **73**) tend to afford more efficient photo-ROMP (higher polymerisation rate).¹⁰²

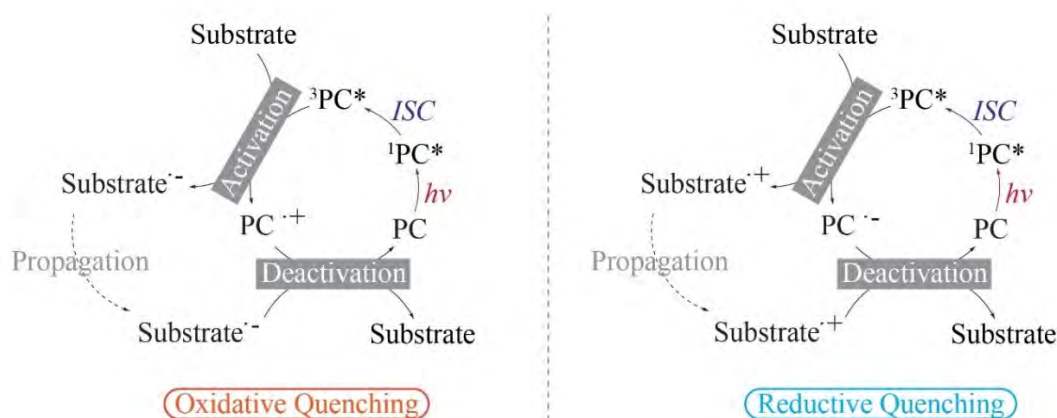


Scheme 2.19 Chemical structures of pyrylium derivatives (**72-74** and **82**) and thiopyrylium derivatives (**80**, **81**, **76** and **83**) used as PCs for photo-ROMP.

2.3 Setting the frame

2.3.1 Structure-property-performance relationships (SPPRs)

As summarised in the previous section, commonly, the photocatalytic activity of a PC in Photo-RDRP involves several key steps. Firstly, photoexcitation of the S_0 state PC by photon absorption generates the S_1 state $^1PC^*$, which then undergo subsequent intersystem crossing (ISC) to T_1 state $^3PC^*$ (**Scheme 2.20**).^{2, 43, 103} An outer-sphere single electron transfer (SET) process can then occur between $^3PC^*$ or $^1PC^*$ and the substrate.¹⁰⁴ However, the bimolecular SET process in dilute solutions of a photo-controlled polymerisation system requires diffusive encounter of the excited PC and the substrate.⁵ Consequently, the much more long-lived $^3PC^*$ is more preferable in dilute-solution-based photo-controlled polymerisation systems.¹⁰⁴ Moreover, the triplet spin configuration of $^3PC^*$ suppresses the wasteful back electron transfer after the initial SET process, allowing more time for diffusive separation of the radical ion pair formed from SET.¹⁰⁴ As aforementioned, it should also be noted that PET-RAFT polymerisation is also reported likely to occur via Dexter energy transfer (i.e., P3T) between $^3PC^*$ and the substrate RAFT agent in the presence of the iridium-based complex **1** and ruthenium-based complex **8**, where $^3PC^*$ is also the desirable excited species.⁷⁷ As mentioned in the previous section, longer-wavelength-absorbing PCs are less likely to undergo P3T in the presence of common RAFT agents. For example, ZnTPP **9** has been found with strong evidence by quantum chemical calculations that it can only undergo PET reactions with common RAFT agents.⁷⁶ However, up to now, other PCs have not been fully revisited by quantum chemical approaches to specify the contribution via PET or P3T in PET-RAFT polymerisation, and thus no definitive conclusions can be made.



Scheme 2.20 The general mechanism of photo-controlled polymerisation catalysed by a PC. Left: the oxidative quenching pathway. Right: the reductive quenching pathway.

Therefore, the key molecular properties of a PC for a photo-RDRP system includes (i) photon absorption (molar extinction coefficients ϵ at a particular wavelength and the maximum absorption wavelength λ_{\max}), (ii) the population of the T_1 state $^3PC^*$ by ISC (Φ_T), and (iii) redox properties describing thermodynamic feasibility of activating/deactivating a photo-controlled polymerisation system.¹⁰⁵ Apparently, these properties of a PC are determined by the wave function of the electronic structure arising from its chemical structure and geometry; on the other hand, variation of these PC properties directly manifest in differences in the performance of the photo-controlled polymerisation systems.⁴⁰⁻⁴¹ The overall relationships can be summarised as SPPRs. Indeed, the SPPRs are the key guiding principles for researchers to rationally design and optimise a PC chromophore deployed as PC to a particular photo-controlled polymerisation system with specific functionalities.

2.3.2 Photon absorption: molar extinction coefficients and absorption wavelengths

Photon absorption is vertical excitation of an S_0 chromophore to generate singlet excited states. It is the first event that a PC undergoes in a photo-controlled polymerisation process. Depending on the electromagnetic radiation energy, a range of singlet excited states may be accessed, but higher-lying singlet excited states will all relax to S_1 via rapid internal conversion (IC) typically within picoseconds (ps).⁵ In a practical system, the basic criterion is that certain degree of overlap must exist between absorption of the chromophore and emission of the light source. As Nicewicz *et al* pointed out in their review paper, notwithstanding that vertical excitation to higher singlet excited states will also result in relaxed S_1 , it is considered most desirable to irradiate the lowest energy absorption (i.e. the most red-shifted absorption).⁵ This is in regard to macroscopic energy efficiency and minimisation of possibility in exciting other reactants which may induce unwanted side reactions.⁵ Given a sufficiently high oscillator strength, $S_0 \rightarrow S_1$ photoexcitation corresponds to the absorption peak occurring at the longest wavelength. Namely, the maximum absorptivity of this most red-shifted peak is expressed as maximum ϵ (ϵ_{\max}) and the corresponding wavelength is λ_{\max} .⁵ There are multiple factors that affect ϵ_{\max} and λ_{\max} of a PC. Indeed, more enhanced ϵ_{\max} for more efficient light absorption and longer λ_{\max} for better solar-to-chemical energy conversion efficiency

combined with better light penetration are the most desirable for a photo-controlled polymerisation system. Tremendous effects have been made by researcher since last century to explore chromophore modification methods to pursue chromophores with higher ϵ_{\max} and longer λ_{\max} .

2.3.3 Electronic transitions: rate constants and quantum yields

In some cases, S_1 may be accessed for reactions. However, S_1 is still an unstable excited state with ns- to μs -scale lifetime and can further decay via a couple of different pathways including ISC to triplet excited states which result in T_1 (vide infra). Among all excited states, T_1 has the longest lifetime owing to the spin-forbidden nature of the $T_1 \rightarrow S_0$ transition. As aforementioned, the long-lived T_1 with a μs - to ms-scale lifetime naturally allows for adequate diffusive encountering of SET reactants. Thereby, the overall triplet quantum yield Φ_T can determine how much active excited states is accessible by the subsequent SET process of photo-RDRP.^{40, 104-105} On the other hand, the exact value of the T_1 lifetime τ_T will not gain much attention in this review, because its μs - to ms-scale is sufficiently long for SET reactions and thus the accessibility of T_1 is not much affected by τ_T .⁵

2.3.4 Activation and deactivation of photo-controlled polymerisation: redox properties

In an outer-sphere bimolecular SET reaction (SET between two individual molecules in the solution by collision), reactants are weakly coupled, with an electron transferring in between.¹⁰⁶⁻¹¹⁰ Because the outer-sphere bimolecular SET only involves transfer of an electron and slight reorganisation of molecular geometries, the reaction barrier of a SET reaction is thus minimal. The molecular geometries of both reactants experience slight fluctuation in the course of the SET event, ending up with new equilibriums after the charge separation. During charge separation, solvent reorganisation and internal reorganisation can together provide a small energy barrier. However, because the reorganisation energies are very small values which do not exert notable effect in thermodynamics, the small energy barrier can be ignored in most practical cases. As a result, the thermodynamic feasibility of activating or deactivating a photo-RDRP system is determined by the Gibbs free energy change (ΔG) of the corresponding SET redox reaction. Experimentally, with respect to the properties on the PC side, this thermodynamic feasibility of activation can be evaluated by the T_1 reduction potential of

the PC, i.e., $E^0(\text{PC}^{\bullet+}/{}^3\text{PC}^*)$, or the T_1 oxidation potential, i.e., $E^0(\text{PC}^{\bullet+}/{}^3\text{PC}^*)$, depending on the quenching pathway of the photo-RDRP or photo-LCP systems. Similar conventions also apply to the evaluation of thermodynamic feasibility of deactivation in photo-RDRP or photo-LCP.

2.4 Spectral properties: bathochromic shift and hyperchromic effect

2.4.1 Theories and structure-property relationships

As discussed in the previous section, ϵ_{max} and λ_{max} of a PC in most cases roughly correspond to $S_0 \rightarrow S_1$ photoexcitation. The $S_0 \rightarrow S_1$ photoexcitation is contributed by a mixture of different molecular orbital (MO) transitions. MO transitions with significant contribution to $S_0 \rightarrow S_1$ photoexcitation are usually transitions between frontier MO (FMO), mostly the highest occupied MO (HOMO) or the second HOMO (HOMO-1) to the lowest unoccupied MO (LUMO) or the second LUMO (LUMO+1) transitions. Depending on the nature of these MOs, the $S_0 \rightarrow S_1$ photoexcitation can commonly be classified as local excitation, charge transfer (CT) excitation. Depending on the wavefunctions of S_0 and S_1 , their energy difference and the corresponding transition electric dipole moment of $S_0 \rightarrow S_1$ transition results in the oscillator strength (f) of the $S_0 \rightarrow S_1$ transition, which directly reflect ϵ_{max} of the PC. On the other hand, the energy level gaps of related MO transition pairs in the $S_0 \rightarrow S_1$ excitation impose an overall impact on the excitation energy, which consequently determines the λ_{max} .

Apparently, by introducing substituents or modifications to the chromophore, the MOs can be tuned, leading to tuned $S_0 \rightarrow S_1$ transition and thus tuned ϵ_{max} and λ_{max} of a PC. Therefore, to achieve tuning of ϵ_{max} and λ_{max} in a certain direction and to a certain degree by rational structure modification/design, the relevant structure-property relationships need to be understood and established. In this view, researchers in the past decades have established a library of structure-property relationships to judiciously tune ϵ_{max} and λ_{max} of a PC by modifying/designing the PC structure, mostly targeting higher ϵ_{max} (the hyperchromic effect) and longer λ_{max} (the bathochromic effect) discussed as below.

2.4.2 Computational methodologies

Direct calculation of absorption spectral properties can be easily performed with common software packages like Gaussian,¹¹¹ ORCA, Dalton,¹¹² BDF¹¹³ and specialized programs

like MOMAP,¹¹⁴ combined with characterisation of MOs to qualitatively assign different excitations with absorption peaks.

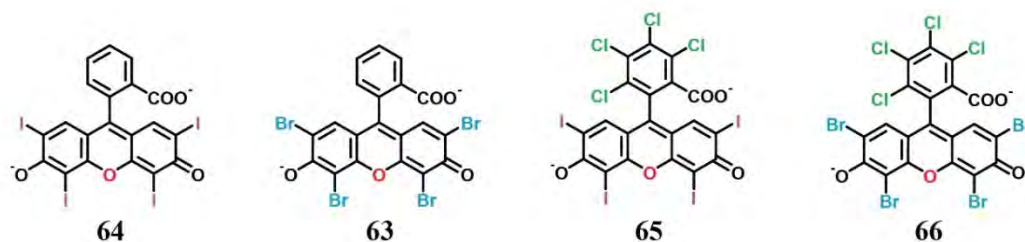
To gain a theoretical insight and a quantitative view into the structure-properties, explicit wavefunction analysis can be done with the most cutting-edged methodologies such as:

1) Hole-electron analysis (based on calculating charge density difference between the excited state and the ground state) to visualize the excitation characteristics and discern localized excitation, bulk excitation or charge transfer excitation. In the meantime, the charge transfer distance, degree of electron/hole separation, contribution of each atom/segment to electron excitation and the Coulomb attraction energy can be quantitatively determined from hole-electron analysis. A more traditional strategy in quantifying charge transfer excitation is Natural Transition Orbital (NBO) analysis and Adaptive Natural Density Partitioning (AdNDP) analysis. Other methods include inter-fragment charge transfer (IFCT) analysis. Packages like Multiwfn¹¹⁵ and NBO can be used for relevant analysis.

2) Analysis of characteristics of π -electrons in a chromophore is of fundamental importance in evaluating the photophysical properties of a PC, since π - π^* excitations usually predominate in photoexcitation of a conjugated organic molecule. This type of analysis can clearly visualize and provide basic information about aromaticity/antiaromaticity, conjugation pathways and dimensions of the conjugation system, which largely influence the excitation energy. Methodologies to evaluate π -electron characteristics include the electron localization function (ELF) analysis, localized-orbital locator (LOL) analysis and π -electron population calculations. Multiwfn¹¹⁵ can be used for relevant analysis.

2.4.3 Bathochromic shift and hyperchromic effect by heavy halogen substituents

Perhaps the most known strategy to tune λ_{\max} and ϵ_{\max} of a chromophore is the introduction of halogen substitution. Whilst it is generally accepted that heavier atom substitution tends to result in higher ϵ_{\max} and longer λ_{\max} ,¹¹⁶ heavy halogen substitution is the most effective and readily applicable method. For example, recent reports on modifying iridium complexes with heavier halogens attributed the observed bathochromic shift and hyperchromic effect to the heavy halogen substituents stabilising LUMO while remaining HOMO mostly unperturbed.¹¹⁷⁻¹¹⁸



Scheme 2.21 Chemical structures of halogenated xanthene dyes **64**, **63**, **65** and **66**.

Similarly, we investigated the use of halogenated xanthene dyes (**64**, **63**, **65** and **66** as examples in **Scheme 2.21**) in PET-RAFT polymerisation and more explicitly explored how the variation of halogen substitutions tunes λ_{\max} and ϵ_{\max} of the chromophore.⁴⁰ TD-DFT calculations showed that the HOMO \rightarrow LUMO transition has more than 98% contribution to the $S_0\rightarrow S_1$ vertical excitation of these halogenated xanthene dyes and indicated that the evolution of λ_{\max} by halogen substitution can be exclusively described by the natures and energy levels of HOMO and LUMO. Specifically, because the non-bonded (n) electrons of halogen substituents in the xanthene core has a significant population of HOMO, heavier halogens naturally exhibit higher energy n electrons (i.e. $I > Br$) and lead to higher HOMO energy level, shown by comparing **64** (**Figure 2.1A**) and **63** (**Figure 2.1B**). On the other hand, there is no population of LUMO localised in these xanthene core halogens and thus LUMO energy levels are less effected comparing **64** (**Figure 2.1A**) and **63** (**Figure 2.1B**). Consequently, the heavier I-substituted **64** has narrower HOMO/LUMO energy gap and longer $\lambda_{\max} = 548$ nm compared to Br-substituted **63** with $\lambda_{\max} = 540$ nm; similar trend was observed for I-substituted **65** with longer $\lambda_{\max} = 563$ nm compared to Br-substituted **66** with $\lambda_{\max} = 555$ nm.⁴⁰

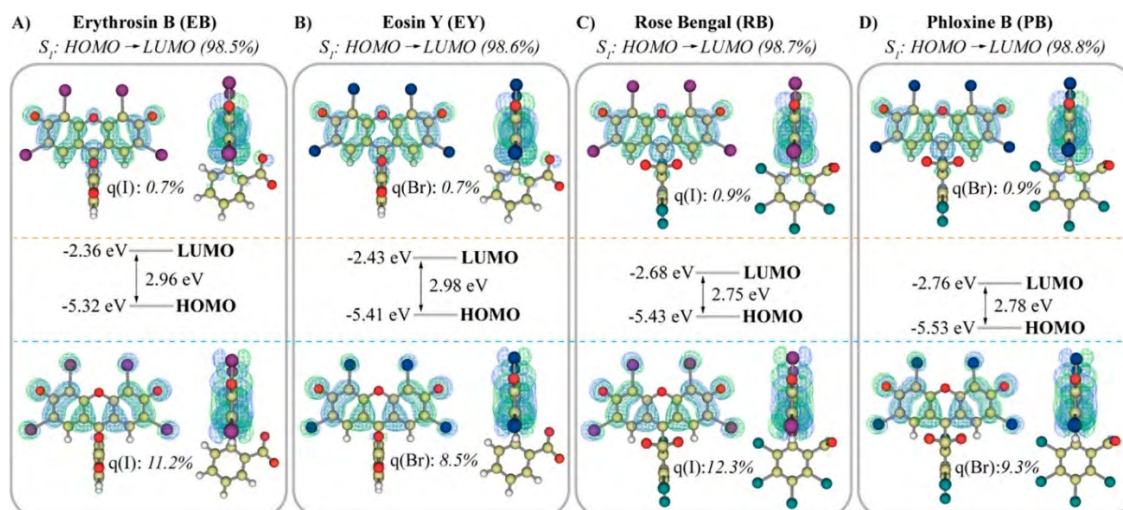


Figure 2.1 FMOs and their energy levels of S_0 state (A) Erythrosine B (**64**), (B) Eosin Y (**63**), (C) Rose Bengal (**65**), and (D) Phloxine B (**66**). q : percentage of the MO localised on the specified element. Reprinted with permission from ref 40. Copyright © 2019, American Chemical Society.⁴⁰

It was also found that heavier halogen substitution also leads to an increase in ϵ_{\max} (**Table 2.1**), contributed by both narrower S_1/S_0 energy difference and higher transition electric dipole moment by the heavy atom effect.⁴⁰

Table 2.1 Spectral Properties of Halogenated Xanthene Dyes.

	Halogen substituents	λ_{\max} (nm)	ϵ_{\max} ($M^{-1} \text{ cm}^{-1}$)
64	4 xanthene-I	548	95000
63	4 xanthene-Br	540	87800
65	4 xanthene-I & 4 phenyl-Cl	563	97300
66	4 xanthene-Br & 4 phenyl-Cl	555	93800

Reproduced with permission from ref 0. Copyright © 2019, American Chemical Society.⁴⁰

2.4.4 Bathochromic shift by chromophore core-twisting

By introducing bulky substituents to the chromophore that produces significant steric hinderance, the originally planar chromophore core can be twisted, which leads to pronounced changes in its wavefunction and consequently large variation in its molecular properties. Researchers have found that core-twisting of same common organic chromophores can lead to notable bathochromic effect and absorption peak broadening. These core-twisted dyes include nanocarbon (e.g. acene) derivatives, perylene diimide (PDI) derivatives and porphyrin derivatives.

Gidron and coworkers recently reviewed the helically locked twisted acene derivatives and focused on the relationship between their twist angles and the resultant effect on their optical and electronic properties.¹¹⁹ Overall, with the increase in the twist angle, the twisted acene derivative exhibit slight destabilisation of its HOMO as well as slight stabilisation of LUMO (**Figure 2.2**).¹¹⁹⁻¹²⁰ This is caused by orbital rehybridization where greater σ character is mixed into π as a result of core-twisting.¹²¹⁻¹²² Consequently, the narrowed HOMO/LUMO energy gap lead to slight bathochromic shift observed in its

absorption spectra.¹¹⁹⁻¹²⁰ This general trend is applicable to most twisting nanocarbons.¹¹⁹

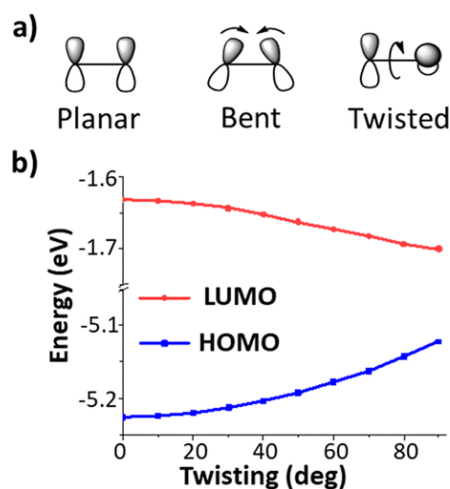
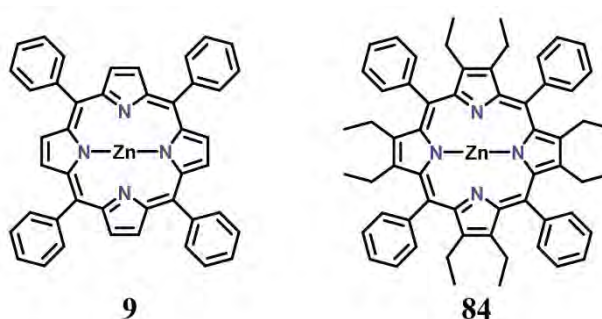


Figure 2.2 (a) The planar, bent, and twisted conformations of two adjacent p-orbitals. (b) Calculated HOMO and LUMO energy levels of anthracene (as a simplified example of twisted acene derivatives) with different twist angles. Reprinted with permission from ref 119. Copyright © 2019, American Chemical Society.¹¹⁹



Scheme 2.22 Chemical structures of **9** and **84**.

Similarly, Holten and coworkers systematically investigated the conformationally distorted porphyrin derivatives and discovered that the non-planarity of the macrocycle induced by the steric hinderance of adjacent bulky peripheral substituents largely affects the S_1 state and hence related photophysical properties.¹²³ Specifically, the saddle deformations of twisted porphyrins tend to destabilise their HOMOs while stabilise LUMOs and thereby yield smaller HOMO/LUMO energy gaps, which naturally leads to bathochromic shift in the absorption spectra.¹²³ Senge more generally reviewed a large library of core-twisted porphyrins and concluded that macrocycle distortion of porphyrin derivatives can destabilise the π system.¹²⁴ For example, zinc(II) 2,3,7,8,12,13,17,18-

octaethyl-5,10,15,20-tetraphenylporphyrin (**84**, Scheme 2.22) is an excellent core-twisting porphyrin dye whose planar porphyrin counterpart is zinc(II) 5,10,15,20-tetraphenylporphyrin (**9**, Scheme 2.22). While **84** only has eight additional peripheral ethyl groups in comparison to **9**, these ethyl groups mostly only impose geometrical impact on the chromophore without any notable electron-donating/withdrawing effect or any conjugated effect. As reported in literature, the experimentally resolved structure of ZnOETPP indeed exhibits a saddle-distorted non-planar macrocycle because of the steric hinderance formed between ethyl groups and phenyl groups.¹²⁴⁻¹²⁵ This distortion has led to a significant ~85 nm bathochromic shift in λ_{\max} from 600nm of ZnTPP⁷⁸ to 685 nm of ZnOETPP.¹²⁶

2.4.5 Bathochromic shift by introduction of alkyl/aryl oxide or sulfide substituents

Recently, Zhao and coworkers synthesised a series of PDI derivatives and reported the strong bathochromic shift in absorption caused by alkyl sulfide substitution on the bay positions of PDI derivatives.¹²⁷ As shown in Figure 2.3, because of the bay substituents, **PDI-2**, **PDI-3**, **PDI-4**, **PDI-5** and **PDI-6** all exhibit slight core-twisting characters as compared to the planar **PDI-1**. However, this nonplanarity is not significant and apparently that the core-twisting halogen-substituted **PDI-4** and **PDI-5** exhibit comparable λ_{\max} to **PDI-1** ($\lambda_{\max} = 523$ nm). Therefore, the alkyl/aryl sulfide substituents of **PDI-2**, ($\lambda_{\max} = 560$ nm), **PDI-3** ($\lambda_{\max} = 552$ nm) must have played an important role in the observed significant ~30 nm bathochromic shift in λ_{\max} as compared to **PDI-1**. The authors observed that the presence of higher energy n electrons in the S atoms notable moves up the HOMO energy level while having much less effect on the LUMO energy level, leading to much narrowed HOMO/LUMO energy gaps (Figure 2.3). Consequently, these n $\rightarrow\pi^*$ characters in $S_0\rightarrow S_1$ excitation (~99% contribution from HOMO \rightarrow LUMO transition) result in the notable bathochromic shift of λ_{\max} in **PDI-2** and **PDI-3** with respect to **PDI-1**. On the other hand, the bathochromic shift in **PDI-6** is smaller, which is because of the strong electron-withdrawing effect of F substituents that greatly withdraw the n electrons on S and reduce their impact on the chromophore.¹²⁷

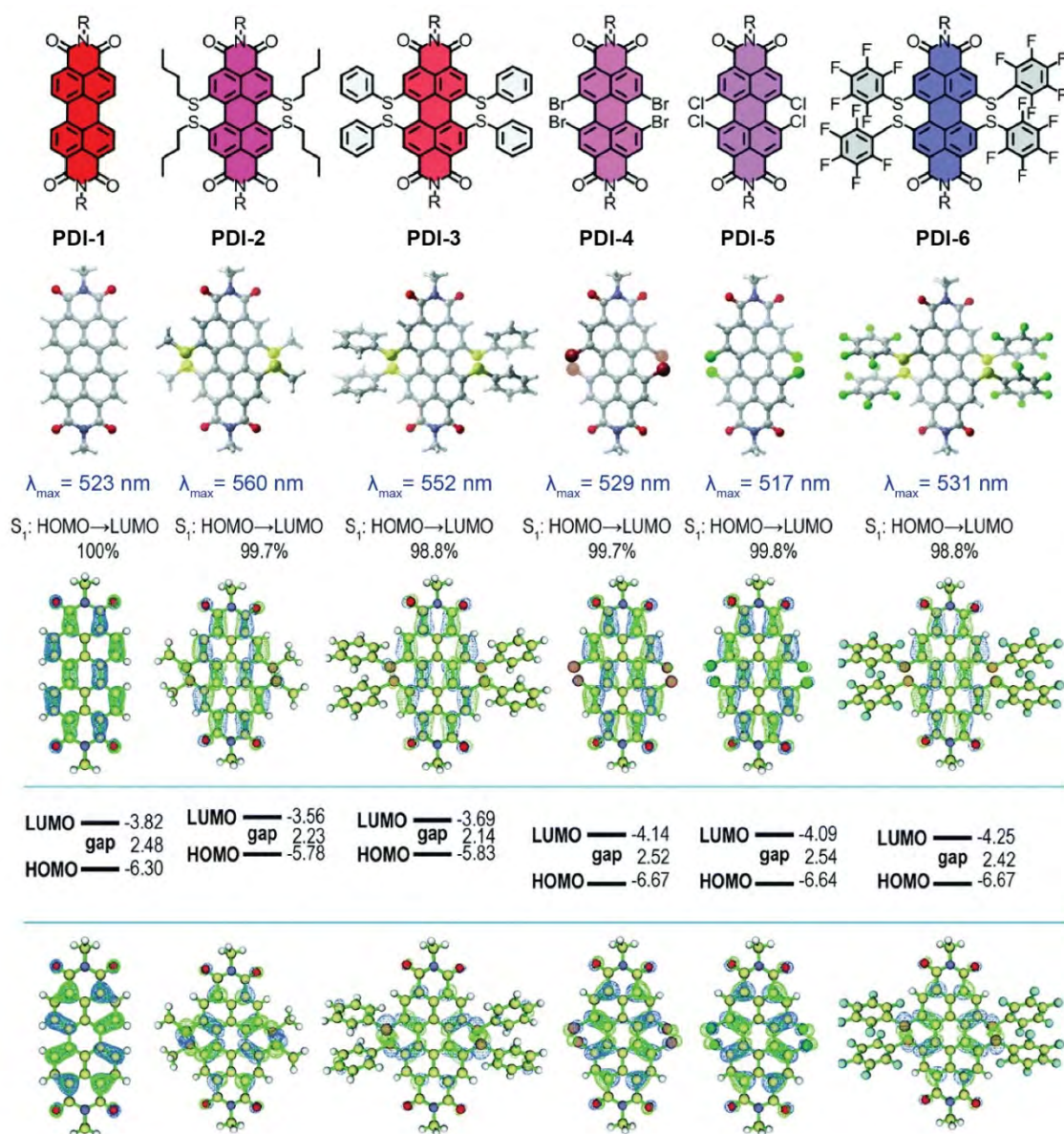


Figure 2.3 Chemical structures, molecular geometries and visualized FMOs (isovalue = 0.03) of PDI derivatives **PDI-1**, **PDI-2**, **PDI-3**, **PDI-4**, **PDI-5** and **PDI-6**. Reprinted with permission from ref 127. Copyright © 2019, The Royal Society of Chemistry.¹²⁷

Würthner and coworkers observed similar bathochromic shifts for PDI derivatives substituted with aryl oxide on bay positions, which can lead up to 56 nm bathochromic shift in λ_{\max} .¹²⁸ More strikingly, the authors observed 181 nm bathochromic shift in λ_{\max} by introducing pyrrolidinyl substituents on bay positions,¹²⁸ which is likely also due to the high energy n electrons in the N atoms contributing to $n \rightarrow \pi^*$ characters of the $S_0 \rightarrow S_1$ excitation.

Very recently, Martynov and coworkers employed (TD)DFT methods and spectroscopic methods to theoretically interpret the spectral properties across a library of unsubstituted and alkoxy-substituted free-base or zinc phthalocyanine derivatives **85**, **86**, **87**, **88**, **89** and **90** (**Figure 2.4**).¹²⁹ Two types of alkoxy substitution are possible for phthalocyanine derivatives, i.e., the peripheral β -alkoxy-substitution (e.g. **86** and **89**, **Figure 2.4**) and the nonperipheral α -alkoxy-substitution (e.g. **87** and **90**, **Figure 2.4**). Interestingly, the two types perform very differently in affecting the spectral properties of the phthalocyanine chromophores. In the context of the peripheral β -alkoxy-substituted **86** and **89**, λ_{\max} of their Q-bands are located at 703 nm and 679 nm respectively, almost the same as their unsubstituted counterparts **85** and **88**. In contrast, the nonperipheral α -alkoxy-substituted **87** ($\lambda_{\max} = 772$ nm) and **90** ($\lambda_{\max} = 751$ nm) exhibit pronounced bathochromic shift in λ_{\max} as large as ~ 70 nm (**Figure 2.4**). The authors concluded that the nonperipheral α -alkoxy-substitution can strongly destabilise HOMO because of larger HOMO population on α -carbons resulting in stronger mesomeric interaction with n electrons of the O atoms, which consequently leads to narrowed HOMO/LUMO energy gap and the observed large Q-band bathochromic shift.¹²⁹ Another report discovered that the Q-band bathochromic shift is enhanced with increasing number of nonperipheral α -alkoxy-substituents.¹³⁰ Similarly, Martin and coworkers observed the same nonperipheral α -alkoxy-substitution effect in generating a large Q-band bathochromic for naphthalocyanines.¹³¹

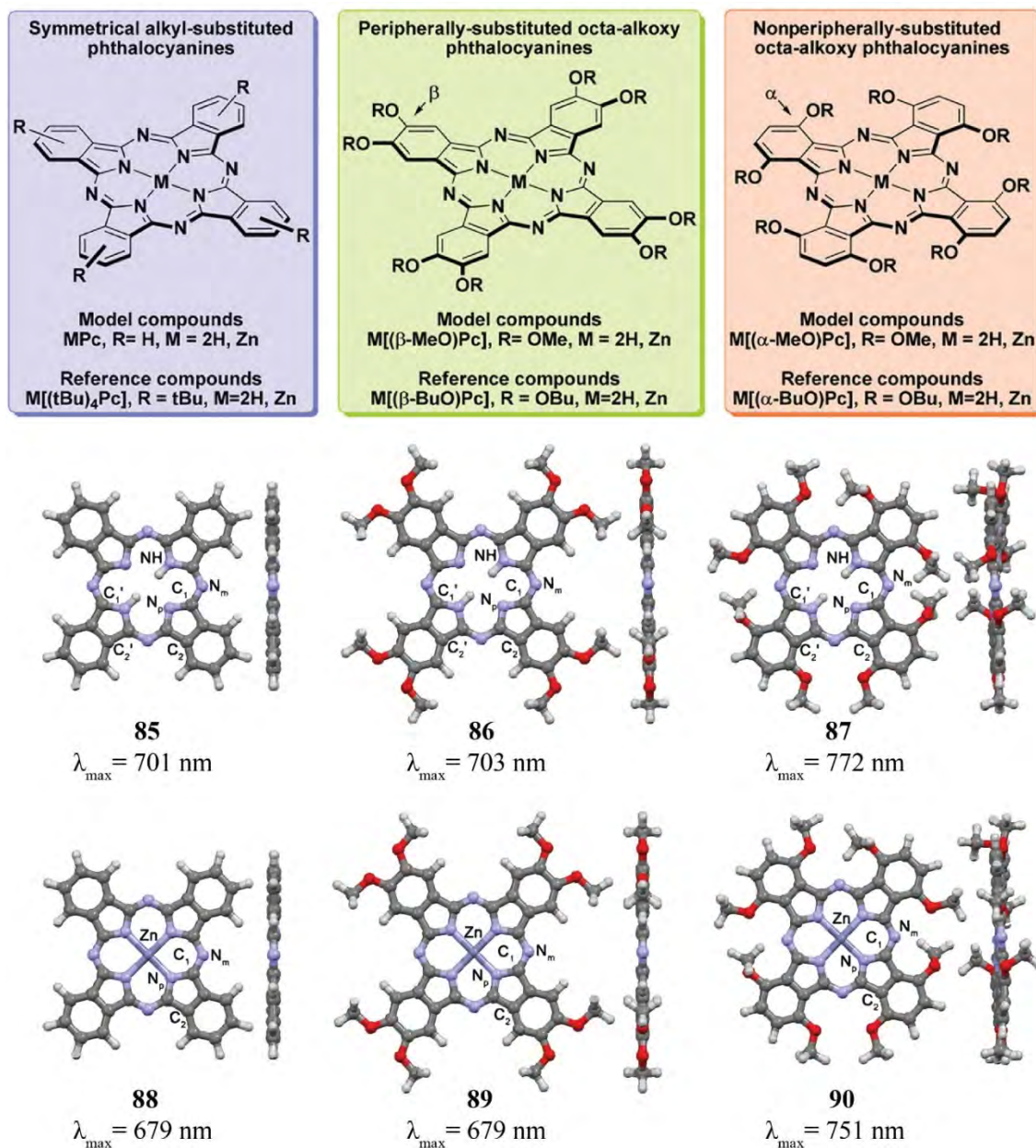


Figure 2.4 Chemical structures and molecular geometries of the free-base phthalocyanine **85**, the free-base β -alkyloxy-substituted phthalocyanine **86**, the free-base α -alkyloxy-substituted phthalocyanine **87**, the zinc(II) phthalocyanine **88**, the zinc(II) β -alkyloxy-substituted phthalocyanine **89**, the zinc(II) α -alkyloxy-substituted phthalocyanine **90**. Reprinted with permission from ref 129. Copyright © 2019, American Chemical Society.¹²⁹

2.4.6 Bathochromic shift and hyperchromic effect by extended π -conjugation

π -Conjugation system extension is one of the most applied guiding principle for designing long-wavelength absorbing dyes.¹³² This is based on the conventional recognition that

“larger π -conjugation contributes to bathochromic shifts”. Although not always true¹³² and can have exceptions,¹³³ this statement is still useful in most cases given sufficient understanding of the core chromophore before modification.¹³² The most commonly seen π -expanded dyes include polyaromatic dyes¹³² and porphyrin derivatives.¹³⁴

Adachi and coworkers reported the effect of π -conjugation extension on polynaphthalenetetracarboxylic dianhydride diimide dyes **91**, **92** and **93** (**Figure 2.5**).¹³² From **91** ($\lambda_{\max} = 526$ nm, $\epsilon_{\max} = 81500$) to **92** ($\lambda_{\max} = 650$ nm, $\epsilon_{\max} = 93300$) and **93** ($\lambda_{\max} = 764$ nm, $\epsilon_{\max} = 16200$), with the π -conjugation extension along the long molecular axis, significant bathochromic shift in λ_{\max} and notable hyperchromic effect in ϵ_{\max} were observed (**Table 2.2**). As shown in **Figure 2.5**, the extended π -conjugation leads to destabilisation of HOMO and move up the HOMO energy level while scarcely affects the LUMO energy level. This overall effect contributes to narrowed HOMO/LUMO energy gap and therefore contribute to notable bathochromic shifts. The authors further explained that all bridges connecting each naphthalene fragments are characterised as antibonding connections in HOMOs of these derivatives; because of increasing content of these antibonding connections from **91** to **92** and **93**, the HOMO is more destabilised and exhibits higher energy level, while the LUMO always has bonding connections in all bridges and thus not affected (**Figure 2.5**).¹³² Meanwhile, the larger π -conjugation which causes destabilisation of the HOMO further leads to an increase in the transition dipole length and consequently yields enhanced ϵ_{\max} .¹³²

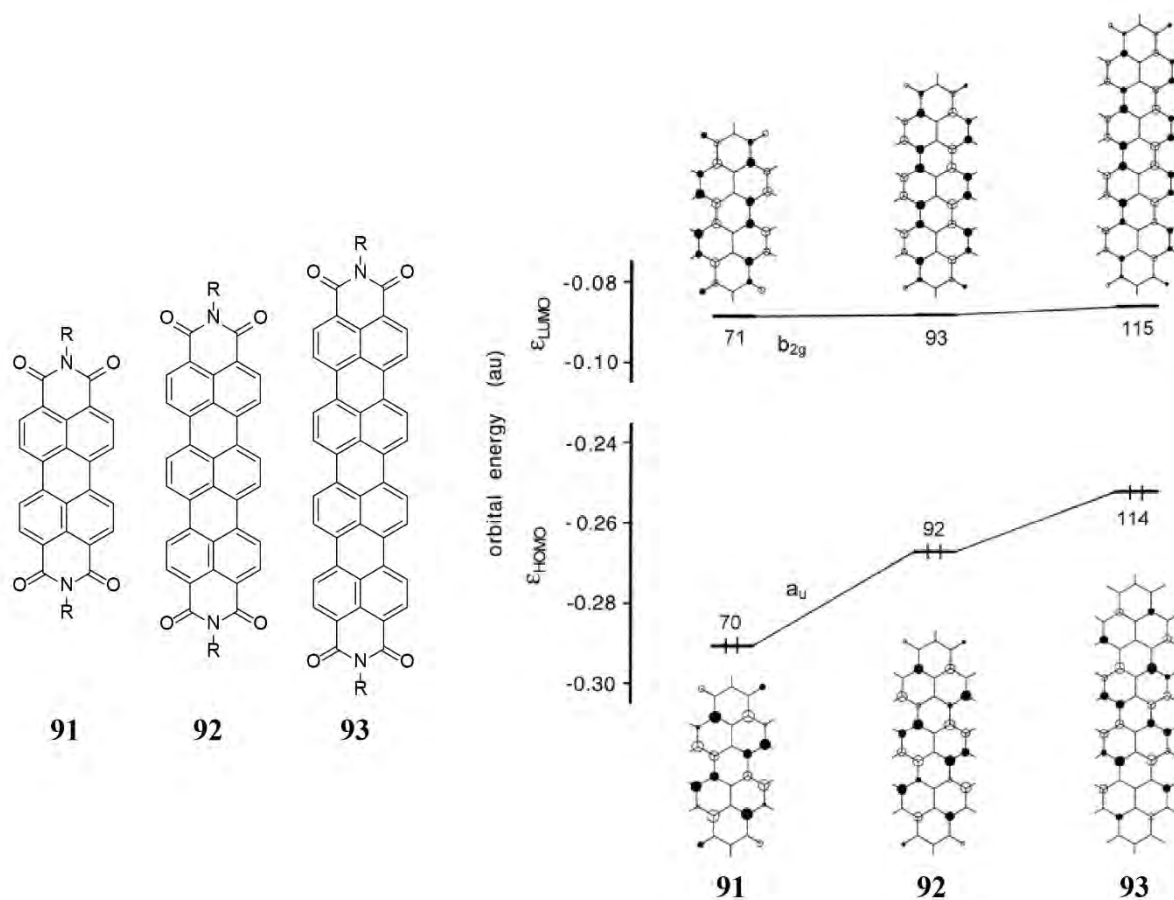


Figure 2.5 Chemical structures and HOMOs/LUMOs (and corresponding energy levels) of polynaphthalenetetracarboxylic dianhydride diimide dyes **91**, **92** and **93**. Reprinted with permission from ref 132. Copyright © 2001, American Chemical Society.¹³²

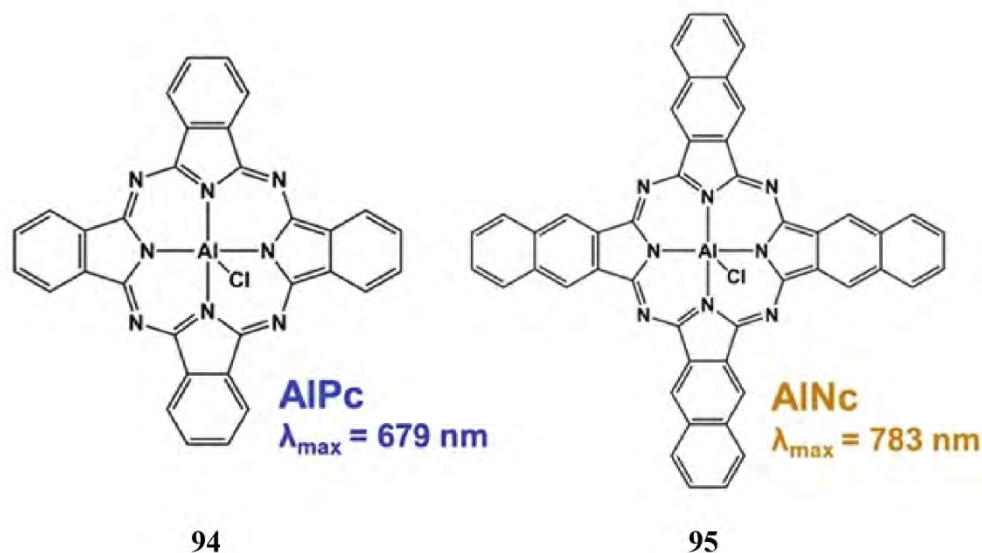
Table 2.2 Observed and calculated absorption spectra of polynaphthalenetetracarboxylic dianhydride diimide dyes **91**, **92** and **93**.

dye	observed		calculated	
	λ_{\max} (nm)	ϵ_{\max}	λ_{\max} (nm)	f
91	526	81 500	441	1.258
92	650	93 300	520	1.834
93	764	162 000	580	2.404

Reprinted with permission from ref 0. Copyright © 2001, American Chemical Society.¹³²

On the other hand, Sessler and coworkers reviewed a large library of π -extended boron dipyrromethenes (BODIPYs), π -extended sapphyrins, π -extended porphycenes, π -extended corroles, π -extended rosarins, π -extended cyclo[n]pyrroles and other types of

expanded porphyrins with π -extension.¹³⁴ All of these π -extended dye classes exhibit larger bathochromic shift in λ_{\max} with larger π -extension.¹³⁴ As a typical example, the phthalocyanine derivative **94** (Scheme 2.23) possesses a λ_{\max} of 679 nm and its π -extended naphthalocyanine counterpart **95** (Scheme 2.23) has a λ_{\max} of 783 nm; the π -extension contributes to a 104 nm bathochromic shift.¹³⁵



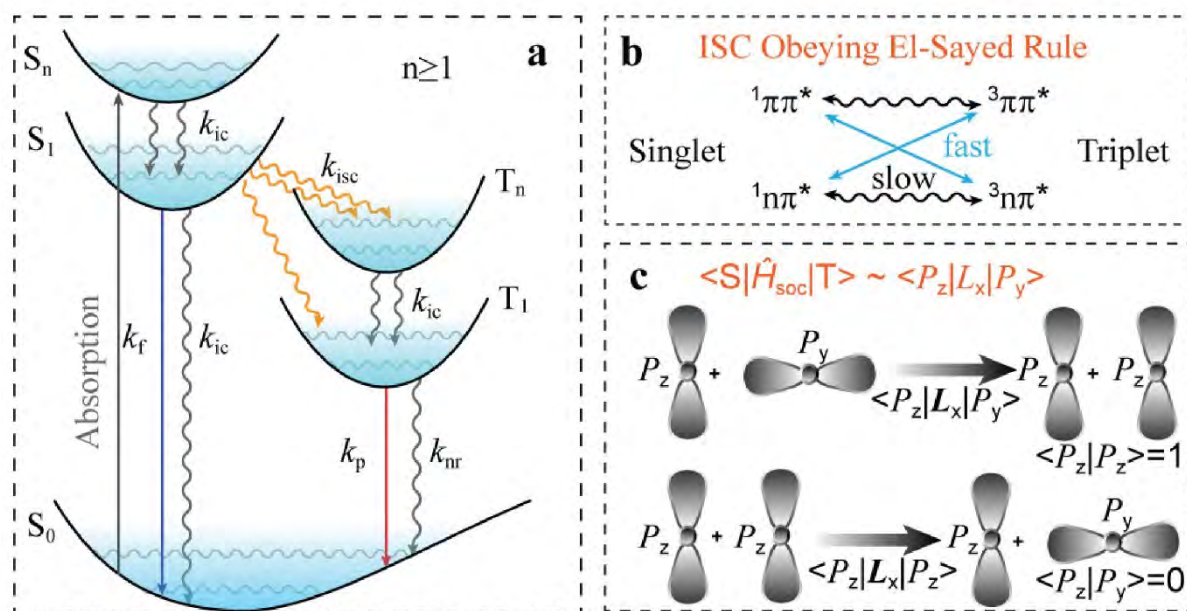
Scheme 2.23 Chemical structures of a phthalocyanine derivative **94** and the corresponding naphthalocyanine derivative **95**. Reprinted with permission from ref 135. Copyright © 2019, John Wiley and Sons.¹³⁵

2.5 Electronic transitions: enhanced triplet quantum yield

2.5.1 Theories and structure-property relationships

As presented in the Jablonski diagram (Scheme 2.24a), the photophysical processes upon irradiation of a chromophore starts from $S_0 \rightarrow S_n$ ($n \geq 1$) photon absorption, followed by $S_n \rightarrow S_1$ IC decay in accordance to Kasha's rule.¹⁰³ From S_1 , subsequent radiative decay (characteristic of fluorescence decay constant k_f) and IC decay (characteristic of IC decay constant k_{ic}) to S_0 and ISC decay to T_n (characteristic of ISC decay constant k_{isc}) followed by $T_n \rightarrow T_1$ IC decay finally result in population of T_1 . The quantum yield of T_1 is correspondingly defined as $\Phi_T = k_{isc}/(k_f + k_{ic} + k_{isc})$, which is a key parameter for a photo-RDRP PC as aforementioned.^{2, 103} In pursuing higher population of long-lived T_1 states for photo-RDRP (i.e. higher Φ_T), there are typically two requirements: (i) faster ISC of $S_1 \rightarrow T_n$ characteristic of higher ISC decay constant k_{isc} ; (ii) reduced fluorescence decay

rate k_f and IC decay rate k_{ic} . To enhance Φ_T by promoting ISC, either heavy substituents with heavy atom effect or orthogonality between S_1 and T_n wavefunctions can be fairly effective, as respectively discussed below.



Scheme 2.24 (a) Jablonski diagram. (b) El-Sayed's rules. (c) Rotational property of the orbital angular momentum. Reprinted with permission from ref 103. Copyright © 2019, American Chemical Society.¹⁰³

2.5.1.1 Heavy atom effect

Because the transitions between pure spin states with different multiplicities is spin-forbidden, these transitions can only occur from SOC, which is a relativistic phenomenon¹³⁶ inducing a quantum mechanical mixing of states with different multiplicities.¹³⁷ Qualitatively, SOC arises from the spin magnetic moment of an electron interacting with the magnetic field generated by the motion of its nucleus.¹³⁸ The magnitude of the nuclear magnetic field is proportionally related to the nuclear charge, i.e. the atomic number Z .¹³⁷ Consequently, SOC, the relativistic phenomenon which contributes to ISC transitions, increases roughly like Z^2 for valence shells.¹³⁶ As such, with heavier atom substitution, the chromophore can exhibit enhanced k_{isc} resulting from enhanced SOC, and thus bear an enhanced Φ_T .

2.5.1.2 Orthogonality between S_1 and T_n wave functions

According to the El-Sayed's rules,¹³⁹ an efficient ISC process via SOC can occur between singlet and triplet states bearing different MO types (i. e, orthogonality between S_1 and

T_n wave functions and thus a change of MO types in the $S_1 \rightarrow T_n$ transition).¹⁰³ This orthogonality (either partial or full) may arise either from the simple ${}^{3,1}(n\pi^*) \leftrightarrow {}^{1,3}(\pi\pi^*)$ transitions¹⁰³ (**Scheme 2.24b**) or transitions between localised $\pi\pi^*$ -type states and CT states ${}^{3,1}(\pi\pi^*)_{CT} \leftrightarrow {}^{1,3}(\pi\pi^*)_{loc}$.³⁸ Moreover, enhanced ISC via SOC was also reported in several cases to be attributed to core-twisting with deviation of aromatic backbones from planarity,¹¹⁹ which is also believed to arise from orthogonality but has not yet been fully addressed in theory. Commonly chromophore core-twisting can be introduced by forming steric hinderance between adjacent substituents.

2.5.2 Computational methodologies

To calculate Φ_T by $\Phi_T = k_{isc}/(k_f + k_{ic} + k_{isc})$, it is a necessity to compute the different excited state decay constants k_f , k_{ic} , and k_{isc} .

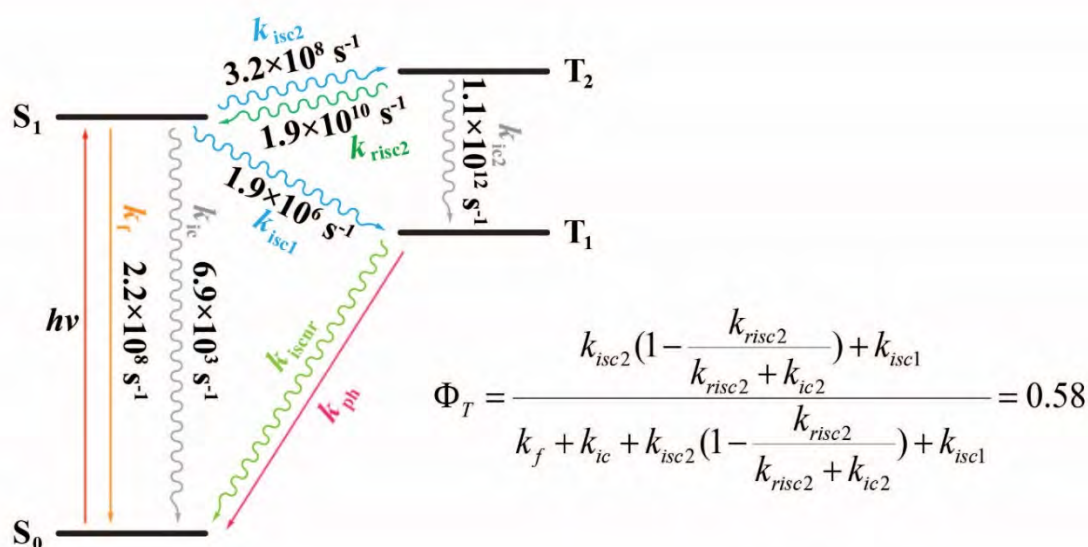
The excited state and ground state geometries, their vibration normal modes, transition energies and electric transition dipole moment can be calculated by the Gaussian software package.

k_f corresponds to the decay constant of the $S_1 \rightarrow S_0$ radiative decay and can be evaluated by the Strickler-Berg equation, which requires inputting the spontaneous transition frequency from S_1 to S_0 , the electric transition dipole moment between S_1 and S_0 and the vibrational functions for S_1 and S_0 .¹⁴⁰⁻¹⁴¹ Computation of k_f can be routinely performed via any of the ORCA, Dalton or MOMAP software package.

k_{ic} corresponds to the decay constant of the $S_1 \rightarrow S_0$ nonradiative decay. Literature reported that the computation of k_{ic} has to be based on the correlation function formalism of the Duschinsky rotation effect,¹⁴⁰ which was found to impose a critical impact on the temperature dependence of luminescence phenomena.¹⁴² Shuai and coworkers have derived a rate formula for the $S_1 \rightarrow S_0$ nonradiative decay process through vibronic coupling by consideration of the Duschinsky rotation effect.^{140, 143} Firstly, the Duschinsky rotation matrix along with the normal mode displacements can be computed by the DUSHIN program;¹⁴⁴⁻¹⁴⁵ secondly, vibronic couplings need to be obtained. On top of these and the relevant information of S_1 and S_0 obtained from TD-DFT calculations, k_{ic} can be calculated by using the MOMAP software package.¹¹⁴

k_{isc} corresponds to the decay constants of the $S_1 \rightarrow T_n$ intersystem crossing processes. Shuai and coworkers proposed a statistical rate analytical formalism on the basis of the second-order perturbation theory which combines both SOC and nonadiabatic couplings.¹⁴⁶ On top of the second perturbation theory, they derived a general ISC rate formalism to calculate k_{isc} including the spin-vibronic coupling where the origin displacements, distortion and the Duschinsky rotation within a multimode harmonic oscillator model are considered.¹⁴⁶ Calculation of k_{isc} by this method can be performed with the MOMAP software package while the SOC matrix elements have to be computed from other software packages. To precisely and efficiently calculate the SOC matrix elements between S_1 and T_n , Liu and coworkers developed an extended spin-adapted TD-DFT (S-TD-DFT) method to treat scalar-relativistic effects to infinite order via the spin-free part of the exact two-component (sf-X2C) Hamiltonian, and treat the SOC perturbatively via an effective one-electron spin-orbit operator from the same X2C Hamiltonian, namely the sf-X2C-S-TD-DFT-SOC approach.^{42, 147} Accordingly, the SOC matrix elements between S_1 and T_n can be reliably calculated by the BDF software package.¹⁴⁷⁻¹⁴⁹ Alternatively, the SOC matrix elements can also be readily calculated by ORCA, pysoc or Dalton software packages.

As an example, in a recent research of ours, we calculated Φ_T of a halogenated xanthene dye and obtained $\Phi_T = 0.58$ as presented in **Scheme 2.25**, which is highly consistent with theoretically expected.²



Scheme 2.25 Computationally derived Jablonski diagram of a synthesised halogenated xanthene dye and its derivation of Φ_T from different excited state decay constants.² Reprinted with permission from ref 2. Copyright © 2019, American Chemical Society.²

2.5.3 Enhanced triplet quantum yield by excited state charge transfer

As aforementioned, it is essential to populate T_1 states in photo-RDRP systems as the long-lived T_1 states can be sufficiently diffused to encounter substrates for SET reactions and can effectively suppress the undesirable back electron transfer upon bimolecular collision in SET.^{5, 38, 104} However, most of the purely organic chromophores lack of efficient SOC and hence bear rather slow ISC and low Φ_T .³⁸ To construct D-A scaffolds characteristic of CT excitation has become a popular strategy to design purely light-atom-based organic chromophores with high Φ_T . On one hand, the orthogonal nature of the ${}^{3,1}(\pi\pi^*)_{CT} \leftrightarrow {}^{1,3}(\pi\pi^*)_{loc}$ transition largely enhances ISC via SOC in the CT states.^{38, 45} On the other hand, the twisted D-A structure bearing largely offset MOs between the donor and acceptor moieties results in minimal HOMO/LUMO offset and thereby has a narrowed singlet-triplet energy gap ΔE_{st} ,^{4, 38} which also effectively facilitates ISC because the ISC rate is jointly determined by SOC and ΔE_{st} .

By attaching aryl groups with low-lying π^* (either by extended conjugation or electron-withdrawing substitution), Miyake and coworkers constructed a library of dihydrophenazine derivatives,³⁶ phenoxazine derivatives³⁷ and dimethyl-dihydroacridine derivatives³⁵ bearing D-A motifs, which are characteristic of CT excited states, as effective O-ATRP PCs with high Φ_T and highly reducing T_1 states. As a typical example, they used two comparable π -extended phenoxazine derivatives to demonstrate the effect of CT characters of excited states on photophysical properties of a PC.⁴³ Damrauer, Miyake and coworkers discovered that the phenoxazine derivative **39** (**Figure 2.6**) possesses a Φ_T (i.e. Φ_{ISC} , **Figure 2.6**) of 0.11. As shown in **Figure 2.6**, right, after local excitation in the phenoxazine core of **39** reaching the Frank-Condon singlet S_{FC} , the electron density is rapidly shifted to one of the biphenyl substituents reaching the CT state $S_{CT-Biph}$ within 10 ps by solvent reorganisation and conformational relaxation. However, the subsequent ISC process occurs as $S_{CT-Biph} \rightarrow T_{CT-Biph}$ transition, which neither has narrow ΔE_{st} nor exhibit orthogonality in their orbital angular momentum modes. Consequently, the k_{isc} of $S_{CT-Biph} \rightarrow T_{CT-Biph}$ transition is limited and cannot effectively compete with $k_f + k_{ic}$ (i.e. $k_f + k_{nr}$) of the $S_{CT-Biph} \rightarrow S_0$ transitions, resulting in a low Φ_T of

0.11 (**Figure 2.6**). In stark contrast, by replacing the N-phenyl group of **39** with the N-naphthyl group, the received π -extended derivative **40** (**Figure 2.6**) exhibit a remarkably high Φ_T of 0.91. As presented in the energy diagram (**Figure 2.6**), upon local excitation in the phenoxazine core of **40** reaching S_{FC} and further $S_{CT-Biph}$, the electron density is further shifted to the N-naphthyl group reaching $S_{CT-Naph}$ within ~ 20 ps. Subsequently, two ISC pathways can occur (respectively denoted as A and B in Figure 2.9). The ISC pathway A has $S_{CT-Naph} \rightarrow T_{CT-Naph}$ transition as the rate-limiting step, which bears a very small ΔE_{st} hence resulting in fast ISC; however, although possible, the pathway A was not observed.⁴³ On the other hand, the ISC pathway B directly couples $S_{CT-Naph}$ with $T_{CT-Biph}$. The k_{isc} of $S_{CT-Naph} \rightarrow T_{CT-Biph}$ transition is greatly enhanced because of the notable change in orbital angular momentum which greatly facilitates SOC as aforementioned. Consequently, **40** exhibits an unprecedented Φ_T of 0.91 arising from the excited state CT characters.⁴³

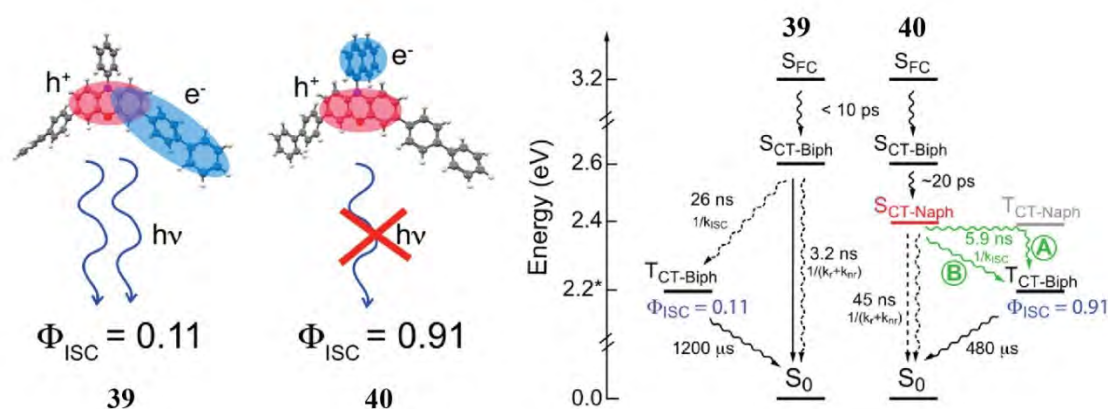


Figure 2.6 Left: molecular geometries of **30** and **40**, with Φ_{ISC} (Φ_T) denoted below. Right: diagram of excited and ground state energy levels with alternative ISC pathways presented for **30** and **40**. Less likely pathways are indicated in dashed lines.⁴³ Reprinted with permission from ref 43. Copyright © 2018, American Chemical Society.⁴³

Following this study, Damrauer, Miyake and coworkers further investigated a class of N-aryl 3,7-diphenyl phenoxazine derivatives **96**, **34** and **35** (**Figure 2.7**) with variation in their N-aryl substitution to establish more detailed relationships between the CT character of excited states and Φ_T .⁴⁵ Unlike the previous report, the chosen 3,7-diphenyl group to replace the 3,7-dibiphenyl group helps isolate the impact of N-aryl substitution on CT characters and Φ_T . For **96**, upon photoexcitation to the Frank-Condon excited state (S_{FC}),

it rapidly relaxed to an emitting state S_{deloc} characteristic exhibiting orbital character delocalised to the whole chromophore. Subsequently, S_{deloc} can both relax to S_0 by fluorescence/IC and $T_{\text{CT-Phen(core)}}$ (exhibiting partial CT to a MO spanning the phenoxazine core and its one-side adjoining phenyl group) via SOC. Because of the orthogonality in $^{1,3}(\pi\pi^*)_{\text{deloc}} \rightarrow ^{3,1}(\pi\pi^*)_{\text{CT,Phen(core)}}$ arising from the CT character, the SOC of the $S_{\text{deloc}} \rightarrow T_{\text{CT-Phen(core)}}$ transition is enhanced leading to a notable k_{isc} able to compete with k_{f} and k_{ic} , which results in $\Phi_{\text{T}} = 0.30$ (**Table 2.3**). On the other hand, by replacing the N-phenyl group with an *N*-1-naphthyl group, the resultant **34** exhibited an additional intermediate singlet state $S_{\text{CT-Naph}}$ with CT character to the *N*-1-naphthyl group, which is relaxed from S_{deloc} (**Figure 2.7**, bottom). Obviously, due to the CT character of the emitting state $S_{\text{CT-Naph}}$, the irradiative $S_{\text{CT-Naph}} \rightarrow S_0$ transition is greatly impeded, leading to a low $k_{\text{f}} = 3.0 \times 10^6 \text{ s}^{-1}$ of **34** as compared to **96** ($k_{\text{f}} = 2.1 \times 10^8 \text{ s}^{-1}$). Meanwhile, the more pronounced CT character of the $S_{\text{CT-Naph}} \rightarrow T_{\text{CT-Phen(core)}}$ transition with promoted orthogonality in $^{1,3}(\pi\pi^*)_{\text{CT,Naph}} \rightarrow ^{3,1}(\pi\pi^*)_{\text{CT,Phen(core)}}$ leads to enhanced SOC. Correspondingly, **34** bears a higher $k_{\text{isc}} = 1.5 \times 10^8 \text{ s}^{-1}$ compared with **96** ($k_{\text{isc}} = 9.3 \times 10^7 \text{ s}^{-1}$). The overall effect of retarded fluorescence and enhanced ISC contribute to the remarkably high $\Phi_{\text{T}} = 0.95$ as compared to **96** ($\Phi_{\text{T}} = 0.30$). On the other hand, the *N*-2-naphthyl counterpart **35** exhibits a naphthyl-to-phenoxazine centre-centre distance of 0.533 nm larger than that of **34** (0.437 nm). As a consequence, the **35** exhibit less coulombic stabilisation than **34** and thus **35** possesses a slightly higher energy $S_{\text{CT-Naph}}$ compared to **34**, resulting in a larger ΔE_{st} of **35** than that of **34**. Therefore, **35** exhibits a slightly lower $\Phi_{\text{T}} = 0.92$ as compared to **34** ($\Phi_{\text{T}} = 0.95$), arising from the variation in the *N*-naphthyl connectivity.⁴⁵

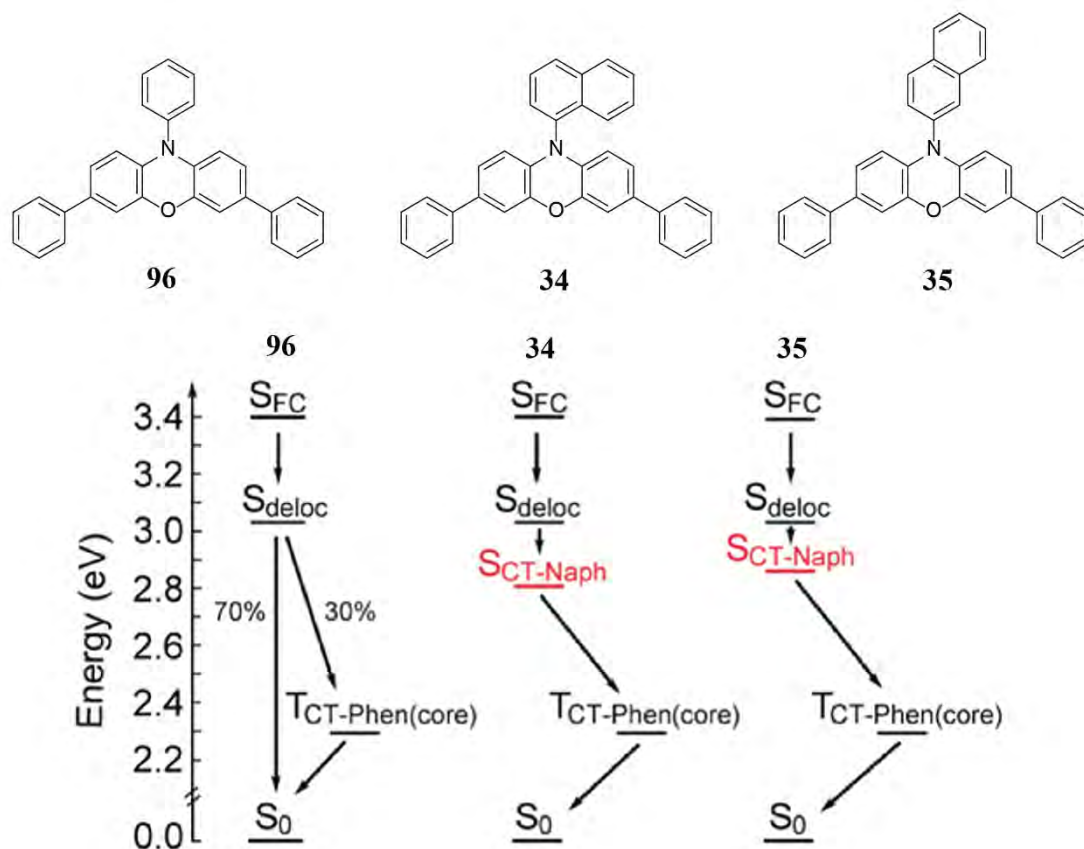


Figure 2.7 Top: chemical structures of **96**, **34** and **35**. Bottom: energy level diagram of **96**, **34** and **35** showing dominant decay pathways of excited states. Reprinted with permission from ref 45. Copyright © 2019, American Chemical Society.⁴⁵

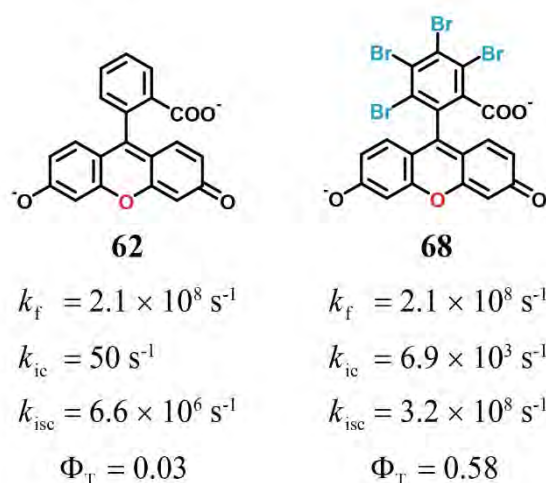
Table 2.3 Photophysical properties of **96**, **34** and **35**.

	k_f (s^{-1})	k_{ic} (s^{-1})	k_{isc} (s^{-1})	Φ_T	τ_T (ms)
96	2.1×10^8	6×10^6	9.3×10^7	0.30	1.5
34	3.0×10^6	5×10^6	1.5×10^8	0.95	1.5
35	3.7×10^6	6×10^6	1.1×10^8	0.92	1.4

Reproduced with permission from ref 45. Copyright © 2019, American Chemical Society.⁴⁵

2.5.4 Enhanced triplet quantum yield by heavy atom effect

Based on the heavy atom effect, Φ_T of fluorescein dyes can be simply tuned by the halogenation strategy, where the SOC between S_1 and T_n is enhanced by halogen substituents with larger atomic numbers Z (roughly like Z^2),¹³⁷ leading to higher k_{isc} and Φ_T . Recently, we reported a synthesised new PC **68** (Scheme 2.26), which possesses $\Phi_T = 0.58$ and features four Br substituents as compared to its non-substituted counterpart fluorescein **62** ($\Phi_T = 0.03$, Scheme 2.26).² As denoted in Scheme 2.26, **62** and **68** bear highly comparable k_f and both exhibit negligible k_{ic} ; however, heavier substituents of **68** results in remarkably higher k_{isc} by enhanced SOC compared to **62**.² Overall, this heavy atom effect leads to much higher $\Phi_T = 0.58$ of **68**.



Scheme 2.26 Chemical structures of **62** and **68**, with k_f , k_{ic} , k_{isc} and Φ_T denoted below. Reproduced with permission from ref 2. Copyright © 2018, American Chemical Society.²

Following this trend, heavier halogen substitution appears to result in higher Φ_T for these halogenated xanthene dyes **64**, **63**, **65** and **66** mentioned in above sections (Table 2.4).⁴⁰

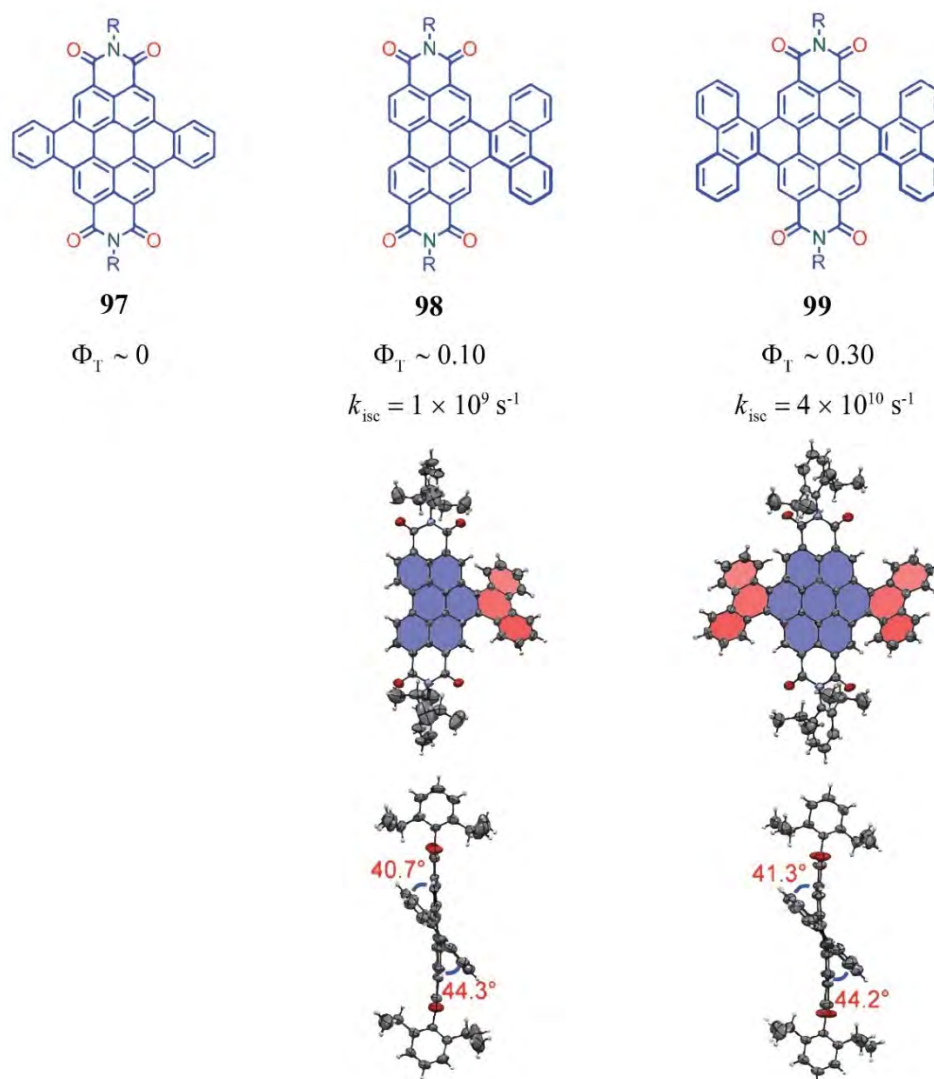
Table 2.4 Photophysical properties of halogenated xanthene dyes **64**, **63**, **65** and **66**.

	Halogen substituents	Φ_T	τ_T (ms)
64	4 xanthene-I	0.62–0.69	0.35–0.65
63	4 xanthene-Br	0.28–0.32	0.6–4.0
65	4 xanthene-I & 4 phenyl-Cl	0.76–0.86	0.26–1.91
66	4 xanthene-Br & 4 phenyl-Cl	0.4	0.12–1.75

Reproduced with permission from ref 0. Copyright © 2019, American Chemical Society.⁴⁰

2.5.5 Enhanced triplet quantum yield by chromophore core-twisting

By state-of-the-art theoretical and experimental studies, researchers clarified the important role of core-twisting/nonplanarity in promoting ISC via enhanced SOC.¹⁵⁰⁻¹⁵¹ Hariharan and coworkers initially investigated a class of core-twisted PSI derivatives with multiple Br substituted in the bay positions and discovered a significant enhancement in triplet generation.¹⁵² However, to explore the isolate effect of core-twisting on ISC, the impact from heavy atoms must be excluded. With this consideration, Hariharan and coworkers further imparted light-atom-based twisting into the core chromophore of PDI derivatives forming **98** and **99** with the planar **97** as comparison (**Scheme 2.27**). Indeed, the planar analogue **97** possesses negligible $\Phi_T \sim 0$ because of the weak SOC diminishing ISC. By imparting H-H repulsion induced core-twisting at one side of the cove regions of the PDI core, **98** is received and the one-side twisting effect yields an enhanced $\Phi_T \sim 0.10$ coupled with a $k_{isc} = 1 \times 10^9 \text{ s}^{-1}$. By imparting this core-twisting at both sides of the cove regions, the resultant more twisted structure exhibits an even higher $\Phi_T \sim 0.30$ with a higher $k_{isc} = 4 \times 10^{10} \text{ s}^{-1}$ (**Scheme 2.27**). Quantum chemical calculations revealed that the C-H and C=C bending vibration modes in the twisted regions contribute to efficient ISC between $^1(\pi\pi^*)$ and $^3(\pi\pi^*)$ driven by the Herzberg-Teller vibronic coupling.¹⁵³⁻¹⁵⁴



Scheme 2.27 Chemical structures and representation of molecular geometries of **97**, **98**, **99**, with Φ_T and k_{isc} denoted below the dye labels. Reproduced with permission from ref 153. Copyright © 2017, The Royal Society of Chemistry.¹⁵³

Very recently, Behrends and coworkers constructed a class of twisted acene derivatives **Ant-C n** ($n = 3-6$) tethered with alkyl tethers ($n =$ propyl-tether to hexyl-tether) to investigate the effect of core-twisting in Φ_T of chromophores (the strategy illustrated as **Figure 2.8**, top).¹⁵⁵ With shortened alkyl bridges, the degree of twisting (twist angle) is increased from 38° with a hexyl-tether (**Ant-C6**), 32° with a pentyl-tether (**Ant-C5**), 30° with a butyl-tether (**Ant-C4**) to 23° with a propyl bridge (**Ant-C3**). As comparison, a planar open reference compound without a tether (**open**) featuring 0° twist angle is also studied. Time-resolved Electron Paramagnetic Resonance (EPR) spectroscopy was performed to obtain the transient EPR spectra of all these compounds (**Figure 2.8**,

bottom). Obviously, the highly similar spectral shapes for **open**, **Ant-C6**, **Ant-C5** and **Ant-C4** allow direct comparison and clearly evidence progressively increased triplet signal intensity indicating higher Φ_T with shorter tethers. Despite a different spectral shape of **Ant-C3** (because of significantly changed spin polarisation caused by stretching-induced impact on the relative orientation of the phenyl side groups relative to the anthracene core), **Ant-C3** bears the biggest absolute signal area and hence the highest Φ_T as expected (**Figure 2.8**, bottom). Overall, a clear trend was observed by the authors towards increased Φ_T for more twisted compounds tethered with shorter alkyl tethers.¹⁵⁵

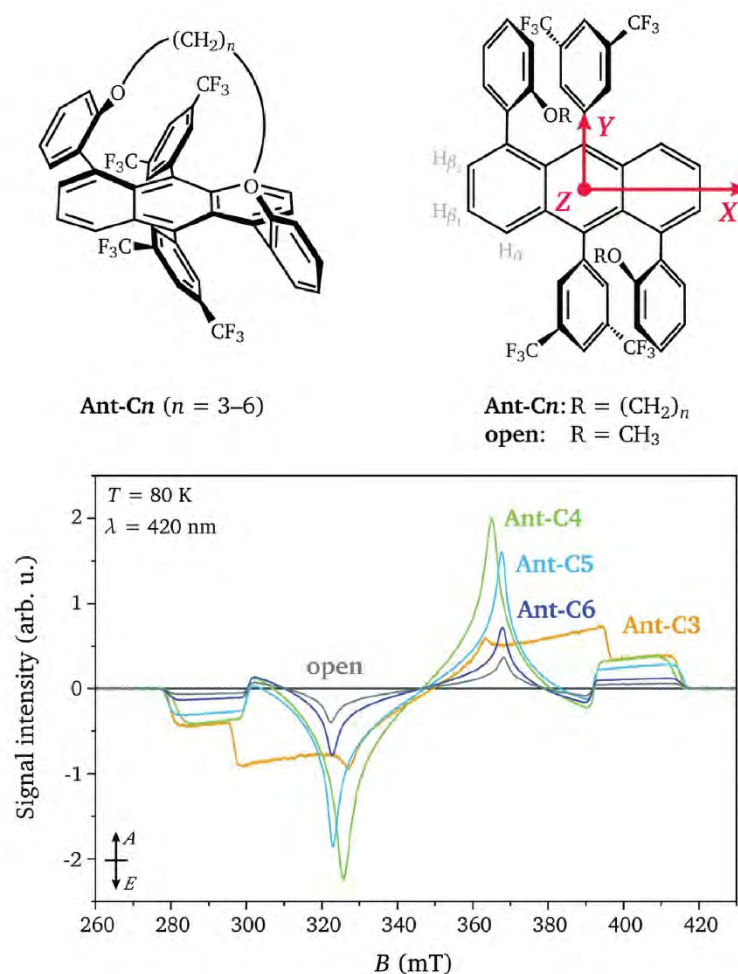


Figure 2.8 Top: chemical structures of twisted acene derivatives **Ant-Cn** ($n = 3-6$) tethered with alkyl bridges ($n =$ propyl bridge to hexyl bridge). Bottom: transient EPR spectra for **Ant-Cn** and the **open** (no alkyl bridges) reference compound. Reproduced with permission from ref 155. Copyright © 2019, The Royal Society of Chemistry.¹⁵⁵

Gidron and coworkers broadly reviewed the consequences of core-twisting nanocarbon molecules on their properties including Φ_T and summarised the proposed mechanisms.¹¹⁹

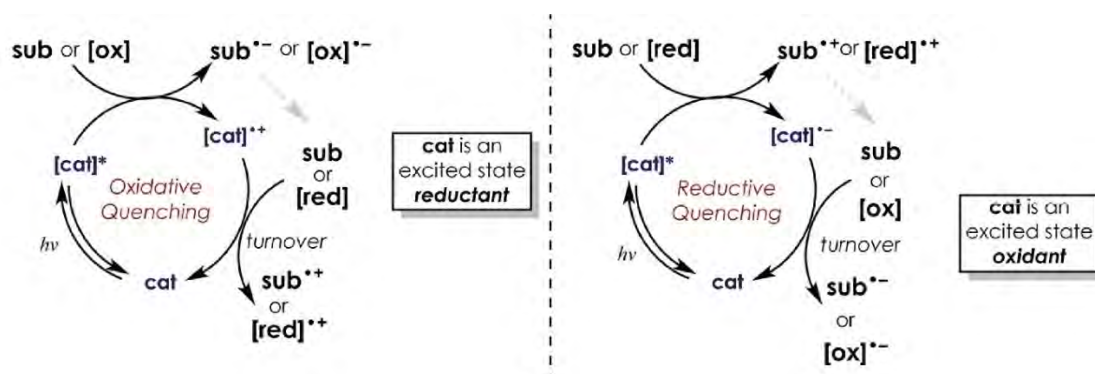
For example, Brédas and coworkers demonstrated a direct correlation between the magnitude of SOC and the degree of nonplanarity in nonplanar aromatic heterocyclic compounds.¹⁵⁶ Combining with the above mentioned findings, chromophore core-twisting can generally enhance SOC and accelerate ISC, thereby enhancing Φ_T of the chromophore.

Similarly, Holten and coworkers investigated a variety of core-twisted nonplanar metal-free porphyrin derivatives substituted with bulky alkyl groups that induced steric hinderance.¹²³ They observed an increase in k_{isc} primarily from enhanced SOC in these nonplanar porphyrin complexes. To interpret this observation, they mentioned that ISC in porphyrins is commonly deemed to rely on the wave function overlap which involves the central N atoms in the macrocycle and arises from out-of-plane distortion in S_1 and/or T_n .¹²³ Indeed, previous theoretical studies¹⁵⁷ and experimental studies¹⁵⁸ on chlorophylls argues that ISC can be modulated by the mentioned N-centred perturbations. Further, Shchupak, Ivashin and Sagun reported that common planar porphyrin derivatives exhibit small SOC matrix elements; however, the nonplanar porphyrin derivatives with more distortion of the macrocycle in T_1 exhibit considerable increase in SOC matrix elements, which is induced by an admixture of s character to π -orbitals in T_1 compared to S_1 and hence enhances SOC.¹⁵⁹

2.6 Redox properties: the catalytic role of PCs in quenching pathways

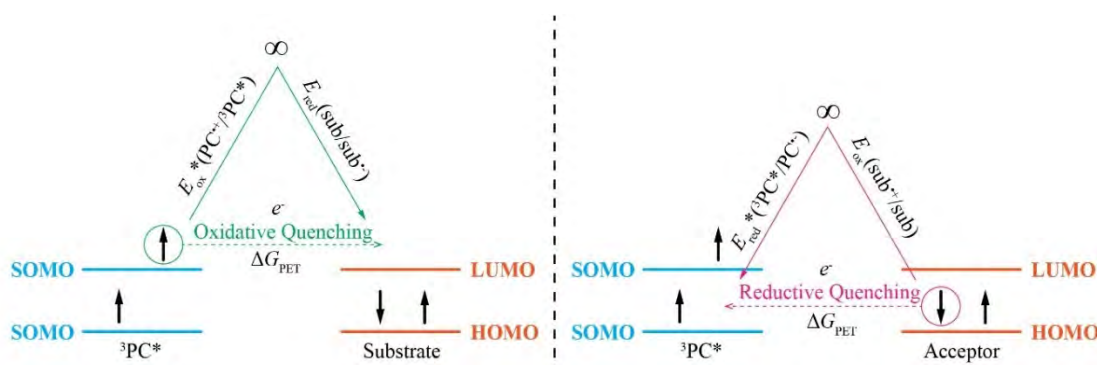
2.6.1 Theories and structure-property relationships

When a PC is excited and reaches a T_1 state $^3PC^*$, its direct SET with a substrate is commonly called photoinduced electron transfer (PET) reactions. Indeed, the first reaction occurs in a quenching pathway of a photo-controlled polymerisation system is the PET process. ΔG of the PET (ΔG_{PET}) represents the thermodynamic favourability of the PET reaction, and can be expressed as $\Delta G_{PET} = -F(E_{red}(sub/sub^{\bullet-}) - E_{ox}^*(PC^{*\bullet}/^3PC^*))$ for the oxidative quenching pathway (**Scheme 2.28**, left) or $\Delta G_{PET} = -F(E_{red}^*(^3PC^*/PC^{\bullet-}) - E_{ox}(sub^{*\bullet}/sub))$ for the reductive quenching pathway (**Scheme 2.28**, right), where F is the Faraday constant ($F = 23.061 \text{ kcal V}^{-1} \text{ mol}^{-1}$) and “sub” stands for the substrate.



Scheme 2.28 The oxidative quenching pathway (left) and the reductive quenching pathway (right) of a PC. “cat” represents PC and “sub” represents the substrate. Reproduced with permission from ref 5. Copyright © 2016, American Chemical Society.⁵

As shown in **Scheme 2.29**, left, in an oxidative quenching pathway, $E_{ox}^*(PC^{*+}/{}^3PC^*)$ represents the reducing ability of a ${}^3PC^*$ to donate an electron, which has to be sufficiently negative to reduce the substrate. Given the same chromophore core and similar excited state nature, more electron-donating substituents can enhance (towards more negative) $E_{ox}^*(PC^{*+}/{}^3PC^*)$ of a PC. Chromophore cores that are intrinsically highly negative in $E_{ox}^*(PC^{*+}/{}^3PC^*)$ includes phenothiazine,⁸⁴ dihydrophenazine,³⁶ phenoxazine,³⁷ dimethyl-dihydroacridine³⁵ and polycyclic aromatic hydrocarbons like perylene.⁸³



Scheme 2.29 Redox potentials for the PET process depicted in the oxidative quenching pathway (left) and the reductive quenching pathway (right) of a PC. “sub” stands for the substrate.

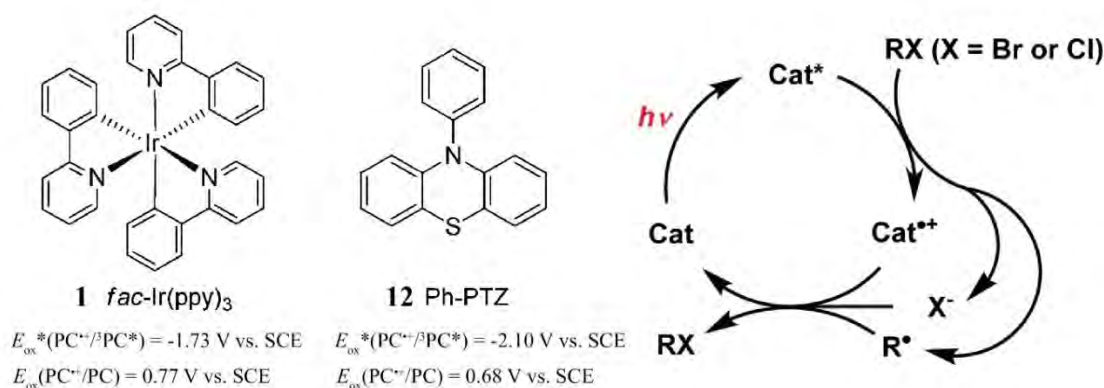
On the other hand, $E_{red}^*({}^3PC^*/PC^{*-})$ represents the reducing ability of a ${}^3PC^*$ to accept an electron, which has to be sufficiently negative to oxidise the substrate. In this case, by installing more electron-withdrawing substituents to the same chromophore core without notable change in the nature of excited states, $E_{red}^*({}^3PC^*/PC^{*-})$ of a PC can be enhanced

(towards more positive). Chromophore cores that are intrinsically highly positive in $E_{\text{red}}^*({}^3\text{PC}^*/\text{PC}^-)$ includes pyrylium^{65, 160-161} and acridinium.¹⁶²

Furthermore, the T_1 excitation energy ${}^3E_{0,0}^*$ reflects how much excitation energy can contribute to a PET process either in an oxidative or a reductive quenching pathway.⁵ These high ${}^3E_{0,0}^*$ chromophores are both strong excited state oxidant and reductant.³⁸ Because of high excitation energies, they mostly exhibit relatively short λ_{max} in the ultraviolet (UV) or blue range. Typical examples include *fac*-[Ir(ppy)₃] (**1**) and [Ru(bpy)₃]²⁺ (**8**) and their derivatives.

2.6.2 Photo-ATRP via the oxidative quenching pathway

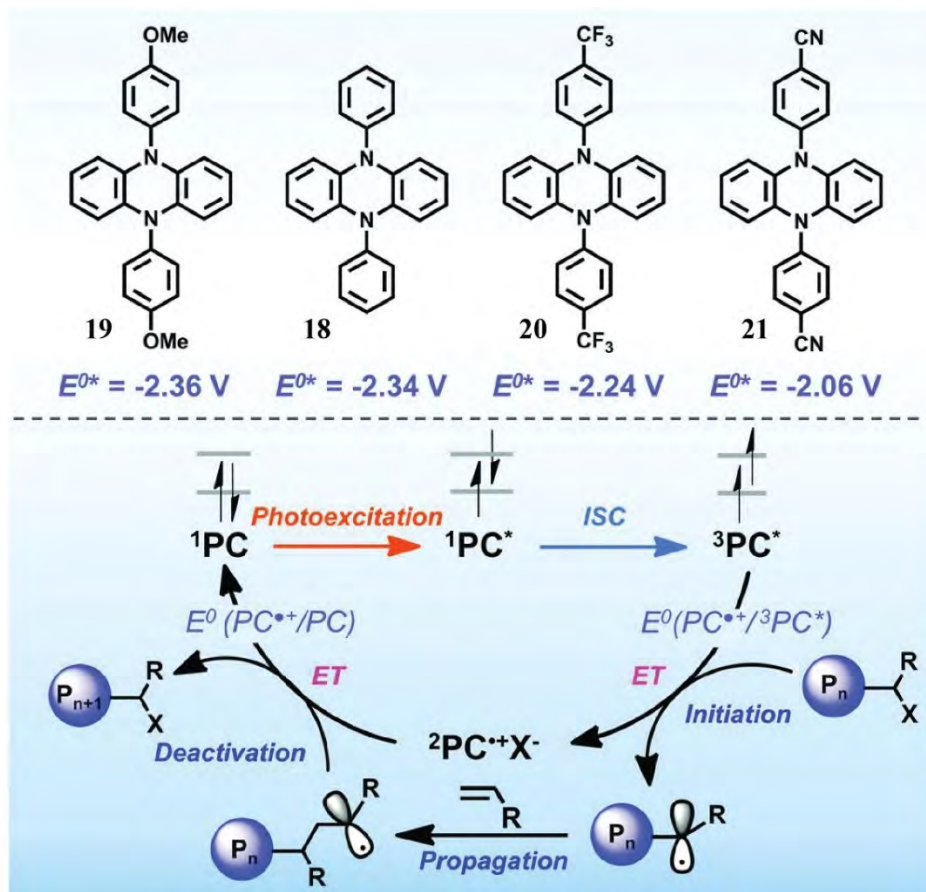
The first photo-ATRP system was catalysed by **1** (i.e., *fac*-[Ir(ppy)₃], **Scheme 2.30**, left), reported by Hawker and coworkers.^{58, 72} As shown in **Scheme 2.30**, right, up irradiation, **1** becomes a strong ${}^3\text{PC}^*$ reductant exhibiting $E_{\text{ox}}^*(\text{PC}^{*+}/{}^3\text{PC}^*) = -1.73$ V, vs. SCE, which is considered sufficiently strong to reduce the alkyl bromide initiator of ATRP and generate a PC^{*+} .⁸⁴ On the other hand, the PC^{*+} species of **1** is a strong oxidant exhibiting $E_{\text{ox}}(\text{PC}^{*+}/\text{PC}) = 0.77$ V, vs. SCE, believed to be sufficiently strong to oxidise the propagating radical and restore the catalytic cycle (**Scheme 2.30**, right).⁸⁴ A metal-free version of photo-ATRP was also proposed by Hawker *et al*⁸¹ and Matyjaszewski *et al*⁸⁴ with **12** (*N*-phenyl phenothiazine, Ph-PTZ, **Scheme 2.30**, left) as the PC. Similar to **1**, **12** also possesses strongly reducing ${}^3\text{PC}^*$ with $E_{\text{ox}}^*(\text{PC}^{*+}/{}^3\text{PC}^*) = -2.10$ V, vs. SCE and highly oxidising PC^{*+} with $E_{\text{ox}}(\text{PC}^{*+}/\text{PC}) = 0.68$ V, vs. SCE to fulfill the oxidative quenching cycle of photo-ATRP.⁸⁴



Scheme 2.30 Left: chemical structures of **1** *fac*-[Ir(ppy)₃] and **12** Ph-PTZ with $E_{\text{ox}}^*(\text{PC}^{*+}/{}^3\text{PC}^*)$ and $E_{\text{ox}}(\text{PC}^{*+}/\text{PC})$ denoted below the dye label. Right: Simplified scheme

for the activation/deactivation mechanism of photo-ATRP. Reproduced with permission from ref 84. Copyright © 2016, American Chemical Society.⁸⁴

Miyake and coworkers reported a new dye class dihydrophenazine derivatives **30-33** (**Scheme 2.31**, top) as PCs for metal-free photo-ATRP or namely O-ATRP.³⁶ As calculated by DFT and confirmed by experimental measurements, **19**, **18**, **20** and **21** all exhibit strong $E_{ox}^*(PC^{*+}/^3PC^*) < -2.0$ V, vs. SCE. Because the ATRP initiator ethyl α -bromophenylacetate (EBP) exhibit a $E_{ox}(sub/sub^{\bullet}) = -0.74$ V, vs. SCE, all these PCs with $E_{ox}^*(PC^{*+}/^3PC^*) < -2.0$ V, vs. SCE are capable of activating EBP via PET (**Scheme 2.31**, bottom). In particular, they demonstrated that by installing electron-donating methoxy groups to **18**, the resultant **30** possesses stronger $E_{ox}^*(PC^{*+}/^3PC^*) = -2.36$ V, vs. SCE compared to **31** (-2.34 V). On the other hand, installation of more electron-withdrawing substituents leads to weaker $E_{ox}^*(PC^{*+}/^3PC^*)$, i.e. -2.24 V for **32** and -2.06 V for **33** compared with -2.34 V for the reference **18** (**Scheme 2.31**, top). Moreover, the relatively stable PC^{*+} of these PCs formed from PET with $E_{ox}(PC^{*+}/PC) = \sim 0.1$ V to 0.2 V are sufficiently oxidising to deactivate the propagating radical. Indeed, the sub^{\bullet} of the EPA initiator has $E_{ox}(sub/sub^{\bullet})$ of -0.74 V, -0.86 V and -0.71 V after zero, one and two monomer (methyl methacrylate) additions, which are much more negative than $E_{ox}(PC^{*+}/PC)$ of these PCs **19**, **18**, **20** and **21**, allowing the O-ATRP oxidative quenching cycle to be fulfilled (**Scheme 2.31**, bottom).



Scheme 2.31 Top: chemical structures of dihydrophenazine derivatives **19**, **18**, **20** and **21**, with $E_{\text{ox}}^*(\text{PC}^{*+}/^3\text{PC}^*)$ denoted below the label. Bottom: the proposed mechanism for O-ATRP. Reproduced with permission from ref 36. Copyright © 2016, American Association for the Advancement of Science.³⁶

The authors further posited that more efficient PCs for O-ATRP should be diaryl dihydrophenazine derivatives displaying sufficiently strong $E_{\text{ox}}^*(\text{PC}^{*+}/^3\text{PC}^*)$ and also spatially separated T_1 singly occupied molecular orbitals (SOMOs), where the higher-lying SOMO is localised over one of the aryl substituents.³⁶ This concluded principle was later discovered to be due to Φ_T enhancement caused by T_1 CT characters^{43, 45} as mentioned in previous sections. Considering this principle, the authors further designed and synthesised **22** and **23** (**Figure 2.9**, left). Indeed, notwithstanding the notable CT characters in T_1 (**Figure 2.9**, right), still exhibit strong $E_{\text{ox}}^*(\text{PC}^{*+}/^3\text{PC}^*)$ of -2.20 V and -2.12 V respectively, which were comparable to the original **18** (**Figure 2.9**), without much sacrifice.

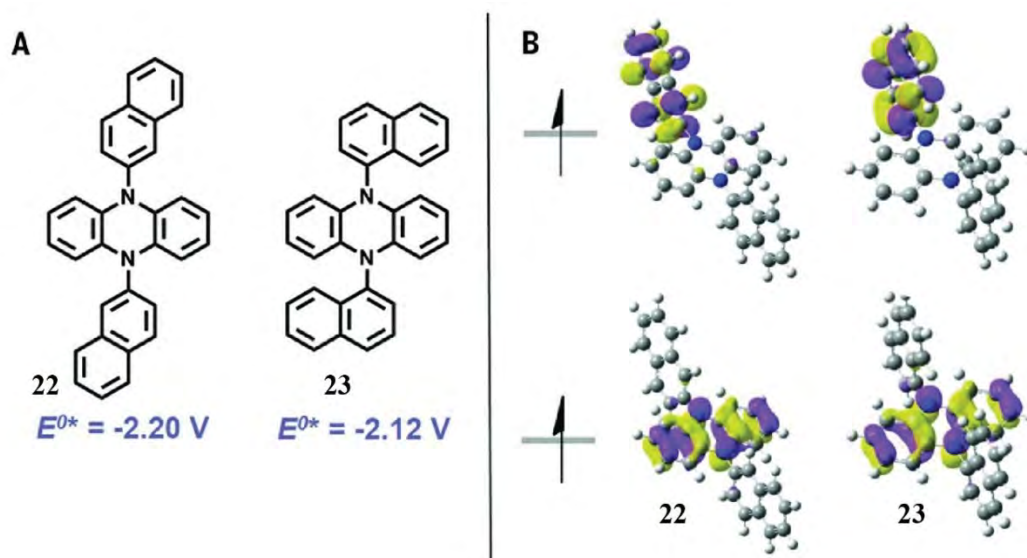


Figure 2.9 (A) Chemical structures of **22** and **23**, with $E_{\text{ox}}^*(\text{PC}^{+\cdot}/{}^{\beta}\text{PC}^{\cdot})$ denoted below the label. (B) T₁ FMOs of **22** and **23** visualising the higher-lying SOMO (top) and the lower lying SOMO (bottom). Reproduced with permission from ref 36. Copyright © 2016, American Association for the Advancement of Science.³⁶

As aforementioned, the type of the chromophore predetermines the benchmark redox properties of its substituted derivatives. Thus, Miyake and coworkers compared the reduction potentials of N-phenyl phenoxazine (**27**, **Figure 2.10**, top), N,N-diphenyl phenazine (**18**, **Figure 2.10**, middle) and N-phenyl phenothiazine (**12**, **Figure 2.10**, bottom).³⁷ The three basic chromophore cores all exhibit highly reducing T₁ states with $E_{\text{ox}}^*(\text{PC}^{+\cdot}/{}^{\beta}\text{PC}^{\cdot}) < -2.0$ V, vs. SCE. Specifically, among the three, N,N-diphenyl phenazine (**18**) has the most negative $E_{\text{ox}}^*(\text{PC}^{+\cdot}/{}^{\beta}\text{PC}^{\cdot})$ of -2.25 V, followed by N-phenyl phenoxazine (**27**) and N-phenyl phenothiazine (**12**). On the other hand, $E_{\text{ox}}(\text{PC}^{+\cdot}/\text{PC})$ of all the three chromophore cores are all much higher than $E_{\text{ox}}(\text{sub}/\text{sub}^{\cdot})$ of the EPA initiator (-0.74 V), sufficient for deactivation of O-ATRP.³⁷

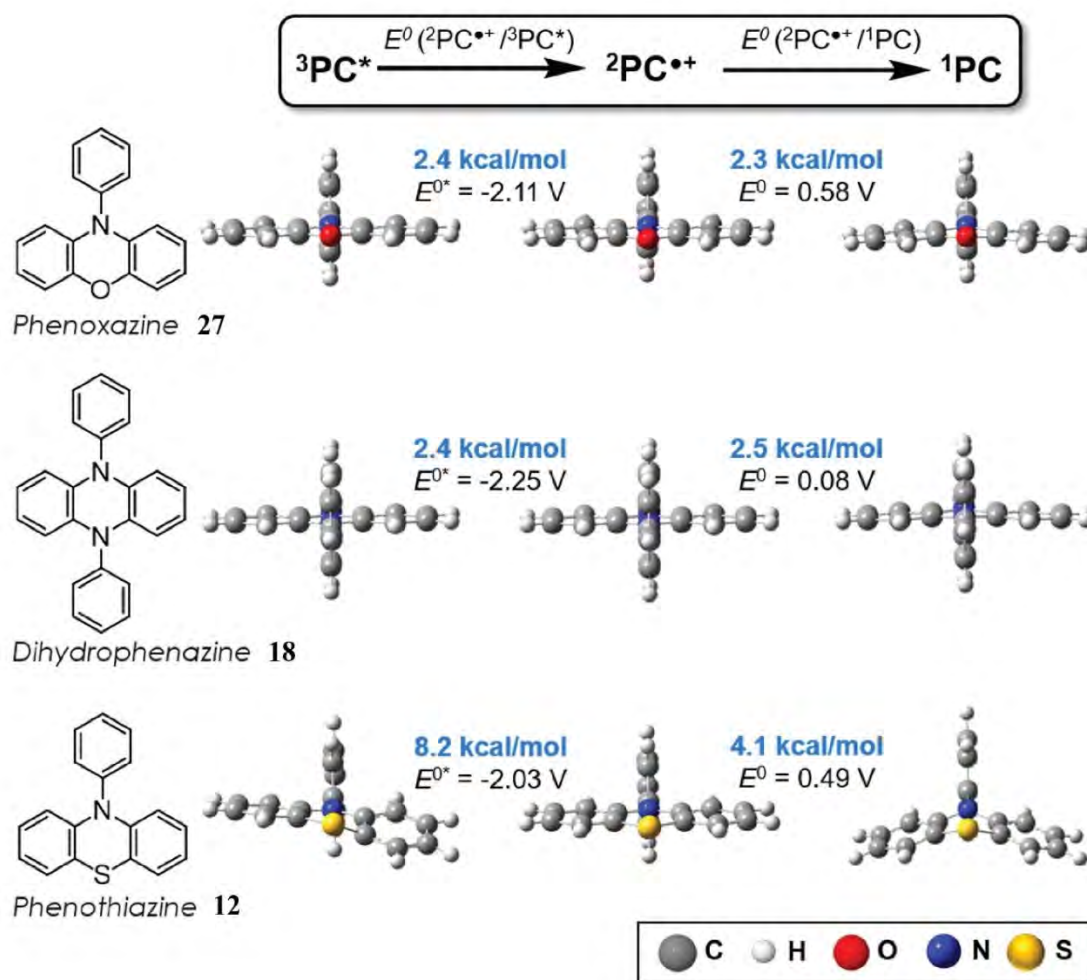


Figure 2.10 (A) Chemical structures, geometric reorganisation energies and reduction potentials (vs. SCE) for the three original chromophore core structures (phenoxazine **27**, dihydrophenazine **18** and phenothiazine **12**). Reproduced with permission from ref 37. Copyright © 2016, American Chemical Society.³⁷

Based on the benchmark $E_{\text{ox}}^*(\text{PC}^{++}/3\text{PC}^*) = 2.11$ V, vs. SCE of **27**, the authors further sought to tune $E_{\text{ox}}^*(\text{PC}^{++}/3\text{PC}^*)$ by modification of the chromophore core with substituents. As shown in **Figure 2.11A**, installation of the electro-withdrawing trifluoromethyl substituent on the para position of the N-phenyl group leads to slightly less negative $E_{\text{ox}}^*(\text{PC}^{++}/3\text{PC}^*) = 2.03$ V, vs. SCE of **28**. By replacing the N-phenyl group with a *N*-1-naphthyl group, the resultant expanded conjugative effect leads to weaker $E_{\text{ox}}^*(\text{PC}^{++}/3\text{PC}^*) = -1.84$ V, vs. SCE of **29**, which makes **29** sufficiently reducing for O-ATRP. Meanwhile, the CT character was incorporated into the T_1 state of **29** by this modification (**Figure 2.11B**), which is believed to improve the O-ATRP performance by

enhancing Φ_T . **30** substituted with a *N*-2-naphthyl group is highly similar to **29**, exhibiting $E_{ox}^*(PC^{+/\beta}PC^*) = -1.90$ V, vs. SCE and a T_1 with the CT character.³⁷

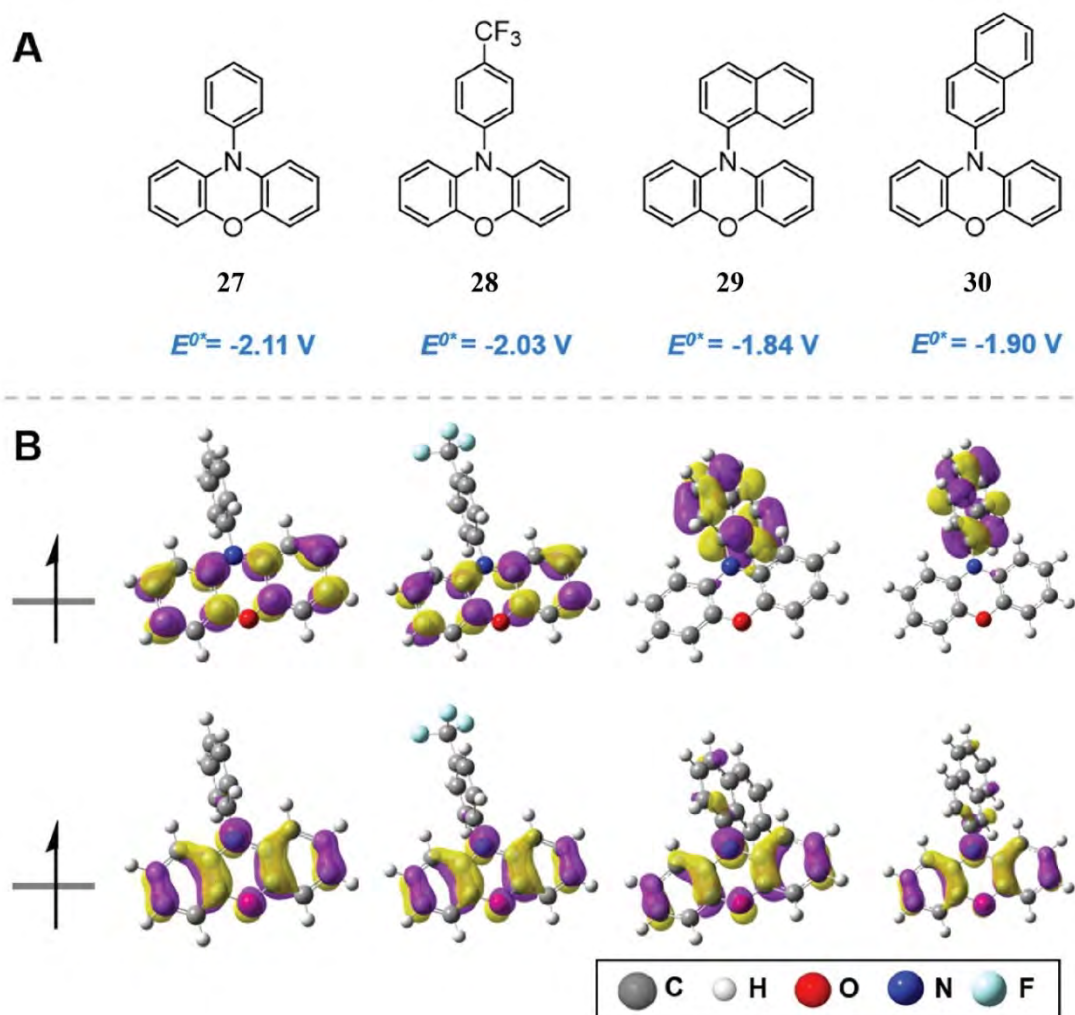
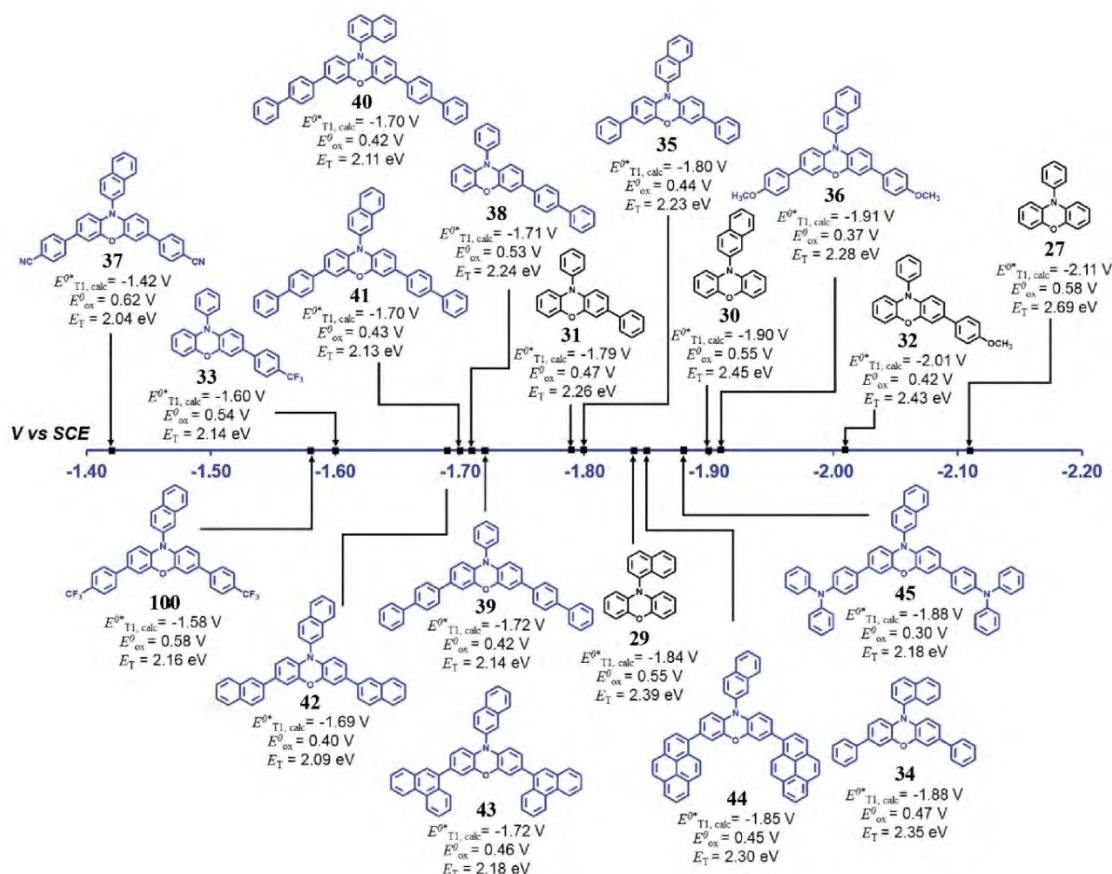


Figure 2.11 (A) Chemical structures of **27-30**, with $E_{ox}^*(PC^{+/\beta}PC^*)$ denoted below the label. (B) T_1 FMOs of **27-30** visualising the higher-lying SOMO (top) and the lower lying SOMO (bottom). Reproduced with permission from ref 37. Copyright © 2016, American Chemical Society.³⁷

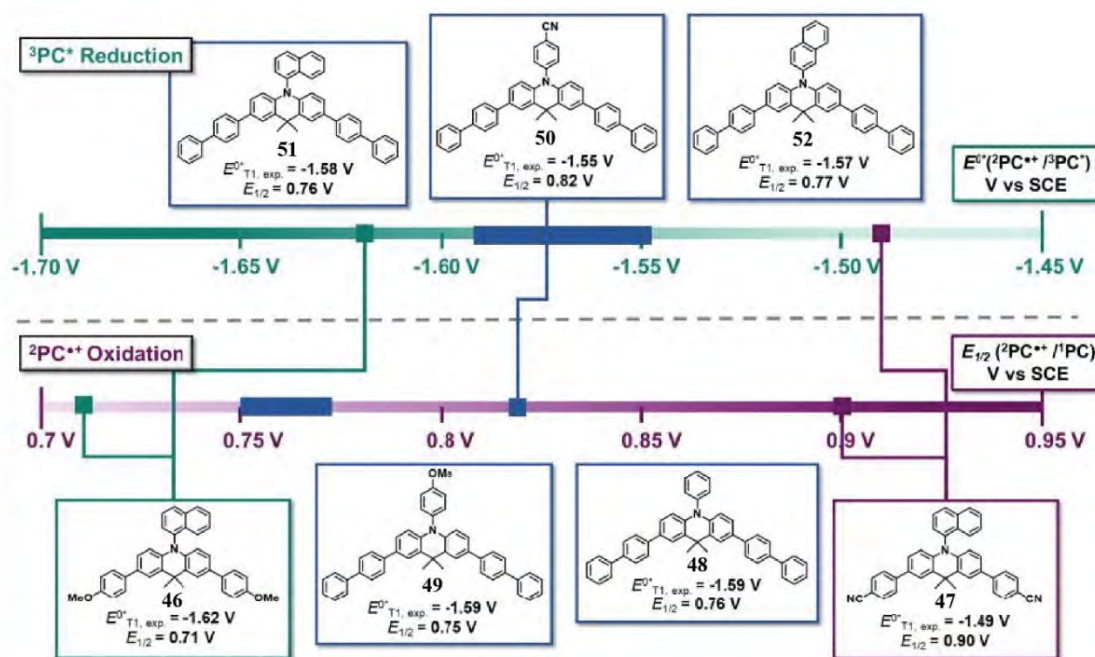
Miyake and coworkers further investigated the possible range of $E_{ox}^*(PC^{+/\beta}PC^*)$ that the phenoxazine PC scaffold can achieved, with substituted derivatives possessing electron-withdrawing, electron-donating or conjugation-extended substituents groups (**27**, **29-45** and **100**, **Scheme 2.32**). As shown in **Scheme 2.32**, the calculated $E_{ox}^*(PC^{+/\beta}PC^*)$ of these phenoxazine dyes were arranged in an $E_{ox}^*(PC^{+/\beta}PC^*)$ axis with a range of -1.40 V, vs. SCE to -2.20 V, vs. SCE. Modification of **27** and **30** with the electro-withdrawing trifluoromethyl group (affording **33** and **100**) or the cyano group (affording **37**) or the

highly conjugated substituents (affording **43** and **44**) reduced $E_{\text{ox}}^*(\text{PC}^{+\cdot}/^3\text{PC}^*)$ of the PCs (Scheme 2.32). On the contrary, installing the electro-donating methoxy group (affording **32** and **36**) or the diphenyl amino group (affording **45**) leads to stronger $E_{\text{ox}}^*(\text{PC}^{+\cdot}/^3\text{PC}^*)$ of the PCs (Scheme 2.32).



Scheme 2.32 (A) Chemical structures of **27**, **29-45** and **100**, arranged by $E_{\text{ox}}^*(\text{PC}^{+\cdot}/^3\text{PC}^*)$, with $E_{\text{ox}}^*(\text{PC}^{+\cdot}/^3\text{PC}^*)$, $E_{\text{ox}}(\text{PC}^{+\cdot}/\text{PC})$ and E_{T} denoted below the label. E_{T}^0 : the calculated $E_{\text{ox}}^*(\text{PC}^{+\cdot}/^3\text{PC}^*)$. E_{ox}^0 : $E_{\text{ox}}(\text{PC}^{+\cdot}/\text{PC})$. E_{T} : the T_1 excitation energy. Reproduced with permission from ref 41. Copyright © 2018, American Chemical Society.⁴¹

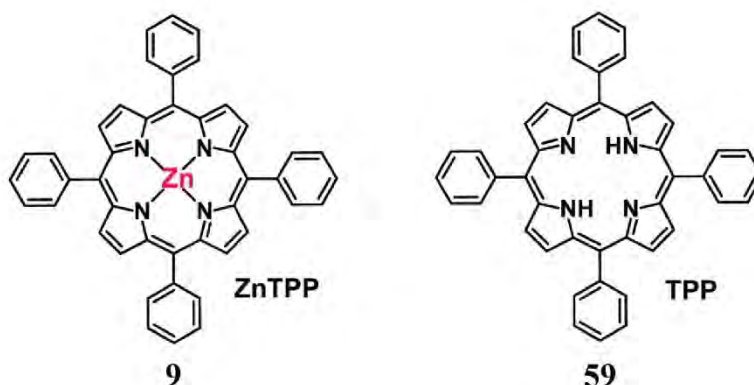
Miyake and coworkers further investigated a new dye class dimethyl-dihydroacridine derivatives **46-52** (Scheme 2.33).³⁵ Apparently, installation of electron-withdrawing, electron-donating and neutral N-aryl groups to this type of chromophore core does not show notable influence on $E_{\text{ox}}^*(\text{PC}^{+\cdot}/^3\text{PC}^*)$, which ranges from -1.59 V to -1.55 V, vs. SCE. Overall, $E_{\text{ox}}^*(\text{PC}^{+\cdot}/^3\text{PC}^*)$ of this dye class is weaker than other dye classes, but sufficient for O-ATRP via an oxidative quenching pathway.



Scheme 2.33 (A) Chemical structures of **46-52**, arranged by $E_{ox}^*(PC^{*+}/^3PC^*)$, with $E_{ox}^*(PC^{*+}/^3PC^*)$, $E_{ox}(PC^{*+}/PC)$ below the label. $E_{T1,exp}^0$: the experimental $E_{ox}^*(PC^{*+}/^3PC^*)$. $E_{1/2}$: $E_{ox}(PC^{*+}/PC)$. Reproduced with permission from ref 35. Copyright © 2019, John Wiley and Sons.³⁵

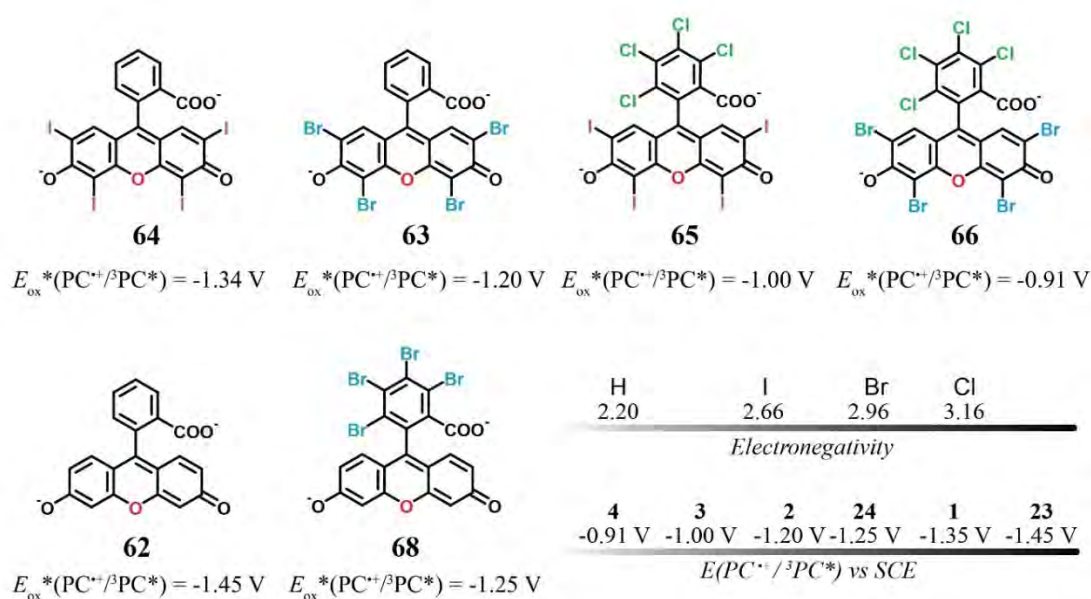
2.6.3 PET-RAFT via the oxidative quenching pathway

Similar to photo-ATRP, the first PET-RAFT system was reported by Boyer *et al* with *fac*-[Ir(ppy)₃] **1** as PC.⁵⁹ As shown in **Scheme 2.34**, top, Upon photoexcitation and electronic transitions, **1** reaches its T₁ state, which can further reduce the RAFT agent (the substrate) within its lifetime and afford PC⁺ of **1** coupled by sub⁻ of the RAFT agent. Consequently, for a PC capable of catalysing PET-RAFT polymerisation, its $E_{ox}^*(PC^{*+}/^3PC^*)$ has to be stronger (i.e. more negative) than $E_{red}(sub/sub^{\bullet-})$ of the RAFT agents. Common RAFT agents for PET-RAFT systems include CPADB ($E_{red}(sub/sub^{\bullet-}) = -0.4$ V, vs. SCE, for methacrylates and methacrylamides), BTPA ($E_{red}(sub/sub^{\bullet-}) = -0.6$ V, vs. SCE, for acrylates, acrylamides and styrene), BSTP ($E_{red}(sub/sub^{\bullet-}) = -0.9$ V, vs. SCE, for acrylates, acrylamides and styrene) and xanthate (for unconjugated monomers). For example, **1** exhibits an $E_{ox}^*(PC^{*+}/^3PC^*) = -1.72$ V, vs. SCE, sufficiently more negative than $E_{red}(sub/sub^{\bullet-})$ of CPADB, BTPA and BSTP; hence, **1** is capable of efficiently activating PET-RAFT polymerisation of common monomers.⁵⁹ On the other hand, because $E_{ox}(PC^{*+}/PC)$ of **1** is 0.77 V, vs. SCE, which is much higher than $E_{red}(sub/sub^{\bullet-})$ of these RAFT agents, deactivation of PET-RAFT polymerisation can be



Scheme 2.35 Chemical structures of ZnTPP **9** and TPP **58**. Reproduced with permission from ref 78. Copyright © 2015, American Chemical Society.⁷⁸

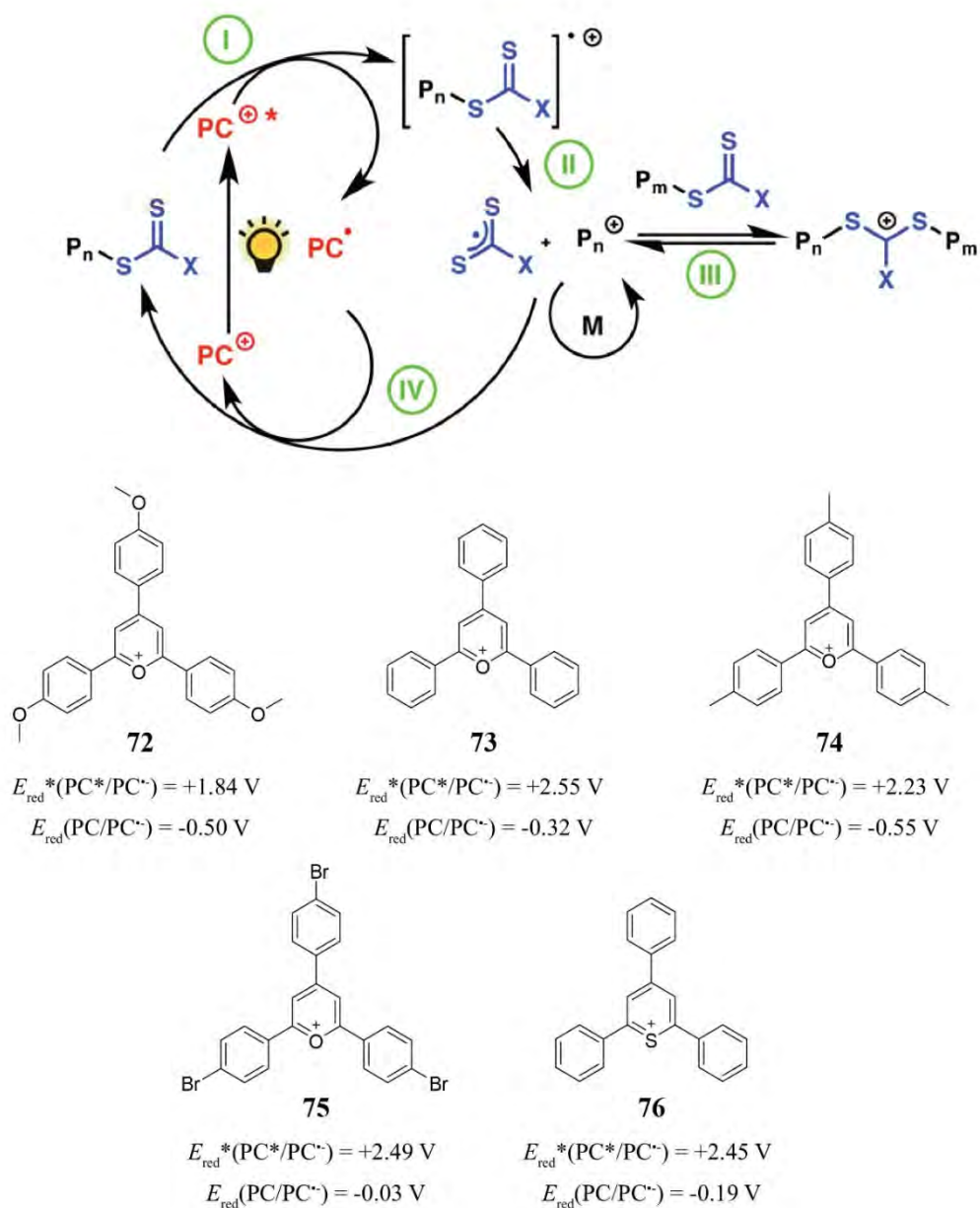
We then investigated the effect of varied halogen substituents (H, Cl, Br and I) on $E_{\text{ox}}^*(\text{PC}^{+\beta}/\text{PC}^*)$ of halogenated xanthene dyes **64**, **63**, **65**, **66**, **62** and **68** as PET-RAFT PCs.^{2, 40} As shown in **Scheme 2.36**, H, I, Br and Cl exhibit increasing electronegativity in order, which makes them increasingly electro-withdrawing substituents in halogenated xanthene dyes. With more halogen substituents of higher electronegativity, the overall more notable electro-withdrawing effect leads to less negative $E_{\text{ox}}^*(\text{PC}^{+\beta}/\text{PC}^*)$ of the PCs. Consequently, **62** without any halogen substitution exhibits the strongest $E_{\text{ox}}^*(\text{PC}^{+\beta}/\text{PC}^*)$ of -1.45 V, while **66** possessing eight strongly electro-withdrawing halogens exhibits the weakest $E_{\text{ox}}^*(\text{PC}^{+\beta}/\text{PC}^*)$ of -0.91 V.



Scheme 2.36 Chemical structures of **64**, **63**, **65**, **66**, **62** and **68** with their $E_{\text{ox}}^*(\text{PC}^{+\cdot}/^3\text{PC}^*)$ denoted below the label. Bottom right: electronegativity of the substituent halogens and $E_{\text{ox}}^*(\text{PC}^{+\cdot}/^3\text{PC}^*)$ of the PCs in comparison. Reproduced with permission from ref 2 and ref 40. Copyright © 2019, American Chemical Society.^{2, 40}

2.6.4 Photo-LCP via the reductive quenching pathway

Photo-LCP of vinyl ethers via the reductive quenching pathway was reported by Fors and coworkers using a library of pyrylium derivatives **72-76** as PCs (**Scheme 2.37**, bottom).⁶⁵ As shown in **Scheme 2.37**, top, upon irradiation, the PC reaches the excited state and is capable of accepting an electron from the substrate RAFT agent. Hence, $E_{\text{red}}^*(\text{PC}^*/\text{PC}^{\cdot-})$ can describe the oxidising ability of the PC. As expected, installation of the highly electron-donating methoxy groups afforded **72** with much lowered $E_{\text{red}}^*(\text{PC}^*/\text{PC}^{\cdot-}) = +1.84$ V, vs. SCE than **73** ($E_{\text{red}}^*(\text{PC}^*/\text{PC}^{\cdot-}) = +2.55$ V, vs. SCE), whereas the slightly electron-donating methyl groups in **74** slightly attenuated its $E_{\text{red}}^*(\text{PC}^*/\text{PC}^{\cdot-}) = +2.23$ V.



Scheme 2.37 Top: the proposed mechanism of photo-LCP regulated by a RAFT agent. Bottom: chemical structures of **72-76** with $E_{\text{red}}^*(\text{PC}^*/\text{PC}^\bullet)$ and $E_{\text{red}}(\text{PC}/\text{PC}^\bullet)$ vs. SCE denoted below the label. Reproduced with permission from ref 65. Copyright © 2017, American Chemical Society.⁶⁵

2.7 References

- (1) Hoffmann, N., *Angewandte Chemie International Edition* **2013**, *52*, 11456.
- (2) Wu, C.; Chen, H.; Corrigan, N.; Jung, K.; Kan, X.; Li, Z.; Liu, W.; Xu, J.; Boyer, C., *Journal of the American Chemical Society* **2019**, *141*, 8207.
- (3) Hashimoto, T.; Choe, Y. K.; Nakano, H.; Hirao, K., *Journal of Physical Chemistry A* **1999**, *103*, 1894.

- (4) Speckmeier, E.; Fischer, T. G.; Zeitler, K., *Journal of the American Chemical Society* **2018**, *140*, 15353.
- (5) Romero, N. A.; Nicewicz, D. A., *Chemical Reviews* **2016**, *116*, 10075.
- (6) Prier, C. K.; Rankic, D. A.; MacMillan, D. W., *Chemical Reviews* **2013**, *113*, 5322.
- (7) Shaw, M. H.; Twilton, J.; MacMillan, D. W., *Journal of Organic Chemistry* **2016**, *81*, 6898.
- (8) MacMillan, D. W., *Nature* **2008**, *455*, 304.
- (9) Corrigan, N.; Shanmugam, S.; Xu, J.; Boyer, C., *Chemical Society Reviews* **2016**, *45*, 6165.
- (10) Chen, M.; Zhong, M.; Johnson, J. A., *Chemical Reviews* **2016**, *116*, 10167.
- (11) Dadashi-Silab, S.; Doran, S.; Yagci, Y., *Chemical Reviews* **2016**, *116*, 10212.
- (12) Judzewitsch, P. R.; Zhao, L.; Wong, E. H. H.; Boyer, C., *Macromolecules* **2019**, *52*, 3975.
- (13) Judzewitsch, P. R.; Nguyen, T. K.; Shanmugam, S.; Wong, E. H. H.; Boyer, C., *Angewandte Chemie International Edition English* **2018**, *57*, 4559.
- (14) Niu, J.; Lunn, D. J.; Pusuluri, A.; Yoo, J. I.; O'Malley, M. A.; Mitragotri, S.; Soh, H. T.; Hawker, C. J., *Nature Chemistry* **2017**, *9*, 537.
- (15) Tucker, B. S.; Coughlin, M. L.; Figg, C. A.; Sumerlin, B. S., *ACS Macro Letters* **2017**, *6*, 452.
- (16) Yeow, J.; Shanmugam, S.; Corrigan, N.; Kuchel, R. P.; Xu, J. T.; Boyer, C., *Macromolecules* **2016**, *49*, 7277.
- (17) Szymański, J. K.; Pérez-Mercader, J., *Polymer Chemistry* **2016**, *7*, 7211.
- (18) Albertsen, A. N.; Szymanski, J. K.; Perez-Mercader, J., *Scientific Reports* **2017**, *7*, 41534.
- (19) Xu, S.; Zhang, T.; Kuchel, R. P.; Yeow, J.; Boyer, C., *Macromolecular Rapid Communications* **2020**, *41*, e1900493.
- (20) Xu, S. H.; Yeow, J.; Boyer, C., *ACS Macro Letters* **2018**, *7*, 1376.
- (21) Poelma, J. E.; Fors, B. P.; Meyers, G. F.; Kramer, J. W.; Hawker, C. J., *Angewandte Chemie International Edition English* **2013**, *52*, 6844.
- (22) Fors, B. P.; Poelma, J. E.; Menyo, M. S.; Robb, M. J.; Spokoyny, D. M.; Kramer, J. W.; Waite, J. H.; Hawker, C. J., *Journal of the American Chemical Society* **2013**, *135*, 14106.
- (23) Pester, C. W.; Narupai, B.; Mattson, K. M.; Bothman, D. P.; Klinger, D.; Lee, K. W.; Discekici, E. H.; Hawker, C. J., *Advanced Materials* **2016**, *28*, 9292.
- (24) Discekici, E. H.; Pester, C. W.; Treat, N. J.; Lawrence, I.; Mattson, K. M.; Narupai, B.; Toumayan, E. P.; Luo, Y. D.; McGrath, A. J.; Clark, P. G.; de Alaniz, J. R.; Hawker, C. J., *ACS Macro Letters* **2016**, *5*, 258.
- (25) Chen, M.; Gu, Y.; Singh, A.; Zhong, M.; Jordan, A. M.; Biswas, S.; Korley, L. T.; Balazs, A. C.; Johnson, J. A., *ACS Cent Sci* **2017**, *3*, 124.
- (26) Zhang, Z.; Corrigan, N.; Bagheri, A.; Jin, J.; Boyer, C., *Angewandte Chemie International Edition English* **2019**, *58*, 17954.
- (27) Jung, K.; Corrigan, N.; Ciftci, M.; Xu, J.; Seo, S. E.; Hawker, C. J.; Boyer, C., *Advanced Materials* **2019**, *n/a*, e1903850.
- (28) Corrigan, N.; Ciftci, M.; Jung, K.; Boyer, C., *Angewandte Chemie International Edition English* **2019**, *n/a*.
- (29) Corrigan, N.; Boyer, C., *ACS Macro Letters* **2019**, *8*, 812.
- (30) Fu, C.; Xu, J.; Boyer, C., *Chemical Communications (Camb)* **2016**, *52*, 7126.
- (31) Kottisch, V.; Michaudel, Q.; Fors, B. P., *Journal of the American Chemical Society* **2017**, *139*, 10665.
- (32) Xiong, X. H.; Xue, L. L.; Cui, J. X., *ACS Macro Letters* **2018**, *7*, 239.

- (33) Hildebrandt, K.; Pauloehrl, T.; Blinco, J. P.; Linkert, K.; Borner, H. G.; Barner-Kowollik, C., *Angewandte Chemie International Edition English* **2015**, *54*, 2838.
- (34) Hildebrandt, K.; Kaupp, M.; Molle, E.; Menzel, J. P.; Blinco, J. P.; Barner-Kowollik, C., *Chemical Communications (Camb)* **2016**, *52*, 9426.
- (35) Buss, B. L.; Lim, C. H.; Miyake, G. M., *Angewandte Chemie International Edition English* **2019**, *n/a*.
- (36) Theriot, J. C.; Lim, C. H.; Yang, H.; Ryan, M. D.; Musgrave, C. B.; Miyake, G. M., *Science* **2016**, *352*, 1082.
- (37) Pearson, R. M.; Lim, C. H.; McCarthy, B. G.; Musgrave, C. B.; Miyake, G. M., *Journal of the American Chemical Society* **2016**, *138*, 11399.
- (38) Singh, V. K.; Yu, C.; Badgular, S.; Kim, Y.; Kwon, Y.; Kim, D.; Lee, J.; Akhter, T.; Thangavel, G.; Park, L. S.; Lee, J.; Nandajan, P. C.; Wannemacher, R.; Milian-Medina, B.; Luer, L.; Kim, K. S.; Gierschner, J.; Kwon, M. S., *Nature Catalysis* **2018**, *1*, 794.
- (39) Lu, J.; Pattengale, B.; Liu, Q.; Yang, S.; Shi, W.; Li, S.; Huang, J.; Zhang, J., *Journal of the American Chemical Society* **2018**, *140*, 13719.
- (40) Wu, C.; Corrigan, N.; Lim, C. H.; Jung, K.; Zhu, J.; Miyake, G.; Xu, J.; Boyer, C., *Macromolecules* **2019**, *52*, 236.
- (41) McCarthy, B. G.; Pearson, R. M.; Lim, C. H.; Sartor, S. M.; Damrauer, N. H.; Miyake, G. M., *Journal of the American Chemical Society* **2018**, *140*, 5088.
- (42) Liu, W.; Xiao, Y., *Chemical Society Reviews* **2018**, *47*, 4481.
- (43) Sartor, S. M.; McCarthy, B. G.; Pearson, R. M.; Miyake, G. M.; Damrauer, N. H., *Journal of the American Chemical Society* **2018**, *140*, 4778.
- (44) Lim, C. H.; Ryan, M. D.; McCarthy, B. G.; Theriot, J. C.; Sartor, S. M.; Damrauer, N. H.; Musgrave, C. B.; Miyake, G. M., *Journal of the American Chemical Society* **2017**, *139*, 348.
- (45) Sartor, S. M.; Lattke, Y. M.; McCarthy, B. G.; Miyake, G. M.; Damrauer, N. H., *Journal of Physical Chemistry A* **2019**, *123*, 4727.
- (46) Song, Y.; Kim, Y.; Noh, Y.; Singh, V. K.; Behera, S. K.; Abudulimu, A.; Chung, K.; Wannemacher, R.; Gierschner, J.; Luer, L.; Kwon, M. S., *Macromolecules* **2019**, *52*, 5538.
- (47) Soo, R. M.; Hemp, J.; Parks, D. H.; Fischer, W. W.; Hugenholtz, P., *Science* **2017**, *355*, 1436.
- (48) Schidowski, M., *Journal of Southeast Asian Earth Sciences, Special Volume, Vol 5, Nos 104* **1991**, *5*, 333.
- (49) Shanmugam, S.; Xu, J.; Boyer, C., *Chem Sci* **2015**, *6*, 1341.
- (50) Gajewska, B.; Raccio, S.; Rodriguez, K. J.; Bruns, N., *Polymer Chemistry* **2019**, *10*, 125.
- (51) Guo, J. T.; Yang, D. C.; Guan, Z.; He, Y. H., *Journal of Organic Chemistry* **2017**, *82*, 1888.
- (52) Rubio, M.; Roos, B. O.; Serrano-Andres, L.; Merchan, M., *Journal of Chemical Physics* **1999**, *110*, 7202.
- (53) Wu, C.; Shanmugam, S.; Xu, J.; Zhu, J.; Boyer, C., *Chemical Communications (Camb)* **2017**, *53*, 12560.
- (54) Hortensteiner, S., *Annu Rev Plant Biol* **2006**, *57*, 55.
- (55) Llewellyn, C. A.; Mantoura, R. F. C.; Brereton, R. G., *Photochemistry and Photobiology* **1990**, *52*, 1043.
- (56) Kottisch, V.; Michaudel, Q.; Fors, B. P., *Journal of the American Chemical Society* **2016**, *138*, 15535.
- (57) Ogawa, K. A.; Goetz, A. E.; Boydston, A. J., *Journal of the American Chemical Society* **2015**, *137*, 1400.

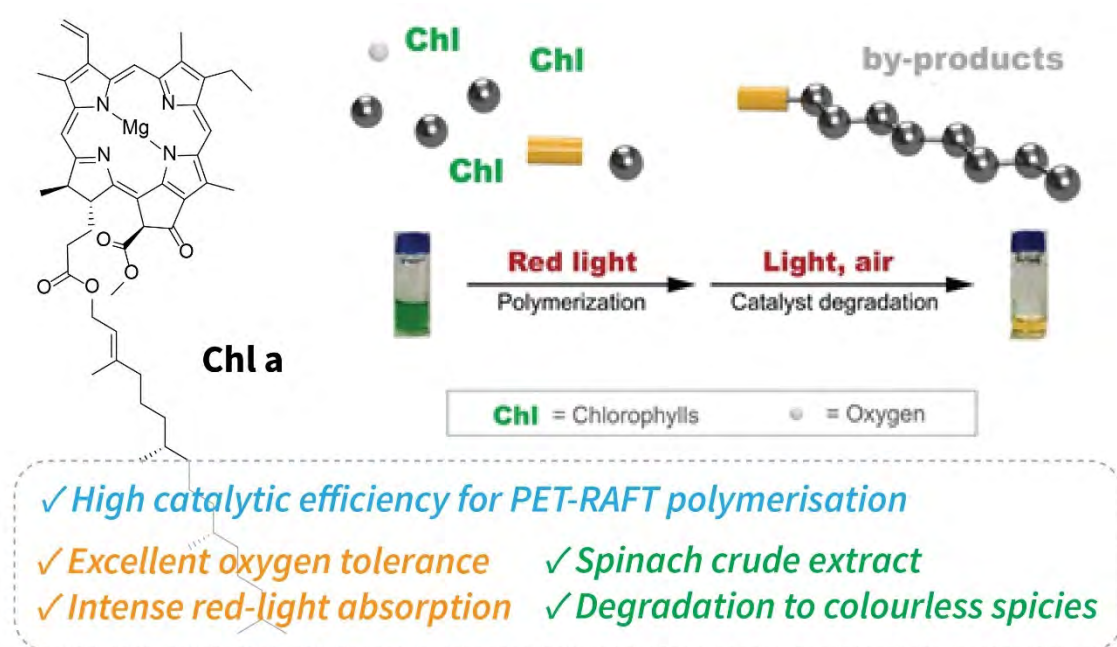
- (58) Fors, B. P.; Hawker, C. J., *Angewandte Chemie International Edition English* **2012**, *51*, 8850.
- (59) Xu, J.; Jung, K.; Atme, A.; Shanmugam, S.; Boyer, C., *Journal of the American Chemical Society* **2014**, *136*, 5508.
- (60) Guillaneuf, Y.; Bertin, D.; Gigmes, D.; Versace, D.-L.; Lalevée, J.; Fouassier, J.-P., *Macromolecules* **2010**, *43*, 2204.
- (61) Corrigan, N.; Xu, J. T.; Boyer, C., *Macromolecules* **2016**, *49*, 3274.
- (62) Koumura, K.; Satoh, K.; Kamigaito, M., *Macromolecules* **2008**, *41*, 7359.
- (63) Nakamura, Y.; Yamago, S., *Beilstein Journal of Organic Chemistry* **2013**, *9*, 1607.
- (64) Kottisch, V.; Supej, M. J.; Fors, B. P., *Angewandte Chemie International Edition English* **2018**, *57*, 8260.
- (65) Michaudel, Q.; Chauvire, T.; Kottisch, V.; Supej, M. J.; Stawiasz, K. J.; Shen, L.; Zipfel, W. R.; Abruna, H. D.; Freed, J. H.; Fors, B. P., *Journal of the American Chemical Society* **2017**, *139*, 15530.
- (66) Matyjaszewski, K., *Macromolecules* **2012**, *45*, 4015.
- (67) Moad, G.; Rizzardo, E.; Thang, S. H., *Australian Journal of Chemistry* **2005**, *58*, 379.
- (68) Moad, G.; Rizzardo, E.; Thang, S. H., *Polymer* **2008**, *49*, 1079.
- (69) Hawker, C. J.; Bosman, A. W.; Harth, E., *Chemical Reviews* **2001**, *101*, 3661.
- (70) Nicolas, J.; Guillaneuf, Y.; Lefay, C.; Bertin, D.; Gigmes, D.; Charleux, B., *Progress in Polymer Science* **2013**, *38*, 63.
- (71) Nicewicz, D. A.; MacMillan, D. W., *Science* **2008**, *322*, 77.
- (72) Treat, N. J.; Fors, B. P.; Kramer, J. W.; Christianson, M.; Chiu, C. Y.; de Alaniz, J. R.; Hawker, C. J., *ACS Macro Letters* **2014**, *3*, 580.
- (73) Alfredo, N. V.; Jalapa, N. E.; Morales, S. L.; Ryabov, A. D.; Le Lagadec, R.; Alexandrov, L., *Macromolecules* **2012**, *45*, 8135.
- (74) Nzulu, F.; Telitel, S.; Stoffelbach, F.; Graff, B.; Morlet-Savary, F.; Lalevee, J.; Fensterbank, L.; Goddard, J. P.; Ollivier, C., *Polymer Chemistry* **2015**, *6*, 4605.
- (75) Telitel, S.; Dumur, F.; Campolo, D.; Poly, J.; Gigmes, D.; Fouassier, J. P.; Lalevee, J., *Journal of Polymer Science Part A-Polymer Chemistry* **2016**, *54*, 702.
- (76) Seal, P.; Xu, J. T.; De Luca, S.; Boyer, C.; Smith, S. C., *Advanced Theory and Simulations* **2019**, *2*, 1900038.
- (77) Corrigan, N.; Xu, J. T.; Boyer, C.; Allonas, X., *ChemPhotoChem* **2019**, *3*, 1193.
- (78) Shanmugam, S.; Xu, J.; Boyer, C., *Journal of the American Chemical Society* **2015**, *137*, 9174.
- (79) Corrigan, N.; Rosli, D.; Jones, J. W. J.; Xu, J. T.; Boyer, C., *Macromolecules* **2016**, *49*, 6779.
- (80) Shanmugam, S.; Xu, J. T.; Boyer, C., *Macromolecules* **2016**, *49*, 9345.
- (81) Treat, N. J.; Sprafke, H.; Kramer, J. W.; Clark, P. G.; Barton, B. E.; Read de Alaniz, J.; Fors, B. P.; Hawker, C. J., *Journal of the American Chemical Society* **2014**, *136*, 16096.
- (82) Pan, X. C.; Lamson, M.; Yan, J. J.; Matyjaszewski, K., *ACS Macro Letters* **2015**, *4*, 192.
- (83) Miyake, G. M.; Theriot, J. C., *Macromolecules* **2014**, *47*, 8255.
- (84) Pan, X.; Fang, C.; Fantin, M.; Malhotra, N.; So, W. Y.; Peteanu, L. A.; Isse, A. A.; Gennaro, A.; Liu, P.; Matyjaszewski, K., *Journal of the American Chemical Society* **2016**, *138*, 2411.
- (85) Cole, J. P.; Federico, C. R.; Lim, C. H.; Miyake, G. M., *Macromolecules* **2019**, *52*, 747.

- (86) Kutahya, C.; Allushi, A.; Isci, R.; Kreutzer, J.; Ozturk, T.; Yilmaz, G.; Yagci, Y., *Macromolecules* **2017**, *50*, 6903.
- (87) Shanmugam, S.; Xu, J.; Boyer, C., *Angewandte Chemie International Edition English* **2016**, *55*, 1036.
- (88) Xu, J. T.; Shanmugam, S.; Boyer, C., *ACS Macro Letters* **2015**, *4*, 926.
- (89) Xu, J.; Shanmugam, S.; Fu, C.; Aguey-Zinsou, K. F.; Boyer, C., *Journal of the American Chemical Society* **2016**, *138*, 3094.
- (90) Cao, H. L.; Wang, G. C.; Xue, Y. D.; Yang, G. L.; Tian, J.; Liu, F.; Zhang, W. A., *ACS Macro Letters* **2019**, *8*, 616.
- (91) Xu, J. T.; Shanmugam, S.; Duong, H. T.; Boyer, C., *Polymer Chemistry* **2015**, *6*, 5615.
- (92) Huang, Z.; Zhang, L.; Cheng, Z.; Zhu, X., *Polymers (Basel)* **2016**, *9*.
- (93) Mateos, J.; Rigodanza, F.; Vega-Penalzo, A.; Sartorel, A.; Natali, M.; Bortolato, T.; Pelosi, G.; Companyo, X.; Bonchio, M.; Dell'Amico, L., *Angewandte Chemie International Edition English* **2020**, *59*, 1302.
- (94) Nomeir, B.; Fabre, O.; Ferji, K., *Macromolecules* **2019**, *52*, 6898.
- (95) Liu, X. D.; Zhang, L. F.; Cheng, Z. P.; Zhu, X. L., *Polymer Chemistry* **2016**, *7*, 689.
- (96) Kutahya, C.; Aykac, F. S.; Yilmaz, G.; Yagci, Y., *Polymer Chemistry* **2016**, *7*, 6094.
- (97) Yilmaz, G.; Yagci, Y., *Polymer Chemistry* **2018**, *9*, 1757.
- (98) Allushi, A.; Jockusch, S.; Yilmaz, G.; Yagci, Y., *Macromolecules* **2016**, *49*, 7785.
- (99) Figg, C. A.; Hickman, J. D.; Scheutz, G. M.; Shanmugam, S.; Carmean, R. N.; Tucker, B. S.; Boyer, C.; Sumerlin, B. S., *Macromolecules* **2018**, *51*, 1370.
- (100) Goetz, A. E.; Pascual, L. M. M.; Dunford, D. G.; Ogawa, K. A.; Knorr, D. B.; Boydston, A. J., *ACS Macro Letters* **2016**, *5*, 579.
- (101) Pascual, L. M. M.; Goetz, A. E.; Roehrich, A. M.; Boydston, A. J., *Macromolecular Rapid Communications* **2017**, *38*.
- (102) Pascual, L. M. M.; Dunford, D. G.; Goetz, A. E.; Ogawa, K. A.; Boydston, A. J., *Synlett* **2016**, *27*, 759.
- (103) Ma, H.; Peng, Q.; An, Z.; Huang, W.; Shuai, Z., *Journal of the American Chemical Society* **2019**, *141*, 1010.
- (104) Orr-Ewing, A. J., *Struct Dyn* **2019**, *6*, 010901.
- (105) Theriot, J. C.; McCarthy, B. G.; Lim, C. H.; Miyake, G. M., *Macromolecular Rapid Communications* **2017**, *38*, 1700040.
- (106) Marcus, R. A., *The Journal of Chemical Physics* **1956**, *24*, 966.
- (107) Marcus, R. A., *The Journal of Chemical Physics* **1956**, *24*, 979.
- (108) Marcus, R. A., *The Journal of Chemical Physics* **1957**, *26*, 872.
- (109) Marcus, R. A., *The Journal of Physical Chemistry* **1963**, *67*, 853.
- (110) Marcus, R. A., *Annual Review of Physical Chemistry* **1964**, *15*, 155.
- (111) Frisch, M. J.; Trucks, G. W.; Schlegel, H. B.; Scuseria, G. E.; Robb, M. A.; Cheeseman, J. R.; Scalmani, G.; Barone, V.; Petersson, G. A.; Nakatsuji, H.; Li, X.; Caricato, M.; Marenich, A. V.; Bloino, J.; Janesko, B. G.; Gomperts, R.; Mennucci, B.; Hratchian, H. P.; Ortiz, J. V.; Izmaylov, A. F.; Sonnenberg, J. L.; Williams; Ding, F.; Lipparini, F.; Egidi, F.; Goings, J.; Peng, B.; Petrone, A.; Henderson, T.; Ranasinghe, D.; Zakrzewski, V. G.; Gao, J.; Rega, N.; Zheng, G.; Liang, W.; Hada, M.; Ehara, M.; Toyota, K.; Fukuda, R.; Hasegawa, J.; Ishida, M.; Nakajima, T.; Honda, Y.; Kitao, O.; Nakai, H.; Vreven, T.; Throssell, K.; Montgomery Jr., J. A.; Peralta, J. E.; Ogliaro, F.; Bearpark, M. J.; Heyd, J. J.; Brothers, E. N.; Kudin, K. N.; Staroverov, V. N.; Keith, T. A.; Kobayashi, R.; Normand, J.; Raghavachari, K.; Rendell, A. P.; Burant, J. C.; Iyengar, S. S.; Tomasi,

- J.; Cossi, M.; Millam, J. M.; Klene, M.; Adamo, C.; Cammi, R.; Ochterski, J. W.; Martin, R. L.; Morokuma, K.; Farkas, O.; Foresman, J. B.; Fox, D. J. *Gaussian 09 Rev. D.01*, Wallingford, CT, 2016.
- (112) Aidas, K.; Angeli, C.; Bak, K. L.; Bakken, V.; Bast, R.; Boman, L.; Christiansen, O.; Cimiraglia, R.; Coriani, S.; Dahle, P.; Dalskov, E. K.; Ekstrom, U.; Enevoldsen, T.; Eriksen, J. J.; Ettenhuber, P.; Fernandez, B.; Ferrighi, L.; Fliegl, H.; Frediani, L.; Hald, K.; Halkier, A.; Hattig, C.; Heiberg, H.; Helgaker, T.; Hennum, A. C.; Hettema, H.; Hjertenaes, E.; Host, S.; Hoyvik, I. M.; Iozzi, M. F.; Jansik, B.; Jensen, H. J.; Jonsson, D.; Jorgensen, P.; Kauczor, J.; Kirpekar, S.; Kjaergaard, T.; Klopper, W.; Knecht, S.; Kobayashi, R.; Koch, H.; Kongsted, J.; Krapp, A.; Kristensen, K.; Ligabue, A.; Lutnaes, O. B.; Melo, J. I.; Mikkelsen, K. V.; Myhre, R. H.; Neiss, C.; Nielsen, C. B.; Norman, P.; Olsen, J.; Olsen, J. M.; Osted, A.; Packer, M. J.; Pawlowski, F.; Pedersen, T. B.; Provasi, P. F.; Reine, S.; Rinkevicius, Z.; Ruden, T. A.; Ruud, K.; Rybkin, V. V.; Salek, P.; Samson, C. C.; de Meras, A. S.; Saue, T.; Sauer, S. P.; Schimmelpfennig, B.; Sneskov, K.; Steindal, A. H.; Sylvester-Hvid, K. O.; Taylor, P. R.; Teale, A. M.; Tellgren, E. I.; Tew, D. P.; Thorvaldsen, A. J.; Thogersen, L.; Vahtras, O.; Watson, M. A.; Wilson, D. J.; Ziolkowski, M.; Agren, H., *Wiley Interdiscip Rev Comput Mol Sci* **2014**, *4*, 269.
- (113) Liu, W. J.; Hong, G. Y.; Dai, D. D.; Li, L. M.; Dolg, M., *Theoretical Chemistry Accounts* **1997**, *96*, 75.
- (114) Niu, Y. L.; Li, W. Q.; Peng, Q.; Geng, H.; Yi, Y. P.; Wang, L. J.; Nan, G. J.; Wang, D.; Shuai, Z. G., *Molecular Physics* **2018**, *116*, 1078.
- (115) Lu, T.; Chen, F., *J Comput Chem* **2012**, *33*, 580.
- (116) Lohmann, W., Halogen-Substitution Effect on the Optical Absorption Bands of Uracil*. In *Zeitschrift für Naturforschung C*, 1974; Vol. 29, p 493.
- (117) De Angelis, F.; Fantacci, S.; Evans, N.; Klein, C.; Zakeeruddin, S. M.; Moser, J. E.; Kalyanasundaram, K.; Bolink, H. J.; Gratzel, M.; Nazeeruddin, M. K., *Inorganic Chemistry* **2007**, *46*, 5989.
- (118) Baranoff, E.; Curchod, B. F.; Monti, F.; Steimer, F.; Accorsi, G.; Tavernelli, I.; Rothlisberger, U.; Scopelliti, R.; Gratzel, M.; Nazeeruddin, M. K., *Inorganic Chemistry* **2012**, *51*, 799.
- (119) Bedi, A.; Gidron, O., *Acc Chem Res* **2019**, *52*, 2482.
- (120) Norton, J. E.; Houk, K. N., *Journal of the American Chemical Society* **2005**, *127*, 4162.
- (121) Haddon, R. C., *Accounts of Chemical Research* **2002**, *21*, 243.
- (122) Jug, K.; Hiberty, P. C.; Shaik, S., *Chemical Reviews* **2001**, *101*, 1477.
- (123) Gentemann, S.; Medforth, C. J.; Forsyth, T. P.; Nurco, D. J.; Smith, K. M.; Fajer, J.; Holten, D., *Journal of the American Chemical Society* **1994**, *116*, 7363.
- (124) Senge, M. O., *Chemical Communications (Camb)* **2006**, 243.
- (125) Sparks, L. D.; Medforth, C. J.; Park, M. S.; Chamberlain, J. R.; Ondrias, M. R.; Senge, M. O.; Smith, K. M.; Shelnut, J. A., *Journal of the American Chemical Society* **1993**, *115*, 581.
- (126) Zhang, L. W.; Wu, C. Y.; Jung, K.; Ng, Y. H.; Boyer, C., *Angewandte Chemie-International Edition* **2019**, *58*, 16811.
- (127) Zhou, Y.; Xue, B.; Wu, C.; Chen, S.; Liu, H.; Jiu, T.; Li, Z.; Zhao, Y., *Chemical Communications (Camb)* **2019**, *55*, 13570.
- (128) Chen, Z.; Baumeister, U.; Tschierske, C.; Wurthner, F., *Chemistry* **2007**, *13*, 450.
- (129) Martynov, A. G.; Mack, J.; May, A. K.; Nyokong, T.; Gorbunova, Y. G.; Tsivadze, A. Y., *ACS Omega* **2019**, *4*, 7265.
- (130) Zhong, A.; Zhang, Y.; Bian, Y., *J Mol Graph Model* **2010**, *29*, 470.

- (131) Jakubikova, E.; Campbell, I. H.; Martin, R. L., *Journal of Physical Chemistry A* **2011**, *115*, 9265.
- (132) Adachi, M.; Nagao, Y., *Chemistry of Materials* **2001**, *13*, 662.
- (133) Adachi, M.; Murata, Y., *The Journal of Physical Chemistry A* **1998**, *102*, 841.
- (134) Roznyatovskiy, V. V.; Lee, C. H.; Sessler, J. L., *Chemical Society Reviews* **2013**, *42*, 1921.
- (135) Wu, Z.; Jung, K.; Boyer, C., *Angewandte Chemie International Edition English* **2020**, *59*, 2013.
- (136) Pyykko, P., *Chemical Reviews* **1988**, *88*, 563.
- (137) Koziar, J. C.; Cowan, D. O., *Accounts of Chemical Research* **2002**, *11*, 334.
- (138) Levine, I. N., *Quantum Chemistry*. Pearson: 2014.
- (139) El-Sayed, M. A., *Accounts of Chemical Research* **2002**, *1*, 8.
- (140) Peng, Q.; Yi, Y.; Shuai, Z.; Shao, J., *Journal of the American Chemical Society* **2007**, *129*, 9333.
- (141) Strickler, S. J.; Berg, R. A., *The Journal of Chemical Physics* **1962**, *37*, 814.
- (142) Yan, Y. J.; Mukamel, S., *Journal of Chemical Physics* **1986**, *85*, 5908.
- (143) Peng, Q.; Yi, Y.; Shuai, Z.; Shao, J., *Journal of Chemical Physics* **2007**, *126*, 114302.
- (144) Weber, P.; Reimers, J. R., *Journal of Physical Chemistry A* **1999**, *103*, 9830.
- (145) Cai, Z. L.; Reimers, J. R., *Journal of Physical Chemistry A* **2000**, *104*, 8389.
- (146) Peng, Q.; Niu, Y.; Shi, Q.; Gao, X.; Shuai, Z., *J Chem Theory Comput* **2013**, *9*, 1132.
- (147) Li, Z. D.; Suo, B. B.; Zhang, Y.; Xiao, Y. L.; Liu, W. J., *Molecular Physics* **2013**, *111*, 3741.
- (148) Li, Z.; Xiao, Y.; Liu, W., *Journal of Chemical Physics* **2012**, *137*, 154114.
- (149) Li, Z.; Xiao, Y.; Liu, W., *Journal of Chemical Physics* **2014**, *141*, 054111.
- (150) Lewis, F. D.; Zuo, X., *Journal of the American Chemical Society* **2003**, *125*, 8806.
- (151) Huertas-Hernando, D.; Guinea, F.; Brataas, A., *Physical Review B* **2006**, *74*, 155426.
- (152) Nagarajan, K.; Mallia, A. R.; Reddy, V. S.; Hariharan, M., *Journal of Physical Chemistry C* **2016**, *120*, 8443.
- (153) Nagarajan, K.; Mallia, A. R.; Muraleedharan, K.; Hariharan, M., *Chem Sci* **2017**, *8*, 1776.
- (154) Henry, B. R.; Siebrand, W., *Journal of Chemical Physics* **1971**, *54*, 1072.
- (155) Tait, C. E.; Bedi, A.; Gidron, O.; Behrends, J., *Phys Chem Chem Phys* **2019**, *21*, 21588.
- (156) Schmidt, K.; Brovelli, S.; Coropceanu, V.; Beljonne, D.; Cornil, J.; Bazzini, C.; Caronna, T.; Tubino, R.; Meinardi, F.; Shuai, Z.; Bredas, J. L., *Journal of Physical Chemistry A* **2007**, *111*, 10490.
- (157) Bowman, M. K., *Chemical Physics Letters* **1977**, *48*, 17.
- (158) Tait, C. D.; Holten, D., *Photobiochemistry and photobiophysics* **1983**, *6*, 201.
- (159) Shchupak, E. E.; Ivashin, N. V.; Sagun, E. I., *Optics and Spectroscopy* **2013**, *115*, 37.
- (160) Gesmundo, N. J.; Nicewicz, D. A., *Beilstein Journal of Organic Chemistry* **2014**, *10*, 1272.
- (161) Perkowski, A. J.; You, W.; Nicewicz, D. A., *Journal of the American Chemical Society* **2015**, *137*, 7580.
- (162) Joshi-Pangu, A.; Levesque, F.; Roth, H. G.; Oliver, S. F.; Campeau, L. C.; Nicewicz, D.; DiRocco, D. A., *Journal of Organic Chemistry* **2016**, *81*, 7244.

Chapter 3 Learning from Natural Photocatalyst Design: Chlorophyll a and its Crude Extract as Efficient Photocatalyst for PET-RAFT Polymerisation with Oxygen Tolerance and Post-Decolourisation Functionalities



Chlorophyll a (Chl a), as the dominant natural PC, has been evolved to exhibit intense 600-700 nm red light absorption and strong catalytic capabilities, which arise from the various functional peripheral substituents on the porphyrin core chromophore of Chl a. Indeed, the overall excellent properties of Chl a as a PC functionalised by substituents have inspired researchers to pursue a rational structural modification strategy to design man-made PCs for specific applications. In this view, this work dedicates to learn from the nature by comprehensively exploring the use of Chl a and its spinach crude extract as a multifunctional PC for photoinduced electron/energy transfer-reversible addition-fragmentation chain transfer (PET-RAFT) polymerisation. The intense Q-band absorption of Chl a at 600-700 nm, resulting from its symmetry-breaking substitution, enabled benign red LED lights as the irradiation source and as low as 12.5 ppm loading

of Chl a can afford efficient PET-RAFT polymerisation. The remarkable triplet quantum yield (Φ_T) of Chl a introduced excellent oxygen tolerance to the PET-RAFT system by efficient singlet oxygen photosensitisation. Moreover, the easy degradability arising from the heavily decorated porphyrin structure of Chl a, enabled it to completely degrade to colourless small molecules upon exposure to ambient air and light, which mimics the metabolism process of Chl a degradation in plants. This post-decolourisation feature circumvents the difficulties in removing colours of synthesised polymers from PET-RAFT polymerisation.

3.1 Introduction

Designing homogeneous catalyst to improve the performance of the catalytic system and address the issue of sustainability requires evaluation of the structure and function as well as the potential environmental impact of the catalyst.¹ An ideal catalyst that adheres to the 12 Principles of green chemistry should be able to accommodate a wide range of functional groups contributing to better efficiency in catalysis, reduce chemical waste, display low toxicity, and require minimal catalyst loadings with extended lifetimes.¹⁻² In addition, the desired catalyst should be obtained with minimal chemical and purification steps.

In this aspect, learning from the nature could provide the best shortcuts. Chlorophylls, represented by chlorophyll a (Chl a), are naturally derived from the Mg porphyrin chromophore core as photocatalysts (PCs) for bio-synthesis, with modifications include one reduced pyrrole ring and a number of functional peripheral substituents. Owing to these judicious substitution resulted from natural evolution, Chl a bears remarkable red-light absorption and extraordinary photocatalytic capability³⁻⁵ of bio-synthesis in plants.

In the field of reversible deactivation radical polymerisation (RDRP), the recent introduction of visible light photocatalysis to initiate and mediate polymerisation of myriad functional monomers has led to the development of spatial, temporal as well as sequence control, and therefore, affording well-defined materials.⁶⁻¹⁷ Photo-controlled systems with RAFT (reversible addition-fragmentation chain transfer), namely photoinduced electron/energy transfer RAFT (PET-RAFT) polymerisation, were initially dependent on trace elements¹⁸⁻¹⁹ and expanded to include Chl a²⁰/bacteriochlorophyll a²¹ and zinc tetraphenylporphyrin (ZnTPP).²² Oxygen tolerance is one of the interesting

features of PET-RAFT techniques, which is enabled by singlet oxygen ($^1\text{O}_2$) generation ability of the PC via triplet-triplet annihilation (TTA).²³ In the course of these initial trials in looking for better PCs of PET-RAFT polymerisation, we were deeply attracted by the excellent properties of Chl a as a PC.

Indeed, the one reduced pyrrole ring and installation of various peripheral substituents on the porphyrin chromophore of Chl a are highly symmetry-breaking, which leads to notably increased lower Q band absorption and large red-shifts in absorption (see **Scheme 3.1B** for chemical structure).²⁴ This overall effect endows Chl a with strong red-light absorption, which could enable efficient red-light catalysis under low catalyst loadings. Moreover, Chl a was reported to exhibit high triplet quantum yield Φ_T and remarkable $^1\text{O}_2$ generation ability,²⁵⁻²⁶ which makes it highly promising for introducing excellent oxygen tolerance to PET-RAFT polymerisation. Last but not least, Chl a features easy degradability for bio-metabolism in plants, due to its heavily decorated porphyrin structure.²⁷⁻³⁰ Hence, Chl a can completely degrade to colourless small molecules upon exposure to ambient air and light.³¹⁻³⁵ In this regard, we propose the use of Chl a capable of degrading at the end of the polymerisation, can eliminates the need for additional purification to remove colours of the synthesised polymers.

In this chapter, we comprehensively investigated the use of Chl a and its spinach crude extract as a naturally “designed” PC for PET-RAFT polymerisation. Indeed, Chl a is highly efficient for PET-RAFT polymerisation under benign red lights with only 12.5 ppm catalyst loading with respect to the monomer. Excellent oxygen tolerance was demonstrated in these systems. Moreover, Chl a is able to degrade to inert by-products to yield ring-opened tetrapyrroles³⁶ in the presence of air and light.³⁵ Utilizing this property in a synthetic environment provides an opportunity to bypass the need for catalyst removal upon completion of PET-RAFT polymerisation. These unique functionalities arising from the heavily substituted structure of Chl a as “designed” by natural evolution is inspiring for rational design of a PC for PET-RAFT polymerisation.

3.2 Experimental section

3.2.1 Monitoring PET-RAFT polymerisation catalysed by Chl a

General procedures for kinetic studies of RAFT photopolymerisation of N,N-dimethylacrylamide (DMA) with Online Fourier Transform Near-Infrared (FTNIR) Spectroscopy in the presence/absence of oxygen

A reaction stock solution consisting of DMSO (551 μL), DMA (0.577 g, 5.83 mmol), BTPA (7 mg, 29.36 μmol) and Chl a (49.1 μL of 1486 μM of Chl a stock solution, 0.072 μmol) was prepared in a glass vial. The stock solution was transferred into two 0.9 mL FTNIR quartz cuvettes (1 cm \times 2 mm) (approximately 0.6 mL in each) sealed with rubber septa and covered with aluminium foil. One of the sealed cuvette was degassed with nitrogen for 20 min. The quartz cuvettes were then irradiated with red LED light (5 W, $\lambda_{\text{max}} = 635 \text{ nm}$) at room temperature. The cuvettes were transferred in sequence to a sample holder manually for FTNIR measurements at specific time points. After 15 s of scanning, the cuvettes were transferred back to the irradiation source. Monomer conversions were calculated by taking the ratio of integrations of the wavenumber area 6210-6115 cm^{-1} for all curves at different reaction times to that of time zero. Aliquots of reaction samples were taken at specific time points during the reaction to be analysed by GPC (DMAc) to determine number average molecular weights (M_n) and polydispersities (M_w/M_n).

3.2.2 General procedures for observation of singlet oxygen in solution

An 1 mL reaction solution consisting of 0.06 mM pure Chl a (identical to the concentration of 12.5 ppm Chl a used in polymerisation solution) as singlet generator (SG) and 2 mM dimethylantracene as singlet oxygen trapper (ST) in acetonitrile (CH_3CN) as solvent was prepared in a glass vial and immediately transferred to a 0.9 mL FTNIR quartz cuvette (1 cm \times 2 mm) till filling up the headspace. The cuvette was sealed with a cap and parafilm without gaseous headspace. The concentration of the SG (Chl a) was chosen identical to 12.5 ppm Chl a used in polymerisation solution whereas that of ST was chosen based on its absorbance peaks in order to be within the detection limits of UV-Vis spectroscopy. The absorbance of the reaction solution before and after irradiation with 650 nm, 102 W/m^2 light using an Oriel VeraSol LED solar simulator was recorded at specific time intervals.

Comparative experiment using DMSO as the solvent was conducted following the same procedures.

3.2.3 Catalyst removal after polymerisation

General procedures for catalyst removal under open air and red-light irradiation after polymerisation in the presence of oxygen and 12.5 ppm Chl a (with respect to the monomer)

A reaction stock solution consisting of DMSO (544 μL), MA (0.577 g, 6.70 mmol), BTPA (7.9 mg, 33.50 μmol) and Chl a (55.7 μL of 1486 μM of Chl a stock solution, 0.084 μmol) was prepared in a glass vial. The stock solution was first transferred into two 0.9 mL FTNIR quartz cuvettes (1 cm \times 2 mm) (approximately 0.6 mL in each) sealed with rubber septa and covered with aluminium foil. One of the cuvettes was kept in darkness as the control sample and the other was irradiated with red LED light (5 W, $\lambda_{\text{max}} = 635$ nm, light intensity = 2.55 mW/cm²) at room temperature. To monitor the monomer conversions, the cuvette was occasionally transferred into a sample holder for FTNIR measurements and put back in the irradiation source afterwards. Monomer conversions were calculated by taking the ratio of integrations of the wavenumber area 6250-6100 cm⁻¹ for all curves at different reaction times to that of time zero. Once the monomer conversion was drive up to 50%, polymerisation was stopped by covering the cuvette with aluminium foil. Subsequently, the remaining monomer in the reaction mixture was evaporated using nitrogen flow (in water bath at 30-40 °C) for 30 min. Subsequently, after removal of the rubber septum, the cuvette was put under open air and back to the irradiation source to remove Chl a from the polymer solution. To monitor photo-degradation of Chl a, the experiment cuvette was placed in the sample holder to record UV-vis spectra before and after irradiation of the polymerisation stage and the catalyst removal stage respectively. Photographs of the experiment sample and the control sample were taken after each UV-vis measurement by transferring the solutions of both samples to two GPC vials respectively.

3.2.4 Characterisation of end-group fidelity

General procedures for chain extension of PMA macroRAFT to DMA by PET-RAFT

The reaction mixture containing PMA ($M_{n,\text{GPC}} = 11\ 700$ g/mol, $M_w/M_n = 1.09$) received after non-degassed polymerisation using pure Chl a as photocatalyst followed by catalyst

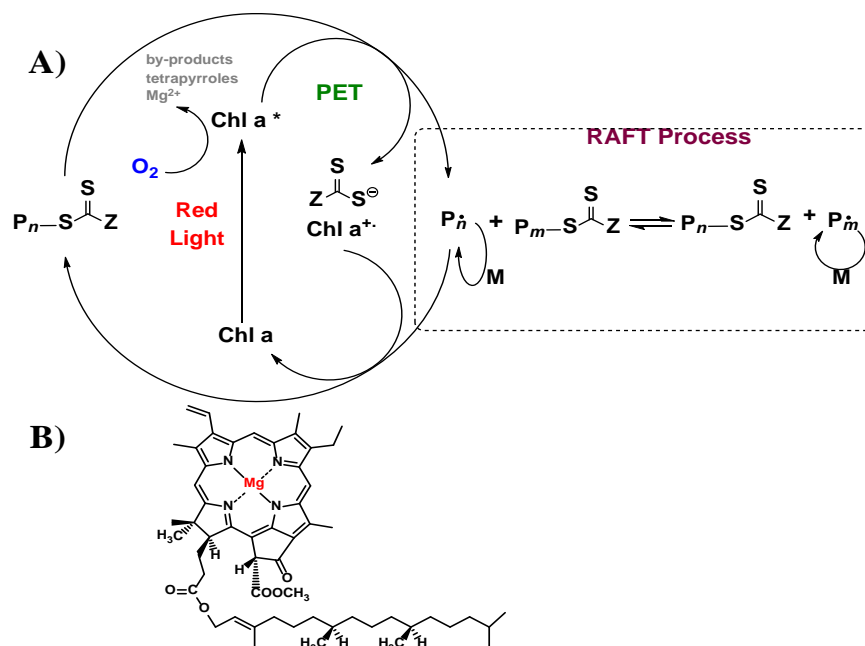
removal was purified by precipitating in a mixture of ethyl ether/petroleum spirit (3/7, v/v). The pale-yellow precipitate was collected and redissolved in minimum amount of dichloromethane before precipitating a second time in diethyl ether/petroleum spirit (3/7, v/v) mixture.

Chain extension of PMA macroRAFT to DMA was carried out in a 0.9 mL FTNIR quartz cuvette (1 cm × 2 mm) in the presence of DMSO (327 μL), DMA (0.317 g, 3.20 mmol), PMA macroRAFT (0.038 g, 3.20 μmol) and Chl a (2.65 μL of 3017 μM of Chl a stock solution, 0.008 μmol) sealed with a rubber septum and covered with aluminium foil. The reaction solution in the cuvette was degassed for 20 min before irradiated with red LED light (5 W, $\lambda_{\text{max}} = 635 \text{ nm}$, light intensity = 2.55 mW/cm^2) for 60 min at room temperature. The synthesised polymer was analysed in GPC: $M_{n,\text{GPC}} = 45\ 100 \text{ g/mol}$, $M_w/M_n = 1.07$ and 40% monomer conversion.

3.3 Results and discussion

3.3.1 Kinetic studies of PET-RAFT polymerisation catalysed by Chl a

Chl a can undergo photoinduced electron transfer (PET) in the triplet excited state and reduces RAFT agent to generate an initial radical which then enters the RAFT cycle (**Scheme 3.1**). After the propagating radical encounters the oxidized Chl a and the reduced RAFT, the neutral RAFT agent and a dormant ground state Chl a can be regenerated. Upon completing its polymerisation cycle, complete degradation of Chl a in the presence of oxygen into colourless and non-photoactive products could obviate catalyst removal steps. In our previous study, we demonstrated the use of Chl a as an efficient and sustainable photocatalyst for PET-RAFT polymerisation, where Chl a was extracted from spinach leaves and purified by column chromatography.²⁰ While chromatography is relatively convenient to perform in laboratories, with a reported production as high as 300 mg Chl a from 20 g spinach leaves,³⁷ it is still time consuming and expensive especially for large-scale industrial production. In an effort to pave the way for potential industrial production of polymer via photoinduced CLRP, we decided to further investigate the use of unpurified Chl a, i.e. crude extract of Chl a, to catalyse PET-RAFT polymerisation.



Scheme 3.1 (A) Proposed mechanism of PET-RAFT polymerisation catalysed by Chl a and post-polymerisation catalyst degradation; (B) the chemical structure of Chl a.

Crude Chl a was extracted from spinach leaves in acetone and used directly after centrifugation without further purification. The concentration of Chl a in the crude extract was determined by UV-vis measurement using the signal at 665 nm and Wellburn equation.³⁸ In an initial attempt, PET-RAFT polymerisations using either 12.5 ppm (with respect to the monomer concentration) of pure Chl a or crude extract were compared. These polymerisations were performed using *N,N'*-dimethylacrylamide (DMA) as the model monomer and 2-(*n*-butyltrithiocarbonate)-propionic acid (BTPA) as the RAFT agent under red light emitting diodes (LEDs) ($\lambda_{\max} = 635$ nm, 2.55 mW/cm²) in dimethyl sulfoxide (DMSO). Before placing the polymerisation mixture under irradiation, the reaction was degassed to remove air. Kinetic studies were performed by online Fourier transform near-infrared (FTNIR) spectroscopy.³⁹ With a molar ratio of [DMA]:[BTPA]:[Chl a (pure or in crude extract)] of 200:1:0.0025, over 80% monomer conversions were detected in both systems upon 2 h (with pure Chl a) and 3 h (with crude extract) irradiation (**Figure 3.1A**, and **Table 3.1**, #1-2).

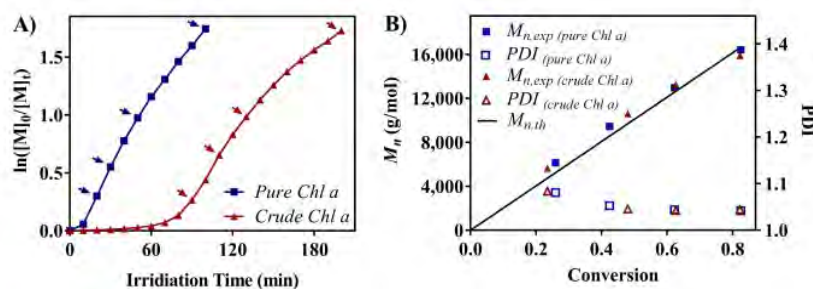


Figure 3.1 Kinetic studies of PET-RAFT polymerisation of DMA with BTPA as the RAFT agent, catalysed by pure Chl a (blue line in (A) and blue square in (B)) or a crude extract with identical Chl a concentration (red line in (A) and red triangle in (B)) under red light irradiation, using a molar ratio of [DMA]:[BTPA]:[Chl a (pure or in crude extract)] = 200:1:0.0025, in degassed systems. (A) Plot of $\ln([M]_0/[M]_t)$ against reaction time and (B) M_n and M_n/M_w (polydispersity PDI) versus monomer conversion.

Table 3.1 PET-RAFT polymerisation of DMA with BTPA using crude and pure Chl a ([DMA]: [RAFT]: [Chl a] = 200: 1: 2.5×10^{-3}) as photoredox catalysts ([Chl a]/[DMA] = 12.5 ppm) under red light irradiation ($\lambda_{\max} = 635$ nm, light intensity = 2.55 mW/cm²) in DMSO.

#	Chl a	N ₂	Time (min)	α^a (%)	$M_{n,th}^b$ (g/mol)	$M_{n,GPC}^b$ (g/mol)	PDI^c
1	Pure	YES	2	83	16 600	16 400	1.04
2	Crude	YES	3	82	16 500	15 900	1.04
3	Pure	NO	2	80	16 100	15 600	1.05
4	Crude	NO	4	76	15 200	15 200	1.06

Notes: ^aMonomer conversion was determined by FTNIR measurements. ^bTheoretical molecular weight was calculated using the following equation: $M_{n,th} = [M]_0/[RAFT]_0 \times MW^M \times \alpha + MW^{RAFT}$, where $[M]_0$, $[RAFT]_0$, MW^M , α , and MW^{RAFT} correspond to initial monomer concentration, initial RAFT concentration, molar mass of monomer, conversion determined by FTNIR, and molar mass of RAFT agent. ^cMolecular weight and M_w/M_n were determined by GPC analysis calibrated to poly(methyl methacrylate).

As revealed by gel permeation chromatography (GPC) traces, both pure Chl a and crude spinach extracts afforded polymers with good control over molecular weights and narrow molecular weight distributions (polydispersity index $M_n/M_w < 1.10$) in accord with controlled/living radical polymerisation (**Figure 3.1B** and **Figure 3.2**).

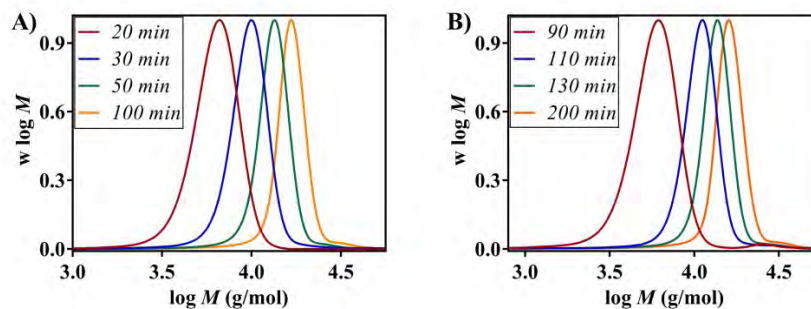


Figure 3.2 Molecular weight distributions at different time points for DMA polymerisation with BTPA (under red light irradiation, using a molar ratio of [DMA]:[BTPA] = 200:1) in nitrogen degassed systems (A) catalysed by 12.5 ppm Chl a (with respect to the monomer concentration) and (B) catalysed by a crude extract containing 12.5 ppm Chl a.

Interestingly, we observed a typical inhibition period of around 60-70 min in the polymerisation containing crude extracts, which was not observed with pure Chl a, consistent with our previous report.³⁹ Considering the composition of spinach extracts,⁴⁰⁻⁴² the inhibition period should be attributed to the presence of β -carotene and other carotenoids in crude extracts that may act as radical quenchers.⁴³⁻⁴⁵ To test this hypothesis, two DMA polymerisations were performed concurrently in the presence of 12.5 ppm of pure Chl a. We added β -carotene (1.25 ppm with respect to the monomer concentration, i.e. 10 mol% to Chl a) in the first polymerisation, while in the second polymerisation, β -carotene was added in the middle of polymerisation. Consistent with our hypothesis, a ~60 min inhibition period (coincidentally matches that in polymerisation with a crude extract, suggesting a similar relative concentration of β -carotene and other carotenoids in the crude extract) was observed (**Figure 3.3**) for the sample with β -carotene added at the beginning, while no inhibition period was observed for the other. Furthermore, the addition of β -carotene during the polymerisation led to a significant decrease in the apparent propagation rate constants ($k_p^{\text{app}} = 1.75 \times 10^{-2} \text{ min}^{-1}$ and $1.05 \times 10^{-2} \text{ min}^{-1}$ before and after addition of β -carotene). The exact mechanism is likely a complex natural

process and hard to investigate which is not a focus of this study; however, the effect of β -carotene to suppress polymerisation is evident.

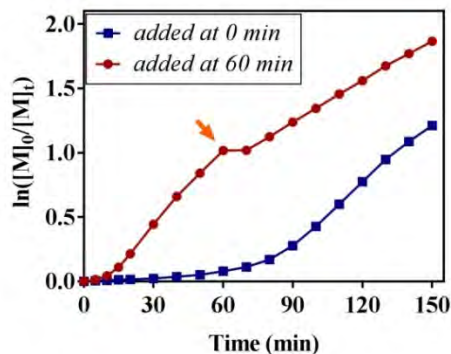


Figure 3.3 Plot of $\ln([M]_0/[M]_t)$ against reaction time measured by online FTNIR for DMA polymerisation with 1.25 ppm β -carotene (with respect to the monomer concentration) added at the beginning (blue curve) and in the middle (red curve) of polymerisation, under red light and deoxygenated conditions. The molar ratio: [DMA]:[BTPA]:[Chl a (pure)] = 200:1:0.0025.

3.3.2 Oxygen tolerance in PET-RAFT polymerisation catalysed by Chl a

Moreover, nitrogen sparging is often required before initiation of polymerisation as the presence of oxygen leads to long inhibition periods and sluggish polymerisation.⁴⁶ Therefore, the need to eliminate oxygen could be a limitation for scaling up photoinduced CLRP. Recent techniques have been proposed for oxygen removal before performing CLRP.^{11, 47-58} For instance, we reported the use of ZnTPP which removed oxygen via a singlet oxygen quenching mechanism before catalysing RAFT photopolymerisation.²³ Considering the similarity in structure of Chl a (see **Scheme 3.1B** for chemical structure) and its derivative ZnTPP, we decided to investigate the possibility of conferring oxygen tolerance for polymerisation catalysed by Chl a. Polymerisations in the presence of air (non-degassed) with pure Chl a were compared with the degassed systems (**Table 3.1**).

As expected, non-degassed polymerisation reached 80% monomer conversion (**Figure 3.4A**, red line and **Table 3.1**, #3) after 2 h irradiation, which was slower than degassed polymerisation (**Figure 3.4A**, blue line and **Table 3.1**, #1). Similar observations were also made for polymerisation catalysed by crude extracts in non-degassed systems, where 76% monomer conversion was detected after 4 h irradiation (**Figure 3.4C**, red line and

Table 3.1, #4). The synthesis of well-defined polymers with reasonable RAFT end group retention was confirmed by GPC (with pure Chl a: **Figure 3.4B** and **Figure 3.5** and crude extract: **Figure 3.4D** and **Figure 3.5F**) and by ^1H NMR in separate experiments under identical conditions (with pure Chl a: **Figure 3.6**; with crude extract: **Figure 3.7**). Importantly, both polymerisations catalysed by pure Chl a and the crude extract in non-degassed systems yielded well-defined polymers ($M_w/M_n < 1.10$) and good correlation between experimental and theoretical molecular weights. We hypothesized that the oxygen tolerance was attributed to fast production of singlet oxygen,²⁶ followed by its deactivation in the presence of DMSO to yield dimethyl sulfone. Experiments performed with a singlet oxygen quencher, dimethyl anthracene (**Figure 3.8**), confirmed the production of singlet oxygen as we observed a rapid decrease in the absorption signals of anthracene.^{23, 59}

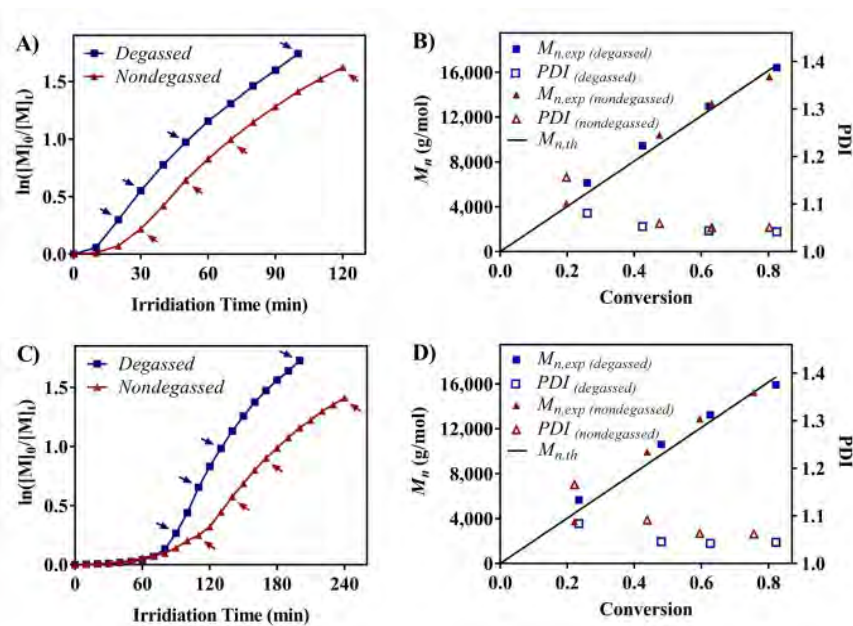


Figure 3.4 Kinetic studies of PET-RAFT polymerisations of DMA using BTPA as RAFT agent and pure Chl a (A and B) or crude extract (C and D) as photo-catalyst under red light irradiation, in degassed systems (blue line in A and C; blue square in B and D) and non-degassed systems (red line in A and C; red triangle in C and D) with a molar ratio of $[\text{DMA}]:[\text{BTPA}]:[\text{Chl a (pure or in crude extract)}] = 200:1:0.0025$. (A and C) $\ln([M]_0/[M]_t)$ versus reaction time of polymerisation. (B and D) M_n and M_w/M_n (polydispersity PDI) versus monomer conversion.

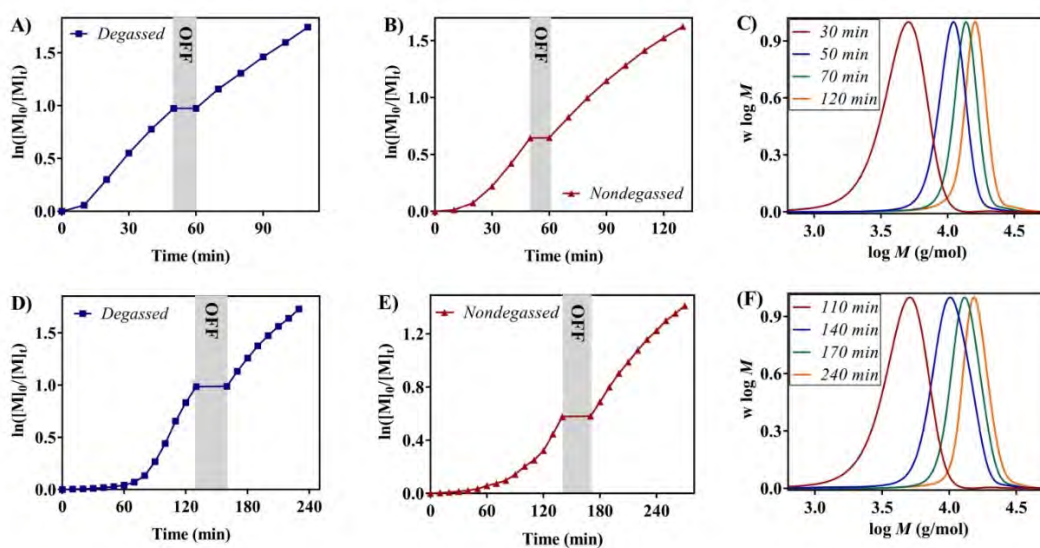


Figure 3.5 (A, B, D and E) Plot of $\ln([M]_0/[M]_t)$ against time with on/off properties measured by online FTNIR for DMA polymerisation with BTPA (under red light irradiation, using a molar ratio of [DMA]:[BTPA] = 200:1); (C and F) molecular weight distributions at different time points; (A) catalysed by 12.5 ppm Chl a in the degassed system, (B and C) catalysed by 12.5 ppm Chl a in the non-degassed system (D) catalysed by a crude extract containing 12.5 ppm Chl a in the degassed system and (E and F) catalysed by a crude extract containing 12.5 ppm Chl a in the non-degassed system. The time interval of sampling in (A-B) and (D-E) is 10 min. The OFF-periods in (A-B) are 10 min while the OFF-periods in (D-E) are 20 min.

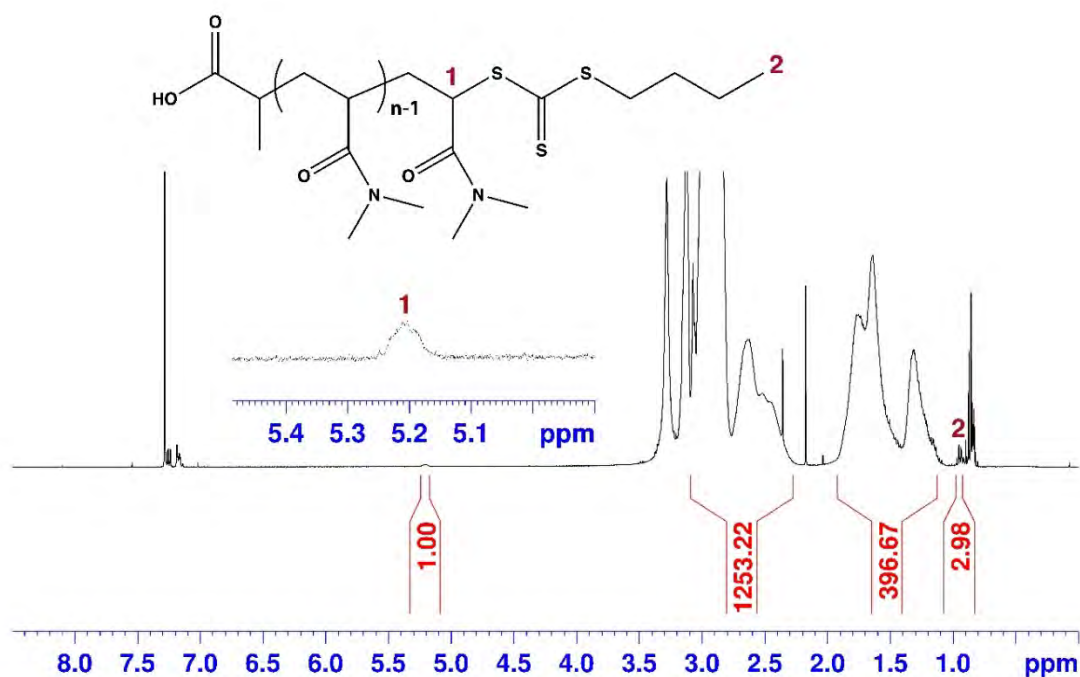


Figure 3.6 ^1H NMR spectrum (300 MHz, CDCl_3) for purified PDMA synthesised in the presence of 12.5 ppm pure Chl a (with respect to the monomer concentration), red LED light and oxygen ($M_{n,\text{GPC}} = 15\,400$ g/mol, $M_{n,\text{th}} = 17\,300$ g/mol, monomer conversion = 86%), obtained from a different experiment from that in Table 3.1, #3 under identical conditions.

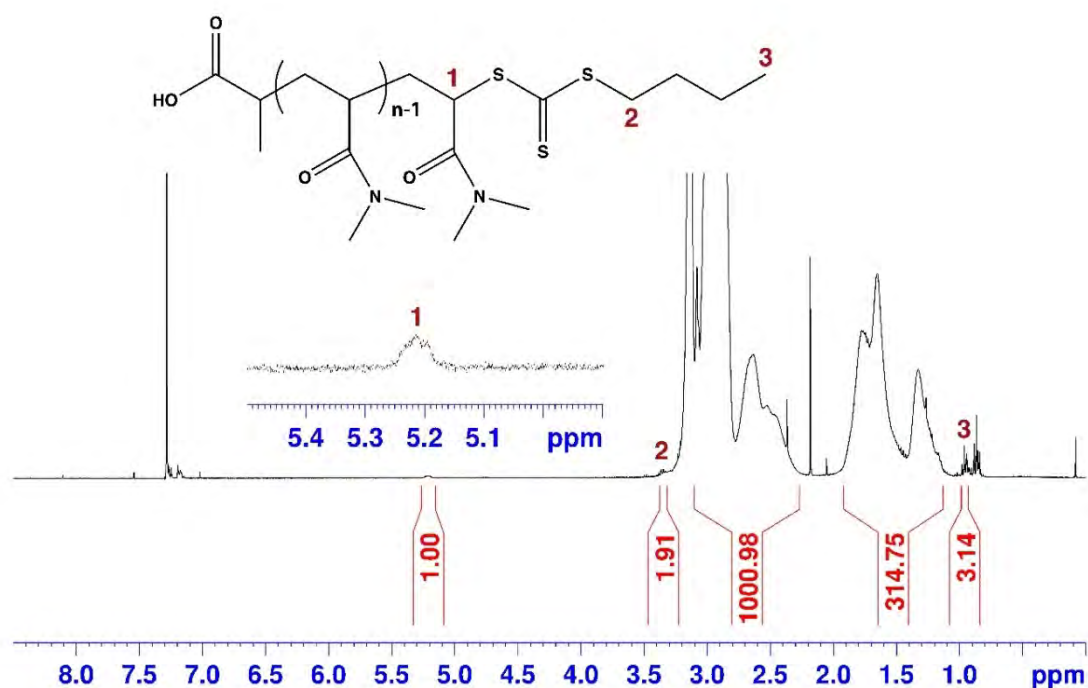


Figure 3.7 ^1H NMR spectrum (300 MHz, CDCl_3) of purified PDMA synthesised in the presence of 12.5 ppm Chl a (crude), red LED light and oxygen ($M_{n,\text{GPC}} = 14\,000$ g/mol, $M_{n,\text{th}} = 14\,700$ g/mol, monomer conversion = 72%), obtained from a different experiment from that in Table 3.1, #4 under identical conditions.

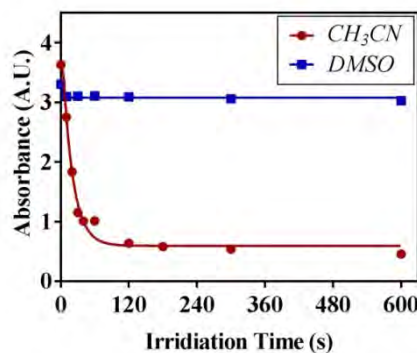


Figure 3.8 Evolution of the absorbance of dimethylantracene in the presence of Chl a overtime in CH_3CN (red line) and DMSO (blue line) under red light irradiation without degassing.

3.3.3 Post-decolourisation of Chl a after polymerisation

Interestingly, we observed that the polymerisation rate decreased during the polymerisation, especially in the non-degassed system, (non-linear plot in **Figure 3.1A** and **Figure 3.4A** and **Figure 3.4C**) using both pure and crude Chl a. Such behaviour is very unusual for a CLRP as it suggests that the concentration of propagating radical decreases during the polymerisation. This trend can be attributed to the photo-degradation of Chl a in the presence of air. In addition, visual inspection showed a change in colour before (green) and after polymerisation (brown). UV-Vis measurements (**Figure 3.9**) also displayed a significant decrease in the Chl a absorbance from 600-700 nm. In the literature, photo-degradation mechanism of Chl a (see **Scheme 3.1B** for chemical structure) has been reported in the presence of oxygen and light to produce a variety of non-photoactive and colourless compounds.^{35, 60} To investigate the photo-degradation of Chl a, pure Chl a in DMSO solutions were initially placed under light and air.³⁹ Upon 12 h irradiation, the blueish-green colour of Chl a completely vanished (**Figure 3.10A**). UV-Vis measurements on the colourless solution confirmed the absence of absorption peaks pertinent to Chl a (**Figure 3.10B**). Subsequently, DMA and RAFT agent (BTPA) were added to the degraded Chl a solution to investigate the photoactivity of the by-products.

The reaction mixtures were first degassed and then placed under red light irradiation. After 5 h of irradiation, negligible monomer conversion (3%) was detected by FTNIR measurement, confirming the absence of photoactive by-products.

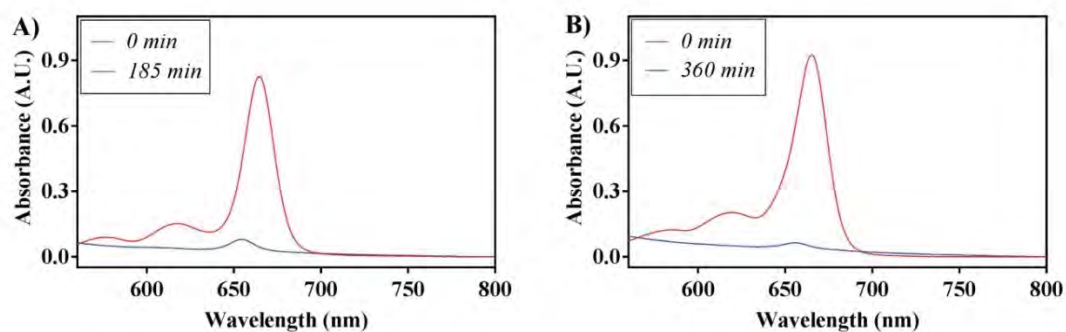


Figure 3.9 UV-Vis spectra before (red curve in A and B) and after (blue curve in A and B) PET-RAFT polymerisations in non-degassed systems (A) catalysed by pure Chl a and (B) catalysed by crude extract using a molar ratio of [DMA]:[BTPA]:[Chl a (pure or in the crude extract)] = 200:1:0.0025.

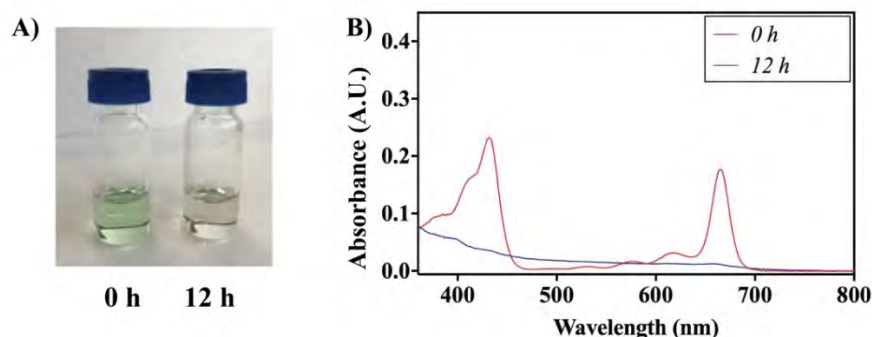


Figure 3.10 (A) Photograph and (B) UV-Vis spectra of pure Chl a solutions in DMSO before and after 12 h red light irradiation ([Chl a] = 4 ppm).

Following these initial observations, we envisaged that Chl a could be employed as a photo-degradable catalyst. While oxygen tolerance obviates the need for degassing procedures, the accompanying post-polymerisation degradation of Chl a into colourless, non-photoactive and non-toxic compounds removes the need of catalyst removal. Consequently, methyl acrylate (MA) was employed as a model monomer where polymerisation of MA was carried out with BTPA ([MA]:[BTPA] = 200:1) and 12.5 ppm of Chl a under red light irradiation in the non-degassed system. Irradiation for 1.5 h led

to monomer conversion of up to 50%. Visual inspection revealed a change in colour (from green to brown) in accord with our previous results with DMA (**Figure 3.11**). The residual monomer was then evaporated, and the open vial of brownish green polymer solution was placed back under the light source to enable catalyst degradation. After 10 h irradiation, the polymer solution turned yellow, which is the characteristic colour of BTPA (**Figure 3.12A**). More importantly, absorption peaks from Chl a were not detected by UV-Vis spectroscopy (**Figure 3.12A**), suggesting complete catalyst removal. The molecular weight distribution before and after catalyst degradation were identical (**Figure 3.12B**, $M_{n,GPC} = 11\,700$ g/mol, PDI = 1.09 and $M_{n,GPC} = 11\,900$ g/mol, PDI = 1.08, respectively), showing no degradation of polymer or side reactions during the removal process.

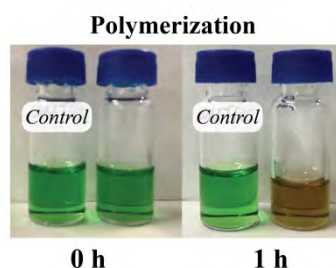


Figure 3.11 Photographs of MA polymerisation using pure Chl a under air with a molar ratio of [MA]:[BTPA]:[Chl a] = 200:1:0.0025 at the beginning and after polymerisation under red light irradiation and the corresponding UV-vis spectrum after polymerisation.

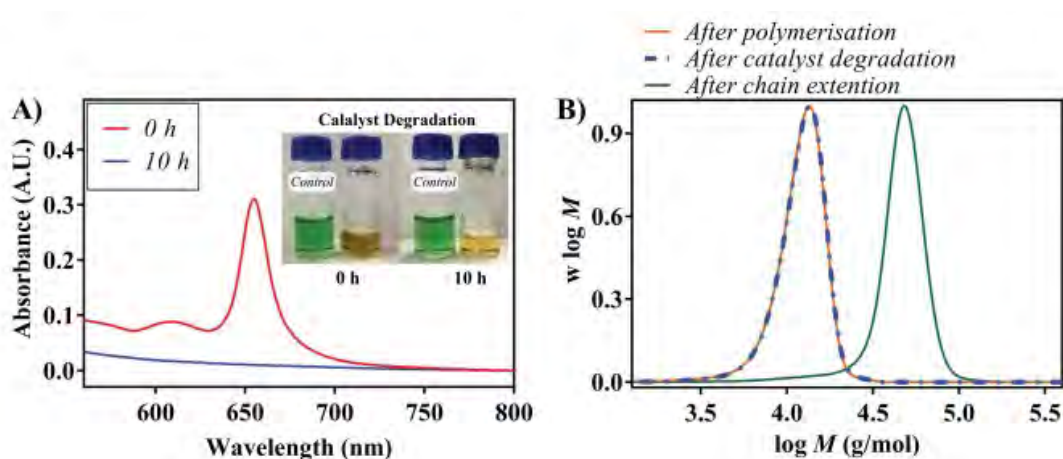


Figure 3.12 Chl a degradation and catalyst removal. (A) photographs of the polymer solution before and after 10 h of catalyst degradation under open air and red light irradiation and their corresponding UV-vis spectra; (B) GPC traces for PMA obtained

after polymerisation (red line) and catalyst degradation (blue dashed line) as well as the diblock copolymer synthesised by chain extension of PMA macroRAFT agent with pure Chl a as the photoredox catalyst in the absence of oxygen ([DMA]:[macroPMA]:[Chl a] = 1000:1:0.0025) (green line).

To investigate the livingness of the polymer after catalyst removal, chain extension of the synthesised PMA was performed. A molar ratio of 1000:1 of DMA to PMA chain transfer agent (macroRAFT agent) was used for chain extension with Chl a as the photoredox catalyst in degassed environment. Successful well-defined diblock copolymer was revealed by GPC ($M_{n, GPC} = 45\ 100$ g/mol, PDI = 1.07) with a monomer conversion around 40%. More importantly, the molecular weight distribution showed a complete shift to higher molecular weights, suggesting high end-group fidelity after catalyst removal (**Figure 3.12B**).

3.4 Conclusions

In this chapter, we demonstrated that both pure Chl a and crude extract can be employed as photocatalyst to catalyse a PET-RAFT polymerisation under red light. Furthermore, these polymerisations can be mediated in the presence of air (without degassing) to achieve a relatively high monomer conversion. In contrast to conventional photocatalysts, where the photocatalyst has to be removed at the end of the polymerisation to avoid possible side reactions, Chl a can be degraded under air into non-photoactive, colourless compounds at the end of the polymerisation. Finally, the direct use of spinach extracts further provided a facile method for polymer production without the need for Chl a purification, degassing or even catalyst removal at the end of the polymerisation.

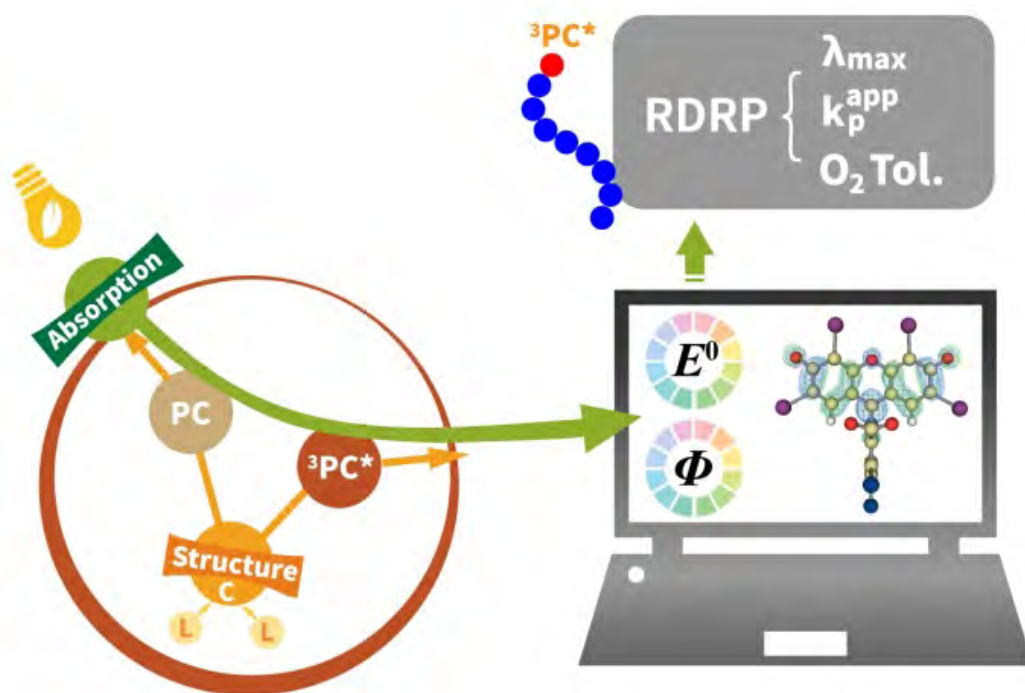
3.5 References

- (1) Schroder, K.; Matyjaszewski, K.; Noonan, K. J. T.; Mathers, R. T., *Green Chemistry* **2014**, *16*, 1673.
- (2) Anastas, P. T.; Warner, J. C., *Green chemistry: theory and practice*. Oxford university press: 2000.
- (3) Shanmugam, S.; Xu, J.; Boyer, C., *Chem Sci* **2015**, *6*, 1341.
- (4) Gajewska, B.; Raccio, S.; Rodriguez, K. J.; Bruns, N., *Polymer Chemistry* **2019**, *10*, 125.
- (5) Guo, J. T.; Yang, D. C.; Guan, Z.; He, Y. H., *Journal of Organic Chemistry* **2017**, *82*, 1888.
- (6) Pan, X.; Malhotra, N.; Simakova, A.; Wang, Z.; Konkolewicz, D.; Matyjaszewski, K., *Journal of the American Chemical Society* **2015**, *137*, 15430.

- (7) Treat, N. J.; Sprafke, H.; Kramer, J. W.; Clark, P. G.; Barton, B. E.; Read de Alaniz, J.; Fors, B. P.; Hawker, C. J., *Journal of the American Chemical Society* **2014**, *136*, 16096.
- (8) McKenzie, T. G.; Fu, Q.; Wong, E. H. H.; Dunstan, D. E.; Qiao, G. G., *Macromolecules* **2015**, *48*, 3864.
- (9) Shen, L. L.; Lu, Q. Z.; Zhu, A. Q.; Lv, X. Q.; An, Z. S., *ACS Macro Letters* **2017**, *6*, 625.
- (10) Tucker, B. S.; Coughlin, M. L.; Figg, C. A.; Sumerlin, B. S., *ACS Macro Letters* **2017**, *6*, 452.
- (11) Dadashi-Silab, S.; Doran, S.; Yagci, Y., *Chemical Reviews* **2016**, *116*, 10212.
- (12) Niu, J.; Lunn, D. J.; Pusuluri, A.; Yoo, J. I.; O'Malley, M. A.; Mitragotri, S.; Soh, H. T.; Hawker, C. J., *Nature Chemistry* **2017**, *9*, 537.
- (13) Anastasaki, A.; Nikolaou, V.; McCaul, N. W.; Simula, A.; Godfrey, J.; Waldron, C.; Wilson, P.; Kempe, K.; Haddleton, D. M., *Macromolecules* **2015**, *48*, 1404.
- (14) Wenn, B.; Martens, A. C.; Chuang, Y. M.; Gruber, J.; Junkers, T., *Polymer Chemistry* **2016**, *7*, 2720.
- (15) Kottisch, V.; Michaudel, Q.; Fors, B. P., *Journal of the American Chemical Society* **2017**, *139*, 10665.
- (16) Pearson, R. M.; Lim, C.-H.; McCarthy, B. G.; Musgrave, C. B.; Miyake, G. M., *Journal of the American Chemical Society* **2016**, *138*, 11399.
- (17) Frick, E.; Anastasaki, A.; Haddleton, D. M.; Barner-Kowollik, C., *Journal of the American Chemical Society* **2015**, *137*, 6889.
- (18) Xu, J.; Jung, K.; Atme, A.; Shanmugam, S.; Boyer, C., *Journal of the American Chemical Society* **2014**, *136*, 5508.
- (19) Xu, J. T.; Jung, K.; Corrigan, N. A.; Boyer, C., *Chemical Science* **2014**, *5*, 3568.
- (20) Shanmugam, S.; Xu, J.; Boyer, C., *Chemical Science* **2015**, *6*, 1341.
- (21) Shanmugam, S.; Xu, J.; Boyer, C., *Angewandte Chemie International Edition* **2016**, *55*, 1036.
- (22) Shanmugam, S.; Xu, J.; Boyer, C., *Journal of the American Chemical Society* **2015**, *137*, 9174.
- (23) Corrigan, N.; Rosli, D.; Jones, J. W. J.; Xu, J. T.; Boyer, C., *Macromolecules* **2016**, *49*, 6779.
- (24) Hashimoto, T.; Choe, Y. K.; Nakano, H.; Hirao, K., *Journal of Physical Chemistry A* **1999**, *103*, 1894.
- (25) Bowman, M. K., *Chemical Physics Letters* **1977**, *48*, 17.
- (26) Krieger-Liszkay, A., *J Exp Bot* **2005**, *56*, 337.
- (27) Hortensteiner, S.; Krautler, B., *Biochim Biophys Acta* **2011**, *1807*, 977.
- (28) Matile, P.; Hortensteiner, S.; Thomas, H., *Annu Rev Plant Physiol Plant Mol Biol* **1999**, *50*, 67.
- (29) Hortensteiner, S., *Annu Rev Plant Biol* **2006**, *57*, 55.
- (30) Christ, B.; Hörtensteiner, S., *Journal of Plant Growth Regulation* **2013**, *33*, 4.
- (31) Zvezdanović, J.; Cvetić, T.; Veljović-Jovanović, S.; Marković, D., *Radiation Physics and Chemistry* **2009**, *78*, 25.
- (32) Lee, E.; Ahn, H.; Choe, E., *Food Science and Biotechnology* **2014**, *23*, 1061.
- (33) Zolla, L.; Rinalducci, S., *Biochemistry* **2002**, *41*, 14391.
- (34) Jen, J. J.; Mackinney, G., *Photochemistry and Photobiology* **1970**, *11*, 303.
- (35) Llewellyn, C. A.; Mantoura, R. F. C.; Brereton, R. G., *Photochemistry and Photobiology* **1990**, *52*, 1043.
- (36) Hörtensteiner, S., *Annu. Rev. Plant Biol.* **2006**, *57*, 55.
- (37) Jubert, C.; Bailey, G., *J Chromatogr A* **2007**, *1140*, 95.

- (38) Wellburn, A. R., *Journal of Plant Physiology* **1994**, *144*, 307.
- (39) Shanmugam, S.; Xu, J.; Boyer, C., *Journal of the American Chemical Society* **2015**, *137*, 9174.
- (40) Johnston, A.; Scaggs, J.; Mallory, C.; Haskett, A.; Warner, D.; Brown, E.; Hammond, K.; McCormick, M. M.; McDougal, O. M., *Journal of Chemical Education* **2013**, *90*, 796.
- (41) Quach, H. T.; Steeper, R. L.; Griffin, G. W., *Journal of Chemical Education* **2004**, *81*, 385.
- (42) Khoo, H. E.; Prasad, K. N.; Kong, K. W.; Jiang, Y. M.; Ismail, A., *Molecules* **2011**, *16*, 1710.
- (43) Mortensen, A.; Skibsted, L. H.; Sampson, J.; Rice-Evans, C.; Everett, S. A., *FEBS Lett* **1997**, *418*, 91.
- (44) Hernandez-Marin, E.; Galano, A.; Martinez, A., *Journal of Physical Chemistry B* **2013**, *117*, 4050.
- (45) Miller, N. J.; Sampson, J.; Candeias, L. P.; Bramley, P. M.; Rice-Evans, C. A., *FEBS Lett* **1996**, *384*, 240.
- (46) Bhanu, V. A.; Kishore, K., *Chemical Reviews* **1991**, *91*, 99.
- (47) Anastasaki, A.; Nikolaou, V.; Haddleton, D. M., *Polymer Chemistry* **2016**, *7*, 1002.
- (48) Balta, D. K.; Arsu, N.; Yagci, Y.; Jockusch, S.; Turro, N. J., *Macromolecules* **2007**, *40*, 4138.
- (49) Fleischmann, S.; Rosen, B. M.; Percec, V., *Journal of Polymer Science Part a-Polymer Chemistry* **2010**, *48*, 1190.
- (50) Gody, G.; Barbey, R.; Danial, M.; Perrier, S., *Polymer Chemistry* **2015**, *6*, 1502.
- (51) Matyjaszewski, K.; Coca, S.; Gaynor, S. G.; Wei, M. L.; Woodworth, B. E., *Macromolecules* **1998**, *31*, 5967.
- (52) Min, K.; Jakubowski, W.; Matyjaszewski, K., *Macromolecular Rapid Communications* **2006**, *27*, 594.
- (53) Niu, J.; Page, Z. A.; Dolinski, N. D.; Anastasaki, A.; Hsueh, A. T.; Soh, H. T.; Hawker, C. J., *ACS Macro Letters* **2017**, 1109.
- (54) Mosnáček, J.; Ilčíková, M., *Macromolecules* **2012**, *45*, 5859.
- (55) Carmean, R. N.; Becker, T. E.; Sims, M. B.; Sumerlin, B. S., *Chem* **2017**, *2*, 93.
- (56) Lv, Y.; Liu, Z.; Zhu, A.; An, Z., *Journal of Polymer Science Part A: Polymer Chemistry* **2017**, *55*, 164.
- (57) Fu, Q.; Xie, K.; McKenzie, T. G.; Qiao, G. G., *Polymer Chemistry* **2017**, *8*, 1519.
- (58) Chapman, R.; Gormley, A. J.; Stenzel, M. H.; Stevens, M. M., *Angewandte Chemie International Edition* **2016**, *55*, 4500.
- (59) Yeow, J.; Chapman, R.; Xu, J.; Boyer, C., *Polym. Chem.* **2017**, *8*, 5012.
- (60) Zolla, L.; Rinalducci, S., *Biochemistry* **2002**, *41*, 14391.

Chapter 4 Guiding the Design of Organic Photocatalyst for PET-RAFT Polymerisation: Halogenated Xanthene Dyes



By examining structurally similar halogenated xanthene dyes, this chapter establishes a guiding principle for resolving structure-property-performance relationships in the photo-controlled PET-RAFT polymerisation system (PET-RAFT: photoinduced electron/energy transfer – reversible addition fragmentation chain transfer). We investigated the effect of the halogen substituents on the photophysical and electrochemical properties of the xanthene dyes acting as photocatalysts, and their resultant effect on the performance of PET-RAFT polymerisation. Consideration of the structure-property-performance relationships allowed design of a new xanthene photocatalyst, where its photocatalytic activity (oxygen tolerance and polymerisation rate) was successfully optimized for PET-RAFT polymerisation. We expect that this study will serve as a theoretical framework in broadly guiding the design of high performance photocatalysts for organic photocatalysis.

4.1 Introduction

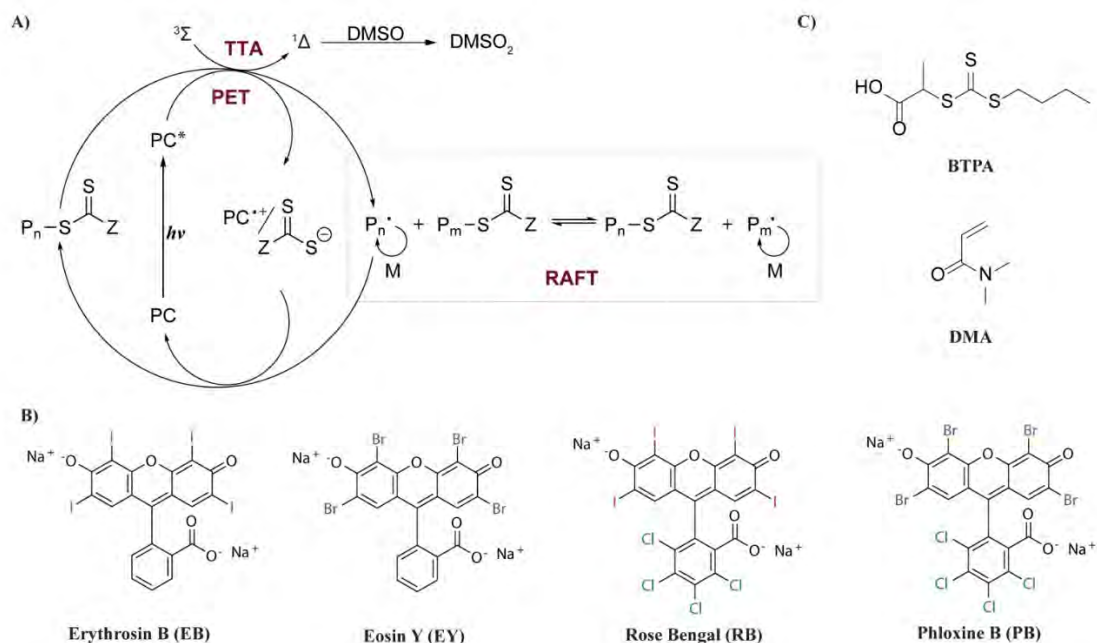
In 1912, Ciamician proposed that the use of visible light could provide a more sustainable approach for chemical production.¹ Ciamician used plants as an example to illustrate the potential of visible light in mediating complex chemical reactions. Indeed, plants and cyanobacteria have exploited the photosynthesis process to sustain life on earth for the last 3.4 billion years. Throughout this time, plants have evolved to derive a variety of chlorophyll and bacteriochlorophyll compounds capable of harvesting a broad spectrum of visible light under different conditions; this natural catalyst selection has allowed these organisms to thrive on the Earth's surface and in oceans. Although visible light was proposed to mediate chemical reactions as early as 1912, it has only become broadly exploited to drive chemical transformations since the turn of this century.²⁻⁵

A variety of photocatalysts (PCs) have been discovered and explored since, and in parallel, PCs have been implemented in controlled/living polymerisation, which has opened up a new avenue for polymer production and provided temporal/spatial control over polymerisation processes.⁶⁻⁷ Exemplary visible-light-catalysed reversible deactivation radical polymerisation (photo-RDRP) systems include photo-atom transfer radical polymerisation (photo-ATRP)⁸⁻¹² and photoinduced electron/energy transfer-reversible addition-fragmentation chain transfer (PET-RAFT) polymerisation.¹³⁻¹⁷ In these systems, PCs play a central role in converting visible light energy through photoinduced electron/energy transfer (PET) processes to activate/deactivate polymerisation and manipulate polymerisation kinetics. In early works, metal-based PCs (e.g. iridium,^{8, 13} ruthenium,¹⁸ copper,^{12, 19-22} iron,¹¹ and zinc¹⁴ based PCs) were recognized in organic synthesis and were thus adopted for photo-RDRP. However, the presence of metal-based PCs usually leads to metal contamination in polymer products, potentially limiting applications. In response, organic analogues were developed, which has paved the way for metal-free photo-RDRP.²³⁻³⁰

Numerous organic PCs have been identified for application in both organic synthetic transformations and photo-RDRP.³¹ In metal-free photo-RDRP, a library of phenothiazine,²³⁻²⁴ dihydrophenazine, phenoxazine,²⁹ polycyclic aromatics,³²⁻³³ eosin Y (EY),²⁵ and others, have been identified as efficient PCs. In order to guide the rational design and optimization of organic PCs that satisfy the specific needs of photo-RDRP and organic synthesis, researchers recently started to explore the relationships between PC

structure and the performance of photocatalysed systems. For example, structure-property relationships have been established for organic PCs that affect excited state redox potentials,²⁷ charge transfer characters,^{27, 34-35} and triplet quantum yields³⁶ based on dihydrophenazine and phenoxazine derivatives in organocatalysed photo-ATRP (O-ATRP). Very recently, Kim, Gierschner, and Kwon also generated a library of donor-acceptor PCs and used a computer-aided strategy to elucidate the PC property-performance relationship in O-ATRP.³⁷ Meanwhile, the structure-property relationships of donor-acceptor PCs were recently investigated to perform organic transformations;³⁸⁻³⁹ for instance, Nicewicz's group gained insight into a range of core-modified acridinium-⁴⁰⁻⁵² and pyrylium-based⁵³⁻⁵⁴ PCs for a series of photocatalysed organic reactions.

Herein, we systematically establish structure-property-performance relationships among xanthene-based PCs mediating PET-RAFT polymerisation (**Scheme 4.1A**). In this regard, we chose to examine a series of halogenated xanthene dyes, including EY, erythrosin B (EB), phloxine B (PB), and rose Bengal (RB, **Scheme 4.1B**). Notably, this class of halogenated xanthene derivatives has found vast applications in food industry as colourant,⁵⁵⁻⁵⁷ in bio-staining,⁵⁸⁻⁶⁰ and in photo-dynamic therapy.⁶⁰ By investigating the photophysical and electrochemical properties of EB, EY, RB, and PB, and subsequently correlating these properties to measured apparent propagation rate (k_p^{app}) and other performance parameters during PET-RAFT polymerisation under identical conditions, the structure-property-performance relationships were elucidated.⁶¹⁻⁶³ Based on the established principles, a new halogenated xanthene dye was designed and synthesised for oxygen-tolerant PET-RAFT polymerisation.



Scheme 4.1 (A) Proposed mechanism of oxygen-tolerant PET-RAFT polymerisation. TTA: triplet-triplet annihilation for oxygen elimination; $^3\Sigma$: molecular oxygen; $^1\Delta$: singlet oxygen; (B) Chemical structures of commercial halogenated xanthene dyes; and (C) the model RAFT agent and monomer for investigation of PC structure-property-performance relationships in this work.

4.2 Experimental section

4.2.1 General procedures for kinetic study of PET-RAFT polymerisation in the presence/absence of oxygen

DMSO (551 μL), DMA (0.577 g, 5.83 mmol), BTPA (6.9 mg, 29.1 μmol) and EB (249 μL of 1 mg/mL EB stock solution in DMSO, 0.117 μmol) were mixed in a glass vial as stock solution. The stock solution was divided in halves and either half (0.6 mL) was transferred into a 0.9 mL FTNIR glass cuvette (1 cm \times 2 mm) sealed with rubber septa and covered with aluminium foil. One of the sealed cuvettes was degassed with nitrogen for 20 min while the other left as prepared (non-degassed). The glass cuvettes were then sent for irradiation at 2 mW/cm² of 530 nm for green light or 560 nm for yellow light under an Oriel VeraSol LED solar simulator at room temperature (25 $^{\circ}\text{C}$). The cuvettes were transferred in sequence to a sample holder manually for FTNIR measurements at specific time points and returned thereafter. Monomer conversions were calculated by taking the ratio of integrations of the wavenumber area 6210-6115 cm⁻¹ for all curves at

different reaction times to that of time zero. Aliquots were taken at designated time points for GPC analysis to determine number average molecular weights (M_n) and polydispersities (M_w/M_n). Other dye-catalysed polymerisations were performed in the same ratios of reagents and the same procedures.

To confirm the equivalence of 2 mW/cm² 530 nm and 2 mW/cm² 560 nm irradiation, we tested the EB-catalysed PET-RAFT polymerisation as EB is spectrally similar under 530 nm and 560 nm in terms of spectral overlap (*vide infra*).

4.3 Results and discussion

4.3.1 Kinetics and oxygen tolerance studies

Table 4.1 and **Figure 4.1** show the photophysical properties of four xanthene dyes selected for this study. The respective λ_{\max} and ε_{\max} values of the xanthene dyes are EB (548 nm, 95000 M⁻¹cm⁻¹), EY (540 nm, 87800 M⁻¹cm⁻¹), RB (563 nm, 97300 M⁻¹cm⁻¹), and PB (555 nm, 93800 M⁻¹cm⁻¹) with all differences < 8%; λ_{\max} : maximum wavelength of absorption and ε_{\max} : molar absorptivity at λ_{\max} . As λ_{\max} of EB, PB, and RB are close to the yellow LED light emission (nominal wavelength: 560 nm), while that of EY is close to the green LED light emission (nominal wavelength: 530 nm), we selected the respective LED light sources corresponding to their maximum absorptions. A light intensity of 2 mW/cm² was employed for both yellow and green lights. The photon flux for 2 mW/cm² green (530 nm, photon flux of 5.34×10¹⁵ s⁻¹cm⁻²) and 2 mW/cm² yellow (560 nm, photon flux of 5.64×10¹⁵ s⁻¹cm⁻²) light irradiation are almost indistinguishable (difference < 6%), and the effect of different wavelengths in this process can therefore be considered negligible. To demonstrate this, a control experiment was performed to compare polymerisation mediated by EB under 2 mW/cm² 530 nm and 2 mW/cm² 560 nm irradiation (experimental details indicated *vide infra*). Indeed, as shown in the SI, **Figure 4.2**, the difference in polymerisation rate is minimal (< 5%).

Table 4.1 Photophysical properties of halogenated xanthene dyes.

Φ_F	$\Phi_T^{55, 64-68}$	$k_r^{69}(10^8 s^{-1})$	$k_{nr}^{69}(10^8 s^{-1})$	$\tau_T^\ddagger (ms)$	λ_{\max}^\ddagger	$\varepsilon_{\max}^\ddagger$
		¹⁾	¹⁾		(nm)	(M ⁻¹ cm ⁻¹)

EB	0.08 ⁶⁹	0.62-0.69	1.60	18.4	0.35- 0.65 ⁷⁰	548	95000
EY	0.60 ⁶⁹	0.28-0.32	1.83	1.22	0.6-4.0 ⁷⁰⁻ 71	540	87800
RB	0.08 ⁶⁹	0.76-0.86	1.22	14.0	0.26- 1.91 ⁷²	563	97300
PB	0.24 ⁷³	0.4	N/A [§]	N/A [§]	0.12- 1.75 ⁷³	555	93800

Note: $\dagger\tau_T$ usually has a wide variability depending on conditions; although their value are in the sub ms range, this is sufficient for PET processes to proceed.³¹ \ddagger Determined in model DMSO solution of a typical PET-RAFT system (*vide infra*). \S Not available. k_r : radiative decay constant; k_{nr} : non-radiative decay constant; Φ_F : fluorescence quantum yield; Φ_T : triplet quantum yield.

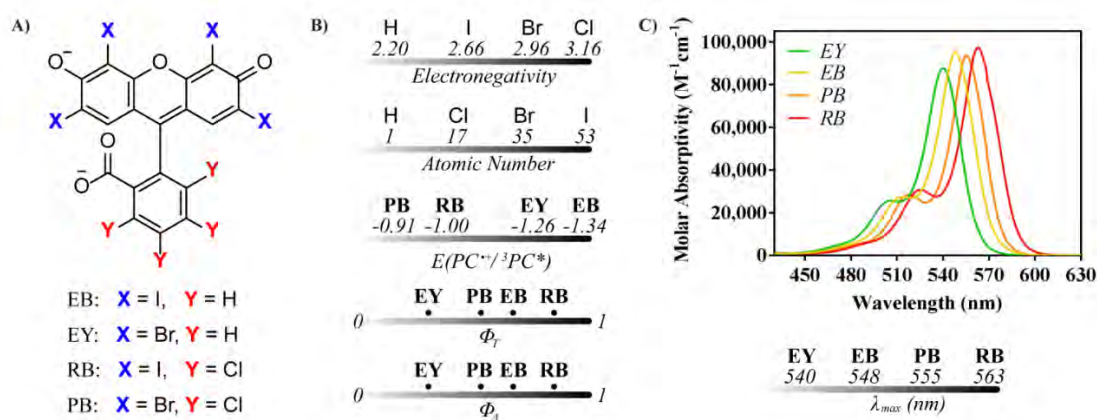


Figure 4.1 (A) Structural variation of halogenated xanthene dyes investigated in this work; (B) properties of PCs and halogen substituents; (C) UV-vis spectra of dyes determined in model DMSO solution of a typical PET-RAFT system (top) and the corresponding λ_{max} (bottom).

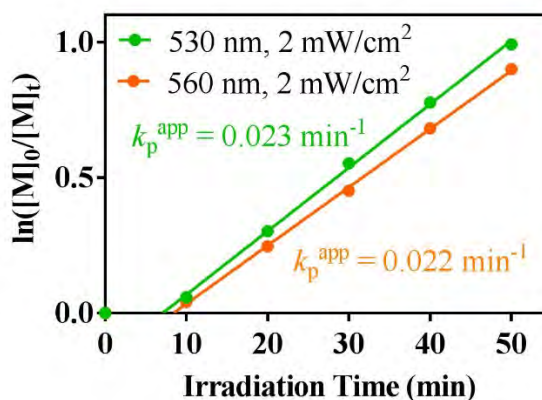


Figure 4.2 $\ln([M]_0/[M]_t)$ versus irradiation time under 2 mW/cm² 530 nm and 2 mW/cm² 560 nm in an EB-catalysed PET-RAFT polymerisation.

We monitored the kinetics of PET-RAFT polymerisation (k_p^{app} , apparent rate constant) in the presence of EB, EY, RB and PB as PCs, using online Fourier transform near-infrared (FTNIR) spectroscopy. *N,N'*-dimethylacrylamide (DMA) and 2-(*n*-butyltrithiocarbonate) propionic acid (BTPA) were selected as the model monomer and RAFT agent (see **Scheme 4.1C**) at a fixed molar ratio of [DMA]:[BTPA]:[PC] = 200:1:0.004, corresponding to a PC concentration of 20 ppm relative to monomer. As expected, we observed that k_p^{app} appeared to be dependent on the PCs employed for polymerisation, where the EB-catalysed system exhibited the highest k_p^{app} (0.023 min⁻¹), followed by EY (0.014 min⁻¹), RB (0.010 min⁻¹), and finally PB (0.007 min⁻¹) (**Figure 4.3A-D**). Linear plots of number-average molecular weights (M_n) versus monomer conversions, and good agreements between theoretical and experimental molecular weights confirmed a controlled polymerisation character (**Figure 4.3E-H**). Furthermore, symmetric and narrow molecular weight distributions ($M_w/M_n < 1.1$) were observed by gel permeation chromatography (GPC, **Figure 4.3I-L**). Finally, for all the four dyes, the polymerisation immediately ceased after switching off the light, which demonstrated good temporal control.

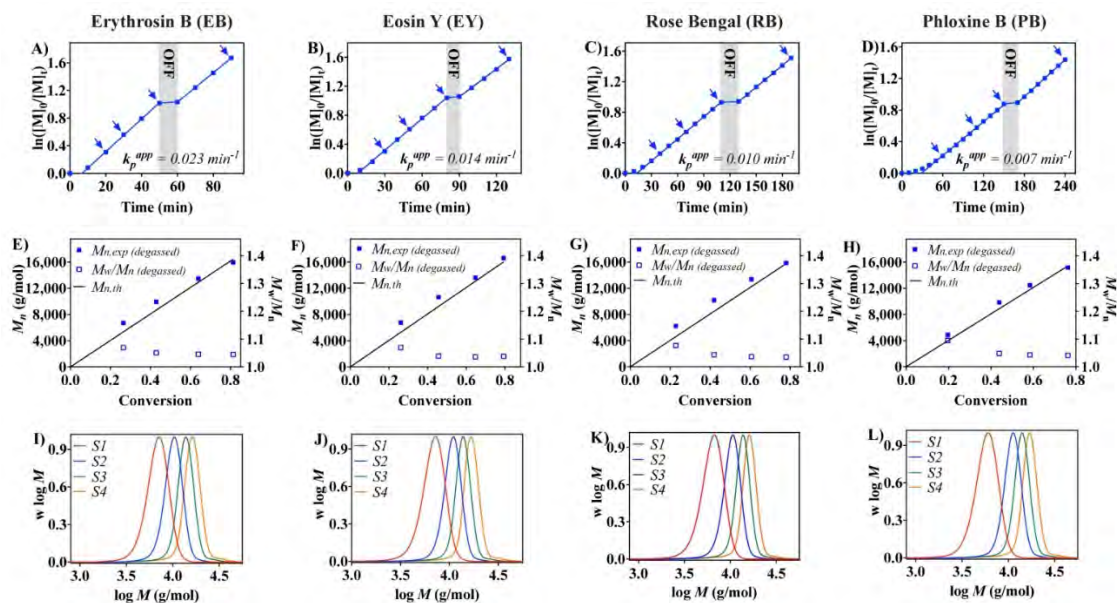


Figure 4.3 Kinetics studies of degassed PET-RAFT polymerisations of DMA catalysed by (A, E and I) EB, (B, F and J) EY, (C, G and K) RB and (D, H and L) PB. (A-D) plot of $\ln([M]_0/[M]_t)$ versus time to reveal k_p^{app} and temporal control; (E-F) M_n and M_w/M_n versus monomer conversion; (I-L) molecular weight distributions of four GPC aliquots taken during polymerisation, denoted as S1, S2, S3, S4, which corresponds to blue arrows in (A-D) following the time order.

As oxygen can rapidly trap and terminate propagating radicals via peroxide formation, most RDRP techniques require deoxygenation prior to polymerisation. In our previous reports, we have demonstrated that PET-RAFT polymerisation could be carried out in the presence of air with some specific PCs. The oxygen tolerance mechanism is based on the elimination of oxygen via the generation of singlet oxygen ($^1\text{O}_2$) in the presence of excited PCs such as zinc tetraphenylporphyrin⁶² (ZnTPP) and chlorophyll a⁶³ (Chl a). Singlet oxygen can be consumed by a variety of reactants, including the solvent DMSO to form dimethyl sulfone, or organic compounds such as anthracene derivatives (**Scheme 4.1A**).⁷⁴ Inspired by some early works in photodynamic therapy using halogenated xanthene dyes,⁷⁵ we decided to test the oxygen tolerance of PET-RAFT polymerisation in the presence of these four xanthene PCs (**Figure 4.4**). Due to the RAFT pre-equilibrium, there is usually a brief induction period at the beginning of PET-RAFT polymerisation (seen in **Figure 4.3A-D**). Meanwhile, PET-RAFT polymerisations in the presence of oxygen (non-degassed) exhibit a longer inhibition period (**Figure 4.3A-D**). Therefore, the delay of non-degassed polymerisation compared to its degassed counterpart, (namely

the oxygen inhibition period) gives an estimation of oxygen tolerance of our systems. Despite different oxygen inhibition periods, each dye-catalysed non-degassed polymerisation exhibited a similar k_p^{app} to its corresponding degassed polymerisation (**Figure 4.4A-D**). Furthermore, good agreement between the experimental and theoretical molecular weights (**Figure 4.4E-H**) as well as low dispersities ($M_w/M_n < 1.1$) confirmed a controlled polymerisation behaviour (**Figure 4.4I-L**).

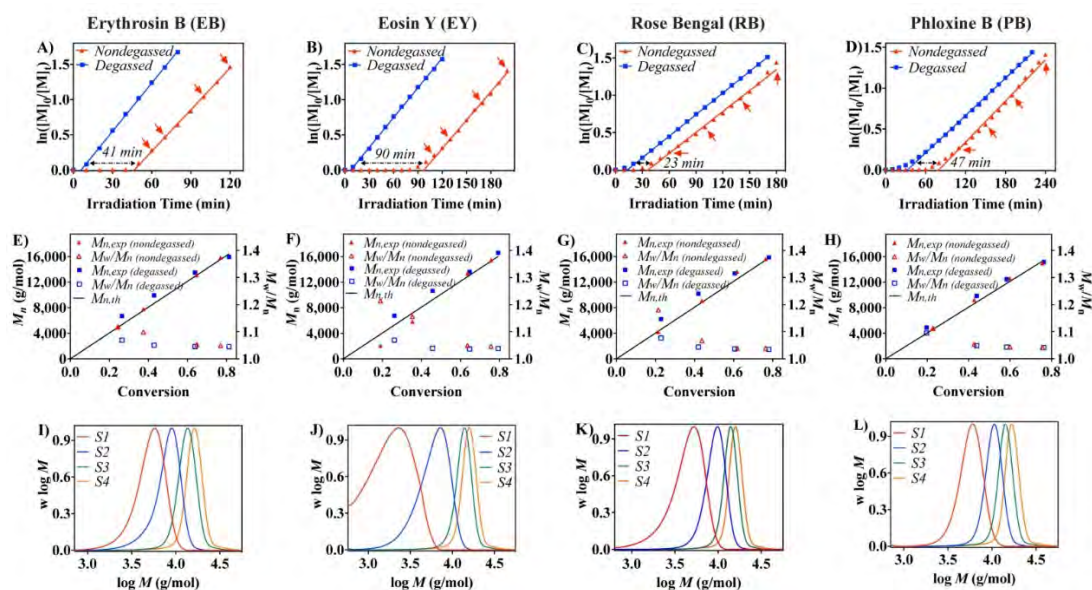


Figure 4.4 Oxygen tolerance studies of PET-RAFT polymerisations of DMA catalysed by (A, E and I) EB, (B, F and J) EY, (C, G and K) RB and (D, H and L) PB. (A-D) Evolution of $\ln([M]_0/[M]_t)$ versus time; (E-F) Evolution of M_n and M_w/M_n versus monomer conversion; (I-L) molecular weight distributions taken during polymerisation, denoted as S1, S2, S3, S4, which correspond to red arrows in (A-D) following the time order.

The high end-group fidelities of polymers prepared via xanthene-dye-catalysed PET-RAFT polymerisations were confirmed by matrix-assisted laser desorption ionization time-of-flight mass spectrometry (MALDI-TOF MS, SI, **Figure 4.5-4.11**). Polymers synthesised via EB-catalysed PET-RAFT polymerisation with and without deoxygenation for end group check by matrix-assisted laser desorption ionization time-of-flight mass spectrometry (MALDI-TOF MS) were obtained following the same polymerisation formulations and procedures in kinetics studies. The polymerisation was stopped at around 10% monomer conversion (degree of polymerisation DP 20) to match the suitable molecular weight range for poly-DMA (PDMA) MALDI-TOF MS analysis.

As shown in **Figure 4.5A**, MALDI-TOF MS reveals evenly distributed mass peaks (separated by 99 m/z) and highly symmetric mass distribution. Magnified into the detailed structure of each mass peak set (from 2200 to 2400 m/z, **Figure 4.5A**, inset), we were able to distinguish two repetitive signals: the main peaks corresponds to PDMA with BTPA chain-end plus Na⁺ and the secondary peaks to PDMA with BTPA chain-end plus K⁺ in excellent agreement with theoretical values within instrumental error (< 1 m/z), showing no evidence for end-group loss. Meanwhile, the polymers synthesised without deoxygenation exhibits similar results with the polymers prepared after deoxygenation (**Figure 4.5B**). Other cases including degassed and non-degassed PET-RAFT polymerisation catalysed by EY, RB and PB were also confirmed by MALDI-TOF MS for high end-group fidelity of the same level (**Figure 4.6-4.11**).

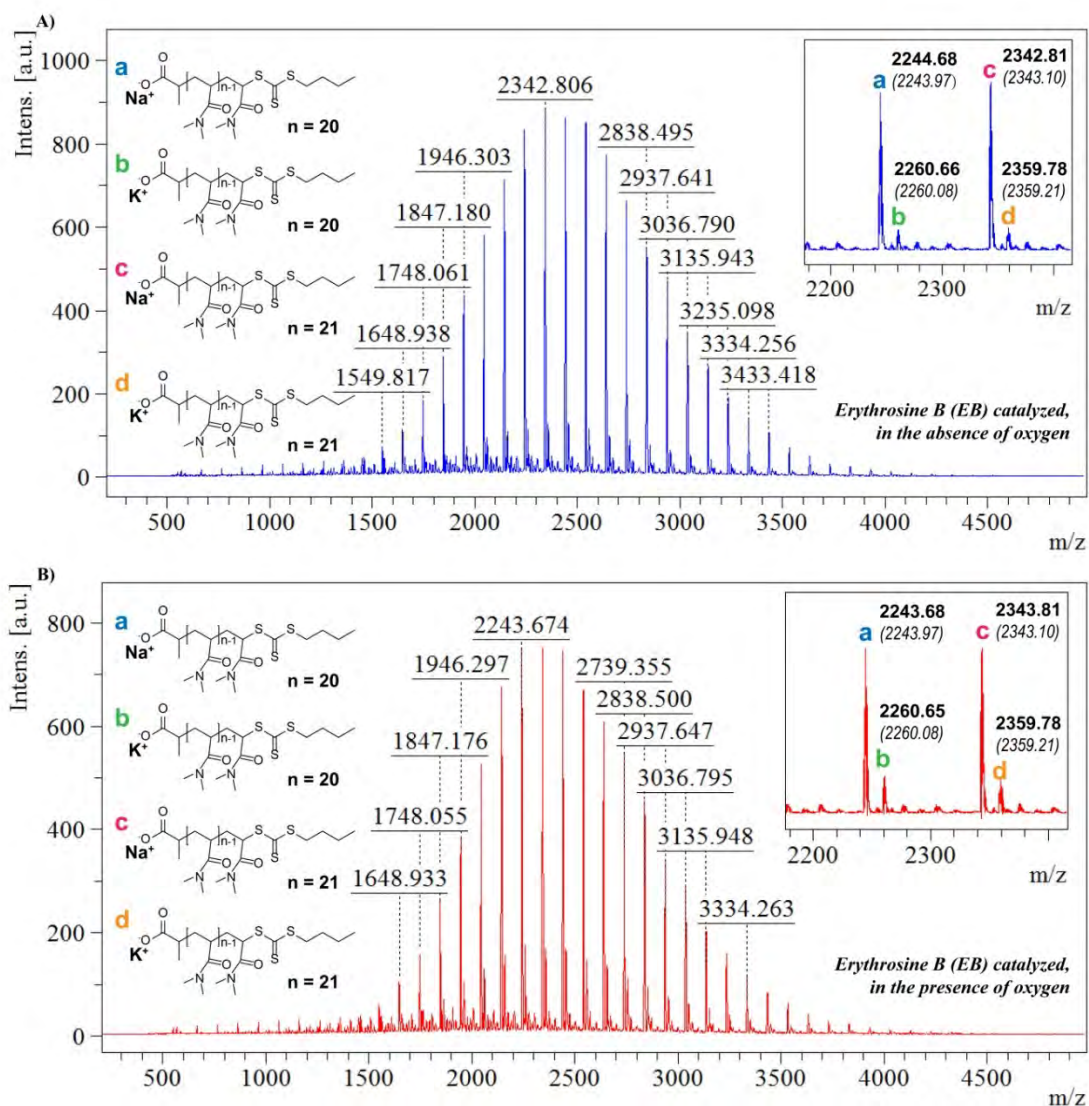


Figure 4.5 MALDI-TOF MS of a PDMA sample synthesised by PET-RAFT polymerisation (A) in the absence of oxygen (degassed polymerisation) and (B) in the presence of oxygen (non-degassed polymerisation) with EB as PC. By zooming into the molecular weights range of 2200-2400 g/mol, we observed that major peaks (a and c) excellently agree with the theoretical values of PDMA with BTPA chain-end group plus Na^+ whereas minor peaks (b and d) can be assigned to PDMA with BTPA chain-end group plus K^+ , all within experimental error ($< 1 \text{ m/z}$). For peaks a and b, number of monomer insertion (n) is determined to be 20, whereas for peaks c and d, it is determined to be 21.

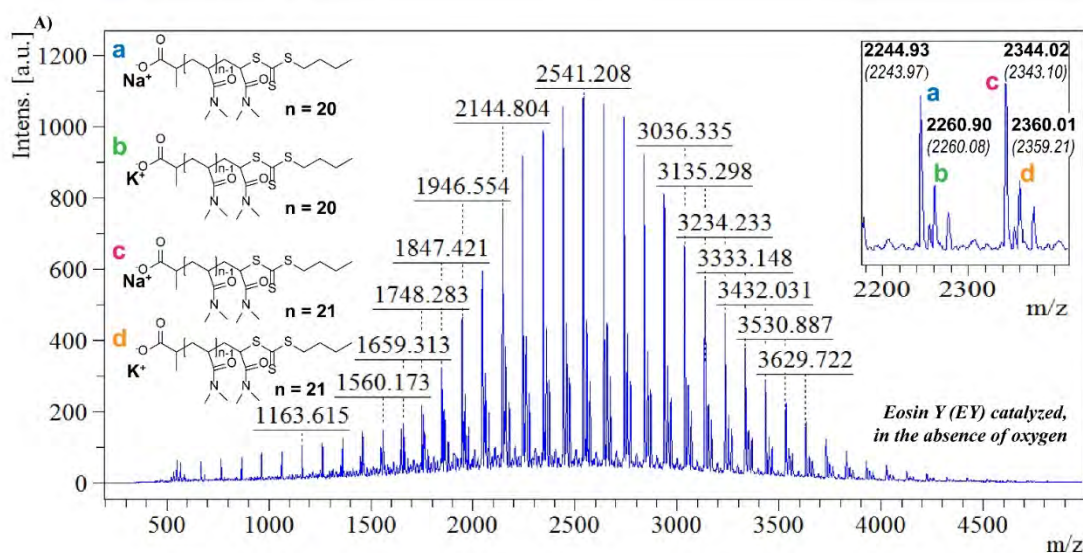


Figure 4.6 MALDI-TOF MS of a PDMA sample synthesised by PET-RAFT polymerisation in the absence of oxygen (degassed polymerisation) with EY as catalyst. By zooming into the molecular weight range of 2200-2400 g/mol, we observed that major peaks (a and c) excellently matches theoretical prediction of PDMA with BTPA chain-end group plus Na^+ while minor peaks can be assigned to PDMA with BTPA chain-end group plus K^+ , all within experimental error ($< 1 \text{ g/mol}$). For peaks a and c, number of monomer insertion (n) is determined to be 20, whereas for peaks c and d, it is determined to be 21. $M_{n,\text{GPC}} = 2,300 \text{ g/mol}$; $\text{PDI} = 1.11$.

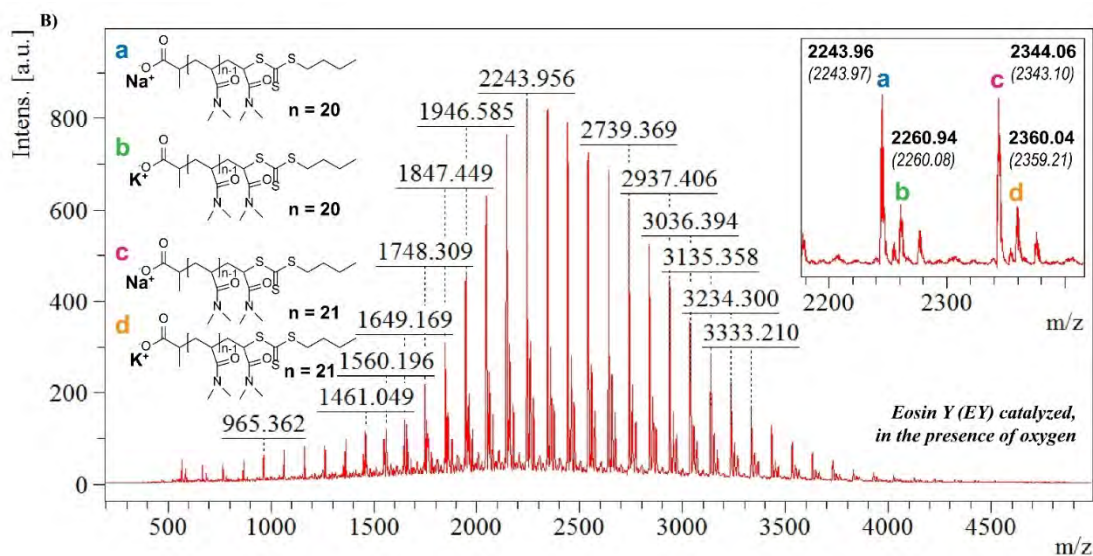


Figure 4.7 MALDI-TOF MS of a PDMA sample synthesised by PET-RAFT polymerisation in the presence of oxygen (non-degassed polymerisation) with EY as catalyst. By zooming into the molecular weight range of 2200-2400 g/mol, we observed that major peaks (a and c) excellently matches theoretical predication of PDMA with BTPA chain-end group plus Na^+ while minor peaks can be assigned to PDMA with BTPA chain-end group plus K^+ , all within experimental error (< 1 g/mol). For peaks a and c, number of monomer insertion (n) is determined to be 20, whereas for peaks c and d, it is determined to be 21. $M_{n,\text{GPC}} = 2,300$ g/mol; PDI = 1.11.

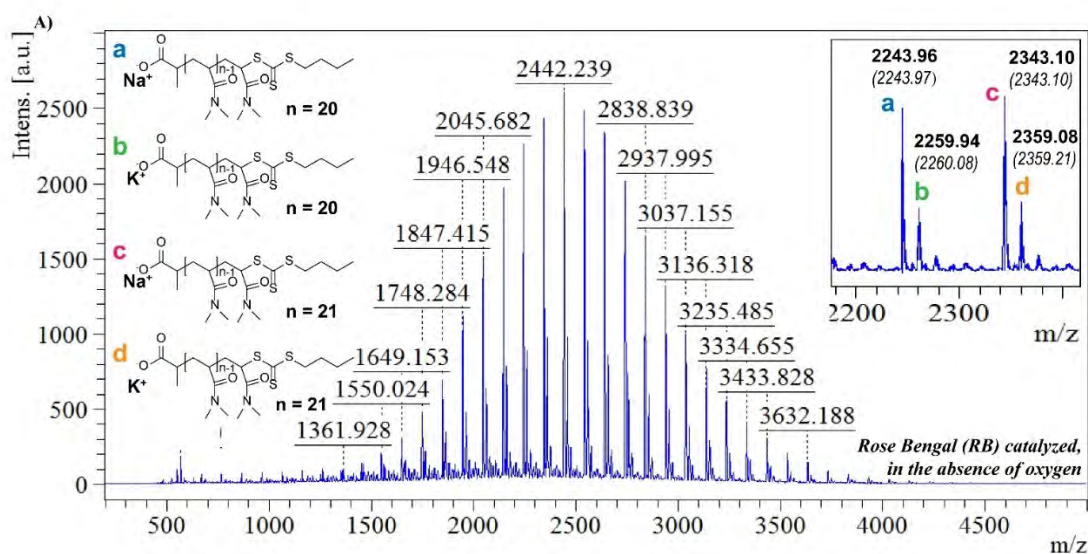


Figure 4.8 MALDI-TOF MS of a PDMA sample synthesised by PET-RAFT polymerisation in the absence of oxygen (degassed polymerisation) with RB as catalyst. By zooming into the molecular weight range of 2200-2400 g/mol, we observed that major peaks (a and c) excellently matches theoretical predication of PDMA with BTPA chain-end group plus Na^+ while minor peaks can be assigned to PDMA with BTPA chain-end group plus K^+ , all within experimental error (< 1 g/mol). For peaks a and c, number of monomer insertion (n) is determined to be 20, whereas for peaks c and d, it is determined to be 21. $M_{n,\text{GPC}} = 2,400$ g/mol; PDI = 1.11.

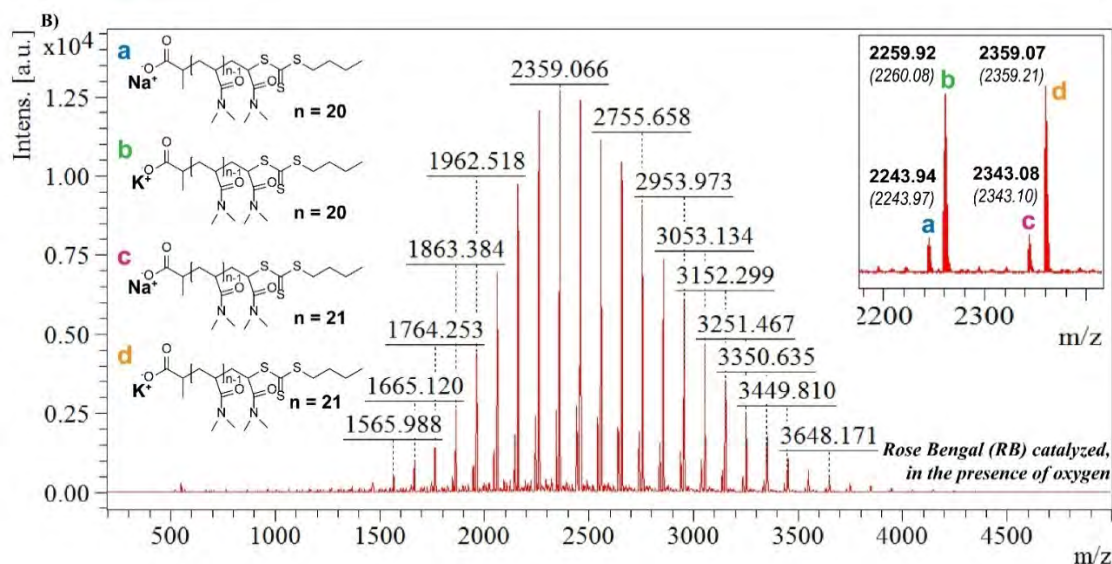


Figure 4.9 MALDI-TOF MS of a PDMA sample synthesised by PET-RAFT polymerisation in the presence of oxygen (non-degassed polymerisation) with RB as catalyst. By zooming into the molecular weight range of 2200-2400 g/mol, we observed that major peaks (a and c) excellently matches theoretical predication of PDMA with BTPA chain-end group plus Na^+ while minor peaks can be assigned to PDMA with BTPA chain-end group plus K^+ , all within experimental error (< 1 g/mol). For peaks a and c, number of monomer insertion (n) is determined to be 20, whereas for peaks c and d, it is determined to be 21. $M_{n,\text{GPC}} = 2,500$ g/mol; PDI = 1.11.

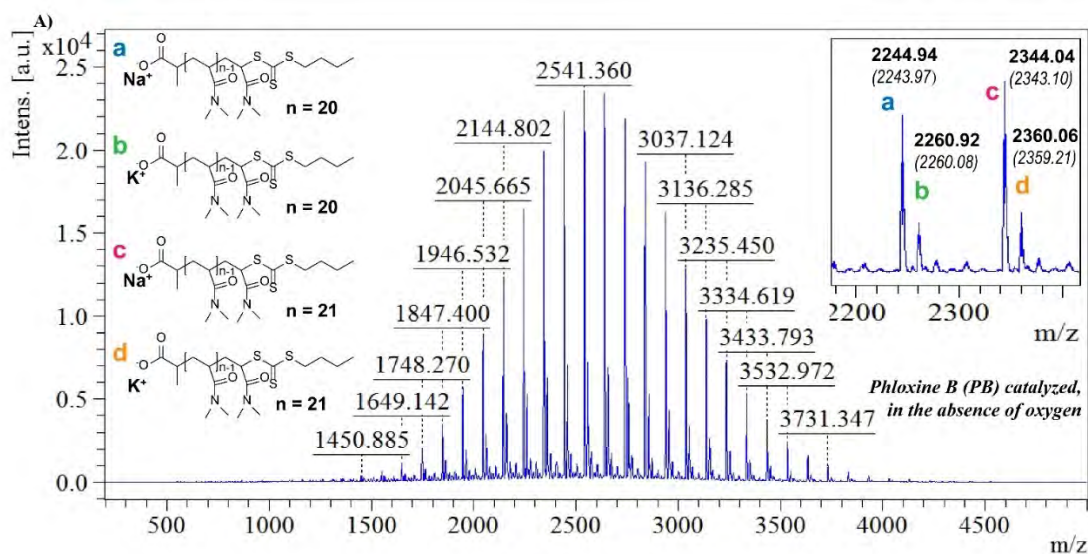


Figure 4.10 MALDI-TOF MS of a PDMA sample synthesised by PET-RAFT polymerisation in the absence of oxygen (degassed polymerisation) with PB as catalyst. By zooming into the molecular weight range of 2200-2400 g/mol, we observed that major peaks (a and c) excellently matches theoretical predication of PDMA with BTPA chain-end group plus Na⁺ while minor peaks can be assigned to PDMA with BTPA chain-end group plus K⁺, all within experimental error (< 1 g/mol). For peaks a and c, number of monomer insertion (n) is determined to be 20, whereas for peaks c and d, it is determined to be 21. $M_{n, GPC} = 2,300$ g/mol; PDI = 1.11.

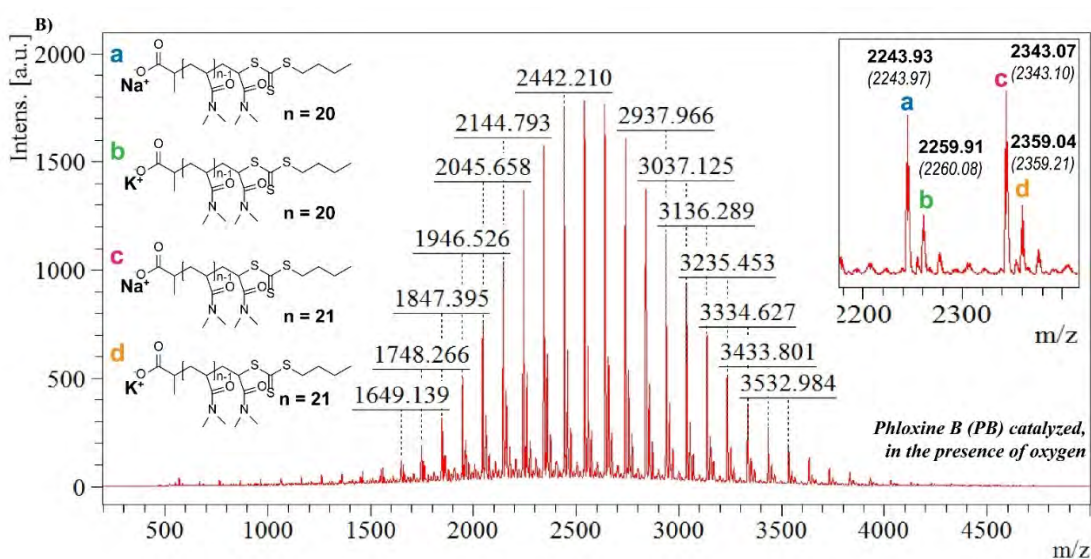


Figure 4.11 MALDI-TOF MS of a PDMA sample synthesised by PET-RAFT polymerisation in the presence of oxygen (non-degassed polymerisation) with PB as catalyst. By zooming into the molecular weight range of 2200-2400 g/mol, we observed that major peaks (a and c) excellently matches theoretical predication of PDMA with BTPA chain-end group plus Na^+ while minor peaks can be assigned to PDMA with BTPA chain-end group plus K^+ , all within experimental error (< 1 g/mol). For peaks a and c, number of monomer insertion (n) is determined to be 20, whereas for peaks c and d, it is determined to be 21. $M_{n,\text{GPC}} = 2,500$ g/mol; PDI = 1.11.

Nuclear magnetic resonance (NMR) analysis was subsequently performed on the purified polymer synthesised with EB as catalyst in the presence of oxygen (**Figure 4.12A**). Characteristic signals of the trithiocarbonate functionality at 5.1 ppm confirmed the retention of end-group. Furthermore, M_n calculated by NMR (15,000 g/mol) was in good agreement with the theoretical value (14,500 g/mol), and the GPC result ($M_{n,\text{GPC}} = 13,300$ g/mol). Finally, chain extension was performed to confirm the high end-group fidelity; GPC traces displayed a complete shift to higher molecular weights from $M_{n,\text{GPC}} = 13,300$ g/mol to $M_{n,\text{GPC}} = 32,500$ g/mol after chain extension, without a significant increase in dispersity (from 1.05 to 1.10) (SI, **Figure 4.12B**). All these results confirmed the high retention of the RAFT end-group.

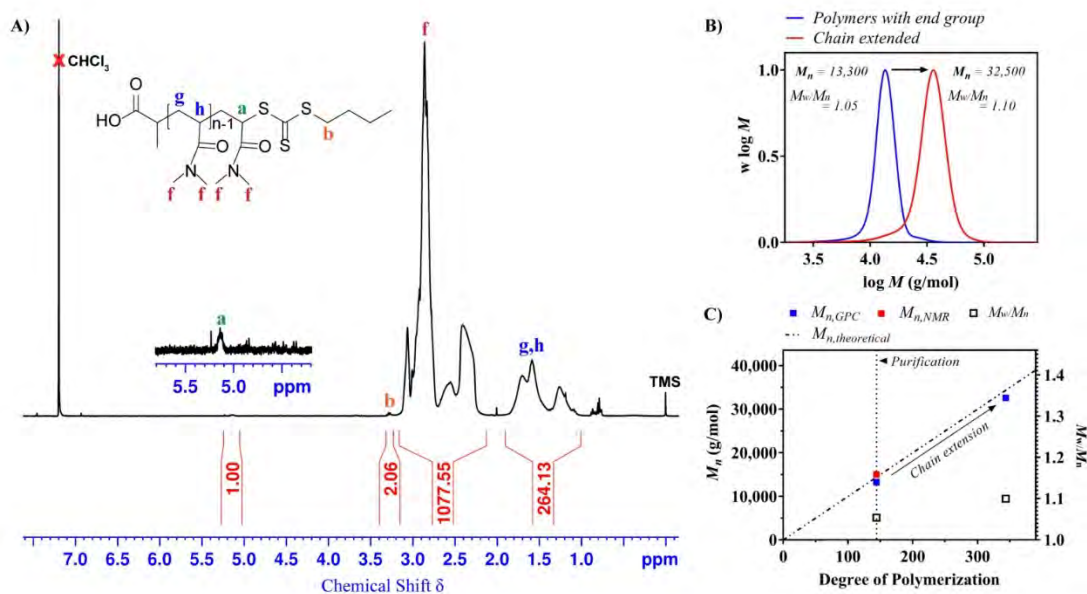


Figure 4.12 (A) ^1H NMR spectrum (400 MHz, CDCl_3) for purified PDMA synthesised through EB-catalysed PET-RAFT polymerisation in the presence of oxygen. (B)

Molecular weight distributions for PDMA in (A) before (blue line) and after (red line) chain extension; (C) corresponding M_n and M_w/M_n versus degree of polymerisation. M_n determined by NMR spectrum in (A) in blue square, as well as M_n determined by GPC for the same polymer before and after chain extension in red square, were all in excellent agreement with theoretical values (in dashed line).

Finally, we used the same batch of the purified PDMA for a subsequent chain extension test to assess the accessibility of the RAFT end-groups ([DMA]:[PDMA-macroRAFT]:[EB] = 1000:1:0.004, under yellow light of 5 mW/cm²). A complete shift of molecular weight distribution to higher molecular weights (from $M_{n, \text{GPC}} = 13,300$ g/mol to $M_{n, \text{GPC}} = 32,500$ g/mol) was observed after chain extension (**Figure 4.12B**) without a significant increase of PDI (from 1.05 to 1.10). Furthermore, the experimental $M_{n, \text{GPC}}$ is in agreement with theoretical value of $M_{n, \text{theoretical}} = 34,300$ g/mol derived from FT-NIR measurement of monomer conversion and calculations (Figure 4C).

To examine the oxygen tolerance in polymerisation targeting high molecular weights, we performed non-deoxygenated PET-RAFT polymerisation catalysed by EB, with [DMA]:[BTPA] = 1400:1 and a concentration of EB to be 20 ppm with respect to DMA. We were still able to observe a good correlation between experimental and theoretical values ($M_{n, \text{GPC}} = 61,000$ g/mol, $M_{n, \text{theoretical}} = 76,000$ g/mol), acceptable dispersities ($M_w/M_n = 1.18$), and a symmetrical GPC profile (**Figure 4.13A**). It should be noted that there is still a ~20% mismatch between $M_{n, \text{GPC}}$ and $M_{n, \text{theoretical}}$, however, this is naturally due to the physical nature of the cuvette we employed for polymerisation. At a ratio of [DMA]:[BTPA] = 1400:1, the EB-catalysed polymerisation in the presence of oxygen quickly reached 50% conversion with high viscosity. Because the top part of the polymerisation solution is close to the head space, the top part exhibits a lower degree of polymerisation whereas the middle and bottom part exhibit a higher degree of polymerisation. Since FTNIR beam detects the middle part (which resulted in $M_{n, \text{theoretical}}$, higher) and GPC aliquot was naturally taken from the top part ($M_{n, \text{GPC}}$, lower), the ~20% is very reasonable. To demonstrate this, we tested the same polymerisation in the presence of oxygen but removing the head space air. Indeed, shown as **Figure 4.13B** we observed much smaller mismatch (~10%) and narrower molecular weight distribution ($M_w/M_n = 1.10$).

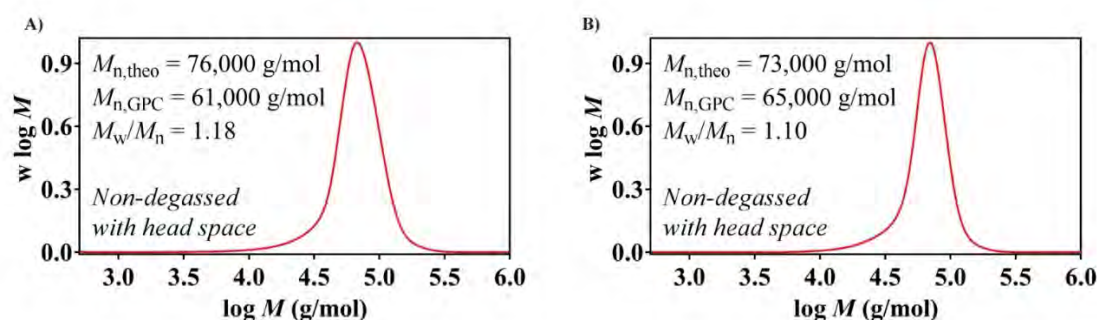


Figure 4.13 Molecular weight distribution of the non-deoxygenated PET-RAFT polymerisation (A) with head space and (B) without head space catalysed by EB, targeting high molecular weights. [DMA]:[BTPA] = 1400:1; the concentration of EB is 20 ppm with respect to DMA. (A) with head space: $M_{n,GPC} = 61,000$ g/mol, $M_{n,theoretical} = 76,000$ g/mol, $M_w/M_n = 1.18$; (B) without head space: $M_{n,GPC} = 65,000$ g/mol, $M_{n,theoretical} = 73,000$ g/mol, $M_w/M_n = 1.10$.

Finally, to demonstrate the robustness of this process, investigation of the solvent compatibility of halogenated xanthene dye-catalysed PET-RAFT polymerisation was performed with EB as an example, with prior deoxygenation. Due to its polar and large conjugated structure, EB can be solubilized in most common polar solvents, including but not limited to water (Table 4.2, entry 12), DMSO (Table 4.2, entry 1), DMF (Table 4.2, entry 3), DMAc (Table 4.2, entry 2), acetone (Table 4.2, entry 5), MeCN (Table 4.2, entry 4), MeOH (Table 4.2, entry 9), EtOH (Table 4.2, entry 6), EtOAc (Table 4.2, entry 10) and THF (Table 4.2, entry 7). The DMSO solvated system displayed the fastest rates, while in all other solvents tested, polymerisation still proceeded to some extent after 2 h irradiation (SI, Table 4.2). Fluorescence spectrophotometry revealed similar emission wavelengths (575-585 nm, Table 4.2) in these different solvents, indicating that solvent polarity does not have a significant impact on the energetics of the relaxed S_1 state of the xanthene dyes. After 2 h of irradiation in the presence of EB, different monomer conversions (from 35 to 94%) were achieved in these solvents. Most importantly, the polymers prepared with EB present narrow molecular weight distributions (Table 4.2). In addition, we also chose DCM (Table 4.2, entry 8) and 1,4-dioxane (Table 4.2, entry 11) as less polar solvents for organocatalysed PET-RAFT where EB was initially dissolved in monomer. Interestingly, well-controlled PET-RAFT polymerisations were also achieved, which confirmed EB to be versatile organocatalyst for PET-RAFT systems with both polar and less polar solvents.

Table 4.2 PET-RAFT polymerisation catalysed by EB in different solvents ([DMA]:[BTPA]:[EB] = 200:1:0.004, monomer/solvent, 1/1 (v/v))

#	Solvent	Time	α	$M_{n,theo}$	$M_{n,exp}$	M_w/M_n	λ_{max}	λ_{em}	ϵ (F m ⁻¹)
1	DMSO	2 h	94%	18,900	18,100	1.06	548 nm	585 nm	46.83
2	DMAc	2 h	76%	15,300	15,200	1.06	548 nm	582 nm	37.78
3	DMF	2 h	68%	13,700	14,200	1.06	548 nm	583 nm	37.22
4	MeCN	2 h	45%	9,200	11,200	1.04	546 nm	581 nm	35.69
5	Acetone	2 h	39%	7,900	9,700	1.06	548 nm	583 nm	20.49
6	EtOH	2 h	35%	7,100	9,300	1.06	543 nm	577 nm	24.85
7	THF	2 h	32%	6,700	8,700	1.06	548 nm	583 nm	7.43
8	DCM	2 h	25%	5,300	6,900	1.07	548 nm	583 nm	8.93
9	MeOH	2 h	24%	5,000	7,000	1.07	541 nm	577 nm	32.61
10	EtOAc	2 h	20%	4,200	5,700	1.08	548 nm	582 nm	6.02
11	Dioxane	2 h	15%	3,200	5,600	1.09	548 nm	584 nm	2.21
12	Water	2 h	11%	2,400	4,300	1.15	544 nm	576 nm	78.36

*Note: ϵ (F m⁻¹) is the dielectric constant of the solvent representing polarity.

4.3.2 Property-performance relationship: correlating PET-RAFT performance with PC properties

The lowest triplet excited state (T_1) for xanthene derivatives typically exhibits a sufficiently long lifetime (0.1-4.0 ms, **Table 4.1**) to allow efficient PET processes,^{31,76} in line with our previous observations.^{14,25,77} Therefore, an ideal PET-RAFT PC is preferred to possess a high Φ_T upon irradiation. On the other hand, the oxidative potential of T_1 , $E^0(PC^{*+}/^3PC^*)$, which defines the ability of $^3PC^*$ to reduce a substrate (e.g., RAFT agent in the case of PET-RAFT) through the oxidative quenching pathway, determines the

change of Gibbs free energy (ΔG^0) of the corresponding electron transfer reaction (see **Equation 4.1-4.3**). According to Marcus theory,⁷⁸⁻⁷⁹ with more negative ΔG^0 (i.e., more negative $E^0(PC^{\bullet+}/^3PC^*)$, **Equation 4.3**), the electron transfer rate k_{et} increases until entering the inverted Marcus region where k_{et} starts to decrease with more negative ΔG^0 values (**Equation 4.4**). However, unlike intramolecular PET in which the distance between donor and acceptor is constant, the inverted Marcus region is scarcely observed in intermolecular PET and more often, a more negative ΔG^0 would lead to an increase in k_{et} up to the diffusion limit where diffusion becomes the rate determining step for even more negative ΔG^0 values (described as Rehm-Weller behaviour,⁸⁰ **Equation 4.5** and **Equation 4.6**). Hence, given the use of the same RAFT agent as an electron acceptor, $E^0(PC^{\bullet+}/^3PC^*)$ largely determines ΔG^0 (**Equation 4.3**) and thereby controls k_{et} (**Equation 4.5** and **Equation 4.6**) which further determines k_p^{app} of PET-RAFT polymerisation at a fixed temperature (**Equation 4.7**).

Equation 4.1 Relation between ΔG_{red} and $E^0(PC^{\bullet+}/^3PC^*)$.

$$E^0(PC^{\bullet+}/^3PC^*) = \frac{-\Delta G_{red}(PC^{\bullet+}/^3PC^*)}{nF}$$

Equation 4.2 The PET reaction in the PET-RAFT polymerisation.



Equation 4.3 Expression of ΔG .

$$\begin{aligned} \Delta G &= [G(PC^{\bullet+}) - G(^3PC^*)] + [G(RAFT^{\bullet-}) - G(RAFT)] \\ &= -\Delta G_{red}\left(\frac{PC^{\bullet+}}{^3PC^*}\right) + \Delta G_{red}\left(\frac{RAFT}{RAFT^{\bullet-}}\right) \\ &= nF[E^0(PC^{\bullet+}/^3PC^*) - E^0(RAFT/RAFT^{\bullet-})] \end{aligned}$$

Equation 4.4 Basic equation of the Marcus Theory,⁷⁸⁻⁷⁹

$$k_{et} = \frac{2\pi}{\hbar} |H_{AB}|^2 \frac{1}{\sqrt{4\pi\lambda k_B T}} \exp\left(-\frac{(\lambda + \Delta G^0)^2}{4\pi\lambda k_B T}\right)$$

where k_{et} is electron transfer rate constant; ΔG^0 is the total Gibbs free energy change for the PET reaction in **Equation 4.2**;

$|H_{AB}|$ is the electronic coupling between the initial and final states; λ is the reorganization energy;

additionally, T is the absolute temperature and k_B is the Boltzmann constant.

Equation 4.5 The electron transfer rate equation for activation-controlled reactions expressed by the Gibbs free energy change of the formation of the transition state.

$$k_{et} = Ae^{-\frac{\Delta G^\ddagger}{RT}}$$

where k_{et} is electron transfer rate constant; ΔG^\ddagger is the Gibbs free energy change of the formation of the transition state.

Equation 4.6 The experimental empirical expression of ΔG^\ddagger for intermolecular electron transfer in solvents according to the Rehm-Weller behaviour.⁸⁰

$$\Delta G^\ddagger = \frac{\Delta G^0}{2} + \sqrt{-\Delta G^\ddagger(0)^2 + \left(\frac{\Delta G^0}{2}\right)^2}$$

where ΔG^0 is the total Gibbs free energy change for the PET reaction in **Equation 4.2**.

Equation 4.7 In PET-RAFT polymerisation, because k_{et} should be positively related to the propagation radical concentration $[R^\bullet]$ (k_{et} defines the rate of electron transfer and each electron transfer should generate a propagating radical which enters the activation-deactivation equilibrium), the apparent propagation rate k_p^{app} should thus also be positively related to k_{et} .

$$k_p^{app} = k_p[R^\bullet] \propto k_p k_{et}$$

where k_p is the propagation rate of the monomer and $[R^\bullet]$ is the propagating radical concentration in PET-RAFT polymerisation.

Overall, with more negative $E^0(PC^{\bullet+}/^{\beta}PC^*)$, k_p^{app} should exhibit an increase followed by a plateau, based on the proposed PET mechanism. Despite this, partial or even complete involvement of energy transfer pathways are still possible in these processes, and there is still debate in most cases of PET transformations (including that for PET-RAFT processes).³¹ However, the driving forces for both pathways (i.e. $E^0(PC^{\bullet+}/^{\beta}PC^*)$ for

electron transfer, and T_1 excited state energy (E_T for energy transfer) are closely related, as the available energy for electron transfer processes from excited state molecules increases with increasing E_T ($E^0(\text{PC}^{*+}/\beta\text{PC}^*) = E^0(\text{PC}^{*+}/\text{PC}) - E_T$). Especially for structurally similar PCs that share similar chromophores, the trend for $E^0(\text{PC}^{*+}/\beta\text{PC}^*)$ and E_T are in principle the same, i.e., higher T_1 energies correspond to a more reducing (more negative $E^0(\text{PC}^{*+}/\beta\text{PC}^*)$) T_1 state. Hence, a more photo-active PC generally tends to exhibit both more negative $E^0(\text{PC}^{*+}/\beta\text{PC}^*)$ and more positive E_T . Indeed, structurally similar PCs normally share the same chromophore and would thereby exhibit similar ground state electrochemical properties; for example, the commercial halogenated xanthene dyes used in this work were reported to exhibit similar ground state redox potential $E^0(\text{PC}^{*+}/\text{PC})$ within the range 0.92-0.96 V (vs. SCE).⁶⁹ As the aim of this work is mainly to propose a guideline for relationships between substitutions of the chromophore and performance of the photocatalysed system on a qualitative basis, to simplify, herein we only consider the electron transfer pathway. However, a purely energy transfer pathway will also fit well in the context of this work and will not affect the main conclusions. In addition, the back electron transfer (BET) process is not discussed in this work on account of three reasons. Firstly BET solely exists in an electron transfer pathway and secondly it should only affect temporal control (does not affect chain transfer; unlike in photo-ATRP and other techniques). Most importantly, accurate redox potential values of the RAFT agent (which are required to study BET) are still in debate despite years of efforts by us and other groups both experimentally and computationally. Indeed, as we observe good temporal control in all experiments and the BET process is beyond the scope of this study, we decided not to discuss about the BET process and the interested readers are directed to related literature.⁸¹

Density functional theory (DFT) calculations were performed to compute $E^0(\text{PC}^{*+}/\beta\text{PC}^*)$ for each PC, which were correlated with the reported values within experimental/computational error (**Table 4.3**). By comparing EB and EY, and considering their comparable $E^0(\text{PC}^{*+}/\beta\text{PC}^*)$, we naturally attributed the higher catalytic efficiency of EB (higher k_p^{app}) to the much higher Φ_T (EB: 0.62-0.69 and EY: 0.28-0.32, **Table 4.3**, entry 1 and entry 2). On the other hand, as EB and RB have similar Φ_T values (EB: 0.62-0.69 and RB: 0.76-0.86, **Table 4.3**, entry 1 and entry 3), the better catalytic efficiency of EB is due to its more negative $E^0(\text{PC}^{*+}/\beta\text{PC}^*)$ compared to RB (EB: -1.34 V and RB: -1.00 V vs. SCE, **Table 4.3**, entry 1 and entry 3). This general trend can be

extended to the full list of **Table 4.3**, where higher Φ_T and more negative $E^0(\text{PC}^{*+}/^3\text{PC}^*)$ lead to higher k_p^{app} in PET-RAFT polymerisation.

Table 4.3 k_p^{app} of PET-RAFT polymerisation in comparison with photophysical and electrochemical properties of the photocatalysts.

Entry	PC	$E^0(\text{PC}^{*+}/^3\text{PC}^*)$ (V, vs. SCE)		Φ_T	k_p^{app} (min^{-1})
		Calculated	Reported ⁸²⁻⁸³		
1	EB	-1.34	-1.39	0.62-0.69	0.023
2	EY	-1.26	-1.35	0.28-0.32	0.014
3	RB	-1.00	-1.16	0.76-0.86	0.010
4	PB	-0.91	N/A	0.4	0.007

The oxygen inhibition period observed in non-degassed PET-RAFT polymerisation is often explained through two different possible mechanisms. One possible mechanism is that the triplet-triplet annihilation (TTA) process between oxygen and $^3\text{PC}^*$ competes with the PET process (between the RAFT agent and $^3\text{PC}^*$) resulting in this short inhibition. Another explanation is that the oxygen is consumed by the presence of radicals (through polymerisation). As mentioned previously, polymers produced in the presence of oxygen display excellent end-group fidelity; moreover, with polymerisation targeting higher M_n , we were still able to observe a good correlation between experimental and theoretical values ($M_{n,\text{GPC}} = 61,000$ g/mol, $M_{n,\text{theoretical}} = 76,000$ g/mol; for detailed discussion of the ~20% mismatch see **Figure 4.13** and relevant discussion), acceptable dispersities ($M_w/M_n = 1.18$), and a symmetrical GPC profile (**Figure 4.13**). Therefore, we can exclude the second potential mechanism in this work. Subsequently, we decided to examine the first mechanism (TTA between oxygen and $^3\text{PC}^*$). Given the short $^1\text{O}_2$ lifetime of only 20-70 μs in common polar solvents,⁸⁴ the quenching of $^1\text{O}_2$ by DMSO should also be rapid, since we have experimentally observed this process previously.⁶² Consequently, $^1\text{O}_2$ generation should be the rate determining step for oxygen elimination

in these systems. We then investigated the oxygen tolerance for these four PCs using FTNIR spectroscopy. As expected, we observed that the length of the oxygen inhibition period (calculated by the delay of the non-degassed polymerisation compared to its degassed counterpart) was correlated with the $^1\text{O}_2$ quantum yield (Φ_Δ) for each catalyst, as higher $^1\text{O}_2$ quantum yields lead to shorter oxygen-induced inhibition periods (**Table 4.4**). Therefore, we can conclude that PCs with higher Φ_Δ present better oxygen tolerance in PET-RAFT polymerisation. Among the four dyes studied, RB is the best candidate for oxygen tolerance in PET-RAFT, followed by EB, PB, and EY.

Table 4.4 Inhibition periods of PET-RAFT in the presence of oxygen and photocatalyst properties.

Entry	PC	$\Phi_{\text{T}}^{55, 64-68}$	$\Phi_{\Delta}^{55, 64-68}$	O₂ inhibition period
		Reported	Reported	Measured
1	RB	0.76-0.86	0.75-0.79	23 min
2	EB	0.62-0.69	0.62-0.63	41 min
3	PB	0.40	0.59-0.65	47 min
4	EY	0.28-0.32	0.39-0.57	90 min

* Φ_{T} : triplet quantum yield, i.e., the quantum yield of the lowest triplet excited state of PC. Φ_{Δ} : singlet oxygen quantum yield. **O₂ inhibition period**: the length of retardation time caused by the presence of oxygen, i.e. the length of right-shift along the time-axis between kinetics of the deoxygenated and non-deoxygenated sample where $k_{\text{p}}^{\text{app}}$ stays constant. The O₂ inhibition periods were determined by measuring the time delay between kinetics in the absence/presence of oxygen in each dye-catalysed PET-RAFT system (**Figure 4.3A-D**).

4.3.3 Structure-property relationship: effect of halogen substitution on photophysical properties

Well established in photoredox catalysis, and recently readdressed in O-ATRP by Miyake and co-workers,³⁴⁻³⁶ and also in organic photoredox catalysis by Nicewicz *et al.*,^{31, 42} photophysical and electrochemical properties of PCs can be tuned by varying functional substituents with electron-donating/withdrawing properties.^{27, 85-87} Similarly, the photophysical and electrochemical properties of organic PCs can be tuned by the introduction/modification of substituents on the aryl chromophore.^{31, 34, 36, 52, 88} Correspondingly, changes to the halogen atoms on the xanthene aryl group lead to large differences in the photophysical and electrochemical properties of the PCs, i.e., Φ_T and $E^0(\text{PC}^{•+}/^3\text{PC}^*)$ (**Table 4.3**). Despite these differences, the spectral profiles of these halogenated xanthene dyes are similar as shown by UV-Vis spectroscopy of the PET-RAFT polymerisation mixtures (**Figure 4.1C**), while ϵ of the dyes at their λ_{max} varies in the range of 87 000 - 98 000 $\text{M}^{-1}\text{cm}^{-1}$ (**Table 4.1**). Since halogen substitution is the only difference of EY, EB, PB, and RB, they are excellent candidates for studying the effect of halogen substitution on their PET-RAFT catalytic activity.

Interestingly, heavier atom substitution appears to increase ϵ and cause a red-shift in the absorption bands (λ_{max}).⁸⁹ Some recent literature on iridium complexes has attributed the spectral red-shift caused by halogen substitution to their effect in notably stabilising the lowest unoccupied molecular orbital (LUMO) of the chromophore, while the highest occupied molecular orbital (HOMO) is less stabilised.⁹⁰⁻⁹¹ Using density functional theory (DFT) calculation, we were able to gain insights into the photoexcitation mechanism from a molecular orbital (MO) perspective of these dyes with C_1 point group.⁹²⁻⁹³ According to time-dependent DFT (TD-DFT) calculations, the most intense absorption peak of these dyes can be assigned to the first singlet excited state (S_1) where π_{HOMO} to π_{LUMO} transition has over 98% contribution (denoted in **Figure 4.14**). Overall, TD-DFT was conducted to analyse λ_{max} with the related S_1 excitation and the major contribution from HOMO→LUMO transitions (> 98%), whereas the latter was inspected to form the structure-property relationships with respect to λ_{max} . Therefore, inspection of frontier orbitals, i.e. HOMO and LUMO, should give us insight into the halogen-controlled spectral changes. Experimentally, structural comparison between EB and EY (or between PB and RB, **Figure 4.1A**) revealed that iodine (I) replacing bromine (Br) substituents in X-positions would cause an 8 nm red shift in maximum absorption wavelength (λ_{max} , from

EY to EB, or from PB to RB). To interpret this change, we inspected the frontier orbitals and found a portion of HOMO located on the X-position halogens, but little LUMO composition on these halogens (**Figure 4.14**). This observation suggested that the outermost-shell n (non-bonding) electrons of X-position halogens should have an impact on the π system energy of the xanthene core⁹⁴ and thereby affect $\pi \rightarrow \pi^*$ transitions. Calculation of frontier orbitals revealed these effects. Specifically, as the n electrons of I substituents have higher energy than those of Br substituents, when compared with LUMO (which is little affected by n electrons), the HOMO energy level of X-position I-substituted EB (or RB) is moved up more than that of X-position Br-substituted EY (or PB), which results in narrower HOMO/LUMO energy gap for the Br substituted xanthenes studied here (**Figure 4.14**). A narrower HOMO/LUMO energy gap leads to lower-energy S_1 excitation which causes the 8 nm red shift in λ_{\max} from EY to EB, and PB to RB.

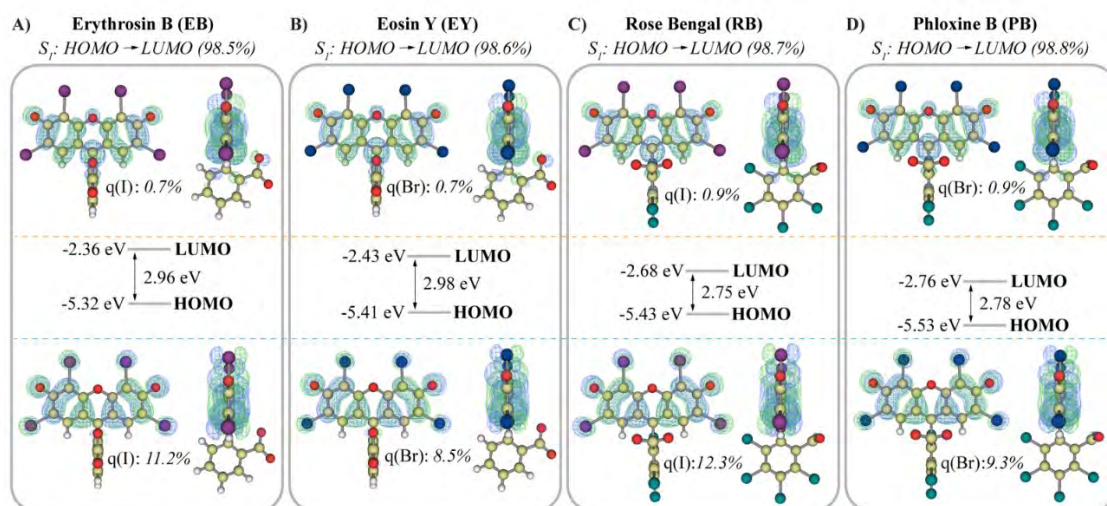


Figure 4.14 Frontier orbitals, energy levels, their gaps and orbital composition on X-position halogens of the ground state (A) EB, (B) EY, (C) RB and (D) PB. Top: LUMO; bottom: HOMO. Contribution of HOMO \rightarrow LUMO transitions to S_1 is denoted under the dye label. DFT calculations for frontier orbitals and TD-DFT calculations for excited state contribution were employed with B3LYP (6-31+G** basis set for C H O and LANL2DZ basis set for heavy atoms Cl Br I) level of theory and the CPCM-DMSO solvation model. Atom colour: C in yellow, H in white, O in red, Cl in green, Br in blue and I in purple. q: the portion of the corresponding molecular orbital located on the enclosed element, in percentage.

In contrast to the X-position halogens that are attached to the xanthene chromophore and directly involved in HOMO→LUMO transitions, the Y-position substitution is on the phenyl group, which can be regarded as an electron-withdrawing group as a whole. Given that $\chi_{\text{Cl}} > \chi_{\text{H}}$ (**Figure 4.1B**), the strong inductive effect of chlorine (Cl) makes Cl-substituted phenyl groups much more electron-withdrawing than H-substituted phenyl groups, and hence more pronouncedly decreases both HOMO and LUMO energies for PB (or RB) compared with EY (or EB) (**Figure 4.14**). While the enhanced electron-withdrawing effect of Cl-substituted phenyl group decreases both HOMO and LUMO, it decreases HOMO to a lesser extent which leads to the 15 nm red-shift in λ_{max} from EY (or EB) to PB (or RB).

Overall, the heavier halogen substitution at the X positions on the xanthene core (I substitution instead of Br on X-positions), in conjunction with the highly electron-withdrawing Cl-substituted phenyl group (Cl substitution instead of H on Y-positions), λ_{max} of RB is 23 nm red-shifted relative to EY, endowing it with the longest-wavelength absorption among these halogenated xanthene dyes (**Figure 4.1C**). Theoretically, longer-wavelength absorption can be obtained by heavier halogenation on the chromophore and the introduction of more electron-withdrawing groups.

It must be noted that the double-anion structure of the investigated dyes was chosen for DFT calculations, as the disodium salt form of these dyes was used in the polymerisation system. For qualitative analysis, this approximation should yield a good comparative basis for revealing the general trends in the evolution of frontier orbitals with the change of halogen substitution. Indeed, this approximation has been shown to be accurate for calculating $E^0(\text{PC}^{+}/{}^3\text{PC}^*)$ which resulted in good agreement with reported values (**Table 4.3**). However, with respect to spectral properties, where other influencing factors are more complex and thus much harder to predict by DFT calculations, possible assembly of a dye molecule with sodium cations, solvent molecules, and/or RAFT agents should all lead to significant changes in the absorption/fluorescence spectra. Indeed, HOMO→LUMO transitions were calculated to have a contribution of over 98% in all cases to the S_1 excitation, which means the HOMO/ LUMO energy gap has the major contribution to the calculated S_1 excited energy and hence the calculated λ_{max} . However, the exact value of the calculated λ_{max} and the related HOMO/ LUMO energy gap still exhibit a relatively large deviation of ca. 30-50 nm to the exact experimentally measured λ_{max} . This is on one hand due to that the TD-DFT method normally has a large error of ~

30 nm, which was widely existent in the literature. Most importantly, possible assembly of an ionised dye molecules with sodium cations, solvent molecules, and/or RAFT agents should all lead to significant changes in the absorption/fluorescence spectra. Indeed, here we experimentally observed around 15 nm red-shift EY/EB and a couple of nanometers red shift for PB/RB upon addition of RAFT agents. Considering the less hindered phenyl group of EY and EB than PB and RB, this red-shift could result from π - π conjugation. However, such factors do not lead to any change in the λ_{max} order on a comparative basis and thus does not affect the main conclusions of this work on the qualitative basis. However, as we aim to qualitatively reveal the general trends for structure-property-performance relationships, and the aforementioned factors generally exert equivalent influence for the structurally analogous halogenated xanthene PCs in this study, the validity of the comparisons is sufficient for us to comment on the relationships between substitution of the chromophore and the resulting changes in spectral properties of these dyes.

As stated above, high Φ_{T} of a PC is one of the key requirements for efficient PET catalysis, which indicates efficient generation of T_1 states that can be accessed by the RAFT agent. However, because the intersystem crossing (ISC) from S_1 to T_1 is spin-forbidden and requires spin-orbit perturbation,⁹⁵ with the competition between slow ISC rates and fast fluorescence postulated to be a primary cause for the low Φ_{T} of most organic PCs.³⁶ In addition to introducing donor-acceptor charge transfer,³⁶ or core-twisted aromatics,⁹⁶ which quench unfavourable fluorescence and allows time for ISC, ISC can be accelerated by enhancing spin-orbit perturbation from the interaction between the electron-spin magnetic moment and the nucleus magnetic field from its apparent motion.⁹⁷ By increasing the atomic number, nuclear charge and the nuclear magnetic field will increase, boosting spin-orbit perturbation and accelerating ISC.^{75,98} This phenomenon is known as the heavy atom effect,⁹⁸ where higher atomic-number substituents would contribute to higher Φ_{T} . Therefore, in halogenated xanthene dyes, substitution at the X position with heavier species is expected to increase Φ_{T} . Indeed, because of atomic numbers in the order $\text{I} > \text{Br} > \text{Cl} > \text{H}$ (**Figure 4.1B**), the heaviest atom substituted RB (I on X-positions and Cl on Y-positions) exhibits highest Φ_{T} among the four dyes, while EY has the lightest atoms (Br on X-positions and H on Y-positions) and the lowest Φ_{T} (**Figure 4.1B**).

On the other hand, Φ_{Δ} of the PCs, which relates to oxygen tolerance in PET-RAFT, is a consequence of TTA process (where $^1\text{O}_2$ is generated from $^3\text{O}_2$ by quenching a triplet

excited PC, **Scheme 4.1A**).⁹⁹ Therefore, Φ_{Δ} should positively correlate to Φ_T (validated by **Table 4.4**), and hence should also be governed by the heavy atom effect (**Figure 4.1B**).

4.3.4 Structure-property relationship: effect of halogen substitution on electrochemical properties

As elucidated in the property-performance relationship, a more negative $E^0(\text{PC}^{*+}/{}^3\text{PC}^*)$ value is an indicator of how strongly reducing a ${}^3\text{PC}^*$ is; briefly, $E^0(\text{PC}^{*+}/{}^3\text{PC}^*)$ is the potential change from the T_1 state of the PC to the cation radical form of the PC. Alternatively, it can be expressed by $E^0(\text{PC}^{*+}/{}^3\text{PC}^*) = E^0(\text{PC}^{*+}/\text{PC}) - E_T$, where $E^0(\text{PC}^{*+}/\text{PC})$ is ground state ionization potential and E_T is the triplet state energy. Hence, $E^0(\text{PC}^{*+}/{}^3\text{PC}^*)$ describes the first ionization potential of ${}^3\text{PC}^*$, i.e. the ability of ${}^3\text{PC}^*$ to donate an electron to the substrate. Inspection of the upper singly occupied molecular orbitals (upper SOMOs) of the triplet state revealed that the electron density was almost exclusively distributed on the xanthene core for all four dyes (**Figure 4.15**), which indicates that the electron participating in PET from the excited state PC should originate from the xanthene core. Therefore, the ligand substitution of the xanthene core should directly affect the electron donating ability of the T_1 state of the PC. Indeed, the PC installed with the most electron-withdrawing atoms, i.e. PB with four Cl on the Y-positions ($\chi_{\text{Cl}} > \chi_{\text{H}}$, **Figure 4.1B**) and four Br on the X-positions ($\chi_{\text{Br}} > \chi_{\text{I}}$, **Figure 4.1B**) has the least negative $E^0(\text{PC}^{*+}/{}^3\text{PC}^*)$ of -0.91 V vs. SCE. In contrast, EB with the least electron-withdrawing atoms yields the most negative $E^0(\text{PC}^{*+}/{}^3\text{PC}^*)$ of -1.34 V vs. SCE. Generally, $E^0(\text{PC}^{*+}/{}^3\text{PC}^*)$ is only tuned by the overall electron affinity of substituents on the chromophore, where less electron-withdrawing (or more electron-donating) substituents would yield more negative $E^0(\text{PC}^{*+}/{}^3\text{PC}^*)$ for the chromophore.

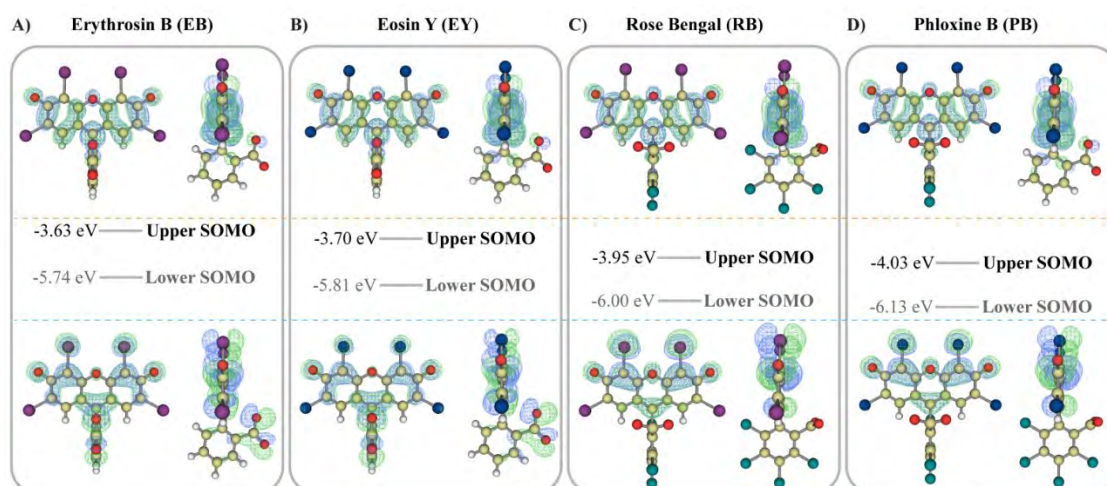


Figure 4.15 Upper and lower SOMOs, their energy levels and gaps between upper SOMO and lower SOMO of the T_1 state of (A) EB, (B) EY, (C) RB and (D) PB. Top: upper SOMO; bottom: lower SOMO. Unrestricted DFT calculations for T_1 frontier orbitals and TD-DFT calculations for excited state contribution were employed with B3LYP (6-31+G** basis set for C H O and LANL2DZ basis set for heavy atoms Cl Br I) level of theory and the CPCM-DMSO solvation model.

4.3.5 Employing the structure-property-performance relationship for on-demand design of PC in PET-RAFT

As oxygen tolerance in PET-RAFT polymerisation relies on the Φ_T of the PC, oxygen tolerant PET-RAFT is currently limited to high Φ_T PC based systems, such as ZnTPP ($\Phi_T = 0.88$).¹⁴ Indeed, ZnTPP has been employed as the PC in non-degassed PET-RAFT-based photo-flow,^{62, 100} photo-polymerisation-induced-self-assembly,¹⁰¹⁻¹⁰² and photo-high-throughput polymerisations.¹⁰³⁻¹⁰⁴ Therefore, we decided to employ the structure-property-performance relationship established in this study to design a new organic PC with high Φ_T equivalent to ZnTPP, and a desirable PET efficiency.

To this end, we set RB as the basis which possesses the highest Φ_T (0.76-0.86) among the xanthene derivatives, and brominated fluorescein (**Figure 4.16**) and further iodinated the intermediate to receive a new PC, Henry 1 (H1, **Figure 4.17**), that replaces Cl on Y-positions of RB with Br. Firstly, tetrabromofluorescein was prepared from tetrabromophthalic anhydride and resorcinol in methanesulfonic acid at 90 °C overnight according to reported procedures.¹⁰⁵ NMR analysis was conducted to confirm the purity (**Figure 4.16**). ¹H NMR (400 MHz, DMSO-d₆): peak-a δ 10.16 (s, 2H), peak-b δ 6.85 (d, $J = 8.68$ MHz, 2H), peak-c δ 6.66 (d, $J = 2.40$ MHz, 2H), peak-d δ 6.55 (dd, $J_1 = 2.40$ MHz, $J_2 = 8.68$ MHz, 2H). Apparently, the signal from the hydrogen a of the hydroxyl group appeared at the low field δ 10.16 assigned as peak-a (**Figure 4.16**). Hydrogen d assigned as peak-d and hydrogen c assigned as peak-c were affected by coupling with hydrogen a characteristic of $J = 2.40$ MHz. Moreover, hydrogen b and hydrogen d were affected by each other with a coupling $J = 8.68$ MHz. Thereby, peak-b (b coupling with d) and peak-c (c coupling with a) are both doublets and peak-d (d coupling with a and b) is a doublet of doublets. 4,5,6,7-Tetrabromo-3',6'-dihydroxy-2',4',5',7'-

tetraiodospiro[isobenzofuran-1(3H),9'-[9H]xanthen]-3-one (H1) was synthesised by iodination of tetrabromofluorescein. Iodination was performed according to reported procedures.¹⁰⁶ NMR analysis was conducted to confirm the purity (**Figure 4.17**). ¹H NMR (400 MHz, DMSO-d₆): peak-a δ 10.21 (s, 2H), peak-b δ 7.50 (s, 2H). Indeed, after iodination, only hydrogen a and hydrogen b were preserved (**Figure 4.17**). Because of the presence of the electro-withdrawing I substituents that decreases the electron density around the hydrogens, peak-a from hydrogen a was slightly shifted to the low field and peak-b from hydrogen b was even more significantly shifted to the lower field because of direct influence by the adjacent I substituent. Indeed, because of the I substituents, peak b has become a singlet indicating no coupling effect experience by hydrogen b. Apparently, the iodination has been sufficiently proceeded according to the spectrum.

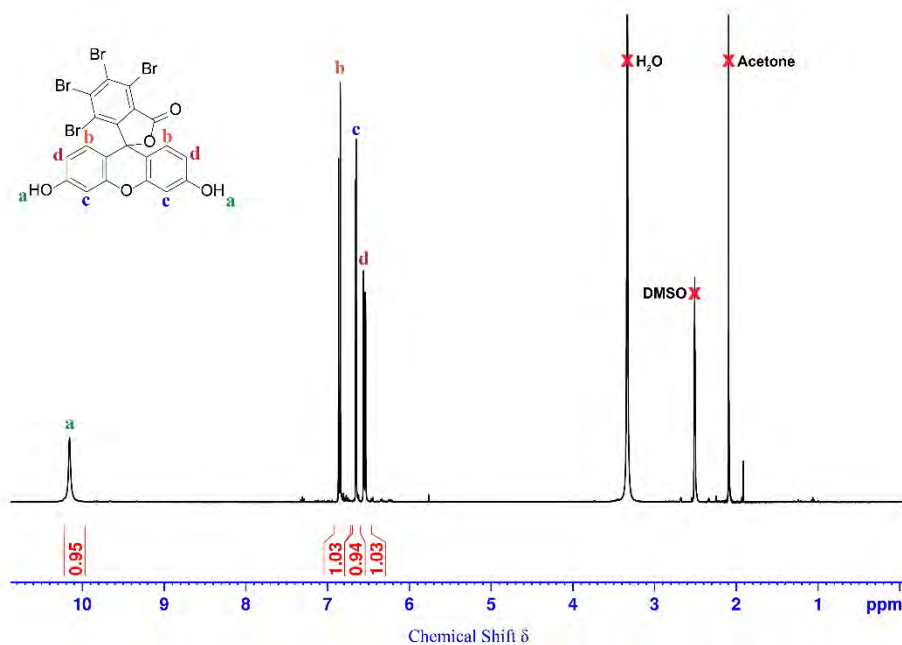


Figure 4.16 ¹H NMR spectrum (400 MHz, DMSO-d₆) of synthesised tetrabromofluorescein.

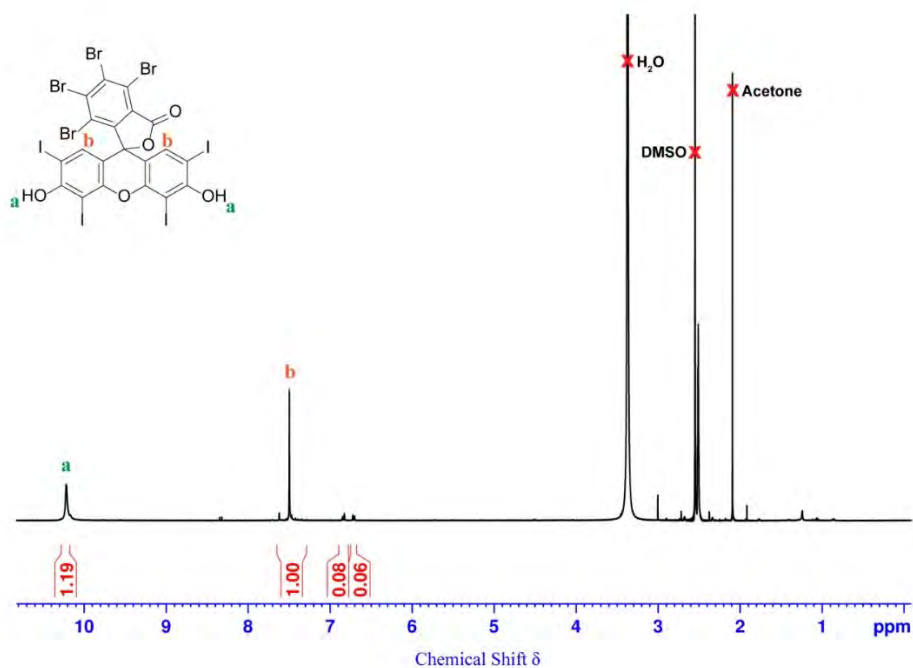


Figure 4.17 ^1H NMR spectrum (400 MHz, DMSO- d_6) of synthesised H1.

As expected, H1 exhibited very similar spectral properties to RB (**Figure 4.18B**), due to similar electronegativity of the Y-position Br and Cl which leads to similar electron-withdrawing effects of the Y position substituted phenyl groups and similar excited state nature (**Figure 4.18G-H**). This similarity also leads to its comparable $E^0(\text{PC}^{*+}/^3\text{PC}^*)$ with RB. DFT calculations revealed an $E^0(\text{PC}^{*+}/^3\text{PC}^*)$ of H1 to be -1.02 V (vs. SCE), slightly more negative than that of RB due to slightly lower electronegativity of Br than Cl (**Figure 4.1B**).

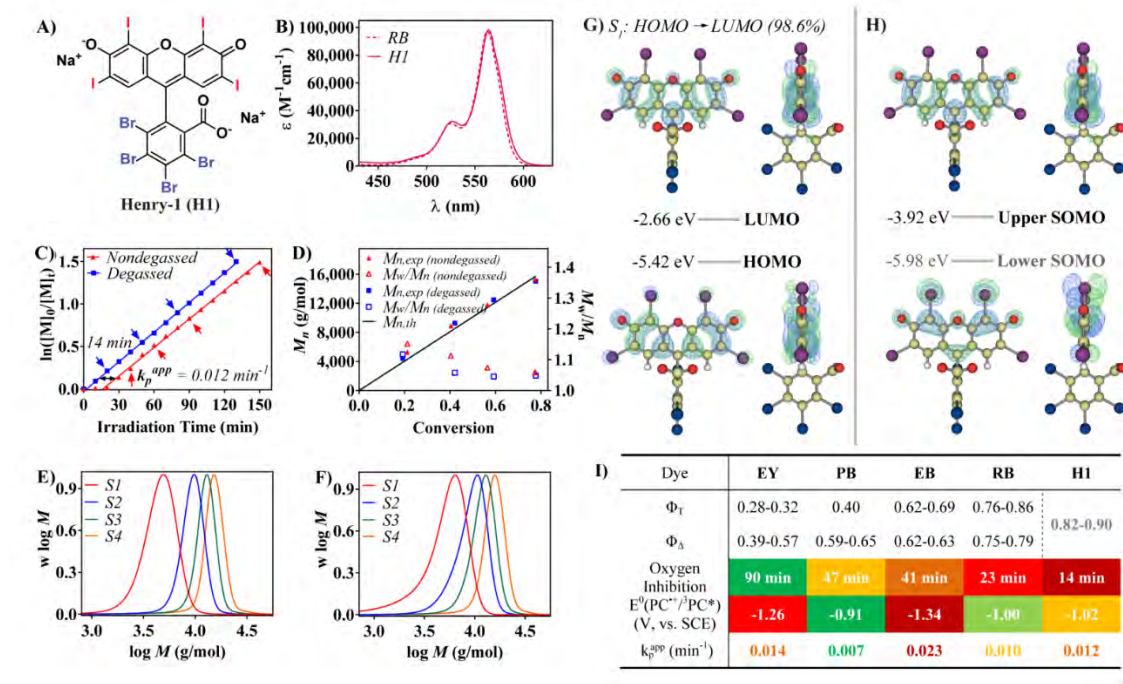


Figure 4.18 (A) Dye structure of the synthesised dye H1 and its (B) UV-vis spectrum determined in model DMSO solution of a typical PET-RAFT system. (C) evolution of $\ln([M]_0/[M]_t)$ versus time, (D) M_n and M_w/M_n versus monomer conversion, (E-F) molecular weight distributions taken during polymerisation in the presence (E) and absence (F) of oxygen, denoted as S1, S2, S3, S4, which corresponds to blue RB arrows in (D) following the time order of H1-catalysed PET-RAFT polymerisation. (G) HOMO, LOMO and their energy levels and (H) upper SOMO, lower SOMOs and their energy levels of H1. (I) Table summarizing property-performance evaluation of four commercial xanthene dyes and the synthesised H1; the quantum yield range of H1 was estimated from the first-order approximation fitting of the reported data for EY, EB, PB and RB (SI, Figure S14), based on the oxygen inhibition time of 14 min for H1-catalysed PET-RAFT polymerisation in the presence of oxygen.

According to the relationships, compared to RB, the only significant impact of the Y-position Br of H1 is from the heavy atom effect, which leads to higher Φ_T and thus provides better oxygen tolerance and higher k_p^{app} in H1-catalysed PET-RAFT polymerisation. An oxygen inhibition period of 14 min and a $k_p^{\text{app}} = 0.012 \text{ min}^{-1}$ measured from the model PET-RAFT system aligned with our expectation (**Figure 4.18B**). Kinetic studies in PET-RAFT polymerisation were performed with H1 (**Figure 4.18C-F**), using identical experimental conditions of previous dyes.

As the ranges of triplet quantum yields (Φ_T) and (Φ_Δ) are in principle similar for each halogenated xanthene dye investigated in this work, they can be regarded as equivalent considering that Φ_Δ of a halogenated xanthene dye is always only slightly inferior to its corresponding Φ_T in the same solvent. Therefore, to establish a prediction model of Φ_T/Φ_Δ of the dyes from O_2 inhibition periods of the dye-catalysed PET-RAFT polymerisations, we employed first-order approximation and fitted all the starting point of both Φ_T and Φ_Δ ranges of each dye in correlation with the O_2 inhibition period determined from its dye-catalysed PET-RAFT polymerisation system, and produced the lower limit fitting line; similarly, an upper limit fitting line was produced from the end points (**Figure 4.19**). Subsequently, to estimate the range of Φ_T for H1 from the corresponding oxygen inhibition period, we drew a horizontal line representing the oxygen inhibition period intersecting with the low and upper fitting lines; in this way, a Φ_T range of 0.82-0.90 was estimated for H1 (**Figure 4.19**).

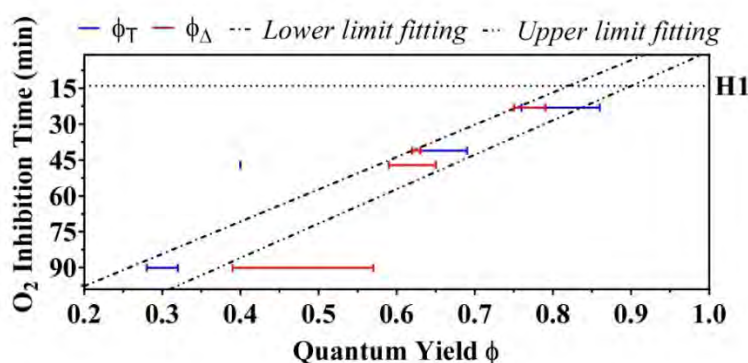


Figure 4.19 Deriving the estimated range of Φ_T and Φ_Δ of H1 by respectively fitting the lower limits and higher limits of the reported values of EB, EY, RB and PB, employing first-order approximation.

Indeed, after fitting the Φ_T and Φ_Δ for the four commercial dyes with a first-order approximation approach (**Figure 4.19**), the estimated Φ_T of H1 to be ranging between 0.82-0.90 is equivalent to that of ZnTPP. Considering that the k_p^{app} for PET-RAFT with H1 (0.012 min^{-1}) is like EY (0.014 min^{-1}), the design of H1 through consideration of the structure-property-performance relationships is considered successful.

4.3.6 An extension of the structure-property-performance relationship

To provide further examination and extension to the postulated relationships developed here, we tested one additional xanthene dye, eosin B (EOB). This molecule is interesting due to its substitution by highly electron-withdrawing nitro groups (-NO₂) on two of the X-positions (**Figure 4.20A**). Because of the reduced number of Br atoms on the xanthene core, ϵ_{\max} of EOB is only around a third of the value for EY. Additionally, due to the stronger electron-withdrawing -NO₂ groups, λ_{\max} of EOB is slightly red-shifted compared to EY (**Figure 4.20B**). Experimentally, performing PET-RAFT polymerisation with EOB as catalyst yielded $k_p^{\text{app}} = 0.003 \text{ min}^{-1}$ (**Figure 4.20C**) and an oxygen inhibition period of 35 min from the oxygen tolerance study (SI, **Figure 4.21A**). Based on the reduced oxygen inhibition period for EOB compared to EY, EOB should exhibit a higher Φ_T compared to EY, however, the xanthene core of EOB is only di-substituted with Br, and the heavy atom effect is not as significant for EB compared to EY. Interestingly, from the ground state frontier orbitals (**Figure 4.20E**), we observed distinct intermolecular charge shift character upon excitation, evidenced by accumulation of electron density on -NO₂ side of LUMO, which was also reported as charge transfer (CT) for EOB¹⁰⁷ (as it is not a typical donor-acceptor CT,³⁴ we prefer the term charge shift, which is used herein). This character is in principle due to the strongly electron-withdrawing -NO₂ groups distributed on a single side of the xanthene core, which results in a charge shift from Br to -NO₂ upon excitation (**Figure 4.20E**). This charge shift effect would reduce fluorescence and boost Φ_T by retarding back transition of S₁ to the ground state. In line with this recognition, incorporating intermolecular charge shift or more commonly donor-acceptor CT is widely known as another way to enhance Φ_T ^{35, 108-109} in addition to heavy atom effects. Indeed, the reported lower Φ_F below 0.1¹⁰⁷ and a higher $\Phi_T = 0.37$ ¹¹⁰ for EOB, compared to the four-Br-substituted EY (despite EOB being only di-substituted with Br), supported our assumption. As a result of the higher Φ_T , higher $\Phi_\Delta = 0.52$ was also reported,¹¹⁰ in line with the oxygen tolerance experiment where an oxygen inhibition period of 35 min was determined for EOB catalysed PET-RAFT (SI, **Figure 4.21A**).

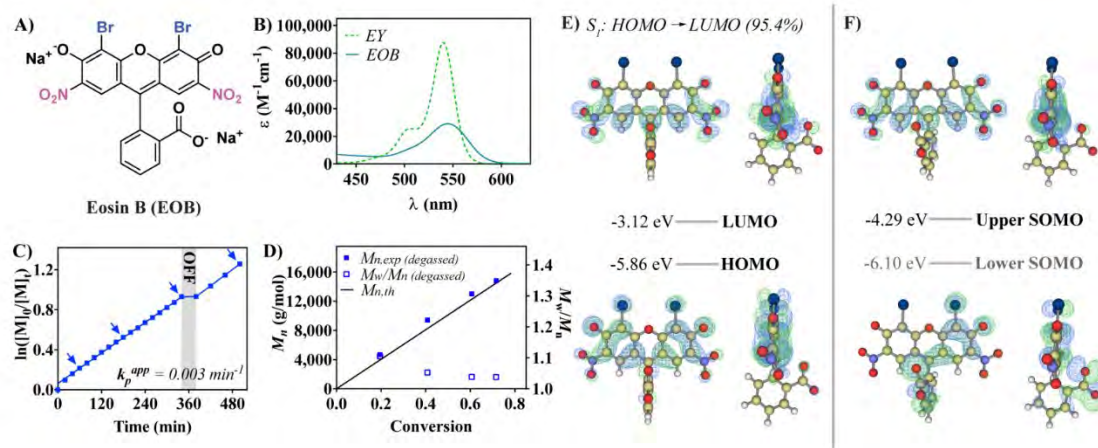


Figure 4.20 (A) EOB chemical structure, (B) UV-vis spectrum determined in DMSO using a typical PET-RAFT concentration, (C) evolution of $\ln([M]_0/[M]_t)$ versus time, (D) evolution of M_n and M_w/M_n versus monomer conversion of the EOB-catalysed PET-RAFT polymerisation. (E) EOB HOMO, LOMO and their energy levels and (F) EOB upper SOMO, lower SOMOs and their energy levels.

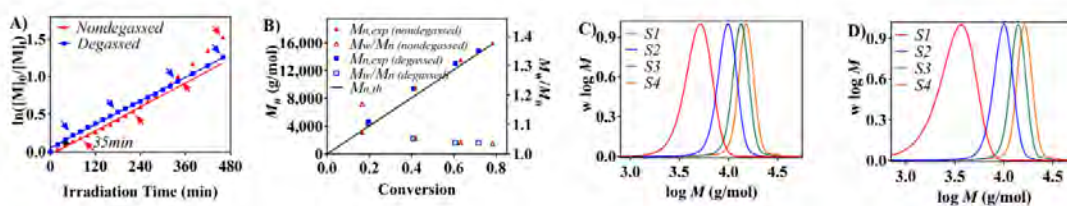


Figure 4.21 Oxygen tolerance study of PET-RAFT polymerisation catalysed by EOB. (A) plot of $\ln([M]_0/[M]_t)$ versus time to reveal k_p^{app} and temporal control; (B) M_n and PDI versus conversion; (C-D) molecular weight distribution of four GPC aliquots taken during polymerisation, denoted as S1, S2, S3, S4, which corresponds to blue arrows in (B) for polymerisation in the absence of oxygen (C) and red arrows in (B) in the presence of oxygen (D) according to time order.

Meanwhile, because of the presence of highly electron-withdrawing $-\text{NO}_2$, a computed $E^0(\text{PC}^{*+}/^3\text{PC}^*)$ as low as -0.72 V for EOB was revealed, which explained the lower k_p^{app} of EOB catalysed PET-RAFT (in spite of the higher Φ_T of EOB) and further strengthened the structure-property-performance relationship theories.

4.4 Conclusions

In this study, we demonstrate the compatibility of halogenated xanthene dyes with PET-RAFT polymerisation systems in the presence or absence of oxygen. By the aid of DFT calculations, detailed comparison of the dyes correlated their structures with their ability to mediate PET-RAFT polymerisation. A red-shift of λ_{\max} was achieved by the combined introduction of heavy halogens and electron-withdrawing substituents in the xanthene structure, whereas higher k_p^{app} were obtained by the introduction of heavy atoms (or CT character, to enhance Φ_T) and less electron-withdrawing/more electron-donating substituents (yielding more negative $E_0(\text{PC}^{*+}/{}^3\text{PC}^*)$). Through heavy atom substitution or incorporation of photoinduced intermolecular CT, better oxygen tolerance was achieved by increased Φ_Δ . Following the relationships, a new halogenated xanthene H1 was designed and synthesised allowing a more efficient oxygen-tolerant PET-RAFT system. To confirm our correlations, an additional xanthene dye, EOB with charge-shift characters, was investigated. By considering these structurally similar xanthene PCs, this work presents a fundamental understanding of the relationships of PC structures with their performances in PET-RAFT polymerisation, as well as their ability to confer oxygen-tolerance in these polymerisation systems.

4.5 References

- (1) Ciamician, G., *Science* **1912**, *36*, 385.
- (2) Boyer, C.; Corrigan, N. A.; Jung, K.; Nguyen, D.; Nguyen, T. K.; Adnan, N. N. M.; Oliver, S.; Shanmugam, S.; Yeow, J., *Chemical Reviews* **2016**, *116*, 1803.
- (3) Narayanam, J. M. R.; Stephenson, C. R. J., *Chemical Society Reviews* **2011**, *40*, 102.
- (4) Prier, C. K.; Rankic, D. A.; MacMillan, D. W. C., *Chemical reviews* **2013**, *113*, 5322.
- (5) Shaw, M. H.; Twilton, J.; MacMillan, D. W. C., *The Journal of Organic Chemistry* **2016**, *81*, 6898.
- (6) Chen, M.; Zhong, M.; Johnson, J. A., *Chemical Reviews* **2016**, *116*, 10167.
- (7) Corrigan, N.; Shanmugam, S.; Xu, J.; Boyer, C., *Chemical Society Reviews* **2016**, *45*, 6165.
- (8) Fors, B. P.; Hawker, C. J., *Angewandte Chemie International Edition English* **2012**, *51*, 8850.
- (9) Liu, Q.; Liu, L.; Ma, Y.; Zhao, C.; Yang, W., *Journal of Polymer Science Part A: Polymer Chemistry* **2014**, *52*, 3283.
- (10) Nzulu, F.; Telitel, S.; Stoffelbach, F.; Graff, B.; Morlet-Savary, F.; Lalevee, J.; Fensterbank, L.; Goddard, J. P.; Ollivier, C., *Polymer Chemistry* **2015**, *6*, 4605.
- (11) Pan, X. C.; Malhotra, N.; Zhang, J. N.; Matyjaszewski, K., *Macromolecules* **2015**, *48*, 6948.

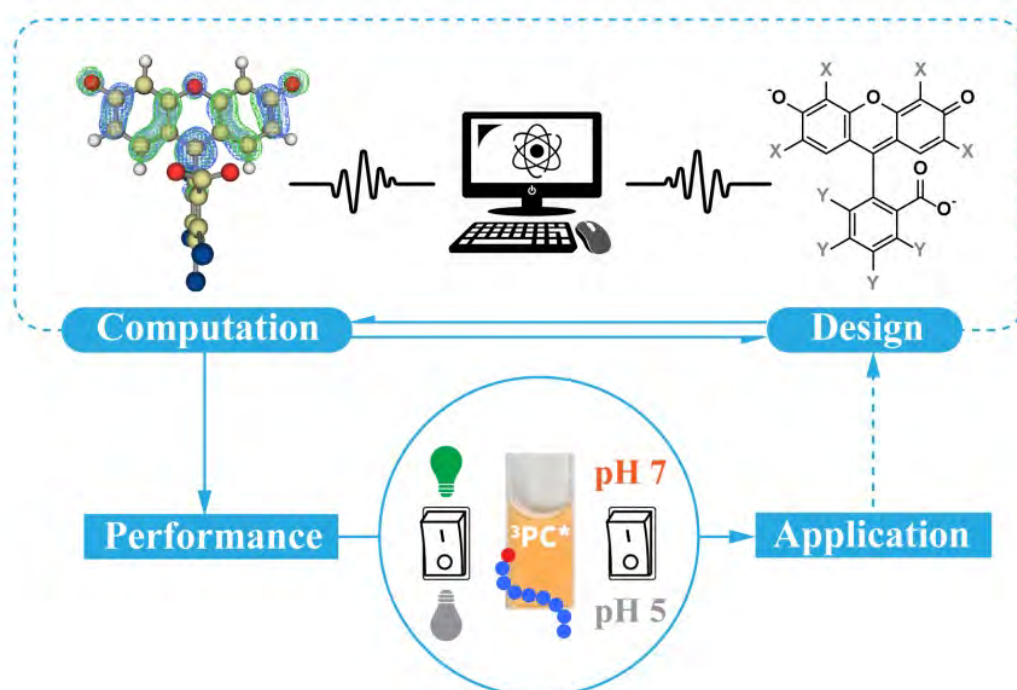
- (12) Yang, Q. Z.; Dumur, F.; Morlet-Savary, F.; Poly, J.; Lalevee, J., *Macromolecules* **2015**, *48*, 1972.
- (13) Shanmugam, S.; Xu, J.; Boyer, C., *Macromolecules* **2014**, *47*, 4930.
- (14) Shanmugam, S.; Xu, J.; Boyer, C., *Journal of the American Chemical Society* **2015**, *137*, 9174.
- (15) Tucker, B. S.; Coughlin, M. L.; Figg, C. A.; Sumerlin, B. S., *ACS Macro Letters* **2017**, *6*, 452.
- (16) Figg, C. A.; Hickman, J. D.; Scheutz, G. M.; Shanmugam, S.; Carmean, R. N.; Tucker, B. S.; Boyer, C.; Sumerlin, B. S., *Macromolecules* **2018**, *51*, 1370.
- (17) Aerts, A.; Lewis, R. W.; Zhou, Y.; Malic, N.; Moad, G.; Postma, A., *Macromolecular Rapid Communications* **2018**, *39*, e1800240.
- (18) Xu, J. T.; Jung, K.; Corrigan, N. A.; Boyer, C., *Chemical Science* **2014**, *5*, 3568.
- (19) Atilla, T. M.; Mustafa, U.; Yusuf, Y., *Macromolecular Chemistry and Physics* **2010**, *211*, 2271.
- (20) Atilla, T. M.; Mustafa, U.; Yusuf, Y., *Macromolecular Rapid Communications* **2011**, *32*, 58.
- (21) Pan, X.; Malhotra, N.; Simakova, A.; Wang, Z.; Konkolewicz, D.; Matyjaszewski, K., *Journal of the American Chemical Society* **2015**, *137*, 15430.
- (22) Zhang, T.; Chen, T.; Amin, I.; Jordan, R., *Polymer Chemistry* **2014**, *5*, 4790.
- (23) Treat, N. J.; Sprafke, H.; Kramer, J. W.; Clark, P. G.; Barton, B. E.; Read de Alaniz, J.; Fors, B. P.; Hawker, C. J., *Journal of the American Chemical Society* **2014**, *136*, 16096.
- (24) Pan, X. C.; Lamson, M.; Yan, J. J.; Matyjaszewski, K., *ACS Macro Letters* **2015**, *4*, 192.
- (25) Xu, J. T.; Shanmugam, S.; Duong, H. T.; Boyer, C., *Polymer Chemistry* **2015**, *6*, 5615.
- (26) Ohtsuki, A.; Lei, L.; Tanishima, M.; Goto, A.; Kaji, H., *Journal of the American Chemical Society* **2015**, *137*, 5610.
- (27) Theriot, J. C.; Lim, C. H.; Yang, H.; Ryan, M. D.; Musgrave, C. B.; Miyake, G. M., *Science* **2016**, *352*, 1082.
- (28) Pearson, R. M.; Lim, C. H.; McCarthy, B. G.; Musgrave, C. B.; Miyake, G. M., *Journal of the American Chemical Society* **2016**, *138*, 11399.
- (29) Du, Y.; Pearson, R. M.; Lim, C. H.; Sartor, S. M.; Ryan, M. D.; Yang, H.; Damrauer, N. H.; Miyake, G. M., *Chemistry* **2017**, *23*, 10962.
- (30) Liu, X. D.; Zhang, L. F.; Cheng, Z. P.; Zhu, X. L., *Polymer Chemistry* **2016**, *7*, 689.
- (31) Romero, N. A.; Nicewicz, D. A., *Chemical Reviews* **2016**, *116*, 10075.
- (32) Miyake, G. M.; Theriot, J. C., *Macromolecules* **2014**, *47*, 8255.
- (33) Allushi, A.; Jockusch, S.; Yilmaz, G.; Yagci, Y., *Macromolecules* **2016**, *49*, 7785.
- (34) McCarthy, B. G.; Pearson, R. M.; Lim, C. H.; Sartor, S. M.; Damrauer, N. H.; Miyake, G. M., *Journal of the American Chemical Society* **2018**, *140*, 5088.
- (35) Lim, C. H.; Ryan, M. D.; McCarthy, B. G.; Theriot, J. C.; Sartor, S. M.; Damrauer, N. H.; Musgrave, C. B.; Miyake, G. M., *Journal of the American Chemical Society* **2017**, *139*, 348.
- (36) Sartor, S. M.; McCarthy, B. G.; Pearson, R. M.; Miyake, G. M.; Damrauer, N. H., *Journal of the American Chemical Society* **2018**, *140*, 4778.
- (37) Singh, V. K.; Yu, C.; Badgujar, S.; Kim, Y.; Kwon, Y.; Kim, D.; Lee, J.; Akhter, T.; Thangavel, G.; Park, L. S.; Lee, J.; Nandajan, P. C.; Wannemacher, R.; Milian-Medina, B.; Luer, L.; Kim, K. S.; Gierschner, J.; Kwon, M. S., *Nature Catalysis* **2018**, *1*, 794.

- (38) Speckmeier, E.; Fischer, T.; Zeitler, K., *Journal of the American Chemical Society* **2018**.
- (39) Lu, J.; Pattengale, B.; Liu, Q.; Yang, S.; Shi, W.; Li, S.; Huang, J.; Zhang, J., *Journal of the American Chemical Society* **2018**.
- (40) Romero, N. A.; Margrey, K. A.; Tay, N. E.; Nicewicz, D. A., *Science* **2015**, *349*, 1326.
- (41) Margrey, K. A.; McManus, J. B.; Bonazzi, S.; Zecri, F.; Nicewicz, D. A., *Journal of the American Chemical Society* **2017**, *139*, 11288.
- (42) Romero, N. A.; Nicewicz, D. A., *Journal of the American Chemical Society* **2014**, *136*, 17024.
- (43) Griffin, J. D.; Zeller, M. A.; Nicewicz, D. A., *Journal of the American Chemical Society* **2015**, *137*, 11340.
- (44) McManus, J. B.; Onuska, N. P. R.; Nicewicz, D. A., *Journal of the American Chemical Society* **2018**, *140*, 9056.
- (45) Margrey, K. A.; Czaplyski, W. L.; Nicewicz, D. A.; Alexanian, E. J., *Journal of the American Chemical Society* **2018**, *140*, 4213.
- (46) McManus, J. B.; Nicewicz, D. A., *Journal of the American Chemical Society* **2017**, *139*, 2880.
- (47) Wilger, D. J.; Grandjean, J.-M. M.; Lammert, T. R.; Nicewicz, D. A., *Nature Chemistry* **2014**, *6*, 720.
- (48) Tay, N. E. S.; Nicewicz, D. A., *Journal of the American Chemical Society* **2017**, *139*, 16100.
- (49) Wilger, D. J.; Gesmundo, N. J.; Nicewicz, D. A., *Chemical Science* **2013**, *4*, 3160.
- (50) Nguyen, T. M.; Nicewicz, D. A., *Journal of the American Chemical Society* **2013**, *135*, 9588.
- (51) Nguyen, T. M.; Manohar, N.; Nicewicz, D. A., *Angewandte Chemie* **2014**, *126*, 6312.
- (52) Joshi-Pangu, A.; Lévesque, F.; Roth, H. G.; Oliver, S. F.; Campeau, L.-C.; Nicewicz, D.; DiRocco, D. A., *The Journal of Organic Chemistry* **2016**, *81*, 7244.
- (53) Gesmundo, N. J.; Nicewicz, D. A., *Beilstein Journal of Organic Chemistry* **2014**, *10*, 1272.
- (54) Perkowski, A. J.; Cruz, C. L.; Nicewicz, D. A., *Journal of the American Chemical Society* **2015**, *137*, 15684.
- (55) Otterstätter, G., *Coloring of Food, Drugs, and Cosmetics*. Taylor & Francis: 1999.
- (56) Kamikura, M., *Food Hygiene and Safety Science (Shokuhin Eiseigaku Zasshi)* **1970**, *11*, 242.
- (57) Register, O. F.; Register, U. S. D. o. t. F.; Division, U. S. F. R.; Register, U. S. O. o. t. F., *The Code of Federal Regulations of the United States of America*. U.S. Government Printing Office: 1991.
- (58) Aragona, P.; Di Stefano, G.; Ferreri, F.; Spinella, R.; Stilo, A., *Br J Ophthalmol* **2002**, *86*, 879.
- (59) Walton, W. R.; Research, U. S. O. o. N., *Techniques for Recognition of Living Foraminifera*. Scripps Institution of Oceanography: 1952.
- (60) Panzarini, E.; Inguscio, V.; Dini, L., *Cell Death Dis* **2011**, *2*, e169.
- (61) Xu, J.; Jung, K.; Atme, A.; Shanmugam, S.; Boyer, C., *Journal of the American Chemical Society* **2014**, *136*, 5508.
- (62) Corrigan, N.; Rosli, D.; Jones, J. W. J.; Xu, J. T.; Boyer, C., *Macromolecules* **2016**, *49*, 6779.
- (63) Wu, C.; Shanmugam, S.; Xu, J.; Zhu, J.; Boyer, C., *Chemical Communications (Camb)* **2017**, *53*, 12560.

- (64) Wilkinson, F.; Helman, W. P.; Ross, A. B., *Journal of Physical and Chemical Reference Data* **1993**, *22*, 113.
- (65) Inbaraj, J. J.; Kukielczak, B. M.; Chignell, C. F., *Photochemistry and Photobiology* **2005**, *81*, 81.
- (66) Jemli, M.; Alouini, Z.; Sabbahi, S.; Gueddari, M., *J Environ Monit* **2002**, *4*, 511.
- (67) Laskin, A. I.; Gadd, G. M.; Sariaslani, S., *Advances in Applied Microbiology*. Elsevier Science: 2009.
- (68) Neckers, D. C.; Valdes-Aguilera, O. M., Photochemistry of the Xanthene Dyes. In *Advances in Photochemistry*, John Wiley & Sons, Inc.: 2007; pp 315.
- (69) Fleming, G. R.; Knight, A. W. E.; Morris, J. M.; Morrison, R. J. S.; Robinson, G. W., *Journal of the American Chemical Society* **1977**, *99*, 4306.
- (70) Garland, P. B.; Moore, C. H., *Biochemical Journal* **1979**, *183*, 561.
- (71) Rodríguez Hernán, B.; Román Enrique, S.; Duarte, P.; Machado Isabel, F.; Vieira Ferreira Luis, F., *Photochemistry and Photobiology* **2012**, *88*, 831.
- (72) Talhavini, M.; Corradini, W.; Atvars, T. D. Z., *Journal of Photochemistry and Photobiology a-Chemistry* **2001**, *139*, 187.
- (73) Elcov, A. W.; Smirnova, N. P.; Ponyaev, A. I.; Martinova, W. P.; Schutz, R.; Hartmann, H., *Journal of Luminescence* **1990**, *47*, 99.
- (74) Ng, G.; Yeow, J.; Xu, J. T.; Boyer, C., *Polymer Chemistry* **2017**, *8*, 2841.
- (75) Gorman, A.; Killoran, J.; O'Shea, C.; Kenna, T.; Gallagher, W. M.; O'Shea, D. F., *Journal of the American Chemical Society* **2004**, *126*, 10619.
- (76) Majek, M.; Jacobi von Wangelin, A., *Accounts of Chemical Research* **2016**, *49*, 2316.
- (77) Xu, J.; Shanmugam, S.; Fu, C.; Aguey-Zinsou, K. F.; Boyer, C., *Journal of the American Chemical Society* **2016**, *138*, 3094.
- (78) Marcus, R. A., *The Journal of Chemical Physics* **1956**, *24*, 966.
- (79) Marcus, R. A., *The Journal of Chemical Physics* **1956**, *24*, 979.
- (80) Dieter, R.; Albert, W., *Berichte der Bunsengesellschaft für physikalische Chemie* **1969**, *73*, 834.
- (81) Zivic, N.; Bouzrati-Zerelli, M.; Kermagoret, A.; Dumur, F.; Fouassier, J. P.; Gignes, D.; Lalevee, J., *Chemcatchem* **2016**, *8*, 1617.
- (82) Shen, T.; Zhao, Z. G.; Yu, Q.; Xu, H. J., *Journal of Photochemistry and Photobiology a-Chemistry* **1989**, *47*, 203.
- (83) Li, X. Z.; Zhao, W.; Zhao, J. C., *Science in China Series B-Chemistry* **2002**, *45*, 421.
- (84) Hurst, J. R.; Mcdonald, J. D.; Schuster, G. B., *Journal of the American Chemical Society* **1982**, *104*, 2065.
- (85) Kottisch, V.; Michaudel, Q.; Fors, B. P., *Journal of the American Chemical Society* **2016**, *138*, 15535.
- (86) Michaudel, Q.; Kottisch, V.; Fors, B. P., *Angewandte Chemie International Edition English* **2017**, *56*, 9670.
- (87) Rybicka-Jasińska, K.; Shan, W.; Zawada, K.; Kadish, K. M.; Gryko, D., *Journal of the American Chemical Society* **2016**, *138*, 15451.
- (88) Margrey, K. A.; Czaplyski, W. L.; Nicewicz, D. A.; Alexanian, E. J., *Journal of the American Chemical Society* **2018**, *140*, 4213.
- (89) Lohmann, W., Halogen-Substitution Effect on the Optical Absorption Bands of Uracil*. In *Zeitschrift für Naturforschung C*, 1974; Vol. 29, p 493.
- (90) De Angelis, F.; Fantacci, S.; Evans, N.; Klein, C.; Zakeeruddin, S. M.; Moser, J. E.; Kalyanasundaram, K.; Bolink, H. J.; Gratzel, M.; Nazeeruddin, M. K., *Inorganic Chemistry* **2007**, *46*, 5989.

- (91) Baranoff, E.; Curchod, B. F. E.; Monti, F.; Steimer, F.; Accorsi, G.; Tavernelli, I.; Rothlisberger, U.; Scopelliti, R.; Grätzel, M.; Nazeeruddin, M. K., *Inorganic Chemistry* **2012**, *51*, 799.
- (92) Lennard-Jones, J. E., *Transactions of the Faraday Society* **1929**, *25*, 0668.
- (93) Hall, G. G., The Lennard-Jones paper of 1929 and the foundations of Molecular Orbital Theory. In *Advances in Quantum Chemistry*, Löwdin, P.-O.; Sabin, J. R.; Zerner, M. C., Eds. Academic Press: 1991; Vol. 22, pp 1.
- (94) Talapatra, G. B.; Rao, D. N.; Prasad, P. N., *Journal of Physical Chemistry* **1984**, *88*, 4636.
- (95) Lower, S. K.; El-Sayed, M. A., *Chemical Reviews* **1966**, *66*, 199.
- (96) Nagarajan, K.; Mallia, A. R.; Muraleedharan, K.; Hariharan, M., *Chem Sci* **2017**, *8*, 1776.
- (97) Levine, I. N., *Quantum Chemistry*. Pearson Education: 2009.
- (98) Koziar, J. C.; Cowan, D. O., *Accounts of Chemical Research* **2002**, *11*, 334.
- (99) Josefsen, L. B.; Boyle, R. W., *Met Based Drugs* **2008**, *2008*, 276109.
- (100) Corrigan, N.; Almasri, A.; Taillades, W.; Xu, J. T.; Boyer, C., *Macromolecules* **2017**, *50*, 8438.
- (101) Yeow, J.; Shanmugam, S.; Corrigan, N.; Kuchel, R. P.; Xu, J. T.; Boyer, C., *Macromolecules* **2016**, *49*, 7277.
- (102) Xu, S. H.; Ng, G.; Xu, J. T.; Kuchel, R. P.; Yeow, J.; Boyer, C., *ACS Macro Letters* **2017**, *6*, 1237.
- (103) Ng, G.; Yeow, J.; Chapman, R.; Isahak, N.; Wolvetang, E.; Cooper-White, J. J.; Boyer, C., *Macromolecules* **2018**.
- (104) Gormley, A. J.; Yeow, J.; Ng, G.; Conway, Ó.; Boyer, C.; Chapman, R., *Angewandte Chemie - International Edition* **2018**, *57*, 1557.
- (105) Singer, J.; Wachter, E. A.; Scott, T. C.; Lutz, M.; Babiak, K. Preparation of rose bengal analogs for pharmaceutical use. WO2011035161A1, 2011.
- (106) Pietrancosta, N.; Kessler, A.; Favre-Besse, F.-C.; Triballeau, N.; Quentin, T.; Giros, B.; Mestikawy, S. E.; Acher, F. C., *Bioorganic & Medicinal Chemistry* **2010**, *18*, 6922.
- (107) Fita, P.; Fedoseeva, M.; Vauthey, E., *Journal of Physical Chemistry A* **2011**, *115*, 2465.
- (108) Ware, W. R.; Richter, H. P., *The Journal of Chemical Physics* **1968**, *48*, 1595.
- (109) Zhang, X. F., *Photochem Photobiol Sci* **2010**, *9*, 1261.
- (110) Gandin, E.; Lion, Y.; Vandevorst, A., *Photochemistry and Photobiology* **1983**, *37*, 271.

Chapter 5 Fully Computer-Guided Rational Design of a pH-Responsive Organic Photocatalyst and Application for pH and Light Dual-Gated Polymerisation



In this chapter, a fully computer-guided strategy is adopted in rationally designing an efficient pH-switchable organic photocatalyst (OPC), sensitively turning colourless at pH 5 and recovering strong visible-light absorption and photoactivity at pH 7. This is the first example of an OPC design fully guided by comprehensive density functional theory (DFT) studies covering electrostatic, electrochemical, and photophysical predictions. Characterisation of the designed OPC after synthesis confirmed the computational predictions. This OPC was applied to mediate an aqueous photoinduced electron/energy transfer - reversible addition fragmentation chain transfer (PET-RAFT) polymerisation under green LED light (nominal emission wavelength: 530 nm, 5 mW/cm²). The polymerisation can be reversibly ceased by a slight change of pH (pH \leq 5.0) or in the absence of light. This is the first example of a pH and light dual-gated polymerisation system with complete and reversible inhibition.

5.1 Introduction

Catalysis plays a critical role in modern chemical processes as well as in nature; for instance, without enzymes, organisms would not be able to adapt to their environments and survive.¹⁻² One of the critical functions of catalysts (or enzymes) in biology is to activate specific chemical reactions and produce distinct proteins in response to a combination of external stimuli, such as pH, temperature, light or/and chemical stimuli. In contrast, traditional synthetic catalysts do not possess responsiveness to multiple stimuli and can usually only be switched “OFF” by the absence of one specific energetic driving force (reaction temperature, reactant concentration, etc.). The incorporation of stimuli-responsiveness into synthetic catalysts can open new opportunities in our modern chemical processes by allowing facile access to more complex reaction protocols, providing enhanced flexibility in the control of such processes.

For example, catalysts that can respond to multiple stimuli can potentially be used to simplify multistep reaction procedures via simple external regulation in a single reaction vessel. This simplification of reaction protocols is especially pertinent for the synthesis of macromolecular materials with defined architectures and microstructure; increased sophistication is generally accompanied by an increase in handling and purification steps.²⁻⁵ With the increasing need for functional polymers with controlled polymer sequences, tacticity, and topology, traditional synthetic strategies have inherent limitations.⁶⁻¹⁰

Furthermore, while controlled/living polymerisation techniques have provided polymer chemists and material scientists with the ability to impart fine control over polymer structures, the broad range of macroscopic properties required in modern polymer materials for their diverse applications dictates the need for an even greater level of control.¹¹⁻¹⁹ Hence, researchers actively seek external manipulation over polymerisation processes to increase the level of sequential, stereochemical, and topological control in synthetic polymer materials.² Recently, the concept of switchable catalysts for selectively toggling between multiple states upon external stimuli^{1,3} has become the most attractive solution to address this challenge. Switchable catalysts include those responding to one or more thermal,²⁰⁻²² pH,²³⁻²⁶ chemical,²⁷⁻²⁸ photochemical,²⁹⁻⁴⁵ electrochemical,⁴⁶⁻⁴⁸ redox,⁴⁹⁻⁵¹ or mechanical⁵²⁻⁵⁴ stimuli. As pH and visible light are triggers most commonly seen in the cellular control of natural processes²⁶ and do not necessarily interfere with

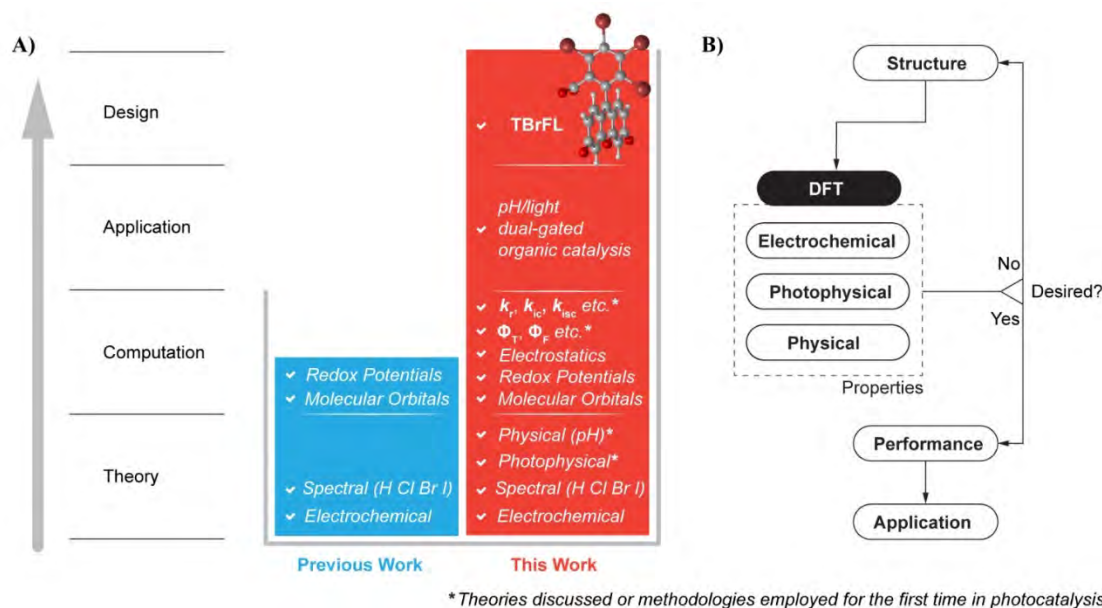
polymerisation and related processes, they are readily applicable, biocompatible, scalable, and arguably more orthogonal compared to other stimuli.² While visible-light control has been widely implemented in reversible deactivation radical polymerisation (RDRP),^{21, 29, 31-39, 41, 55-81} pH control with reversible inhibition over the course of polymerisation has much less been exploited. Current pH-gated systems rely on the transition-metal-based catalysts where pH control is either induced through blocking coordination sites⁸²⁻⁸⁴ or by changing the electron density around the metal center.⁸⁵⁻⁸⁶ Recently, we employed the latter strategy and demonstrated the first example of photo and pH dual-gated polymerisation using zinc meso-tetra (4-sulfonatophenyl) porphyrin (ZnTPPS⁴⁻) as photocatalyst in a photoinduced electron/energy transfer-reversible addition-fragmentation chain transfer (PET-RAFT) polymerisation system.²⁵ However, in that report, the polymerisation rate was only reduced below pH 3.5 and could not be completely stopped solely by pH modulation (partial inhibition by reduced electron density of the metal center at lower pH). Johnson and co-workers proposed another strategy where they prepared a temperature responsive organo-/hydrogel where 10-phenylphenothiazine (PTH) was covalently bound. These gels allowed facile control over the polymerisation by varying the temperature or by turning light “ON”/“OFF”.²¹ Despite these few examples, we still seek reversibly switchable catalysts that can be applied in a broader range of applications, especially bioapplications, under mild conditions. In this regard, a catalyst that can be switched by mild pH changes and visible light presents a superior alternative to other stimuli, particularly heat and electrochemistry. Additionally, fully organic catalytic systems are more favourable for bioapplications.⁸⁷⁻⁸⁸

From a scan of commercial pH-responsive molecules, we noticed that the structurally similar halogenated organic dyes eosin Y (EY) and phloxine B (PB) were reported as pH indicators responsive at different pH;⁸⁹ these molecules also exhibit desirable photophysical and electrochemical properties for PET-RAFT photocatalysis.⁹⁰ While EY turns bright yellow below pH 1.0, PB turns colourless below pH 2.0. Thus, PB can potentially serve as a pH/light-dual switchable photocatalyst. However, the harsh conditions at pH 2.0 may interfere with polymerisation and undoubtedly limits potential bioapplications. To tune the transition to milder pH ranges, we decided to investigate the structure-property relationship of similar organic dyes and their responsive pH; to streamline the experimental process, we employed a computationally aided strategy. In this way, the combination of predictions in both photocatalytic and pH-responsive

properties may enable judicious design of pH/light dual-responsive organic photocatalysts (OPCs) without laborious synthesis and screening processes.

Herein, we present a fully computer-guided strategy in discovering a highly pH-responsive OPC with high catalytic efficiency for dual-gated PET-RAFT polymerisation. Firstly, we associated the pH responsive nature of the halogenated dyes to their structure from electrostatic analysis, by the aid of density functional theory (DFT) calculations. Guided by Miyake and co-workers' highly inspiring work,^{57,91-94} very recent advances in computer-aided OPC design,⁹⁵⁻⁹⁷ and our previous experience⁹⁰ in studying structure-property-performance relationships for the development of highly efficient OPCs, we performed a comprehensive DFT investigation to predict a suitable candidate, and subsequently synthesised a desirable pH/light dual responsive OPC. Compared to previous contributions, this work is substantially advanced, with an expanded scope of theories discussed and computational methodologies employed (**Scheme 5.1**). In particular, this is the first computational example for OPCs where triplet quantum yield calculations were enabled (based on photophysical calculations of excited state decay rate constants, k_r , k_{ic} , k_{isc} , etc.) and transitions between excited states were successfully predicted; this was performed by combining the Gaussian 09 software package (DFT and TD-DFT calculations), the Molecular Materials Property Prediction Package (MOMAP)⁹⁸⁻¹⁰⁰ developed by Shuai and coworkers (excited state decay theory calculations), and the Beijing Density Functional (BDF) program package¹⁰¹⁻¹⁰⁴ (relativistic spin-orbit coupling calculations). Synthesis of the designed OPC and polymerisation under green light confirmed its highly efficient catalytic activity in neutral aqueous solution ("ON" state, strong orange colour, maximum absorption at ~500 nm, pH 7.0) and reversible inhibition at pH 5.0 ("OFF" state, colourless). Corresponding dual-gated PET-RAFT polymerisation with HCl/N₂ fumes to provide the pH 5.0 "OFF" state, and trace amounts of NaHCO₃ to recover the pH 7.0 "ON" state allows orthogonal visible-light- and pH-control. Additionally, CO₂ ($pK_a = 6.1$) and N₂ were introduced as conceptual gas controlled logic gates in gas and light dual-gated PET-RAFT polymerisation, where a gas-induced retardation was achieved after brief CO₂ purging (apparent polymerisation rate, k_p^{app} , cut down by half); the gas-gated "ON" state was recovered after N₂ purging. As the pH/light dual-gated strategies employed in this work present highly reversible control without any liquid phase, and do not interfere with any

aspect of the polymerisation process, this strategy is capable of rapid orthogonal switching over the course of polymerisation.



Scheme 5.1 (A) Comparison of the current work with our previous work.⁹⁰ Whereas the previous work revealed the foundations for structure-property-performance (SPP) relationships of OPCs in the scope of PET-RAFT polymerisation, the current work expands upon the SPP relationships to physical and photophysical properties by predicting quantum yields and excited state transition rate constants. Additionally, this work demonstrates a fully computer-guided catalyst design (TBrFL) for application in the first reported example of pH/light dual-gated organic catalysis. (B) Flow chart of application-directed OPC design fully guided by computational predictions.

5.2 Experimental section

5.2.1 Synthesis of the RAFT agent: BTPA-M

The precursor 2-(*n*-butyltrithiocarbonate)propionic acid (BTPA) was synthesised according to literature.¹⁰⁵ The synthesis of BTPA-M was performed by esterification of BTPA with methanol in the presence of DCC/DMAP. A mixture of BTPA (348 mg, 1.465 mmol, 1 equiv.), methanol (84.97 mg, 2.930 mmol, 2 equiv.) and DMAP (18 mg, 0.145 mmol) were weighed into a 10 mL round bottom flask with a magnetic stir bar. The flask was purged under nitrogen and dry DCM (3.75 mL) was added. Upon stirring until the mixture was fully dissolved, the flask was placed in an ice-water bath during stirring and a separate solution of DCC (301.5mg, 1.465 mmol) in dry DCM (1.25 mL) was added

dropwise. The mixture was stirred for 10 min in the water-ice bath and sealed with a rubber septum, purged with nitrogen for another 5 min. Subsequently, the nitrogen inlet and outlet were both removed leaving the flask properly sealed to avoid evaporation of methanol or DCM. The mixture continued to be stirred overnight resulting in a uniform light yellow suspension. The suspension was placed in dark till dryness and redissolved in 5 mL hexane revealing a clear yellow solution and white precipitates. After removing the white precipitates by the centrifuge method, the yellow solution ran through a silica column with hexane/ethyl acetate 10:3 (v/v). The collected yellow solution was evaporated under reduced pressure until dryness yielding BTPA-M as a golden yellow liquid (254 mg, 68.9% yield). The obtained product was then characterised by ^1H NMR (**Figure 5.1**) and ^{13}C NMR (**Figure 5.2**) with CDCl_3 as the solvent. It should be noted that the central carbon of the trithiocarbonate ($-\text{S}-\text{C}(=\text{S})-\text{S}-$) cannot be seen in Figure 5.2 because it was identified as a ($\text{R}-\text{C}(=\text{S})-\text{R}'$) which should appear at >220 ppm beyond the measured scope.

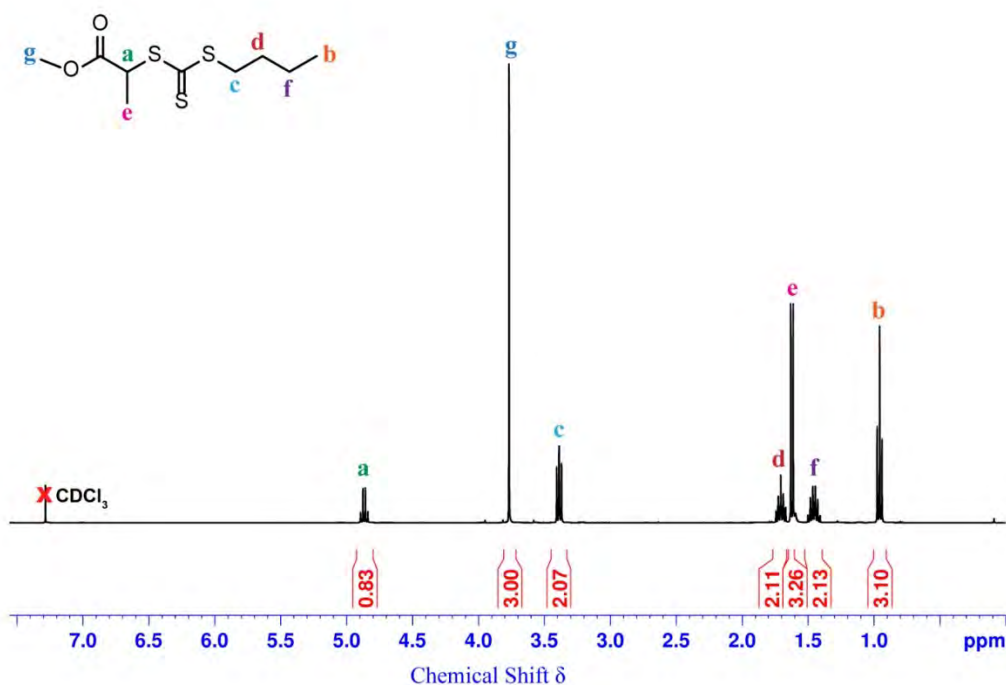


Figure 5.1 ^1H NMR spectrum (400 MHz, CDCl_3) of the synthesised BTPA-M.

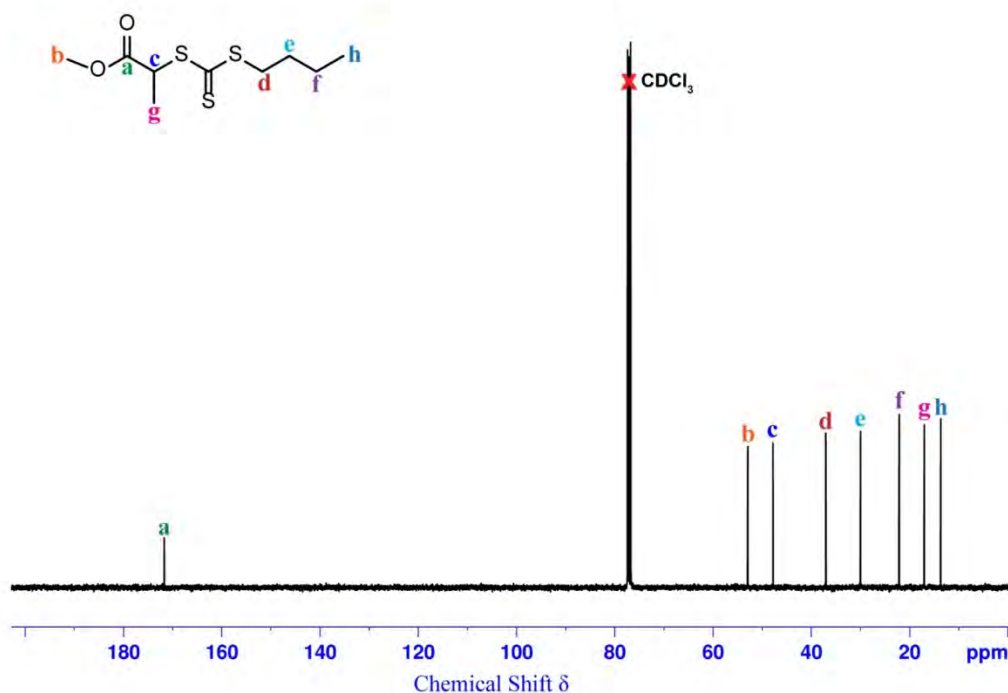


Figure 5.2 ^{13}C NMR spectrum (400 MHz, CDCl_3) of the synthesised BTPA-M.

5.2.2 General procedures for PET-RAFT polymerisation

Deionized water (266 μL), DMA (0.416 g, 4.20 mmol), BTPA-M (4.90 mg, 19.4 μmol) and TBrFL (the designed catalyst, vide infra, 134 μL of 1 mg/mL TBrFL stock solution in deionized water, 0.194 μmol) were mixed in a glass vial as stock solution. The stock solution was divided in halves and either half (0.4 mL) was transferred into a 0.9 mL FTNIR glass cuvette (1 cm \times 2 mm \times 5 cm) sealed with rubber septa and covered with aluminium foil. One of the sealed cuvettes was degassed with nitrogen for 10 min while the other left as prepared (non-degassed). The glass cuvettes were then sent for irradiation at 5 mW/cm² of 530 nm green light under an Oriel VeraSol LED solar simulator at room temperature. The cuvettes were transferred in sequence to a sample holder manually for FTNIR measurements at specific time points. Monomer conversions were calculated by taking the ratio of integrations of the wavenumber area 6210-6115 cm⁻¹ for all curves at different reaction times to that of time zero. Aliquots were taken occasionally during the reaction for GPC analysis to determine number average molecular weights (M_n), polydispersities (M_w/M_n) and molecular weight distributions. In the process of preparation, it should be noted that BTPA-M was weighed in the glass vial first and then dissolved by

the liquid-state monomer DMA. Deionized water and the TBrFL solution was mixed in afterwards, producing a uniform suspension due to poor solubility of BTPA-M in water. However, this does not affect polymerisation in any aspect and the suspension becomes clear once polymerisation gets started. Herein, BTPA-M was used to retain the neutral condition of the polymerisation system (the acidity of BTPA will lower the polymerisation solution to a pH below 5). If there is a certain need of a clear starting solution for some reason, PEGylated BTPA can be used instead.

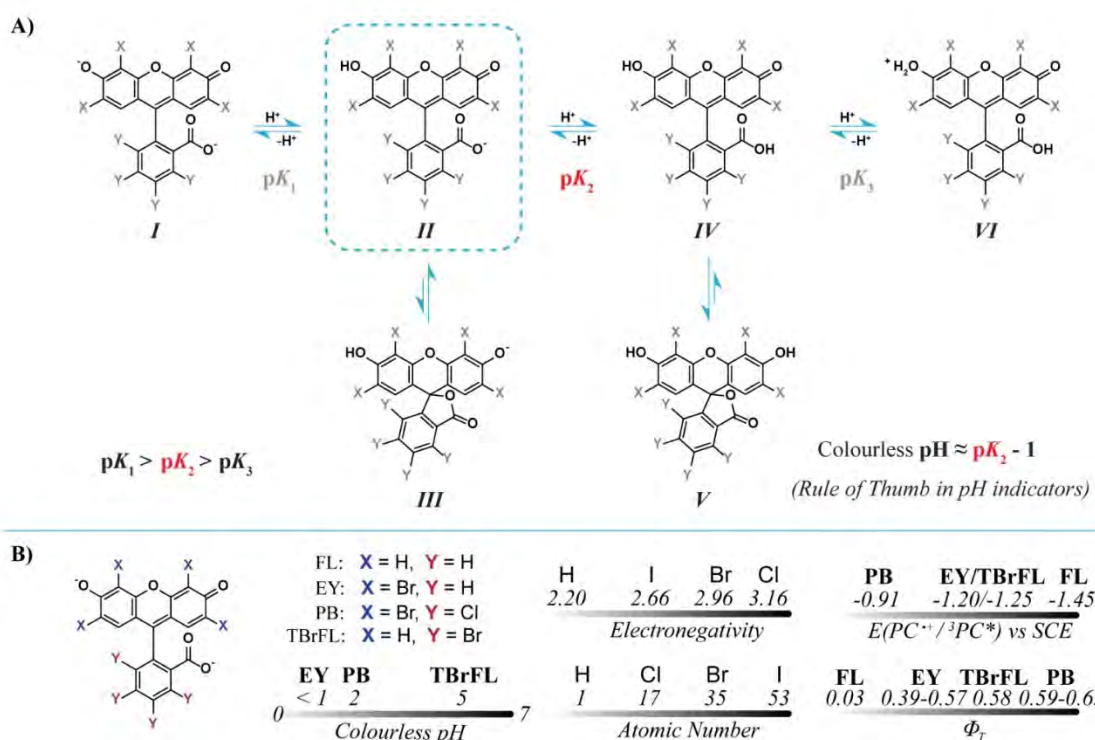
5.2.3 Polymer purification

After polymerisation, 0.5 mL of the aqueous polymer solution was collected and dried under reduced pressure until dryness. Subsequently, the crude solid was dissolved with minimal DCM and the resultant solution was added dropwise to 12 mL diethyl ether/petroleum spirit 7:3 (v/v) for precipitation. After centrifuging, the precipitates were collected and left dry before dissolving in minimal DCM. By repeating this centrifugation process for a couple of times until the precipitate is a uniform and well-defined layer, the obtained solid was placed under reduced pressure until dryness overnight.

5.3 Results and discussion

5.3.1 Establishing structure-property relationships for functional OPC design

In a typical quantum chemical view, all the properties and thus derived functionalities of a molecule stem from its molecular/chemical and electronic structures. In the context of this work, structure-property relationships refer to how the structure of xanthene dyes affects their (i) pH-responsive properties (**Scheme 5.2 A-B**) and (ii) photophysical/electrochemical properties that determine their catalytic capability (**Scheme 5.2 B**). To enable a wholly computer-based methodology in guiding the design of new functional OPCs, explicit understanding of these structure-property relationships is required.



Scheme 5.2 (A) pH dependence of fluorescein derivative equilibria.¹⁰⁶⁻¹⁰⁷ Structure *I* is the major and most stable light-absorbing species whereas structure *V* is the major and most stable ring-closed colourless species. pK_2 is the key pK_a equilibrium constant that describes the critical point for the change between a light-absorbing-species-dominant condition and a colourless-species-dominant condition. According to the rule of thumb in pH indicators, dye solutions visually turn colourless at the colourless $pH \approx pK_2 - 1$.¹⁰⁸ (B) Summary of structure-property relationships investigated in this work to guide OPC design. Structure of FL, EY, PB, and the designed TBrFL with substituent variations (left); colourless pH (physical property, middle left bottom); electronegativity and atomic number of the substituents in comparison (middle right); electrochemical and photophysical properties (determining photocatalysis efficacy) of FL, EY, PB, and the designed TBrFL (right).

5.3.2 Structure-property relationship: electrostatic studies of pH-responsive xanthene dyes

As we demand an OPC with facile pH-response, the most desirable candidates should be capable of structure toggling at different pH values to exhibit reversible discolouration or significant spectral variation. Many existing pH indicators could match this standard, which include a class of both naturally occurring dyes (such as the anthocyanin families

in plants) and synthetic organic dyes (over 50 acid-base indicators spanning across the pH scale⁸⁹). These pH indicators have found broad applications in biology and analytical chemistry.⁸⁹ However, none of these existing dyes are good candidates as they either lack capability (or not discovered yet) in PET-RAFT polymerisation or complete colour transitions at extreme pH values (e.g. EY at pH < 1 and PB at pH = 2). We argue that pH 5-8 is more practical for facile pH modulation and potential bioapplications. Despite the profound tradition in applications of pH indicators, there was little understanding of their pH-responsive nature from the structure-property relationship perspective, due to a lack of accessibility to molecular electrostatic characterisation in early works. To uncover this knowledge, we started investigating EY and PB, which are highly analogous in structure and only differ in halogen substitution (**Scheme 5.2B**). While PB is capable of transitioning to a colourless state at pH 2.0, EY retains yellow colouring and cannot be turned colourless even below pH 1.0.⁸⁹ Seizing this trend, we decided to correlate the structure of EY and PB with their pH-responsive properties.

As long recognized by synthetic chemists, colour transition occurs when the disodium salt form of fluorescein derivative (structure **I**, **Scheme 5.2A**) is doubly protonated and converted to the ring-closed colourless species (structure **V**, **Scheme 5.2A**).¹⁰⁶⁻¹⁰⁷ The pK_a equilibrium constant pK_2 in **Scheme 5.2A** describes the critical point for the change between a light absorbing species-dominant condition and a colourless species-dominant condition. As a widely accepted rule of thumb, the pH range for colour transition of all pH indicators falls between pK_a value minus one (the acid form) and pK_a plus one (the salt form).¹⁰⁸⁻¹⁰⁹ Therefore, the colourless pH (the dye solution visually turns colourless) in the context of this work basically refers to colourless pH = $pK_2 - 1$ (**Scheme 5.2A**). Meanwhile, as seen from **Scheme 5.2A**, the electrostatic nature of the structure **II** species should describe how easily the second protonation occurs, thus determining pK_2 and the colourless pH. In this regard, we decided to investigate the structure **II** intermediates of EY (**Figure 5.3A**, left, colourless pH < 1) and PB (**Figure 5.3A**, middle, colourless pH = 2) to determine the structure-property relationships regarding the pH-responsive properties of fluorescein derivatives.

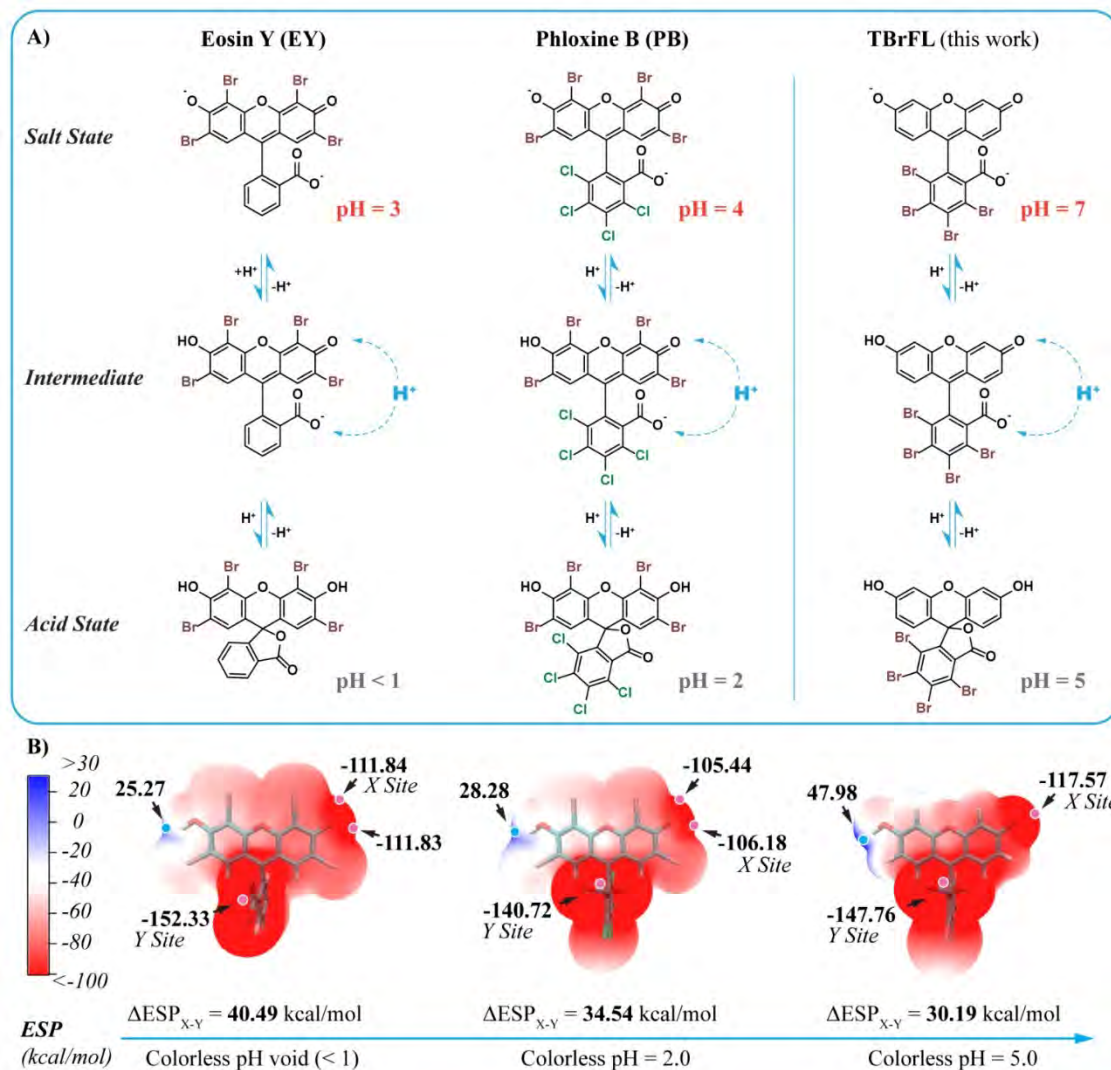


Figure 5.3 (A) Mechanism of the structural transition with response to specific pH (indicated below the corresponding dye structure at that pH) for EY (left), PB (middle), and the designed tetrabrominated benzoic acid group substituted-fluorescein (TBrFL, right).¹⁰⁶ (B) Electrostatic potential (ESP) maps (presented as molecular surface coloured by ESP) calculated at the mono-protonated “intermediate” state structure of EY (left), PB (middle), and TBrFL (right) with the extreme points of interest indicated, correlating with their colourless transition pH (bottom). DFT calculations were performed at the BLY3P level of theory with the 6-31+G** basis set for C H O and the LanL2DZ basis set for heavy atoms Cl and Br under the SMD-water solvation model.

As shown in the equilibria (**Scheme 5.1A**), pK_2 describes the equilibrium between structure **II** and **IV**; the further the equilibrium is driven towards **IV**, the higher the pK_2

and colourless pH of the dye will be. Additionally, if the transition from structure **IV** to structure **V** is more preferred (more consumption of **IV**), the pK_2 equilibrium will be driven toward **IV** and result in a higher colourless pH (**Scheme 5.2A**). Based on the wave functional data from DFT calculations, we performed electrostatic analysis on the mono-protonated intermediates of EY and PB.

Electrostatic potential (ESP) maps of the mono-protonated intermediate of EY (EYH⁻) and PB (PBH⁻) were calculated to evaluate their capability in capturing a proton to form the ring-closed structure. Geometry optimization for the ground state EYH⁻ and PBH⁻ was performed at the B3LYP level of theory with the 6-31+G** basis set for C H O and the LanL2DZ basis set for Br and I. The SMD solvation model of water was employed. Quantitative analysis of the molecular surface was performed with the Multiwfn software package.¹¹⁰ ESP maps were visualized by the VMD package.¹¹¹ As shown in the respective electrostatic potential (ESP) maps for EY and PB (**Figure 5.3B**, left: EY and middle: PB), the intermediate has a negative charge shared around both the deprotonated hydroxyl group on the xanthene core (*X site*) and the deprotonated carboxyl group on the benzoic acid (*Y site*), indicated in **Figure 5.3B**. As both the *X* and the *Y* sites are possible sites for protonation, the difference between ESPs of the *X/Y sites* (ΔESP_{X-Y}) should represent the ability for the *X site* to abstract a proton compared to the *Y-site*, in turn prompting formation of the closed ring species (**Figure 5.3B**). In other words, the lower the value for ΔESP_{X-Y} is, the more easily the **IV** to **V** transition will occur, which drives the pK_2 equilibrium toward **IV** and results in a higher colourless pH. Indeed, EY is characterised by a high ΔESP_{X-Y} of 40.40 kcal/mol and displays a colourless transition below pH 1.0, while PB has a lower ΔESP_{X-Y} of 34.54 kcal/mol and displays a colourless transition at pH 2.0 (**Figure 5.3B**).

Based on their chemical structures, we noted that the lower ΔESP_{X-Y} of PB, compared to EY, was due to the additional four electron-withdrawing chlorine (Cl) atoms in the benzoic acid group, which actively draw the negative ESP from the carboxyl *Y site*. With this knowledge, we postulated that for fluorescein derivatives with equivalent structure, more electron-withdrawing substituents on the benzoic acid group and less electron-withdrawing groups on the xanthene core should afford a dye with lower ΔESP_{X-Y} and hence higher/milder colourless transition pH. In the context of this work, H substituents

in the xanthene core and a maximum of four halogens ($F > Cl > Br > I$ in electron-withdrawing ability) will be the most ideal structure (**Scheme 5.2B**).

5.3.3 Structure-property relationship: photophysical and electrochemical studies of OPCs

To enable pH/light dual-gated catalysis, the OPC should exhibit sufficient photocatalytic efficacy simultaneously with high colourless pH by the aforementioned principle. As demonstrated in recent studies by Miyake et al.,^{57, 91-94, 112} our recent collaborative work,⁹⁰ and also in organic photocatalysis,¹¹³ the long-lived lowest triplet excited state (T_1) of most OPCs should be the catalytically active state for PET-RAFT polymerisation, with lifetimes (τ_T) at the sub-ms to ms level. Hence, the T_1 oxidative potential $E^0(PC^{*+}/{}^3PC^*)$ and the T_1 quantum yield, Φ_T , should jointly determine the efficacy of an OPC in catalysing PET-RAFT polymerisation.

As explicitly illustrated in the previous report,⁹⁰ less electron-withdrawing substituents lead to more negative $E^0(PC^{*+}/{}^3PC^*)$ values and thus higher PET-RAFT catalytic efficiency (**Scheme 5.2B**). On the other hand, higher Φ_T indicates a higher probability of populating T_1 , which will enhance the conversion efficiency of an absorbed photon for the PET process in PET-RAFT polymerisation.^{90, 94} Higher Φ_T can be achieved by introducing heavier atoms (heavy atom effect, HAE)⁹⁰ to enhance spin-orbit coupling (SOC) between singlets and triplets, or by providing charge transfer excited states⁹⁴ or core-twisted structures¹¹⁴ to retard fluorescence. As this aspect has not been clearly revealed, herein we decided to firstly illuminate the structure-property relationships by examining the electronic structure and excitations in a relativistic quantum chemical view.

In the context of this work, Φ_T of fluorescein derivatives can be easily tuned by varying halogen substituents. This halogenation strategy is based on the HAE, where SOC between singlet and triplet excited states is enhanced by increasing the atomic number of substituents.¹¹⁵ Consequently, the enhanced SOC increases the rate constants of spin-forbidden transitions (e.g. intersystem crossing constant, k_{isc}) and thereby boosts Φ_T of the molecule.^{90, 115} As reported in the literature, FL bears a fluorescence rate constant k_f of $2.1 \times 10^8 \text{ s}^{-1}$, an internal conversion rate constant from the S_1 to the S_0 state (k_{ic}) of 50 s^{-1} , and a k_{isc} from the S_1 to the T_1 state of $6.6 \times 10^6 \text{ s}^{-1}$, which results in a very low Φ_T of 0.03.¹⁰⁶ As discussed in the previous section, installation of four electron-withdrawing halogens in the benzoic acid group of fluorescein would be favourable for a more pH-

responsive dye. Among halogens, fluorine (F) exhibits much higher electronegativity than others (**Scheme 5.2B**) and thus should have the greatest effect on the pH sensitivity. However, as F is a light atom it only scarcely enhances Φ_T due to the absence of notable HAE, and also greatly weakens $E^0(PC^{*+}/{}^3PC^*)$ compared to fluorescein. Cl and Br bear similar electronegativity, and indeed, electrostatic studies reveal highly similar ΔESP_{X-Y} between the halogenated benzoic acid group of four-Br-substituted fluorescein (TBrFL, 30.19 kcal/mol) and the halogenated benzoic acid group of four-Cl-substituted fluorescein (TCIFL, 29.99 kcal/mol). On the other hand, Br substituents should provide more pronounced HAE, since relativistic effects in the fourth period elements provide sufficiently enhanced SOC,¹¹⁶ while Cl is still considered a light element.¹¹⁷ Additionally, we investigated the photophysical properties of TBrFL by DFT calculations; k_f of TBrFL was revealed as $2.1 \times 10^8 \text{ s}^{-1}$, which is identical to that of FL (reported $2.1 \times 10^8 \text{ s}^{-1}$)¹⁰⁶ due to the same localized excitation in their shared xanthenic core chromophore. Also like FL, the k_{ic} of TBrFL was calculated to be negligible ($6.9 \times 10^3 \text{ s}^{-1}$). Despite these similarities, as expected, installation of Br on the benzoic acid group provided TBrFL with considerable SOC compared to FL, which results in $k_{isc} = 3.2 \times 10^8 \text{ s}^{-1}$ and consequently $\Phi_T = 0.58$. This calculated Φ_T of TBrFL is sufficient for serving as a PET-RAFT OPC. It should be noted that using even heavier iodine (I) substituents will reduce the pH sensitivity because of lower electronegativity (**Scheme 5.2B**), and as such, it is not a worthwhile candidate for this work.

5.3.4 Quantum chemical calculations

5.3.4.1 Calculation for ESP maps

ESP maps of the mono-protonated intermediate of Eosin Y (EYH⁻), Phloxine B (PBH⁻) and TBrFLH⁻ (**Figure 5.3**) were calculated to evaluate their capability in capturing a proton to form the ring-closed structure. Geometry optimization for the ground state EYH⁻, PBH⁻, TBrFLH⁻ and TCIFLH⁻ was performed at the B3LYP level of theory with the 6-31+G** basis set for C H O and the LanL2DZ basis set for Br and I. The SMD solvation model of water was employed. Quantitative analysis of the molecular surface was performed with the Multiwfn software package.¹¹⁰ ESP maps were visualized by the VMD package.¹¹¹ In addition, The ESP potential minima of TCIFLH⁻ (*X-site* -146.11 kcal/mol, *Y-site* -116.12 kcal/mol) are very similar to those of TBrFLH⁻.

5.3.4.2 Calculation for frontier orbitals and spectral properties

Visualization of frontier orbitals was performed with the Multiwfn software package.¹¹⁰ TD-DFT calculations were performed with the td(50-50, nstates=10) keyword.

5.3.4.3 Calculation for redox potentials

Standard redox potentials (E_0) were calculated according to literature,^{57, 92, 118} where $E_0 = (-100.5 - \Delta G)/23.06$ (V vs. SHE),^{57, 118} $\Delta G = G(^3PC^*) - G(PC^{*+})$ for $E^0(PC^{*+}/^3PC^*)$, while for $E_0(PC^{*+}/PC)$. Triplet energies of PCs were obtained by $^3\Delta G^* = G(^3PC^*) - G(PC)$, in kcal/mol. The Gibbs free energies of $G(^3PC^*)$, $G(PC^{*+})$, and $G(PC)$ were calculated at B3LYP level of DFT theory in SMD-water solvent (single point energy) using geometries optimized at B3LYP level of theory in SMD-water solvent. 6-31+G** basis set were employed for light atoms H, C and O whereas LanL2DZ was included for heavy atoms Cl, Br and I, which was proved to be accurate mixed basis sets for heavy-atom containing molecules.¹¹⁹ All E_0 (vs. SHE) were converted to E^0 (vs. SCE) by E^0 (vs. SCE) = E^0 (vs. SHE) - 0.24 V. TD-DFT calculations were also performed to predict contribution of transitions to S_1 with td = (50-50, nstates = 10).

5.3.4.4 Calculation for the radiative decay (fluorescence) rate constant

The radiative decay (fluorescence) rate constant k_f of TBrFL ($k_f = 2.19292941 \times 10^8$ s⁻¹) was calculated by the MOMAP software toolkit⁹⁸⁻⁹⁹ based on the Fermi's Golden Rule and the Born-Oppenheimer approximation in consideration of the Duschinsky effect and the Herzberg-Tell effect. Minimum energy structures of the lowest excited state (S_1) and the ground state (S_0) were optimized by Gaussian 09 software package at the B3LYP level of theory with the 6-31+G** basis set for C H O and the LanL2DZ basis set for Br and I in SMD-water solvent. The adiabatic excitation energy E_{ad} was calculated by the change between the adiabatic S_1 energy and the S_0 energy. The electronic transition dipole moment absorption (EDMA) was derived based on the optimized S_0 structure and the electronic transition dipole moment emission (EDME) was derived from the optimized S_1 structure.

5.3.4.5 Calculation for the non-radiative radiative decay (internal crossing) rate constant

The non-radiative decay (internal crossing) rate constant k_{ic} of TBrFL ($k_{ic} = 6.91663949 \times 10^3$ s⁻¹) was calculated by the MOMAP software toolkit.⁹⁸⁻⁹⁹ Minimum energy structures of the lowest excited state (S_1) and the ground state (S_0) were included. The non-adiabatic coupling matrix elements were obtained.

5.3.4.6 Calculation for the spin-orbit coupling (SOC) matrix elements

As the intersystem crossing processes require spin-orbit coupling (SOC) to overcome the spin-forbidden transitions, SOC matrix elements need to be calculated beforehand as input to the MOMAP software.

The past decades have seen a surge in relativistic quantum chemistry¹¹⁶ and modern computation capacity, which recently has made relativistic quantum mechanical studies on molecules readily possible. Now using Beijing Density Functional (BDF) program package¹⁰⁴ developed by Wenjian Liu et al, SOC matrix elements between singlet/triplet excited states can be revealed.¹⁰¹⁻¹⁰³ Apart from the SOC matrix element module between T₁ and S₁ ($|\langle S_1 | H_{\text{soc}} | T_1 \rangle| = 0.61 \text{ cm}^{-1}$), intersystem coupling between S₁ and T₂ is also favourable, which exhibits $|\langle S_1 | H_{\text{soc}} | T_2 \rangle| = 28.33 \text{ cm}^{-1}$. Minimum energy structure of T₂ was optimized by Gaussian 09 software package using td(root=2,nstates=5) at B3LYP level of theory with the 6-31+G** basis set for C H O and the LanL2DZ basis set for Br and I in SMD-water solvent. The optimized structure was then input in BDF package¹⁰⁴ for SOC calculations with the sf-X2C-TD-DFT/soc-DKH1 approach¹⁰¹⁻¹⁰³ in conjunction with the B3LYP functional and the cc-pVTZ-DK basis set.

5.3.4.7 Calculation for the intersystem crossing rate constants $k_{\text{isc}2}$, $k_{\text{isc}2}$ and $k_{\text{risc}2}$

The second intersystem crossing (S₁ → T₂) rate constant $k_{\text{isc}2}$ of TBrFL ($k_{\text{isc}2} = 3.23 \times 10^8 \text{ s}^{-1}$) was calculated by the MOMAP software toolkit⁹⁸⁻⁹⁹ with $|\langle S_1 | H_{\text{soc}} | T_2 \rangle| = 28.33 \text{ cm}^{-1}$ calculated by BDF.¹⁰¹⁻¹⁰⁴ Minimum energy structures of S₁ and T₂ were included, with coordinates as listed in previous sections. At the same time, the reversed second intersystem crossing (T₂ → S₁) rate constant $k_{\text{risc}2}$ of TBrFL is ($k_{\text{risc}2} = 1.9 \times 10^{10} \text{ s}^{-1}$) because of a bit higher energy of T₂ than S₁ (see the following section). Despite $k_{\text{risc}2}$ being two orders of magnitude greater than $k_{\text{isc}2}$, the following T₂ → T₁ internal crossing has an even higher rate constant $k_{\text{Tic}} = 1.08 \times 10^{12} \text{ s}^{-1}$, which naturally prohibits T₂ → S₁ and only favours T₂ → T₁ transitions (see the following section).

The first intersystem crossing (S₁ → T₁) rate constant $k_{\text{isc}1}$ of TBrFL ($k_{\text{isc}1} = 1.91 \times 10^6 \text{ s}^{-1}$) was calculated by the MOMAP software toolkit⁹⁸⁻⁹⁹ with $|\langle S_1 | H_{\text{soc}} | T_1 \rangle| = 0.61 \text{ cm}^{-1}$ calculated by BDF.¹⁰¹⁻¹⁰⁴ Minimum energy structures of S₁ and T₁ were included, with coordinates as listed in previous sections.

5.3.4.8 Transition map and calculation of triplet quantum yield Φ_T of TBrFL

Historically, the photophysical HAE was discovered in 1949 by McClure with regard to phosphorescence lift times (τ_{ph})¹²⁰ and later expanded to phosphorescence quantum yields (Φ_{ph}) by Ermolaev, Svitashv and LaPaglia.¹²¹⁻¹²² However, due to limitations that only Φ_{ph} and τ_{ph} can be experimentally observed (the real Φ_T which includes both irradiative parts and non-irradiative parts of multiple related transitions is not experimentally accessible), in the next half century till now, little advances in the study of the HAE have occurred. Meanwhile, the past decades have seen a surge in relativistic quantum chemistry¹¹⁶ and modern computational capacity, which has made relativistic quantum mechanical studies on the HAE readily possible. Now the HAE on Φ_T and all other photophysical properties can be mechanistically understood by using the Beijing Density Functional (BDF) program package¹⁰¹⁻¹⁰⁴ by Wenjian Liu et al to reveal SOC matrix elements between singlet/triplet excited states and using Molecular Materials Property Prediction Package (MOMAP)⁹⁸⁻¹⁰⁰ by Zhigang Shuai et al to investigate the radiative and non-radiative processes following prior calculations by the Gaussian 09 D01 software package.

By placing all the rate constants between states calculated above in a single map (**Figure 5.4**), the mechanism of T_1 population upon photoexcitation of TBrFL becomes obvious. Following the map, Φ_T of TBrFL can be derived as

Equation 5.1 Calculation of Φ_T based on electronic transition decay constants.

$$\Phi_T = \frac{k_{isc2} \left(1 - \frac{k_{risc2}}{k_{risc2} + k_{ic2}}\right) + k_{isc1}}{k_f + k_{ic} + k_{isc2} \left(1 - \frac{k_{risc2}}{k_{risc2} + k_{ic2}}\right) + k_{isc1}}$$

Accordingly, based on values calculated above (listed in **Figure 5.4**), Φ_T of TBrFL was calculated as 0.58, similar to the reported value range for EY (0.39-0.57).⁹⁰

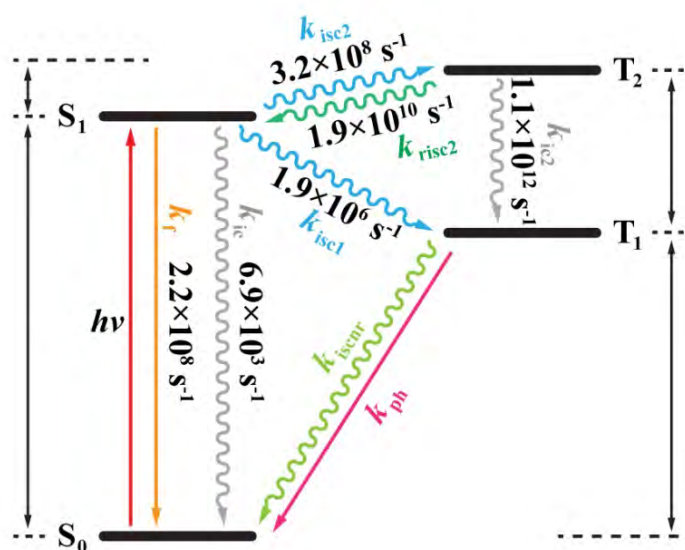


Figure 5.4 Computationally derived ground and excited state transition map of TBrFL.

5.3.5 Computer-guided design of highly pH-responsive OPC and theoretical predictions

Following the above discussions covering electrostatic, electrochemical, and photophysical studies of structure-property relationships, we theoretically identified TBrFL as the most promising candidate for pH-light dual-responsive PET-RAFT polymerisation (**Figure 5.3A**, right). Electrostatic analysis by DFT computation revealed an ΔESP_{X-Y} of TBrFL as low as 30.19 kcal/mol, which is lower than that of PB; this theoretically guarantees TBrFL pH-responsiveness at much higher pH (**Figure 5.3B**).

To further evaluate the possible existence of a visible-light absorbing “ON” state (TBrFL²⁻, **Figure 5.5A**, top) and a colourless “OFF” state (ring-closed TBrFLH₂, **Figure 5.5A**, bottom), we performed time-dependent density functional theory (TD-DFT) calculations for the two states (**Figure 5.5B**, left for TBrFL²⁻ and **2C** for ring-closed TBrFLH₂). From a TD-DFT calculation, the HOMO-LUMO transition almost exclusively (93.9%) contributed to the lowest singlet excited state (S₁) excitation of TBrFL²⁻. The HOMO-LUMO gap of TBrFL²⁻ is highly similar to the values we previously reported for EY, indicating similar visible-light absorption wavelengths. Indeed, as revealed by TD-DFT methods (see SI, section 6.2 for details), the longest-wavelength absorption of TBrFL (459 nm, oscillator strength $f = 0.71$; experimental 500 nm, *vide infra*), is very close to that of EY (450 nm, $f = 0.80$; experimental 514 nm).⁸⁹

Practical reasons for the deviations in computational and experimental spectra are discussed in our previous report.⁹⁰ This result supports TBrFL²⁻ to be a strongly visible-light absorbing compound which should absorb green light, similar to EY²⁻. On the other hand, TD-DFT calculations of the ring-closed TBrFLH₂ revealed no absorption in the visible range at all, confirming it to be a colourless inactive state.

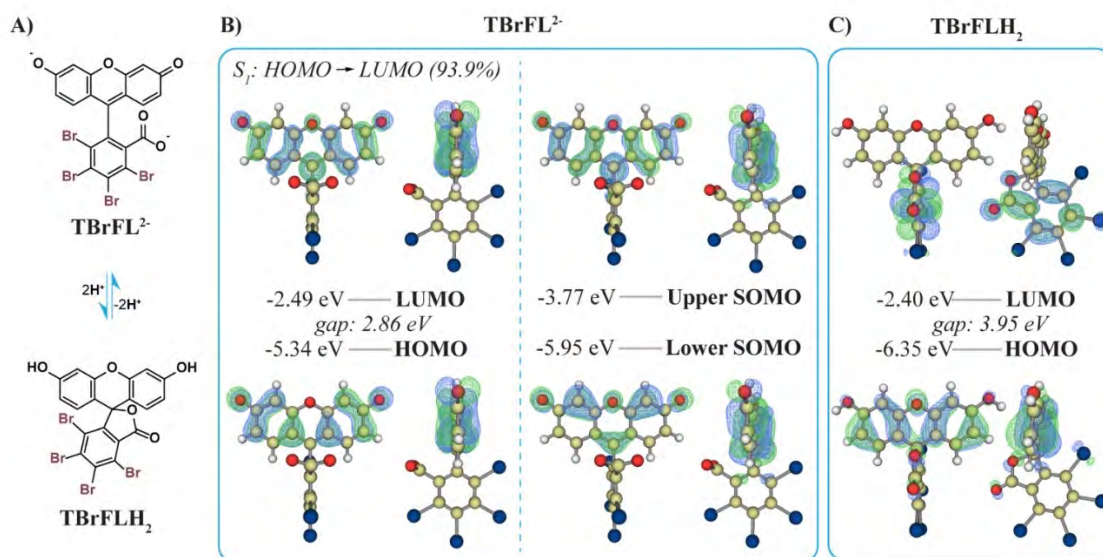


Figure 5.5 (A) Chemical structures of the active state (TBrFL²⁻, top) and the inactive/colourless state (TBrFLH₂, bottom) of TBrFL and their transition mechanism. (B) Frontier orbitals, energy levels (and their gaps) of the ground state TBrFL²⁻ (left) and the T₁ state TBrFL²⁻ (right). (C) Frontier orbitals, energy levels and their gaps of the ground state TBrFLH₂. Top: LUMO; bottom: HOMO. Contribution of HOMO→LUMO transitions to S₁ is denoted under the dye label. DFT calculations for frontier orbitals and TD-DFT calculations for orbital transition to S₁ were employed with B3LYP (6-31+G** basis set for C H O and LanL2DZ basis set for Br) level of theory and the SMD-water solvation model. Atom colour: C in yellow, H in white, O in red and Br in blue.

In order to evaluate the capability of the TBrFL²⁻ state for PET-RAFT catalysis, we computed the electronic nature of T₁ and its oxidative potential E⁰(PC^{•+}/³PC^{*}), as well as Φ_T for TBrFL²⁻. More negative E⁰(PC^{•+}/³PC^{*}) and higher Φ_T have been judiciously inferred in our previous report as the key parameters that determine a better OPC^{92, 94} when the molar extinction coefficients (or *f*) and the natures of T₁ of two dyes are similar. As EY, PB, and TBrFL share comparable visible-light absorption and local electronic distribution of the T₁ in the xanthene core (**Figure 5.5B**, right for TBrFL, and our previous

report for EY and PB⁹⁰), we compared their $E^0(\text{PC}^{*+}/\beta\text{PC}^*)$ and Φ_{T} as shown in **Table 5.1**. DFT computation revealed an $E^0(\text{PC}^{*+}/\beta\text{PC}^*)$ for TBrFL of -1.25 V *vs* SCE, which was similar to EY (-1.26 V *vs* SCE). This demonstrates that TBrFL should be electrochemically favourable as a PET-RAFT OPC. $E^0(\text{PC}^{*+}/\beta\text{PC}^*)$ for PB is much less negative (-0.91 V *vs* SCE) and is hence less favourable for PET-RAFT catalysis as observed before.⁹⁰ With respect to Φ_{T} , it has been demonstrated in the previous section that TBrFL has a Φ_{T} of 0.58 due to HAE induced by Br substituents, which is sufficient for PET-RAFT catalysis and is again similar to EY (reported $\Phi_{\text{T}} = 0.39\text{-}0.57$ ⁹⁰). Conversely, the non-halogenated FL only displays Φ_{T} of 0.03. Indeed, despite FL having a calculated $E^0(\text{PC}^{*+}/\beta\text{PC}^*)$ as strong as -1.45 V *vs* SCE, it was shown to be inefficient in catalysing PET-RAFT polymerisation due to a low Φ_{T} .¹²³ The discussed properties are listed as **Table 5.1** for comparison.

Table 5.1 Electrostatic, electrochemical, photophysical and pH responsive properties of dyes mentioned in this work in comparison.

Dye	$E^0(\text{PC}^{*+}/\beta\text{PC}^*)$ V <i>vs</i> SCE	Φ_{T}	$\Delta\text{ESP}_{\text{X-Y}}$ kcal/mol	Colourless pH
FL	-1.45	0.03 ¹⁰⁷	N/D ^a	N/D ^a
TBrFL	-1.25	0.58	30.19	5 ^b
EY	-1.20	0.39-0.57 ⁹⁰	40.49	< 1 ⁸⁹
PB	-0.91 ⁹⁰	0.59-0.65 ⁹⁰	34.54	2 ⁸⁹

^aNot determined. ^bThe colourless pH for TBrFL is determined by pH-UV-vis kinetics. Otherwise cited or indicated, the values were computed by DFT calculations (methods presented in SI).

As such, we have computationally ascertained that the proposed TBrFL is both highly pH-sensitive (exhibiting colour transition at higher pH) and catalytically efficient (comparable to EY) as an OPC for PET-RAFT polymerisation. It must also be noted that $E^0(\text{PC}^{*+}/\beta\text{PC}^*)$ and Φ_{T} are compared here only to present qualitative analysis regarding possible ability of the dye to catalyse PET-RAFT polymerisation. In addition, as an

inferior but commercially available alternative, Rose Bengal (RB, X = I, Y = Cl) was also analysed. Although RB is commercially available, the lower colour change pH restricts its ability to be used as a switchable photocatalyst under more mild conditions. We note that RB is estimated by our theory to have a colourless pH situated between those of PB and TBrFL due to electronegativity differences for the atoms on the benzoic acid group ($\text{Br} > \text{I} > \text{H}$ in electronegativity). Indeed, considering X_r of Cl (3.16) $>$ Br (2.96) $>$ I (2.66) $>$ H (2.20), RB can only have a colourless pH higher than PB but lower than TBrFL and TCIFL. Its coloured to colourless transition was measure to be at $\text{pH} \sim 4.0$ by pH-UV-Vis analysis (**Figure 5.6**), which is consistent with the reported $\text{pK}_a = 4.5$ ¹²⁴. According to the rule of thumb for pH indicators,¹⁰⁸ its colourless pH should be 3.5, which should not be as good as TBrFL.

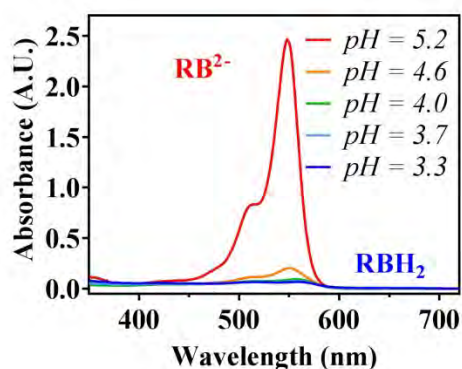


Figure 5.6 pH-UV-vis kinetics of a RB aqueous solution (1.01×10^{-4} mol/L) demonstrating the spectral transition of RB with pH change.

5.3.6 Synthesis and characterisation of the designed OPC

To experimentally confirm our predication and validate the system design of TBrFL, we firstly synthesised TBrFL (**Figure 5.7** and **Figure 5.8**) via a one-step Brønsted-acid-catalysed reaction¹⁰⁶ from commercially available precursors. The powder-state tetrabromophthalic anhydride (1507.0 mg, 3.25 mmol, 1 eqv.) and the flake-state resorcinol (751.5 mg, 6.825 mmol, 2.1 eqv.) were weighed in to a 10 mL sealed glass tube. A stir bar, a long needle nitrogen inlet and a short needle outlet were introduced; 5 mL neat methanesulfonic acid was slowly added under an inert atmosphere. After purging with nitrogen for 5 min, the pinkish-white solution in the tube was placed in an oil bath heating to 90 °C and kept stirring for 5 h. After 5 h, additional resorcinol (107.4 mg, 0.3 eqv) was added to the dark red solution. The reaction was continued for another 2 h and

resulted in a dark orange-red solution. 100 mL deionized water was filled in a 500 mL conical flask chilled by an ice-water bath and stirred with a large magnetic stir bar. The hot reaction solution was slowly and carefully precipitated in the chilled water, revealing a black solid that was gradually stirred into a uniform black suspension. Subsequently, this 100 mL suspension was charged into two 50 mL centrifuge tubes. A brown solid was obtained following 3 rounds of centrifugation with deionized water. 10 mL acetone was then added to each tube to fully dissolve the brown solid and was followed by reprecipitation in 35 mL deionized water. After two more rounds of centrifugation with deionized water, the obtained wet product (pink solid) was dried under high vacuum (35 °C) to yield the acid-form of TBrFL (TBrFLH₂) as a light pink powder (1529 mg, 72.8% yield). The obtained product was then characterised by ¹H NMR (**Figure 5.7**) and ¹³C NMR (**Figure 5.8**) with DMSO-d₆ as the solvent. ¹H NMR (400 MHz, DMSO-d₆): peak-a δ 10.15 (s, 2H), peak-b δ 6.86 (d, *J* = 8.68 MHz, 2H), peak-c δ 6.66 (d, *J* = 2.40 MHz, 2H), peak-d δ 6.55 (dd, *J*₁ = 2.40 MHz, *J*₂ = 8.68 MHz, 2H). Apparently, the signal from the hydrogen a of the hydroxyl group appeared at the low field δ 10.15 assigned as peak-a (**Figure 5.7**). Hydrogen d assigned as peak-d and hydrogen c assigned as peak-c were affected by coupling with hydrogen a characteristic of *J* = 2.40 MHz. Moreover, hydrogen b and hydrogen d were affected by each other with a coupling *J* = 8.68 MHz. Thereby, peak-b (b coupling with d) and peak-c (c coupling with a) are both doublets and peak-d (d coupling with a and b) is a doublet of doublets. ¹³C NMR (400 MHz, DMSO-d₆): peak-a δ 164.38, peak-b δ 160.23, peak-c δ 152.77, peak-d δ 151.65, peak-e δ 137.51, peak-f δ 132.92, peak-g δ 129.32, peak-h δ 127.01, peak-i δ 123.60, peak-j δ 121.73, peak-k δ 113.06, peak-l δ 107.19, peak-m δ 102.67, peak-n δ 82.60. To prepare the stock solution for its use in polymerisation photocatalysis, 3 mg of TBrFLH₂ (4.65 μmol, 1 eqv.) was weighed in a vial and mixed with 0.37 mg sodium hydroxide (9.29 μmol, 2 eqv.); minimal deionized water was introduced to fully dissolve the mixture, revealing a strong and bright orange colour. The orange mixture was then evaporated till dryness in a high vacuum oven at 35 °C. Finally, 3 mL deionized water was charged to produce a 1 mg/mL TBrFL stock solution for subsequent use (here and below the molecular weight of TBrFL is kept consistent as the molecular weight for the acid-form TBrFL, i.e. TBrFLH₂).

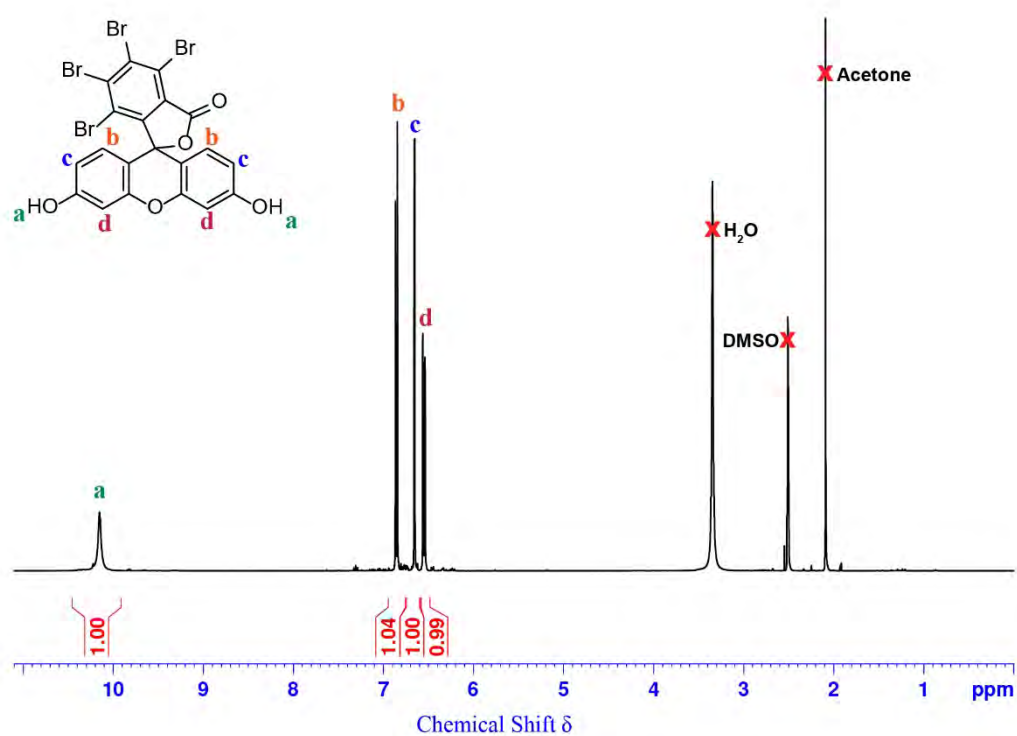


Figure 5.7 ^1H NMR spectrum (400 MHz, DMSO-d_6) of the synthesised TBrFL.

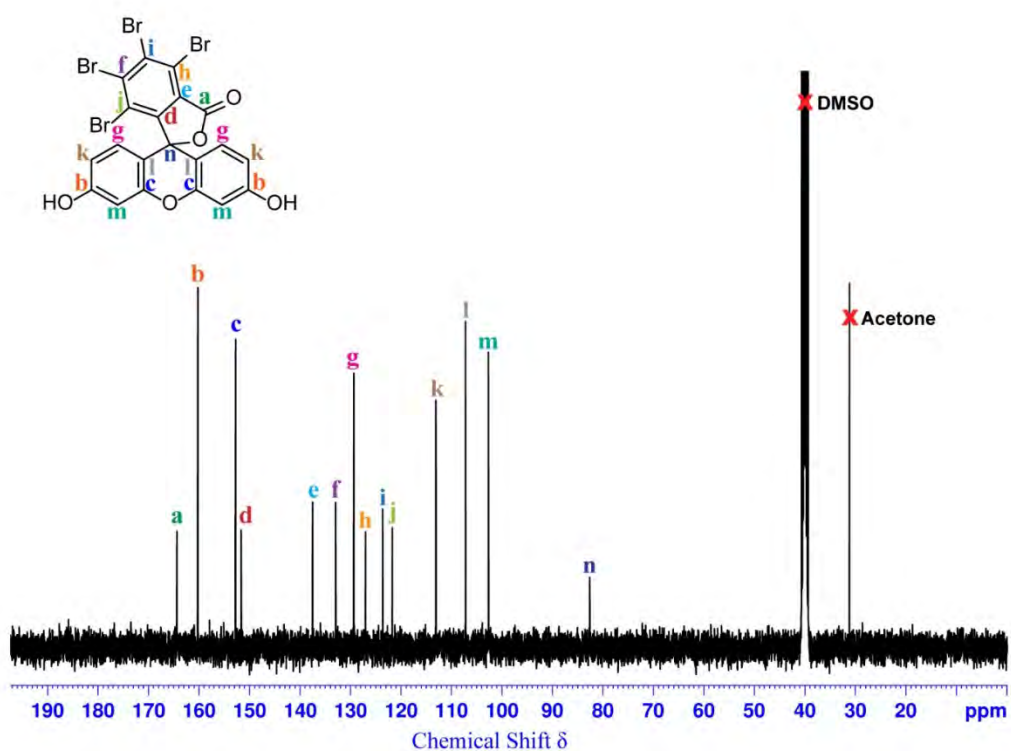


Figure 5.8 ^{13}C NMR spectrum (400 MHz, DMSO-d_6) of the synthesised TBrFL.

The pH-UV-vis kinetics of a 1.68×10^{-10} mol/L TBrFL aqueous solution (equivalent loading to that used in PET-RAFT polymerisation, *vide infra*) was determined by combination of a pH-meter and a UV-Vis spectrophotometer. As a classic rule of thumb, the pH range for colour transition of all pH indicators falls between $\text{p}K_a$ value minus one (the acid form) and $\text{p}K_a$ plus one (the salt form).¹⁰⁸ As shown in **Figure 5.9**, TBrFL performs colour transition in the pH range 5.0-7.0 and most sensitively responds between pH 5.9-6.3.

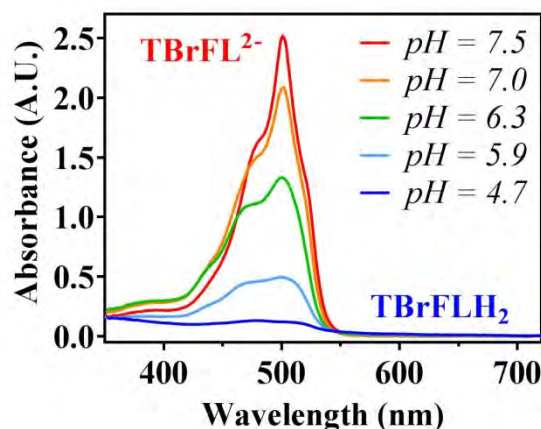


Figure 5.9 pH-UV-vis kinetics of a TBrFL aqueous solution (1.68×10^{-4} mol/L) demonstrating the spectral transition of TBrFL with pH change.

The transition was characterised by proton nuclear magnetic resonance (^1H NMR) spectroscopy (**Figure 5.10** and **Figure 5.11**) and indicates a $\text{p}K_a$ of ~ 6.0 for TBrFL. Historic investigation of fluorescein has uncovered that the di-anion state is a highly fluorescent form of fluorescein and the di-protonated ring-closed form is non-fluorescent.¹⁰⁶⁻¹⁰⁷ Researchers have found similar equilibria for other fluorescein derivatives. The di-anion state TBrFL^{2-} is proposed to be responsible for the strong orange colour in its aqueous solution at pH ~ 7 while the di-protonated ring-closed TBrFLH_2 is proposed to be the colourless species in the pH < 5 solution. Although DFT calculations in the work have computationally confirmed this deduction, we further performed NMR analysis to gain an experimental confirmation. Firstly, we dissolved 5 mg TBrFLH_2 and introduced ~ 2 mg NaHCO_3 in 0.6 mL DMSO-d_6 (strong orange colour solution) and conducted ^1H NMR analysis (**Figure 5.10**). ^1H NMR (400 MHz, DMSO-d_6): peak-a δ

6.84 (d, $J = 8.76$ MHz, 2H), peak-b δ 6.58 (s, 2H), peak-c δ 6.51 (d, $J = 8.76$ MHz, 2H). Obviously, because of the absence of the hydrogen (H^+) in the previous hydroxyl group, peak-b corresponding to hydrogen b was adjacent to no other hydrogen and is thus a singlet peak. Hydrogen a assigned as peak-a and hydrogen d assigned as peak-c were affected by each other with a coupling $J = 8.76$ MHz, and thereby resulted in doublet peaks. Subsequently, we dissolved 5 mg TBrFLH₂ in 0.6 mL DMSO-d₆ bubbling with HCl/N₂ fume for 10 s (colourless solution) and conducted ¹H NMR analysis (**Figure 5.11**). ¹H NMR (400 MHz, DMSO-d₆): peak-a δ 6.86 (d, $J = 8.68$ MHz, 2H), peak-b δ 6.66 (d, $J = 2.40$ MHz, 2H), peak-c δ 6.55 (dd, $J_1 = 2.40$ MHz, $J_2 = 8.68$ MHz, 2H). Hydrogen c assigned as peak-c and hydrogen b assigned as peak-b were affected by coupling with the hydrogen in the adjacent hydroxyl group characteristic of $J = 2.40$ MHz. Hydrogen a and hydrogen c were affected by each other with a coupling $J = 8.68$ MHz. Thereby, peak-a (a coupling with c) and peak-b (b coupling with the hydrogen in the hydroxyl group) are both doublets and peak-c (c coupling with a and the hydrogen of the hydroxyl group) is a doublet of doublets. Comparing both spectra, we found the signal peaks of the xanthene aryl protons furthest from the hydroxyl groups remained the same for both the orange and colourless solution (denoted as “a” in **Figure 5.10** and **Figure 5.11**). However, for TBrFLH₂ (**Figure 5.10, inset**), the four protons most adjacent to hydroxyl groups (denoted as “b” and “c”) exhibited an evident split character characteristic of coupling with the hydrogen in the hydroxyl group resulting in doublets compared to TBrFL²⁻ in the orange solution (**Figure 5.11, inset**). This is evidence of the double presence of protons on the hydroxyl group of the colourless ring-closed TBrFLH₂ (pH < 5, **Figure 5.11**) and the existence of the non-protonated $-O^-$ or $=O$ groups of the orange ring-opened TBrFL²⁻ (pH > 7, **Figure 5.10**).

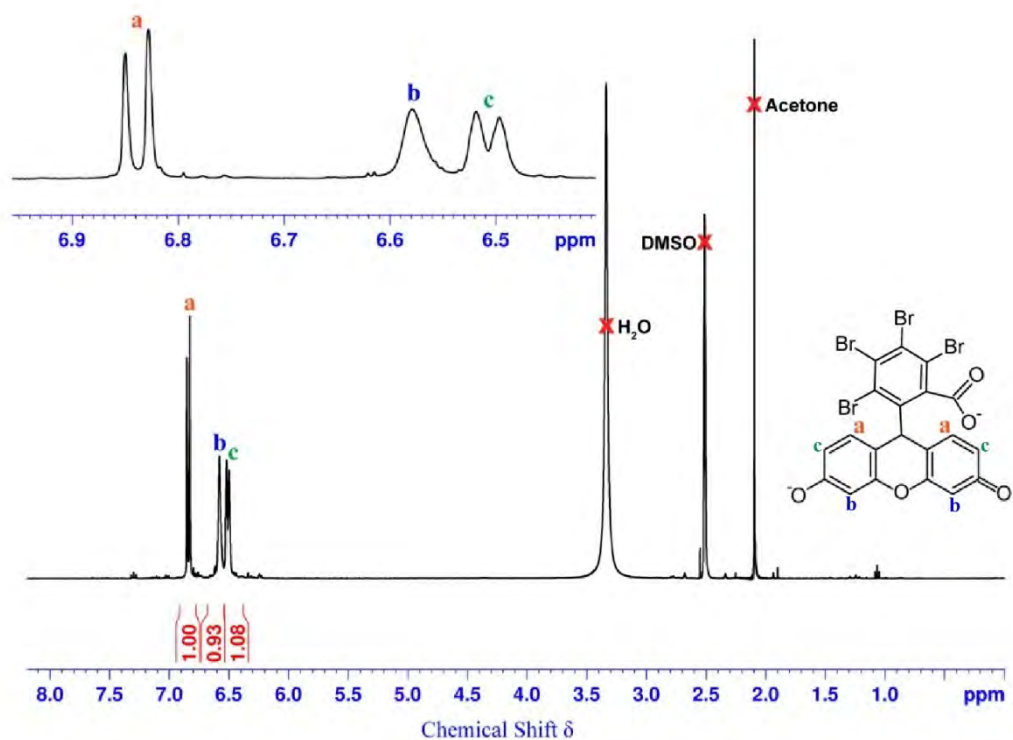


Figure 5.10 ^1H NMR spectrum (400 MHz, DMSO-d_6) of TBrFL^{2-} in a solution containing 5 mg TBrFL and ~ 2 mg NaHCO_3 .

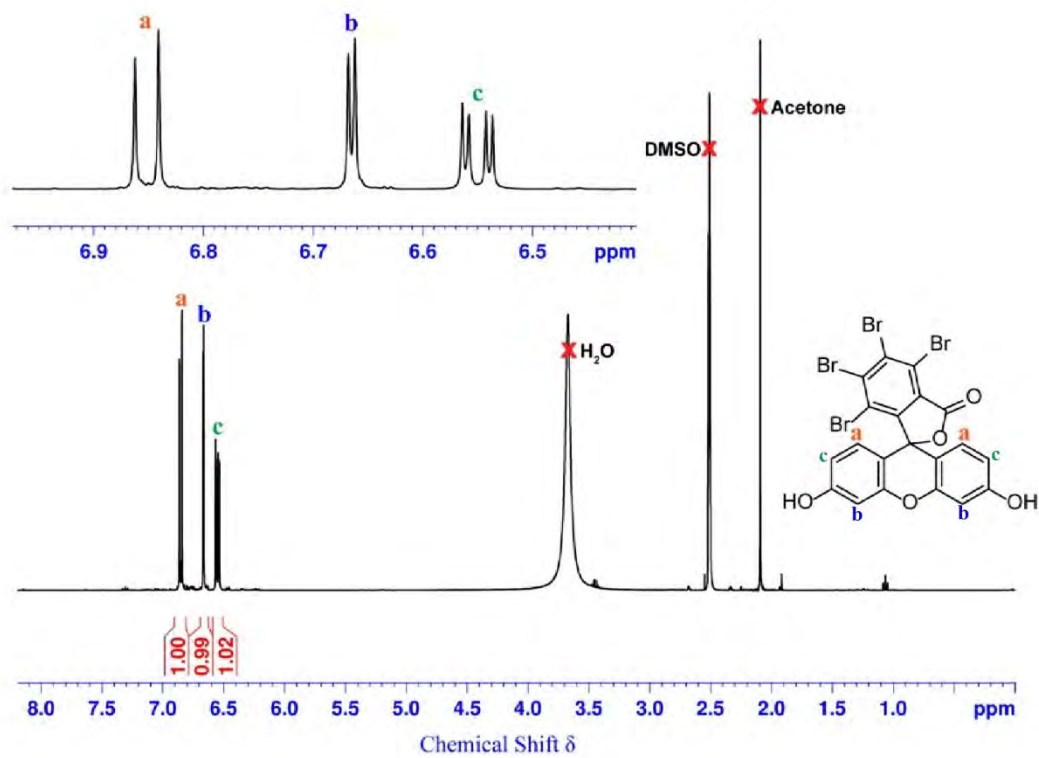


Figure 5.11 ^1H NMR spectrum (400 MHz, DMSO-d_6) of TBrFLH_2 in a solution containing 5 mg TBrFL and bubbled with HCl/N_2 fume for 10 s. The split character in peaks for the four protons most adjacent to hydroxyl groups (denoted as “b” and “c”) confirmed the double presence of protons on the hydroxyl groups of the colourless ring-closed TBrFLH_2 .

Therefore, at pH 7.0, TBrFL is mostly present as the active TBrFL^{2-} , exhibiting strong absorbance at around 500 nm and correspondingly a deep orange colour at low concentration. Conversely, at pH 5.0, TBrFL almost completely transitions to the colourless TBrFLH_2 state and loses its visible light absorption. Therefore, pH 7.0 (and above) can ideally serve as the “ON” logic gate to the visible-light absorption and pH 5.0 can be the complete “OFF” logic gate; this enables facile pH-control of TBrFL photocatalysis in a mild pH range.

Upon confirming the visible-light absorption and the pH-responsive property of TBrFL , we subsequently performed kinetic studies of TBrFL -catalysed PET-RAFT polymerisation in the presence and absence of oxygen in neutral aqueous solutions (pH = 7). We selected the model monomer N,N' -dimethylacrylamide (DMA) and model RAFT agent 2-(*n*-butyltrithiocarbonate) propionic acid methyl ester (BTPA-M, SI, **Figure 5.1** and **Figure 5.2**) in the aqueous system at a fixed molar ratio of $[\text{DMA}]:[\text{BTPA-M}]:[\text{TBrFL}] = 200:1:0.01$, where the monomer is 1:1 (v/v) to milliQ water and the loading of TBrFL is 50 ppm relative to monomer. Green LED light (nominal emission wavelength: 530 nm, 5 mW/cm^2) of an Oriel solar simulator served as the light source. We monitored k_p^{app} by online Fourier transform near infrared (FTNIR) spectroscopy (**Figure 5.12A**). While both polymerisations in the presence and absence of oxygen possessed highly similar k_p^{app} , polymerisation in the absence of oxygen (degassed) presented a brief 5-min induction period due to the RAFT pre-equilibrium, while polymerisation in the presence of oxygen (non-degassed) displayed a longer inhibition period. The delay of the onset of the non-degassed polymerisation was due to an oxygen inhibition period (19 min) resulting from continuous oxygen photosensitization and consumption. Both degassed and non-degassed TBrFL -catalysed PET-RAFT polymerisation presented excellent instantaneous temporal control (“ON/OFF” properties, **Figure 5.12B-C**). We observed a linear evolution of number-average molecular weights (M_n) versus monomer conversions (α), and excellent agreement between theoretical and experimental molecular weights for both polymerisations, as is ideal for controlled polymerisations (**Figure 5.12D**).

Meanwhile, gel permeation chromatography (GPC) revealed symmetric and narrow profiles for molecular weight distributions of polymers produced in both degassed and non-degassed systems ($M_w/M_n < 1.1$, **Figure 5.12D-F**).

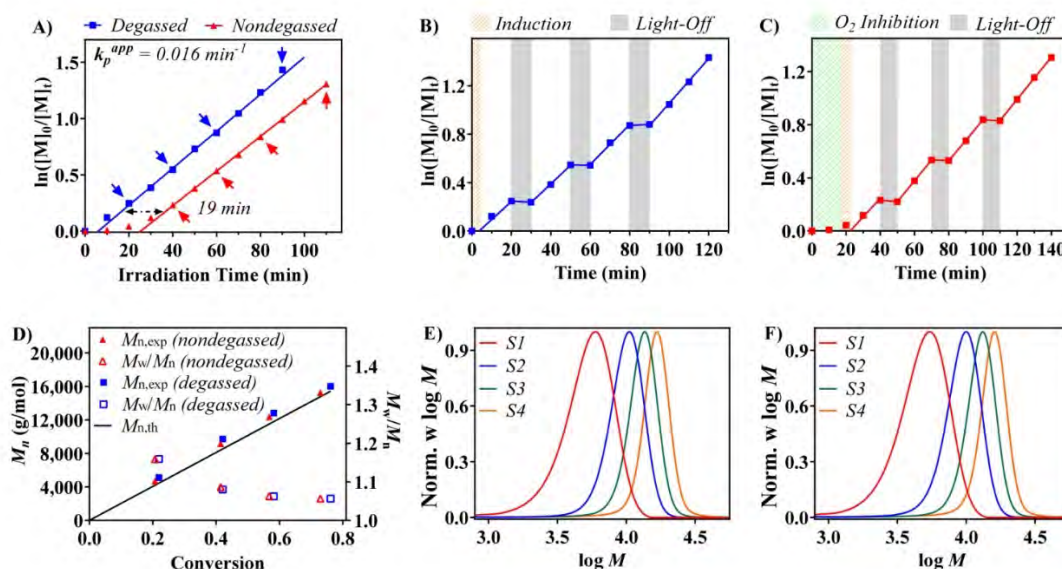


Figure 5.12 Kinetic studies of TBrFL-catalysed PET-RAFT polymerisation of DMA in the presence or absence of oxygen. (A-C) Plot of $\ln([M]_0/[M]_t)$ versus time revealing (A) k_p^{app} and oxygen inhibition time, (B) temporal control in the absence of oxygen and (C) temporal control in the presence of oxygen; (D) M_n and M_w/M_n versus conversion, and (E-F) normalized molecular weight distribution of four GPC aliquots taken during polymerisation, denoted as S1, S2, S3, S4, (E) in the absence of oxygen corresponding to blue arrows in (A) and (F) in the presence of oxygen corresponding to red arrows in (A), following the time order.

To characterise the end group fidelity of the synthesised polymers, oligomers were analysed by ^1H - ^{13}C HSQC 2D NMR spectroscopy (**Figure 5.13**) and ^1H NMR spectroscopy (**Figures 5.14** and **Figure 5.15**) to precisely assign the signals. To carefully assign signals, we studied short oligomers in the first place. Firstly, we prepared an oligomer of DMA with monomer to RAFT ratio of 5:1, under 5 mW/cm^2 530 nm irradiation for 2 h. Oligomers were characterised by ^1H - ^{13}C HSQC 2D NMR spectroscopy (**Figure 5.13**) and ^1H NMR spectroscopy (**Figure 5.14**) in deuterated chloroform (CDCl_3) and we successfully determined the chemical shifts (δ) of different protons in the R-group (α) and the Z-group (ω). We then performed ^1H NMR characterisation of DMA polymerisation aliquot from the batch in **Table 5.2**, entry 11. As this sample has a degree

of polymerisation as low as ~ 20 and was not purified (to avoid contamination from solvents), the proton signals were clearly identified (**Figure 5.15**).

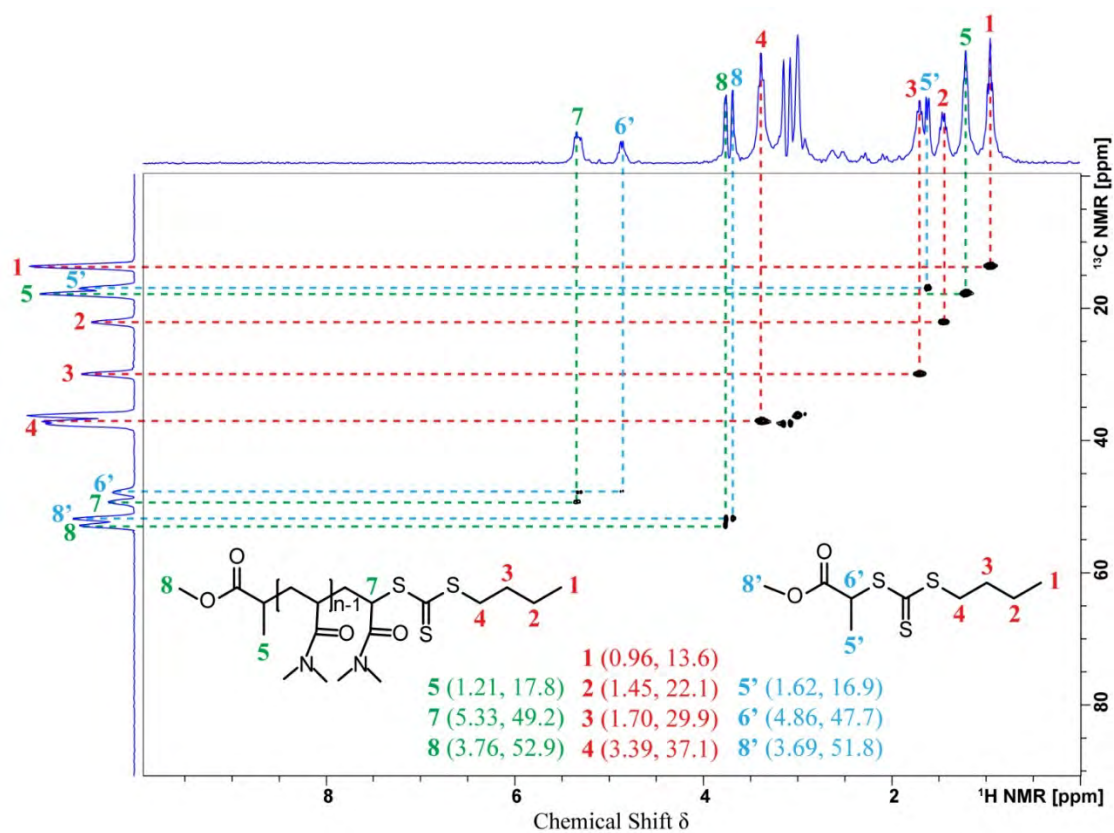


Figure 5.13 ^1H - ^{13}C HSQC NMR (CDCl_3 , 400 MHz, ^1H : δ 0~10 ppm; ^{13}C : δ 0~90 ppm) spectrum of the PDMA oligomers.

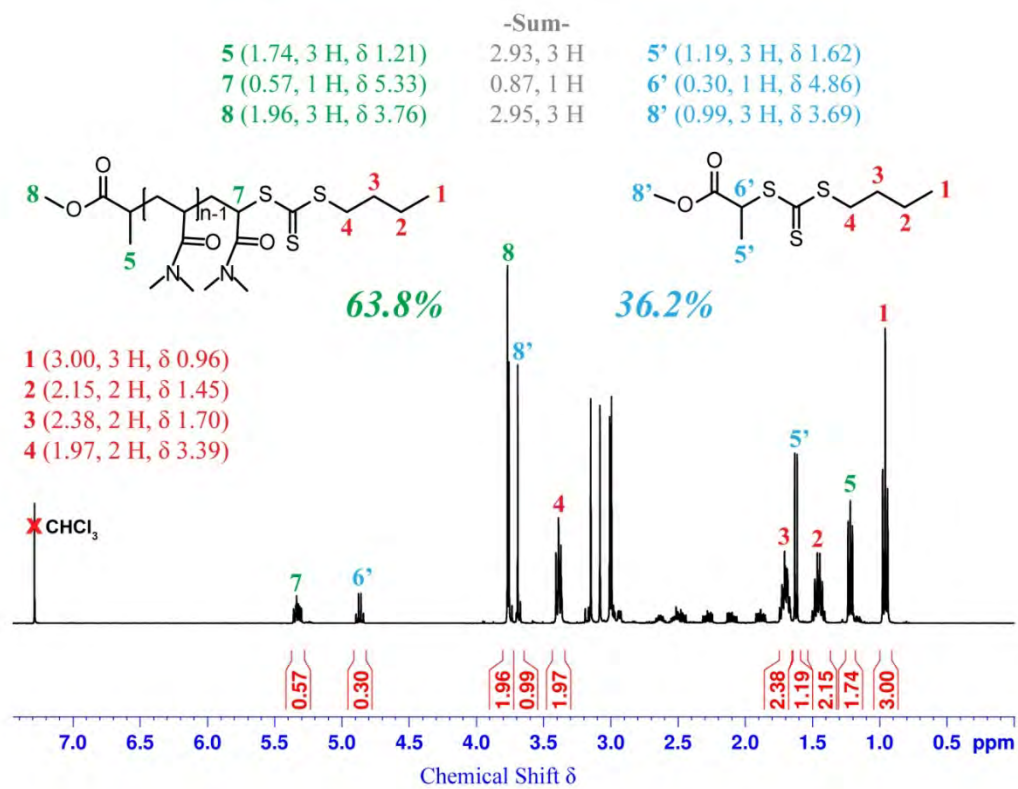


Figure 5.14 ^1H NMR spectrum (400 MHz, CDCl_3) of a mixture of 63.8% PDMA-BTPA-M oligomers and 36.2% BTPA-M as determined by specific proton signals.

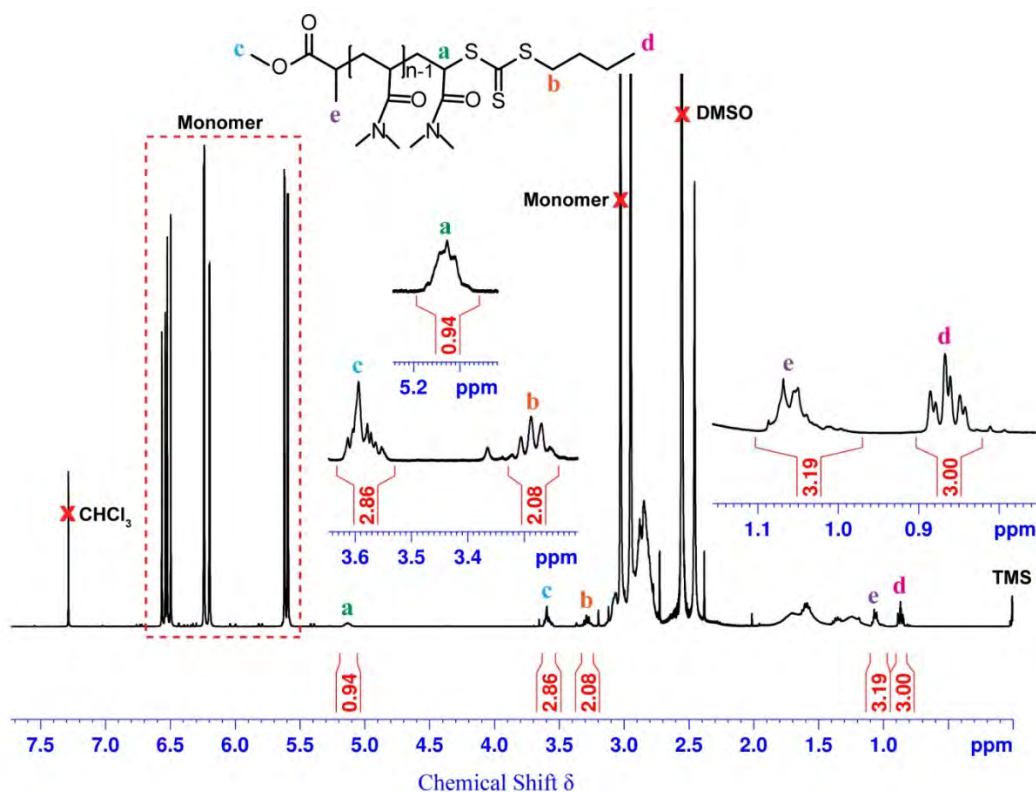


Figure 5.15 ^1H NMR spectrum (400 MHz, CDCl_3) of an unpurified mixture of a DMA polymerisation aliquot from the batch in Table 2, entry 11. As this sample has a degree of polymerisation as low as ~ 20 , the typical shape of proton signals as is in a polymer can be clearly identified.

We then conducted 400 MHz ^1H NMR spectroscopy on the synthesised polymers (**Figure 5.16** and **Figure 5.17**) by dissolving the purified polymers in 0.6 mL CDCl_3 . Using the different signals, we were able to quantify the end group fidelity by using the ester methyl group of the α end (c, δ 3.67, 3 H), the alkyl tail of the ω end adjacent to the trithiocarbonate group (b, δ 3.39, 2 H), the last added monomer on the carbon backbone adjacent to the trithiocarbonate group (a, δ 5.21, 1 H), the methyl in the alkyl tail of the ω end (d, δ 0.96, 3 H) and the methyl group in the α end (e, δ 1.21, 3 H). These confirmed the high end group fidelity of the synthesised polymers after TBrFL-catalysed polymerisation in the absence of oxygen (**Figure 5.16**), in the presence of oxygen (**Figure 5.17**).

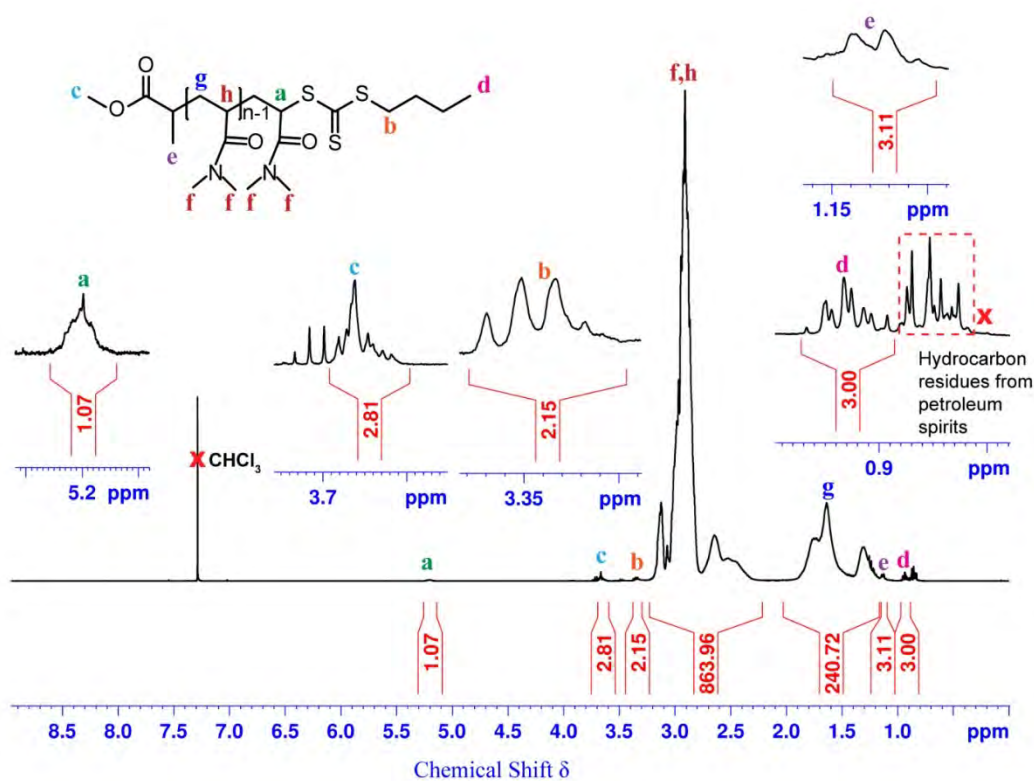


Figure 5.16 ^1H NMR spectrum (400 MHz, CDCl_3) of purified PDMA synthesised through TBrFL-catalysed PET-RAFT polymerisation in the absence of oxygen (degassed).

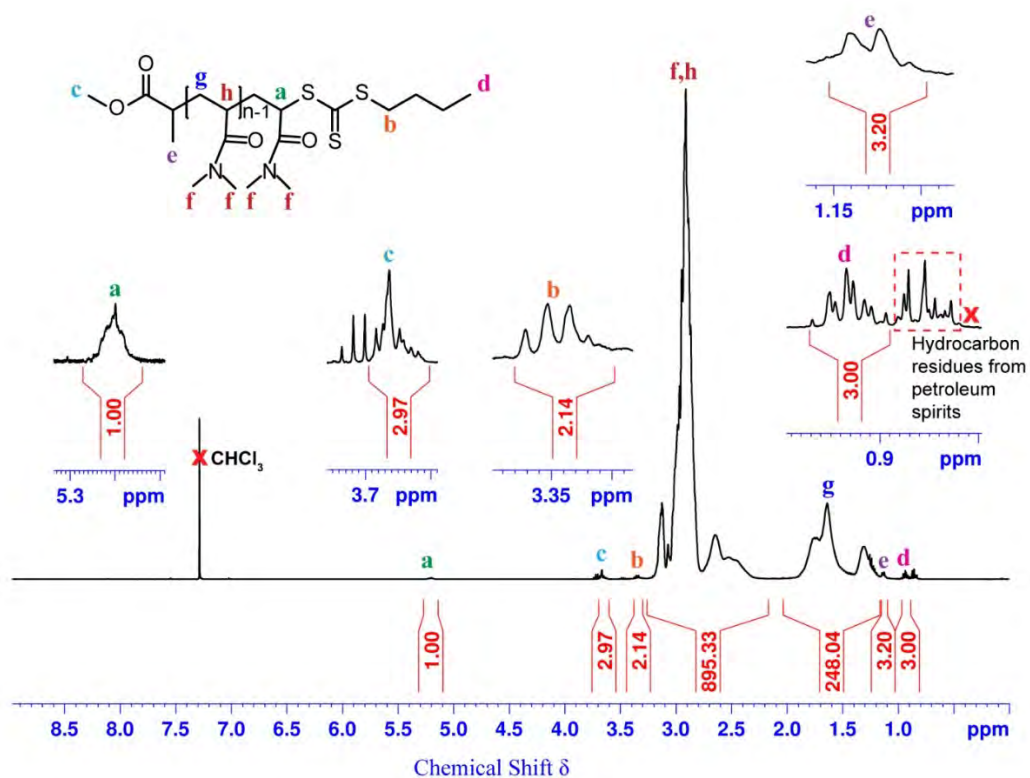


Figure 5.17 ^1H NMR spectrum (400 MHz, CDCl_3) of purified PDMA synthesised through TBrFL-catalysed PET-RAFT polymerisation in the presence of oxygen (non-degassed).

Subsequently, we performed chain extension tests to assess the accessibility of the RAFT end-groups using the same batches of the purified PDMA ($[\text{DMA}]:[\text{PDMA-macroRAFT}]:[\text{EB}] = 1000:1:0.004$, under 5 mW/cm^2 530 nm irradiation). A complete shift of the molecular weight distribution to higher molecular weights confirmed the high retention of trithiocarbonate end groups after TBrFL-catalysed polymerisation in the absence of oxygen (**Figure 5.18**), in the presence of oxygen (**Figure 5.19**), which also confirmed high end-group fidelity with no detectable loss regardless of whether the system was degassed or non-degassed.

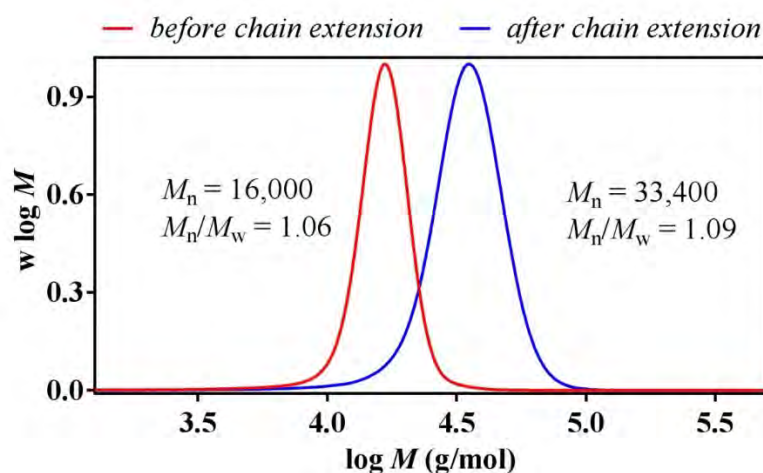


Figure 5.18 Molecular weight distributions for the synthesised PDMA after TBrFL-catalysed PET-RAFT polymerisation in the absence of oxygen (red line) and the chain-extended PDMA-*b*-PDMA after chain extension EB-catalysed PET-RAFT polymerisation (blue line). Complete shift of molecular weight distributions to higher molecular weights confirmed the high retention of the trithiocarbonate chain end group.

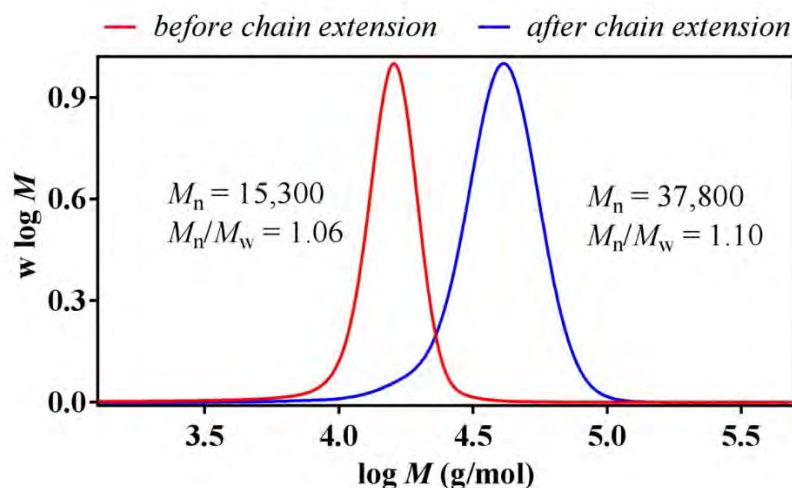


Figure 5.19 Molecular weight distributions for the synthesised PDMA after TBrFL-catalysed PET-RAFT polymerisation in the presence of oxygen (red line) and the chain-extended PDMA-*b*-PDMA after chain extension EB-catalysed PET-RAFT polymerisation (blue line). Complete shift of molecular weight distributions to higher molecular weights confirmed the high retention of the trithiocarbonate chain end group.

Matrix assisted laser desorption/ionization time-of-flight mass spectrometry (MALDI-TOF MS) was also conducted for polymers synthesised via TBrFL-catalysed PET-RAFT polymerisation of DMA in the presence or absence of oxygen, which revealed a pure discrete distribution of the polymers with RAFT derived end-groups in either case (**Figure 5.20** and **Figure 5.21**). Both polymerisations in the presence and absence of oxygen were stopped at around 10% monomer conversion (degree of polymerisation DP 20) to match the suitable molecular weight range for poly-DMA (PDMA) MALDI-TOF MS analysis. As shown in **Figure 5.20** and **Figure 5.21**, MALDI-TOF MS reveals evenly distributed mass peaks (separated by 99.13 m/z) and highly symmetric mass distribution. Magnified into the detailed structure of each mass peak set (from 2500 to 2700 m/, **Figure 5.20** and **Figure 5.21**, inset), we were able to distinguish the main peaks corresponds to PDMA with BTPA chain-end plus Na⁺ and tiny secondary peaks to PDMA with BTPA chain-end plus K⁺ (only visible in the **Figure 5.21**, inset) in excellent agreement with theoretical values within instrumental error (< 1 m/z), showing no evidence for end-group loss. Therefore, oxygen cannot exert any influence on the end group fidelity during TBrFL-catalysed PET-RAFT polymerisation of DMA in aqueous solution. These results

confirmed the excellent oxygen tolerance of the present system. Hence, we decided to skip the degassing procedures in subsequent tests.

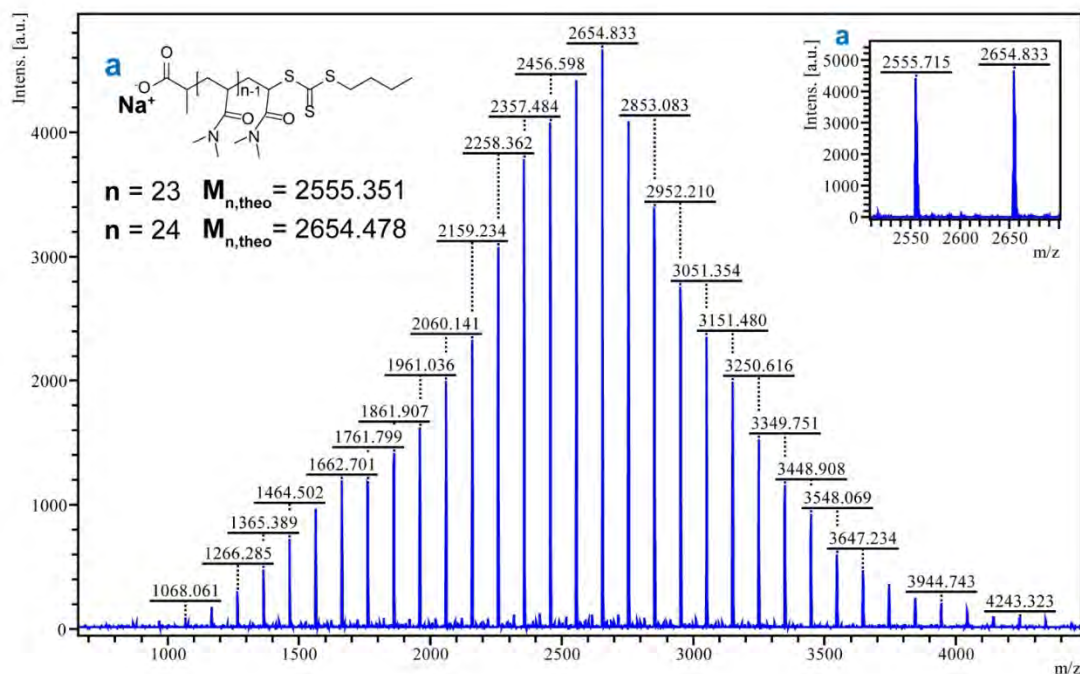


Figure 5.20 MALDI-TOF MS of a PDMA sample synthesised by TBrFL-catalysed PET-RAFT polymerisation in the absence of oxygen (degassed). By zooming into the molecular weight range of 2500-2700 g/mol, we observed that major peaks (inset a) excellently matches theoretical prediction of PDMA with BTPA chain-end group plus Na^+ (indicated on the left of the full spectrum), within experimental error (< 1 g/mol). For the left peaks in the inset a, the number of monomer insertion (n) is determined to be 23, whereas for the right peaks in the inset a, it is determined to be 24. $M_{n,\text{GPC}} = 3,300$ g/mol; $\text{PDI} = 1.21$.

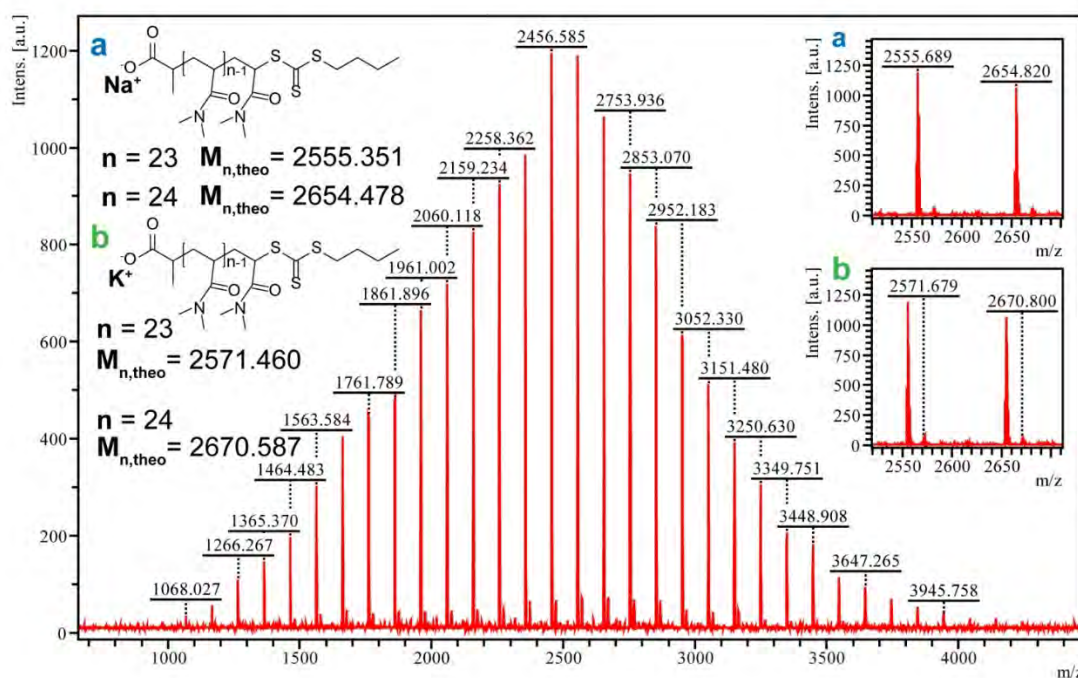
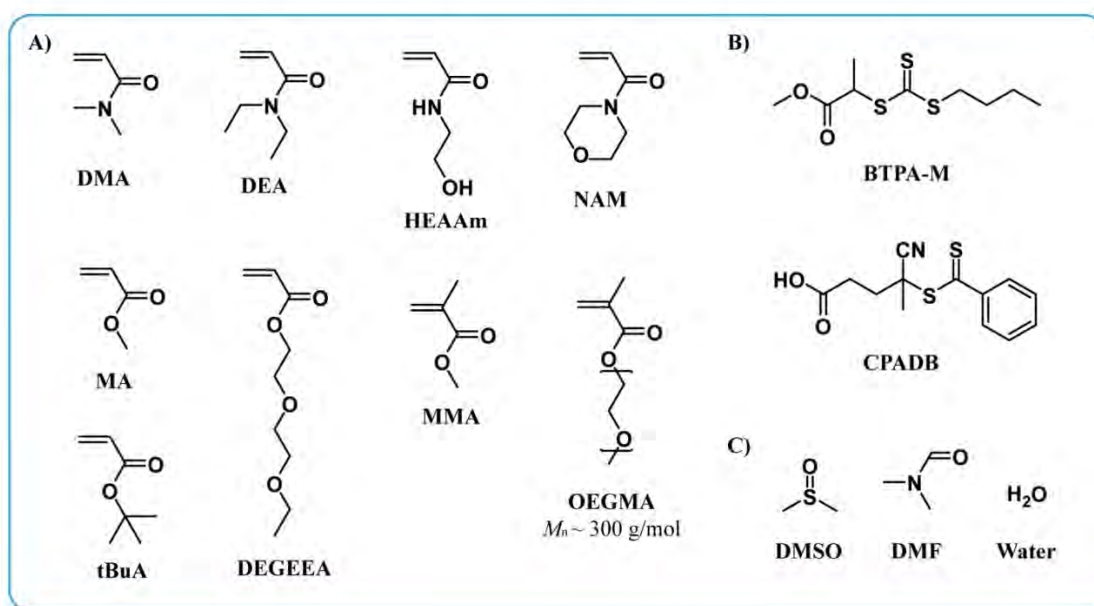


Figure 5.21 MALDI-TOF MS of a PDMA sample synthesised by TBrFL-catalysed PET-RAFT polymerisation in the absence of oxygen (degassed). By zooming into the molecular weight range of 2500-2700 g/mol, we observed that major peaks (inset a) excellently matches theoretical prediction of PDMA with BTPA chain-end group plus Na^+ (indicated on the left of the full spectrum), while minor peaks (inset b) can be assigned to PDMA with BTPA chain-end group plus K^+ (indicated on the left of the full spectrum), all within experimental error (< 1 g/mol). For the left peaks in the inset a and b, the number of monomer insertion (n) is determined to be 23, whereas for the right peaks in the inset a and b, it is determined to be 24. $M_{n,\text{GPC}} = 2,700$ g/mol; PDI = 1.21.

To further demonstrate the viability of TBrFL for catalysing polymerisation, a broad range of monomer families was investigated, which included acrylamides (dimethyl acrylamide (DMA), diethyl acrylamide (DEA), hydroxyethyl acrylamide (HEAAm), and 4-acryloylmorpholine (NAM)), acrylates (methyl acrylate (MA), *tert*-butyl acrylate (*t*BuA), and di(ethylene glycol) ethyl ether acrylate (DEGEEA)), and methacrylates (methyl methacrylate (MMA) and oligoethylene glycol methacrylate (OEGMA)) in water, DMSO, or DMF as solvent depending on their solubility. TBrFL-catalysed PET-RAFT polymerisation of these monomers were respectively performed using two different RAFT agents according to their compatibility in RAFT polymerisation;⁵⁵ CPADB was used for polymerisation of methacrylates while BTPA-M was used for all other

monomers (**Scheme 5.3**). As shown in **Table 5.2**, entry 1-9, all polymerisations proceeded efficiently and resulted in the production of polymers with low M_w/M_n . As TBrFL is highly pH responsive, for polymerisations in DMSO, a small amount of NaHCO_3 (1~2 mg) was added to neutralize the weak acidity of DMSO.¹²⁵ Most polymerisations displayed excellent correlation between experimental M_n (determined by GPC and/or NMR) and theoretical M_n values. Low $M_w/M_n < 1.2$ was observed except for OEGMA ($M_w/M_n = 1.34$).



Scheme 5.3 Chemical structures of (A) monomers, (B) RAFT agents, and (C) solvents used.

Table 5.2 Details for polymerisation with different monomers, RAFT agents, solvents, and ratios.

#	Monomer	RAFT agent	Solvent	Ratio ^b	Time (h)	α^c (%)	$M_{n,theo}^d$ (kg/mol)	$M_{n,GPC}$ ($M_{n,NMR}^e$) (kg/mol)	M_w/M_n
1	DMA	BTPA-M	Water	200:1	2	87.1	17.5	16.1(15.7)	1.07
2	DEA	BTPA-M	Water	200:1	2	50.7	13.1	8.0	1.14
3	DEGEEA	BTPA-M	DMSO	200:1	3	43.0	16.4	15.3(16.5)	1.16

4	MA	BTPA-M	DMSO	200:1	3	60.9	10.7	13.0(8.8)	1.08
5	MMA	CPADB	DMSO	200:1	8	77.5	15.8	26.7(25.9)	1.19
6	OEGMA	CPADB	Water	200:1	6	84.3	50.9	41.3(46.5)	1.34
7	tBuA	BTPA-M	DMF	200:1	6	94.2	24.4	19.4(18.5)	1.09
8	HEAAm	BTPA-M	Water	200:1	3	35.2	8.4	23.2(10.8)	1.08
9	NAM	BTPA-M	Water	200:1	3	38.3	11.1	10.6(9.6)	1.15
10	DEA	MacroRAFT ^a	Water	500:1	2	52.1	49.3	43.3	1.10
11	DMA	BTPA-M	Water	50:1	2	39.0	2.2	1.8(2.0)	1.14

^aMacroRAFT used here is polyDMA(PDMA) with BTPA-M end group ($M_{n,GPC} = 16,100$ g/mol, $M_w/M_n = 1.07$ from the polymerisation in entry 1). ^bThis ratio refers to [monomer]:[RAFT agent]. ^c α refers to monomer conversion determined by NMR spectroscopy. ^d $M_{n,theo}$ is the theoretical number average molecular weight calculated based on the equation $M_{n,theo} = [M]_0/[RAFT]_0 \times MW^M \times \alpha + MW^{RAFT}$, where $[M]_0$, $[RAFT]_0$, MW^M , α , and MW^{RAFT} correspond to initial monomer concentration, initial RAFT concentration, molar mass of monomer, conversion determined by ¹H NMR, and molar mass of RAFT agent. ^e $M_{n,NMR}$ is obtained from NMR spectroscopy.

In addition, PDMA-*b*-PDEA block copolymers were successfully synthesised by targeting higher molecular weights (**Table 5.2**, entry 10 and **Figure 5.22**), which confirmed the compatibility of TBrFL with block copolymer synthesis. Block PDMA-*b*-PDEA copolymer was synthesised in water at a ratio of [monomer]:[PDMA-BTPA-M] = 500:1 (**Table 5.2**, entry 10), with low M_w/M_n (1.10) and good correlation between $M_{n,GPC}$ (43,300 g/mol) and $M_{n,theo}$ (49,300 g/mol). Symmetrical molecular weight distribution profile and a complete shift after chain extension was observed (**Figure 5.22**).

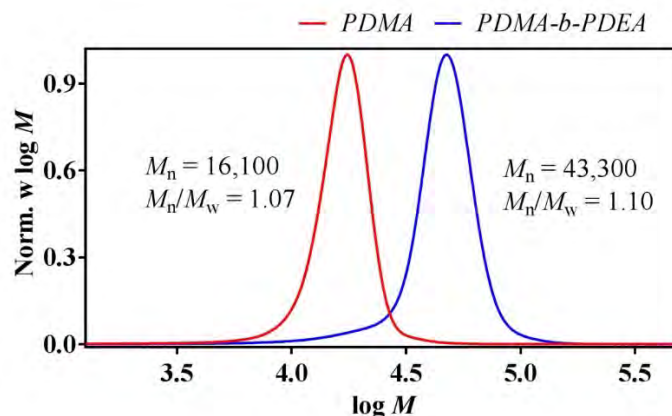


Figure 5.22 Molecular weight distributions for PDMA before chain extension (red) and PDMA-*b*-PDEA after chain extension (blue), **Table 5.2**, entry 10.

Moreover, polymerisation targeting lower molecular weights was also successfully conducted (**Table 5.2**, entry 11), showing good control at lower degrees of polymerisation. These successful polymerisations confirmed the robustness of TBrFL as an efficient PC for PET-RAFT polymerisations in different solvents as well as with different types of RAFT agents (dithioester and trithiocarbonate).

5.3.7 Application of the designed OPC for dual-switchable PET-RAFT polymerisation

Subsequently, we tested the expected pH control of the TBrFL-catalysed PET-RAFT polymerisation. Considering the mild colourless transition pH 5.0 of TBrFL, we enabled a non-liquid strategy, where a few bubbles (~1 mL) of gaseous HCl/N₂ were introduced to decolourize TBrFL and completely cease the polymerisation under light, achieving an “OFF” state (**Figure 5.23A**). To recover the colour of TBrFL and return to the “ON” state of PET-RAFT polymerisation, we introduced a small amount of NaHCO₃ (~0.5 mg), which allowed the polymerisation to be restarted under light (**Figure 5.23A**); this successfully demonstrated the completely reversible inhibition through pH control of the dual-gated PET-RAFT polymerisation. The change in colour and visible-light absorption of the TBrFL containing polymerisation solution during the pH “ON/OFF” control was monitored by photography (**Figure 5.23A**, inset) and UV-vis spectroscopy (**Figure 5.23B**). As no liquid phase was involved in the reversible switching, the only additional product left after each cycle of switching was small amount of NaCl, which exerted no effect on the polymerisation.

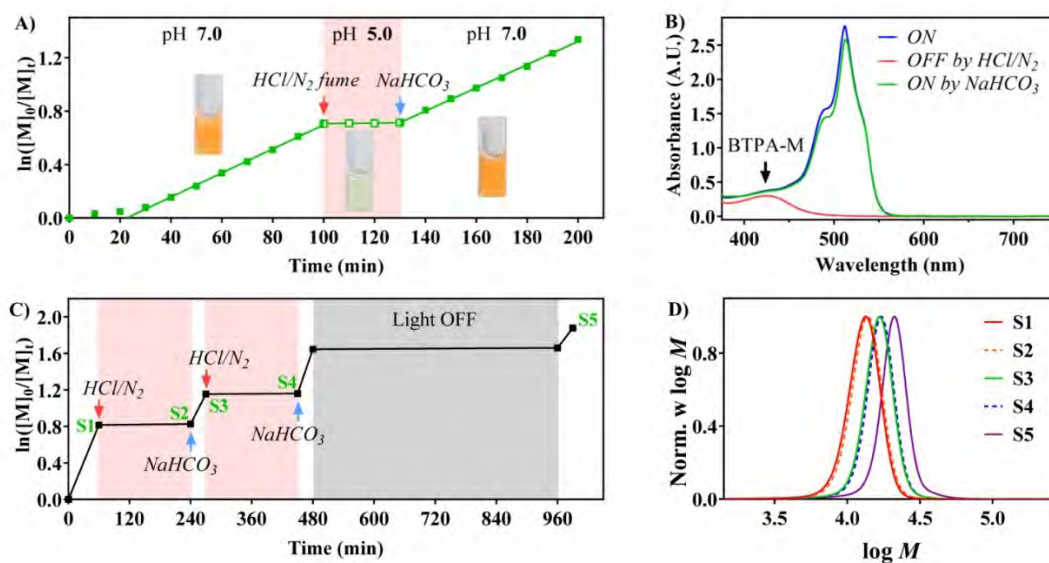


Figure 5.23 (A) Plot of $\ln([M]_0/[M]_t)$ versus time of TBrFL-catalysed PET-RAFT polymerisation of DMA in water in the presence of oxygen under green light using a few bubbles (~ 1 mL) of gaseous HCl/N_2 to generate pH-"OFF" state and small amount of $NaHCO_3$ powder (~ 0.5 mg) to generate pH-"ON" state. (B) Corresponding UV-vis spectra of different states in (A). (C) Plot of $\ln([M]_0/[M]_t)$ versus time of TBrFL-catalysed PET-RAFT polymerisation of DMA in water with two 3 h periods of pH-"OFF" and one 8 h-period of light-"OFF". (D) Molecular weight distribution of five GPC aliquots taken during polymerisation in (C), denoted as S1, S2, S3, S4 and S5.

High end-group fidelity with no detectable loss of the obtained polymer was confirmed by 1H NMR spectroscopy (**Figure 5.24**) and the chain extension experiment (**Figure 5.25**).

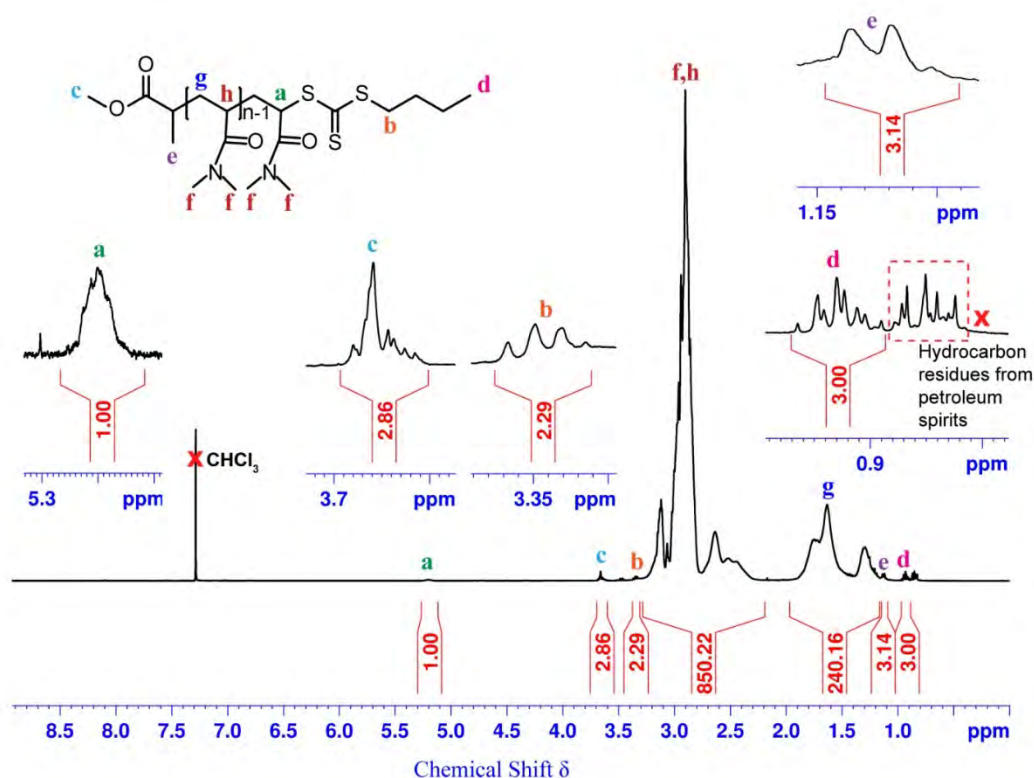


Figure 5.24 ^1H NMR spectrum (400 MHz, CDCl_3) of purified PDMA synthesised through non-degassed TBrFL-catalysed PET-RAFT polymerisation where HCl/N_2 and NaHCO_3 mediated pH manipulation was introduced.

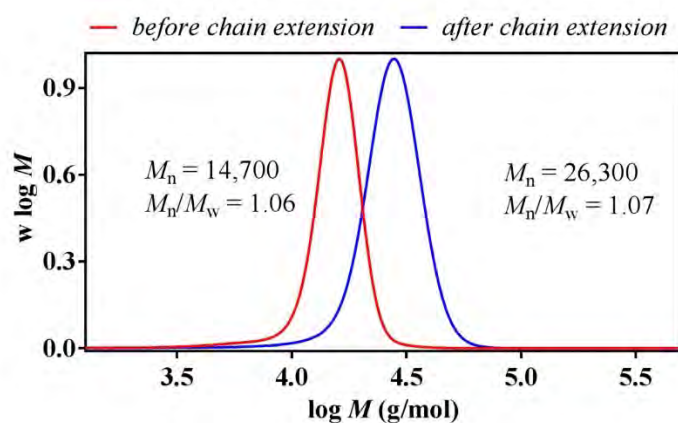


Figure 5.25 Molecular weight distributions for the synthesised PDMA after non-degassed TBrFL-catalysed PET-RAFT polymerisation where HCl/N_2 and NaHCO_3 mediated pH manipulation was introduced (red line) and the chain-extended PDMA-*b*-PDMA after chain extension EB-catalysed PET-RAFT polymerisation (blue line). Complete shift of molecular weight distributions to higher molecular weights confirmed the high retention of the trithiocarbonate chain end group.

Finally, we performed a kinetic study of DMA with two 3 h pH-“OFF” periods and one 8 h light-“OFF” period. As shown in **Figure 5.23** and **Table 5.3**, for each “OFF” -period no monomer conversion was observed by NMR analysis, which confirmed an ideal temporal control using two different stimuli.

Table 5.3 GPC characterisation of S1, S2, S3 ,S4 and S5 in pH and light dual-controlled DMA polymerisation in the kinetic study shown as **Figure 5.23**.

Entry ^a	Monomer	Stage	Time (min)	α^b %	$M_{n,theo}^c$ (kg/mol)	$M_{n,GPC}$ (kg/mol)	M_w/M_n
S1	DMA	before pH-“OFF”	1 st 60	55.8	11.3	12.6	1.07
S2	DMA	after pH-“OFF”	1 st 240	56.3	11.4	13.0	1.07
S3	DMA	before pH-“OFF”	2 nd 270	68.5	16.3	16.0	1.05
S4	DMA	after pH-“OFF”	2 nd 450	68.7	16.3	16.4	1.05
S5	DMA	final product	990	84.7	17.0	20.3	1.05

^aTBrFL-catalysed PET-RAFT polymerisation of DMA in water ([DMA]:[BTPA-M]:[TBrFL] = 200:1:0.01) under 5 mW/cm² 530 nm irradiation with two 3-h-periods of pH-“OFF” and one 8-h-period of light-“OFF”. ^b α refers to monomer conversion determined by NMR spectroscopy. ^c $M_{n,theo}$ is the theoretical number average molecular weight calculated based on the equation $M_{n,theo} = [M]_0/[RAFT]_0 \times MW^M \times \alpha + MW^{RAFT}$, where $[M]_0$, $[RAFT]_0$, MW^M , α , and MW^{RAFT} correspond to initial monomer concentration, initial RAFT concentration, molar mass of monomer, conversion determined by ¹H NMR, and molar mass of RAFT agent.

To examine the robustness of this pH and light dual-gated strategy, we tested a longer pH-“OFF” and confirmed the complete inhibition over extended periods of time. We

performed a long pH off (pH = 5.0) of 90 min in **Figure 5.26**, which confirms that in acidic pH, no polymerisation was observed under prolonged 530 nm irradiation.

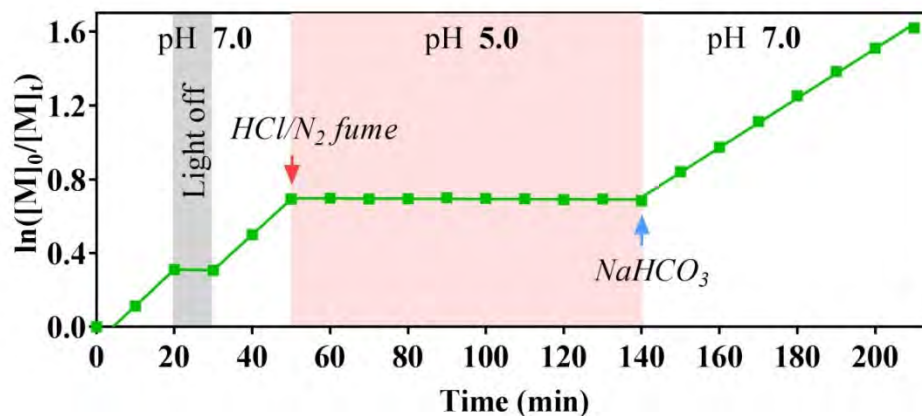


Figure 5.26 Plot of $\ln([M]_0/[M]_t)$ versus time of TBrFL-catalysed PET-RAFT polymerisation of DMA in water ($[DMA]:[BTPA-M]:[TBrFL] = 200:1:0.01$) under 5 mW/cm^2 530 nm irradiation with a 90 min prolonged pH-“OFF” period and 10 min light-“OFF” period.

Furthermore, to confirm the absence of polymerisation for a longer period when the pH is below 6, we performed a polymerisation of DMA under 530 nm irradiation (5 mW/cm^2) for 4 h (**Figure 5.27**). There is no polymerisation for this extended “OFF” period.

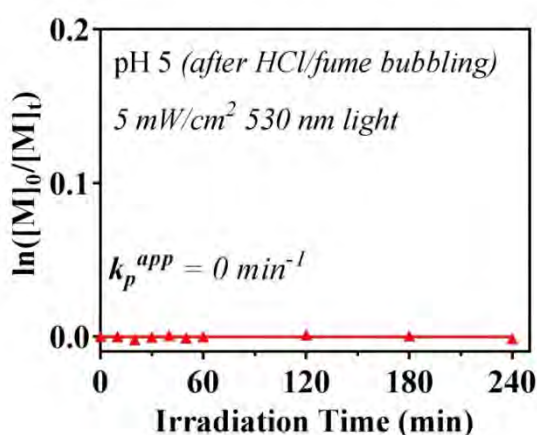


Figure 5.27 Plot of $\ln([M]_0/[M]_t)$ versus time of TBrFL-catalysed PET-RAFT polymerisation of DMA in water at pH 5.0 ($[DMA]:[BTPA-M]:[TBrFL] = 200:1:0.01$) under 5 mW/cm^2 530 nm irradiation. No polymerisation was observed over 4 h irradiation.

Other monomers and solvent systems were also tested to confirm that the dual-gated strategy was independent of the type of monomers and solvents employed. Similar levels of control were observed. As shown in **Figure 5.28** and **Table 5.4**, a 3 h pH-“OFF” period was achieved for MA polymerisation in DMSO using HCl/NaHCO₃ “pH” manipulation. However, it should be noted that unlike water, DMSO does not dissolve NaHCO₃ and NaCl well.

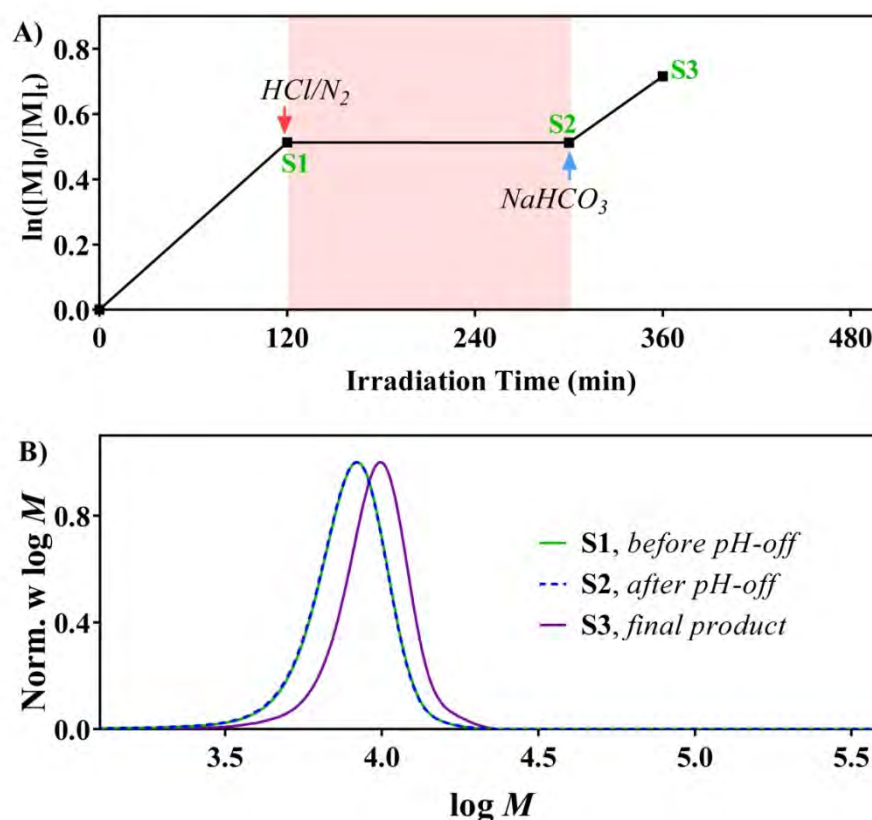


Figure 5.28 (A) Plot of $\ln([M]_0/[M]_t)$ versus time of TBrFL-catalysed PET-RAFT polymerisation of MA in DMSO ($[MA]:[BTPA-M]:[TBrFL] = 200:1:0.01$, MA to DMSO 1:1 v/v) under 5 mW/cm^2 530 nm irradiation with a 3 h period of pH-“OFF”. (B) Molecular weight distribution of GPC aliquots taken during polymerisation, denoted as S1, S2 and S3.

Table 5.4 GPC characterisation of S1, S2 and S3 in pH-gated MA polymerisation in the kinetic study shown as **Figure 5.28**.

Entry ^a	Monomer	Stage	Time	α^b	$M_{n,theo}^c$	$M_{n,GPC}$	M_w/M_n
--------------------	---------	-------	------	------------	----------------	-------------	-----------

			(min)	%	(kg/mol)	(kg/mol)	
S1	MA	before pH-”OFF”	120	40.1	7.2	7.8	1.07
S2	MA	after pH-”OFF”	300	40.0	7.2	7.8	1.06
S3	MA	final product	360	51.1	9.1	9.4	1.05

^aTBrFL-catalysed PET-RAFT polymerisation of MA in DMSO ([MA]:[BTPA-M]:[TBrFL] = 200:1:0.01) under 5 mW/cm² 530 nm irradiation with a 3-h-periods of pH-”OFF”. ^b α refers to monomer conversion determined by NMR spectroscopy. ^c $M_{n,theo}$ is the theoretical number average molecular weight calculated based on the equation $M_{n,theo} = [M]_0/[RAFT]_0 \times MW^M \times \alpha + MW^{RAFT}$, where $[M]_0$, $[RAFT]_0$, MW^M , α , and MW^{RAFT} correspond to initial monomer concentration, initial RAFT concentration, molar mass of monomer, conversion determined by ¹H NMR, and molar mass of RAFT agent.

We then included polymerisation of another monomer NAM in water (**Figure 5.29**) to demonstrate pH and light control (**Figure 5.29B-C** and **Table 5.5**).

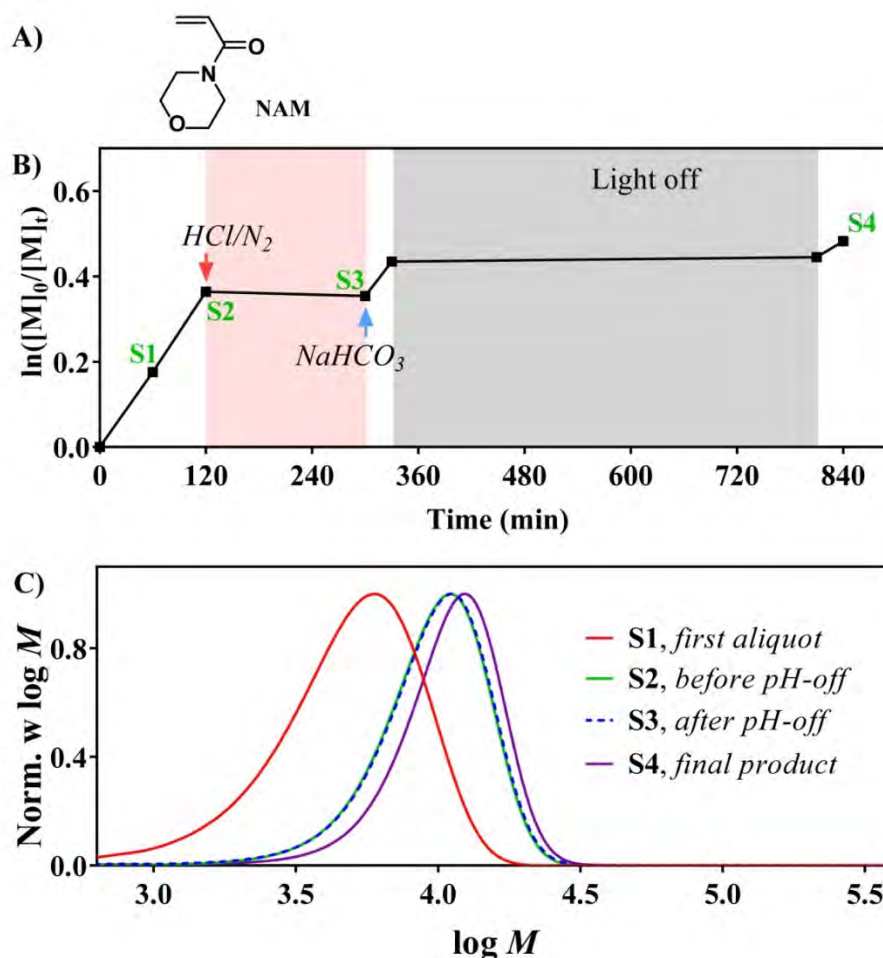


Figure 5.29 (A) Chemical structure of NAM. (B) Plot of $\ln([M]_0/[M]_t)$ versus time of TBrFL-catalysed PET-RAFT polymerisation of NAM in water ($[NAM]:[BTPA-M]:[TBrFL] = 200:1:0.01$, NAM to water 1:1 v/v) under 5 mW/cm^2 530 nm irradiation with a 3 h period of pH-“OFF” (pH = 5.0) and a 3 h period of light-“OFF”. (C) Molecular weight distributions of GPC aliquots taken during polymerisation, denoted as S1, S2, S3 and S4.

Table 5.5 GPC characterisation of S1, S2, S3 and S4 in pH and light dual-controlled DMA polymerisation in the kinetic study shown as **Figure 5.29**.

Entry ^a	Monomer	Stage	Time	α^b	$M_{n,theo}^c$	$M_{n,GPC}$	M_w/M_n
			(min)	%	(kg/mol)	(kg/mol)	
S1	NAM	first aliquot	60	16.1	11.3	12.6	1.24

S2	NAM	before pH-“OFF”	120	30.5	11.4	13.0	1.17
S3	NAM	after pH-“OFF”	300	29.8	16.3	16.0	1.18
S4	NAM	final product	840	38.3	16.3	16.4	1.15

^aTBrFL-catalysed PET-RAFT polymerisation of NAM in water ([NAM]:[BTPA-M]:[TBrFL] = 200:1:0.01) under 5 mW/cm² 530 nm irradiation with a 3-h-periods of pH-“OFF” and an 8-h-period of light-“OFF”. ^b α refers to monomer conversion determined by NMR spectroscopy. ^c $M_{n,theo}$ is the theoretical number average molecular weight calculated based on the equation $M_{n,theo} = [M]_0/[RAFT]_0 \times MW^M \times \alpha + MW^{RAFT}$, where $[M]_0$, $[RAFT]_0$, MW^M , α , and MW^{RAFT} correspond to initial monomer concentration, initial RAFT concentration, molar mass of monomer, conversion determined by ¹H NMR, and molar mass of RAFT agent.

Additionally, since the pK_a of CO₂ in water is 6.1,¹²⁶ which falls in the sensitive responding range of TBrFL (pH 5.9-6.3) and can potentially partly decolourize TBrFL, we decided to further demonstrate the potential for using gas to control PET-RAFT polymerisation; such a concept has never been utilized for polymerisation control and is an attractive prospect for polymerisation at industrial scales. During the TBrFL-catalysed PET-RAFT polymerisation, we purged the solution with CO₂ for one minute; as expected, we observed a quasi-“OFF” state (k_p^{app} cut down by half, from 0.011 to 0.006 min⁻¹, **Figure 5.30A**). After purging with N₂ for 10 min, we were fully able to recover the “ON” state (k_p^{app} back to 0.011 min⁻¹, **Figure 5.30A**). A corresponding change in the solution colour and visible-light absorption during the gas “ON”/quasi-“OFF” control was monitored by photography (**Figure 5.30A**, inset) and UV-vis spectroscopy (**Figure 5.30B**). High end-group fidelity with no detectable loss of the obtained polymer was confirmed by ¹H NMR spectroscopy (**Figure 5.31**) and the chain extension experiment (**Figure 5.32**).

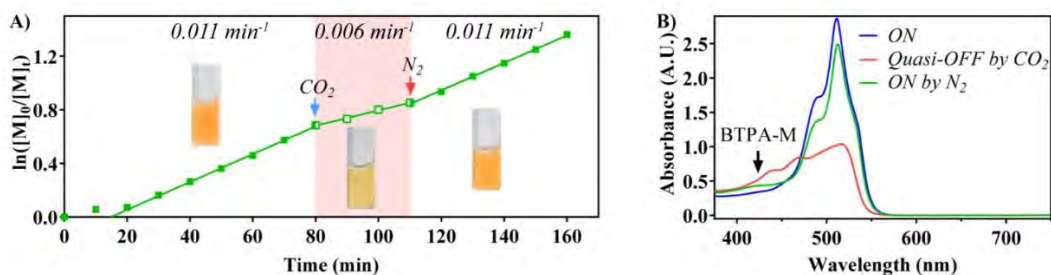


Figure 5.30 (A) Plot of $\ln([M]_0/[M]_t)$ versus time of TBrFL-catalysed PET-RAFT polymerisation in the presence of oxygen under green light using 1 min CO_2 purging to generate gas-quasi-“OFF” state and 10 min N_2 purging to generate gas-on state. (B) Corresponding UV-vis spectra of different states in (A).

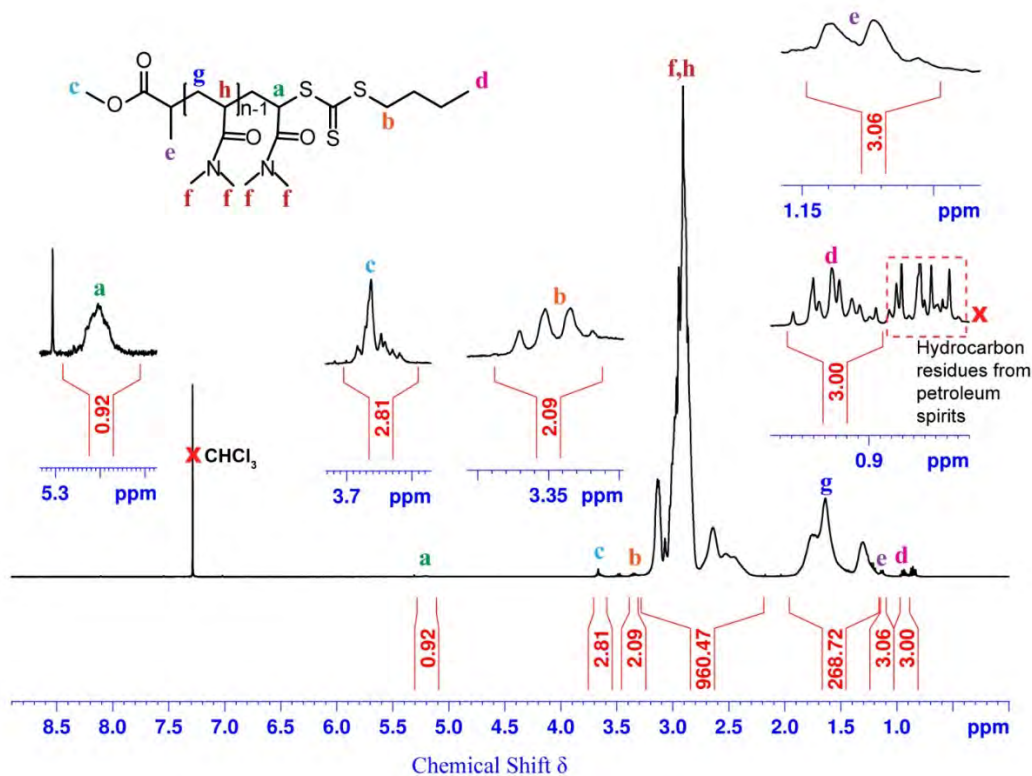


Figure 5.31 ^1H NMR spectrum (400 MHz, CDCl_3) of purified PDMA synthesised through non-degassed TBrFL-catalysed PET-RAFT polymerisation where CO_2 and N_2 were used to manipulate the polymerisation rate.

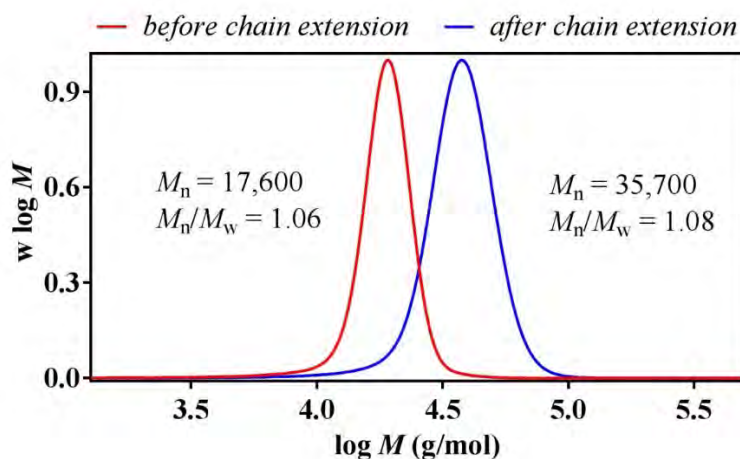


Figure 5.32 Molecular weight distributions for the synthesised PDMA after non-degassed TBrFL-catalysed PET-RAFT polymerisation where CO₂ and N₂ mediated pH manipulation was introduced (red line) and the chain-extended PDMA-*b*-PDMA after chain extension EB-catalysed PET-RAFT polymerisation (blue line). Complete shift of molecular weight distributions to higher molecular weights confirmed the high retention of the trithiocarbonate chain end group.

5.4 Conclusion

With the concept of computer-guided functional OPC design, we established structure-property relationships in this work. In addition, we introduced a set of applicable methodologies to enable the full computational screening of OPCs, allowing prediction of photocatalytic activity to mediate PET-RAFT polymerisation. Specifically, electrostatic studies helped uncover the pH sensitivity of fluorescein derivatives with variation in substitution; electrochemical and photophysical properties changed with the dye structures and were investigated to aid in designing an efficient OPC. Through DFT, TD-DFT, and relativistic DFT calculations in this work, key parameters that describe an OPC with special functionality (pH response as an example) were fully predicted, which successfully helped to circumvent the time consuming and usually costly experimental screening. As an example, we applied our computational studies for the design of a pH-responsive OPC, where the catalyst changes its catalytic activity according to a specific pH. TBrFL, as an efficient OPC reversibly turning colourless below pH 5 and recovering colour at pH 7, was designed by this methodology and synthesised accordingly. Notably, the range of pH control displayed by the designed photocatalyst lies in a more relevant range for bioapplications (pH \approx 5-7). By changing the pH of the solution via gaseous

HCl/N₂, NaHCO₃ powder, or gaseous CO₂, the polymerisation rate was seamlessly manipulated while using the designed TBrFL catalyst, and “ON/OFF” control could be exerted over the polymerisation. As such, application of this new functional OPC enabled the first pH and light dual-gated polymerisation. The methodology developed in this work can be applied for the design of photocatalysts which can be utilized in organic transformation as well as in polymer synthesis.

5.5 References

- (1) Blanco, V.; Leigh, D. A.; Marcos, V., *Chemical Society Reviews* **2015**, *44*, 5341.
- (2) Teator, A. J.; Lastovickova, D. N.; Bielawski, C. W., *Chemical Reviews* **2016**, *116*, 1969.
- (3) Leibfarth, F. A.; Mattson, K. M.; Fors, B. P.; Collins, H. A.; Hawker, C. J., *Angewandte Chemie International Edition* **2013**, *52*, 199.
- (4) Anastasaki, A.; Oschmann, B.; Willenbacher, J.; Melker, A.; Van Son, M. H. C.; Truong, N. P.; Schulze, M. W.; Discekici, E. H.; McGrath, A. J.; Davis, T. P.; Bates, C. M.; Hawker, C. J., *Angewandte Chemie International Edition* **2017**, *56*, 14483.
- (5) Anastasaki, A.; Nikolaou, V.; Nurumbetov, G.; Truong, N. P.; Pappas, G. S.; Engelis, N. G.; Quinn, J. F.; Whittaker, M. R.; Davis, T. P.; Haddleton, D. M., *Macromolecules* **2015**, *48*, 5140.
- (6) Lutz, J. F.; Lehn, J. M.; Meijer, E. W.; Matyjaszewski, K., *Nature Reviews Materials* **2016**, *1*, 16024.
- (7) Nakano, T.; Mori, M.; Okamoto, Y., *Macromolecules* **1993**, *26*, 867.
- (8) Ishitake, K.; Satoh, K.; Kamigaito, M.; Okamoto, Y., *Macromolecules* **2011**, *44*, 9108.
- (9) Tselepy, A.; Schiller, T. L.; Harrisson, S.; Guerrero-Sanchez, C.; Moad, G.; Keddie, D. J., *Macromolecules* **2018**, *51*, 410.
- (10) Shanmugam, S.; Boyer, C., *Journal of the American Chemical Society* **2015**, *137*, 9988.
- (11) Wang, J. S.; Matyjaszewski, K., *Journal of the American Chemical Society* **1995**, *117*, 5614.
- (12) Chiefari, J.; Chong, Y. K.; Ercole, F.; Krstina, J.; Jeffery, J.; Le, T. P. T.; Mayadunne, R. T. A.; Meijs, G. F.; Moad, C. L.; Moad, G.; Rizzardo, E.; Thang, S. H., *Macromolecules* **1998**, *31*, 5559.
- (13) Aoshima, S.; Kanaoka, S., *Chemical Reviews* **2009**, *109*, 5245.
- (14) Hadjichristidis, N.; Pitsikalis, M.; Pispas, S.; Iatrou, H., *Chemical Reviews* **2001**, *101*, 3747.
- (15) Nguyen, S. T.; Johnson, L. K.; Grubbs, R. H.; Ziller, J. W., *Journal of the American Chemical Society* **1992**, *114*, 3974.
- (16) Hawker, C. J.; Bosman, A. W.; Harth, E., *Chemical Reviews* **2001**, *101*, 3661.
- (17) Percec, V.; Barboiu, B., *Macromolecules* **1995**, *28*, 7970.
- (18) Percec, V.; Guliashvili, T.; Ladislaw, J. S.; Wistrand, A.; Stjerndahl, A.; Sienkowska, M. J.; Monteiro, M. J.; Sahoo, S., *Journal of the American Chemical Society* **2006**, *128*, 14156.
- (19) Kato, M.; Kamigaito, M.; Sawamoto, M.; Higashimura, T., *Macromolecules* **1995**, *28*, 1721.

- (20) Ben-Asuly, A.; Tzur, E.; Diesendruck, C. E.; Sigalov, M.; Goldberg, I.; Lemcoff, N. G., *Organometallics* **2008**, *27*, 811.
- (21) Chen, M.; Deng, S.; Gu, Y.; Lin, J.; MacLeod, M. J.; Johnson, J. A., *Journal of the American Chemical Society* **2017**, *139*, 2257.
- (22) Zhang, Z.; Zeng, T.-Y.; Xia, L.; Hong, C.-Y.; Wu, D.-C.; You, Y.-Z., *Nature Communications* **2018**, *9*, 2577.
- (23) P'Pool, S. J.; Schanz, H. J., *Journal of the American Chemical Society* **2007**, *129*, 14200.
- (24) Peeck, L. H.; Leuthausser, S.; Plenio, H., *Organometallics* **2010**, *29*, 4339.
- (25) Shanmugam, S.; Xu, J. T.; Boyer, C., *Polymer Chemistry* **2016**, *7*, 6437.
- (26) Shanmugam, S.; Boyer, C., *Science* **2016**, *352*, 1053.
- (27) Yoon, H. J.; Kuwabara, J.; Kim, J. H.; Mirkin, C. A., *Science* **2010**, *330*, 66.
- (28) Coulembier, O.; Moins, S.; Todd, R.; Dubois, P., *Macromolecules* **2014**, *47*, 486.
- (29) Chen, M.; Zhong, M.; Johnson, J. A., *Chemical Reviews* **2016**, *116*, 10167.
- (30) Corrigan, N.; Yeow, J.; Judzewitsch, P.; Xu, J.; Boyer, C., *Angewandte Chemie International Edition English* **2018**, *0*.
- (31) Fors, B. P.; Hawker, C. J., *Angewandte Chemie International Edition English* **2012**, *51*, 8850.
- (32) Treat, N. J.; Sprafke, H.; Kramer, J. W.; Clark, P. G.; Barton, B. E.; Read de Alaniz, J.; Fors, B. P.; Hawker, C. J., *Journal of the American Chemical Society* **2014**, *136*, 16096.
- (33) Treat, N. J.; Fors, B. P.; Kramer, J. W.; Christianson, M.; Chiu, C. Y.; de Alaniz, J. R.; Hawker, C. J., *ACS Macro Letters* **2014**, *3*, 580.
- (34) Jiang, J.; Ye, G.; Wang, Z.; Lu, Y.; Chen, J.; Matyjaszewski, K., *Angewandte Chemie International Edition English* **2018**, *57*, 12037.
- (35) Konkolewicz, D.; Schroder, K.; Buback, J.; Bernhard, S.; Matyjaszewski, K., *ACS Macro Letters* **2012**, *1*, 1219.
- (36) Pan, X.; Malhotra, N.; Simakova, A.; Wang, Z.; Konkolewicz, D.; Matyjaszewski, K., *Journal of the American Chemical Society* **2015**, *137*, 15430.
- (37) Pan, X. C.; Lamson, M.; Yan, J. J.; Matyjaszewski, K., *ACS Macro Letters* **2015**, *4*, 192.
- (38) Pan, X. C.; Malhotra, N.; Zhang, J. N.; Matyjaszewski, K., *Macromolecules* **2015**, *48*, 6948.
- (39) Anastasaki, A.; Nikolaou, V.; Brandford-Adams, F.; Nurumbetov, G.; Zhang, Q.; Clarkson, G. J.; Fox, D. J.; Wilson, P.; Kempe, K.; Haddleton, D. M., *Chemical Communications* **2015**, *51*, 5626.
- (40) Anastasaki, A.; Nikolaou, V.; McCaul, N. W.; Simula, A.; Godfrey, J.; Waldron, C.; Wilson, P.; Kempe, K.; Haddleton, D. M., *Macromolecules* **2015**, *48*, 1404.
- (41) Anastasaki, A.; Nikolaou, V.; Pappas, G. S.; Zhang, Q.; Wan, C.; Wilson, P.; Davis, T. P.; Whittaker, M. R.; Haddleton, D. M., *Chemical Science* **2014**, *5*, 3536.
- (42) Anastasaki, A.; Nikolaou, V.; Zhang, Q.; Burns, J.; Samanta, S. R.; Waldron, C.; Haddleton, A. J.; McHale, R.; Fox, D.; Percec, V.; Wilson, P.; Haddleton, D. M., *Journal of the American Chemical Society* **2014**, *136*, 1141.
- (43) Wenn, B.; Conradi, M.; Carreiras, A. D.; Haddleton, D. M.; Junkers, T., *Polymer Chemistry* **2014**, *5*, 3053.
- (44) Pan, X. C.; Tasdelen, M. A.; Laun, J.; Junkers, T.; Yagci, Y.; Matyjaszewski, K., *Progress in Polymer Science* **2016**, *62*, 73.
- (45) Kreutzer, J.; Yagci, Y., *Polymers* **2018**, *10*, 35.
- (46) Magenau, A. J.; Strandwitz, N. C.; Gennaro, A.; Matyjaszewski, K., *Science* **2011**, *332*, 81.

- (47) Wang, Y.; Fantin, M.; Park, S.; Gottlieb, E.; Fu, L.; Matyjaszewski, K., *Macromolecules* **2017**, *50*, 7872.
- (48) Peterson, B. M.; Lin, S.; Fors, B. P., *Journal of the American Chemical Society* **2018**, *140*, 2076.
- (49) Savka, R.; Foro, S.; Gallei, M.; Rehahn, M.; Plenio, H., *Chemistry* **2013**, *19*, 10655.
- (50) Varnado, C. D., Jr.; Rosen, E. L.; Collins, M. S.; Lynch, V. M.; Bielawski, C. W., *Dalton Trans* **2013**, *42*, 13251.
- (51) Rosen, E. L.; Varnado, C. D.; Arumugam, K.; Bielawski, C. W., *Journal of Organometallic Chemistry* **2013**, *745*, 201.
- (52) Piermattei, A.; Karthikeyan, S.; Sijbesma, R. P., *Nature Chemistry* **2009**, *1*, 133.
- (53) Wang, Z. H.; Pan, X. C.; Yan, J. J.; Dadashi-Silab, S.; Xie, G. J.; Zhang, J. N.; Wang, Z. H.; Xia, H. S.; Matyjaszewski, K., *ACS Macro Letters* **2017**, *6*, 546.
- (54) Wang, Z. H.; Pan, X. C.; Li, L. C.; Fantin, M.; Yan, J. J.; Wang, Z. Y.; Wang, Z. H.; Xia, H. S.; Matyjaszewski, K., *Macromolecules* **2017**, *50*, 7940.
- (55) Xu, J.; Jung, K.; Atme, A.; Shanmugam, S.; Boyer, C., *Journal of the American Chemical Society* **2014**, *136*, 5508.
- (56) Kottisch, V.; Michaudel, Q.; Fors, B. P., *Journal of the American Chemical Society* **2016**, *138*, 15535.
- (57) Theriot, J. C.; Lim, C. H.; Yang, H.; Ryan, M. D.; Musgrave, C. B.; Miyake, G. M., *Science* **2016**, *352*, 1082.
- (58) Niu, J.; Lunn, D. J.; Pusuluri, A.; Yoo, J. I.; O'Malley, M. A.; Mitragotri, S.; Soh, H. T.; Hawker, C. J., *Nature Chemistry* **2017**, *9*, 537.
- (59) Pester, C. W.; Narupai, B.; Mattson, K. M.; Bothman, D. P.; Klinger, D.; Lee, K. W.; Discekici, E. H.; Hawker, C. J., *Advanced Materials* **2016**, *28*, 9292.
- (60) Figg, C. A.; Hickman, J. D.; Scheutz, G. M.; Shanmugam, S.; Carmean, R. N.; Tucker, B. S.; Boyer, C.; Sumerlin, B. S., *Macromolecules* **2018**, *51*, 1370.
- (61) Tan, J. B.; Sun, H.; Yu, M. G.; Sumerlin, B. S.; Zhang, L., *ACS Macro Letters* **2015**, *4*, 1249.
- (62) McKenzie, T. G.; Fu, Q.; Wong, E. H. H.; Dunstan, D. E.; Qiao, G. G., *Macromolecules* **2015**, *48*, 3864.
- (63) McKenzie, T. G.; Fu, Q.; Uchiyama, M.; Satoh, K.; Xu, J.; Boyer, C.; Kamigaito, M.; Qiao, G. G., *Advanced Science* **2016**, *3*, 1500394.
- (64) Fu, Q.; Xie, K.; McKenzie, T. G.; Qiao, G. G., *Polymer Chemistry* **2017**, *8*, 1519.
- (65) Chen, M.; Johnson, J. A., *Chemical Communications (Camb)* **2015**, *51*, 6742.
- (66) Dadashi-Silab, S.; Doran, S.; Yagci, Y., *Chemical Reviews* **2016**, *116*, 10212.
- (67) Tasdelen, M. A.; Uygun, M.; Yagci, Y., *Macromolecular Rapid Communications* **2011**, *32*, 58.
- (68) Tasdelen, M. A.; Uygun, M.; Yagci, Y., *Macromolecular Chemistry and Physics* **2010**, *211*, 2271.
- (69) Yang, Q. Z.; Dumur, F.; Morlet-Savary, F.; Poly, J.; Lalevee, J., *Macromolecules* **2015**, *48*, 1972.
- (70) Zivic, N.; Bouzrati-Zerelli, M.; Kermagoret, A.; Dumur, F.; Fouassier, J. P.; Gignes, D.; Lalevee, J., *Chemcatchem* **2016**, *8*, 1617.
- (71) Al Mousawi, A.; Schmitt, M.; Dumur, F.; Ouyang, J.; Favereau, L.; Dorcet, V.; Vanthuyne, N.; Garra, P.; Toufaily, J.; Hamieh, T.; Graff, B.; Fouassier, J. P.; Gignes, D.; Crassous, J.; Lalevée, J., *Macromolecules* **2018**, *51*, 5628.
- (72) Sardon, H.; Zivic, N.; Kuroishi, P. K.; Dumur, F.; Gignes, D.; Dove, A. P., *Angewandte Chemie International Edition English* **2018**, *0*.
- (73) Kamigaito, M.; Satoh, K., *Chem* **2017**, *2*, 13.

- (74) Carmean, R. N.; Becker, T. E.; Sims, M. B.; Sumerlin, B. S., *Chem* **2017**, *2*, 93.
- (75) Asandei, A. D.; Adebolu, O. I.; Simpson, C. P.; Kim, J.-S., *Angewandte Chemie International Edition* **2013**, *52*, 10027.
- (76) Yamago, S.; Nakamura, Y., *Polymer* **2013**, *54*, 981.
- (77) Wang, C. G.; Li, F. F.; Goto, A., *Journal of Photopolymer Science and Technology* **2017**, *30*, 379.
- (78) Ohtsuki, A.; Lei, L.; Tanishima, M.; Goto, A.; Kaji, H., *Journal of the American Chemical Society* **2015**, *137*, 5610.
- (79) Kütahya, C.; Schmitz, C.; Strehmel, V.; Yagci, Y.; Strehmel, B., *Angewandte Chemie International Edition* **2018**, *57*, 7898.
- (80) Borská, K.; Moravčíková, D.; Mosnáček, J., *Macromolecular Rapid Communications* **2017**, *38*, 1600639.
- (81) Mosnáček, J.; Ilčíková, M., *Macromolecules* **2012**, *45*, 5859.
- (82) Blanco, V.; Carlone, A.; Hanni, K. D.; Leigh, D. A.; Lewandowski, B., *Angewandte Chemie International Edition English* **2012**, *51*, 5166.
- (83) Blanco, V.; Leigh, D. A.; Marcos, V.; Morales-Serna, J. A.; Nussbaumer, A. L., *Journal of the American Chemical Society* **2014**, *136*, 4905.
- (84) Beswick, J.; Blanco, V.; De Bo, G.; Leigh, D. A.; Lewandowska, U.; Lewandowski, B.; Mishiro, K., *Chem Sci* **2015**, *6*, 140.
- (85) Balof, S. L.; P'Pool S, J.; Berger, N. J.; Valente, E. J.; Shiller, A. M.; Schanz, H. J., *Dalton Trans* **2008**, 5791.
- (86) Balof, S. L.; Yu, B.; Lowe, A. B.; Ling, Y.; Zhang, Y.; Schanz, H. J., *European Journal of Inorganic Chemistry* **2009**, *2009*, 1717.
- (87) Nikolaou, V.; Anastasaki, A.; Alsubaie, F.; Simula, A.; Fox, D. J.; Haddleton, D. M., *Polymer Chemistry* **2015**, *6*, 3581.
- (88) Yilmaz, G.; Yagci, Y., *Polymer Chemistry* **2018**, *9*, 1757.
- (89) Green, F. J., *The Sigma-Aldrich Handbook of Stains, Dyes, and Indicators*. Aldrich Chemical Company: 1990.
- (90) Wu, C.; Corrigan, N.; Lim, C.-H.; Jung, K.; Zhu, J.; Miyake, G.; Xu, J.; Boyer, C., *Macromolecules* **2018**, *52*, 236.
- (91) Lim, C. H.; Ryan, M. D.; McCarthy, B. G.; Theriot, J. C.; Sartor, S. M.; Damrauer, N. H.; Musgrave, C. B.; Miyake, G. M., *Journal of the American Chemical Society* **2017**, *139*, 348.
- (92) McCarthy, B. G.; Pearson, R. M.; Lim, C. H.; Sartor, S. M.; Damrauer, N. H.; Miyake, G. M., *Journal of the American Chemical Society* **2018**, *140*, 5088.
- (93) Pearson, R. M.; Lim, C. H.; McCarthy, B. G.; Musgrave, C. B.; Miyake, G. M., *Journal of the American Chemical Society* **2016**, *138*, 11399.
- (94) Sartor, S. M.; McCarthy, B. G.; Pearson, R. M.; Miyake, G. M.; Damrauer, N. H., *Journal of the American Chemical Society* **2018**, *140*, 4778.
- (95) Singh, V. K.; Yu, C.; Badgujar, S.; Kim, Y.; Kwon, Y.; Kim, D.; Lee, J.; Akhter, T.; Thangavel, G.; Park, L. S.; Lee, J.; Nandajan, P. C.; Wannemacher, R.; Milian-Medina, B.; Luer, L.; Kim, K. S.; Gierschner, J.; Kwon, M. S., *Nature Catalysis* **2018**, *1*, 794.
- (96) Lu, J.; Pattengale, B.; Liu, Q.; Yang, S.; Shi, W.; Li, S.; Huang, J.; Zhang, J., *Journal of the American Chemical Society* **2018**, *140*, 13719.
- (97) Speckmeier, E.; Fischer, T. G.; Zeitler, K., *Journal of the American Chemical Society* **2018**, *140*, 15353.
- (98) Niu, Y. L.; Li, W. Q.; Peng, Q.; Geng, H.; Yi, Y. P.; Wang, L. J.; Nan, G. J.; Wang, D.; Shuai, Z. G., *Molecular Physics* **2018**, *116*, 1078.
- (99) Peng, Q.; Yi, Y.; Shuai, Z.; Shao, J., *Journal of the American Chemical Society* **2007**, *129*, 9333.

- (100) Niu, Y.; Peng, Q.; Shuai, Z., *Science in China Series B-Chemistry* **2008**, *51*, 1153.
- (101) Li, Z.; Xiao, Y.; Liu, W., *Journal of Chemical Physics* **2014**, *141*, 054111.
- (102) Li, Z.; Xiao, Y.; Liu, W., *Journal of Chemical Physics* **2012**, *137*, 154114.
- (103) Li, Z. D.; Suo, B. B.; Zhang, Y.; Xiao, Y. L.; Liu, W. J., *Molecular Physics* **2013**, *111*, 3741.
- (104) Liu, W.; Hong, G.; Dai, D.; Li, L.; Dolg, M., *Theoretical Chemistry Accounts* **1997**, *96*, 75.
- (105) Ferguson, C. J.; Hughes, R. J.; Nguyen, D.; Pham, B. T. T.; Gilbert, R. G.; Serelis, A. K.; Such, C. H.; Hawzett, B. S., *Macromolecules* **2005**, *38*, 2191.
- (106) Sun, W. C.; Gee, K. R.; Klaubert, D. H.; Haugland, R. P., *Journal of Organic Chemistry* **1997**, *62*, 6469.
- (107) Sjoback, R.; Nygren, J.; Kubista, M., *Spectrochimica Acta Part a-Molecular and Biomolecular Spectroscopy* **1995**, *51*, L7.
- (108) Reager, D. L.; Goode, S. R.; Ball, D. W., *Chemistry: Principles and Practice*. Cengage Learning: 2009.
- (109) Papariello, G. J.; Commanday, S., *Analytical Chemistry* **1964**, *36*, 1028.
- (110) Lu, T.; Chen, F., *Journal of Computational Chemistry* **2012**, *33*, 580.
- (111) Humphrey, W.; Dalke, A.; Schulten, K., *J Mol Graph* **1996**, *14*, 33.
- (112) Du, Y.; Pearson, R. M.; Lim, C. H.; Sartor, S. M.; Ryan, M. D.; Yang, H.; Damrauer, N. H.; Miyake, G. M., *Chemistry* **2017**, *23*, 10962.
- (113) Romero, N. A.; Nicewicz, D. A., *Chemical Reviews* **2016**, *116*, 10075.
- (114) Nagarajan, K.; Mallia, A. R.; Muraleedharan, K.; Hariharan, M., *Chem Sci* **2017**, *8*, 1776.
- (115) Koziar, J. C.; Cowan, D. O., *Accounts of Chemical Research* **2002**, *11*, 334.
- (116) Liu, W., *Handbook of Relativistic Quantum Chemistry*. Springer Berlin Heidelberg: 2017.
- (117) Senga, R.; Suenaga, K., *Nat Commun* **2015**, *6*, 7943.
- (118) Tossell, J. A., *Computational and Theoretical Chemistry* **2011**, 977, 123.
- (119) Yang, Y.; Weaver, M. N.; Merz, K. M., Jr., *Journal of Physical Chemistry A* **2009**, *113*, 9843.
- (120) McClure, D. S., *Journal of Chemical Physics* **1949**, *17*, 905.
- (121) Ermolaev, V. L.; Svitashv, K. K., *Optika I Spektroskopiya* **1959**, *7*, 664.
- (122) La Paglia, S. R., *Spectrochimica Acta* **1962**, *18*, 1295.
- (123) Xu, J. T.; Shanmugam, S.; Duong, H. T.; Boyer, C., *Polymer Chemistry* **2015**, *6*, 5615.
- (124) Narayanaswamy, R.; Wolfbeis, O. S., *Optical Sensors: Industrial Environmental and Diagnostic Applications*. Springer Berlin Heidelberg: 2013.
- (125) Brown, I. D., *Journal of Solution Chemistry* **1987**, *16*, 205.
- (126) Barash, P. G.; Cullen, B. F.; Stoelting, R. K.; Cahalan, M.; Stock, M. C., *Clinical Anesthesia*. Wolters Kluwer Health: 2011.

Chapter 6 Conclusions and Future Work

6.1 Conclusions

This thesis has established and streamlined a fully computer-guided rational strategy of designing a functional PC for PET-RAFT polymerisation, which can circumvent the excessive costs and efforts needed in a traditional trial-and-error strategy in PC discoveries. By initially investigating the naturally occurring Chl a with various functional substituents evolved for efficient photocatalysis, its photocatalytic performance and functionalities in PET-RAFT polymerisation inspired the general orientations for developing efficient PCs for PET-RAFT polymerisation systems with specific functionalities. On top of the initial inspiration, comprehensive structure-property-performance relationships were established as guiding principles for rational design of PET-RAFT PCs, by combining experimental and computational studies on a library of halogenated xanthene dyes. Finally, the fully computer-guided strategy of functional PC design for PET-RAFT polymerisation was enabled based on broadened structure-property-performance relationships by the aid of the most cutting-edged computational tools.

To derive the general orientations for rational PC design in PET-RAFT polymerisation, the naturally evolved Chl a with a heavily decorated chromophore structure and thus derived superior photocatalysis-related properties was comprehensively investigated for PET-RAFT polymerisation performance in **Chapter 3**. The remarkable visible-light absorption at long-wavelengths, high Φ_T , sufficient triplet energy and appropriate redox properties of Chl a have resulted in its remarkable catalytic efficiency, oxygen tolerance performance and capability of post-polymerisation decolouration in PET-RAFT polymerisation. Inspired by this naturally derived excellent PET-RAFT PC with evolved functional substituents, the practices in this work extensively shed light on the general orientations for rational PC design of PET-RAFT polymerisation.

Acknowledging the general orientations, the full scope of structure-property-performance relationships were established and generalised for PET-RAFT systems in **Chapter 4** by relating experimental observations to quantum chemical calculations and using halogenated xanthene dyes as examples. Specifically, the effect of substituents of the xanthene chromophore on the electronic-spectral, photophysical and electrochemical

properties of these dyes were summarised as the structure-property relationships. Meanwhile, the effect of these properties on the performance of PET-RAFT polymerisation like photocatalytic efficiency, activation wavelengths and oxygen tolerance were evaluated as the property-performance relationships in detail. A theoretical framework in guiding the design of high-performance PCs for PET-RAFT polymerisation was hence established.

With the solid foundation of the theoretical framework, in **Chapter 5**, a fully computer-guided rational strategy for PC design was established based on broadened structure-property-performance relationships and a collection of the most cutting-edged quantum chemical tools. Specifically, this fully computer-guided strategy was adopted in rationally designing an efficient pH-switchable organic PC, sensitively turning colourless at pH 5 and recovering strong visible-light absorption and photoactivity at pH 7. This is the first example of a PC design fully guided by comprehensive quantum chemical studies covering electrostatic, electrochemical, and photophysical predictions. Application of this designed PC in PET-RAFT polymerisation resulted in the first organocatalysed pH and light dual-gated controlled polymerisation.

6.2 Future work

The computer-guided rational strategy of PC design for photo-controlled polymerisation not only provides a rapid and economic methodology in discovering new PCs, but most importantly enables precise tuning of the performance and functionality of the polymerisation system by judiciously customising the structure of the PC. Compared to the traditional trial-and-error strategy by experimental screening, computer-guided PC design generates significant opportunities in developing advanced polymerisation techniques for complex macromolecular synthesis. Despite recent efforts in rational PC design and the realisation of fully computer-guided PC design, more knowledge and further developments of rational PC design for photo-controlled polymerisation systems are needed.

Firstly, the structure-property relationships concerning some novel structural modification strategies such as chromophore core-twisting, porphyrin reduction and introduction of alkyloxy or sulfide groups, are still yet to be more deeply investigated and understood at the quantum chemical level. Although structure-property relationships

concerning π -conjugation extension, heavy atom effect and excited-state charge transfer are relatively well established, many of the dye classes can have their own special features and yield exceptions deviating from general rule, which need more comprehensive studies. Indeed, better understanding on the structure-property relationships contributes to higher-level of rationality, preciseness and customisability in PC design for broadened scope of applications.

Secondly, it is still considered a challenge to develop highly efficient photo-controlled polymerisation systems activated by longer-wavelength light for better light penetration and energy efficiency. In particular, the 3D/4D printing¹ technology based on photo-controlled polymerisation can afford cross-linked polymeric networks with designed composition and architecture leading to optimised mechanical properties. Most importantly, the “living” chain ends on the surface of the printed object can be reactivated under irradiation for continued printing, making the printed object highly manufacturable, post-modifiable and fixable. However, 3D printing has a tough requirement for high photocatalytic efficiency of the PC to reach fast polymerisation and high printing speed; this requires the PC to be designed with high absorbance, triplet quantum yield and favourable redox properties, which can only be realised via a computer-guided rational approach. Additionally, longer-wavelength light exhibiting better light penetration can benefit photo-curing processes with higher efficiency and increase the contact strength between printed layers. Moreover, the benign long-wavelength lights within the visible-to-near-infrared range can avoid side reactions and self-polymerisation of monomers, thus highly desirable for 3D printing.

Thirdly, understanding of the thermodynamic interplay between the photoexcited PC and other catalytic species in photo-controlled polymerisation is critical in quantitatively determining by computation whether a PC can work for a particular mechanism. Currently, there has been no sufficient work on detailed theoretical evaluation of the thermodynamic relationships and the exact thermodynamic criteria of activation/deactivation remain unclear. Systematic thermodynamic studies on different mechanisms of photo-controlled polymerisation can not only provide mechanistic understanding but also shed light on possible new mechanisms or quenching pathways for photo-controlled polymerisation. Relevant work is well under way.

Fourthly, the ultimate goal of fully computer-guided rational PC design is to be integrated into deep learning technologies. Based on sufficient amount of knowledge in structure-property-performance relationships and effective integration of a series quantum chemical software packages, it is possible to develop deep learning networks that can suggest possible candidates of PC structures affording desired properties.

6.3 References

- (1) Zhang, Z.; Corrigan, N.; Bagheri, A.; Jin, J.; Boyer, C., *Angewandte Chemie International Edition English* **2019**, *58*, 17954.

Chapter 7 Appendix

7.1 Materials

N,N'-dimethylacrylamide (DMA), diethyl acrylamide (DEA), hydroxyethyl acrylamide (HEAAm), 4-acryloylmorpholine (NAM), methyl acrylate (MA), *tert*-butyl acrylate (*t*BuA), di(ethylene glycol) ethyl ether acrylate (DEGEEA), methyl methacrylate (MMA) and oligoethylene glycol methacrylate (OEGMA) were purchased from Sigma-Aldrich and used after percolation over a plug of basic alumina (Ajax Chemical, AR) to remove inhibitors. Deionized water was produced by a Sartorius Milli-Q water purification system with a resistivity of $18.2 \text{ M}\Omega \text{ cm}^{-1}$. 2-(*n*-butyltrithiocarbonate)propionic acid methyl ester (BTPA-M) was synthesised by methylation of 2-(*n*-butyltrithiocarbonate)propionic acid (BTPA); BTPA was synthesised according to literature.¹ Tetrabromofluorescein (TBrFL) was synthesised by a modified version of fluorescein derivative synthetic procedures in literature.² 4-Dimethylaminopyridine (DMAP) and 1,3-dicyclohexylcarbodiimide (DCC), tetrabromophthalic anhydride and resorcinol were purchased from Sigma-Aldrich and used as received. Dimethyl sulfoxide (DMSO), *N,N'*-dimethylacetamide (DMAc), *N,N'*-dimethylformamide (DMF), acetonitrile (MeCN), methanol (MeOH), ethanol (EtOH), ethyl acetate (EtOAc), dichloromethane (DCM), tetrahydrofuran (THF), acetone and dioxane, methanol, hexane, diethyl ether and petroleum spirit were purchased from Ajax Chemical and used as received. Xanthene dyes in sodium salt form erythrosine B (EB), eosin Y (EY), rose bengal (RB), phloxine B (PB) and eosin B (EOB) were purchased from Sigma Aldrich and used as received.

7.2 Instrumentation

Photopolymerisation Setup. Photopolymerisation was performed in $1 \text{ cm} \times 2 \text{ mm} \times 5 \text{ cm}$ glass cuvettes (6G) sealed with a rubber septa. The polymerisation solutions were irradiated at 5 mW/cm^2 of 530 nm green light in an Oriel VeraSol-2 LED solar simulator at room temperature. The Oriel VeraSol-2 LED solar simulator is composed of an LSS-7120 LED controller and an LSH-7520 LED head.

Online Fourier Transform Near-Infrared (FTNIR) spectroscopy. FTNIR spectra were recorded to monitor the monomer signal of the vinylic C-H stretching overtone at ~ 6200

cm^{-1} . Monomer conversions were calculated by the decrease of the integration of vinylic C-H peak divided by the initial value. The Bruker IFS 66/S Fourier transform spectrometer for recording FTNIR spectra was equipped with a tungsten halogen lamp, a CaF_2 beam splitter and liquid-nitrogen-cooled InSb detector. After every 10 min irradiation during photopolymerisation, the sample was manually placed in the sample holder for FTNIR scanning and each spectrum composed of 16 scans with a resolution of 4 cm^{-1} (15 s per spectrum). Peak analysis was performed in OPUS software.

UV-Vis Spectroscopy. UV-vis spectra were recorded by a Varian CARY 300 spectrophotometer.

pH measurements. pH was measured by a Mettler Toledo SevenCompact pH/Ion meter.

Gel Permeation Chromatography (GPC). Molecular weight distribution of synthesised polymers was characterised by GPC with DMAc as the eluent. The Shimadzu GPC modular system composed of an auto-injector and a Phenomenex 5.0 μM bead size guard column ($50 \times 7.5 \text{ m}$) followed by four Phenomenex 5.0 μM bead size columns (10^5 , 10^4 , 10^3 and 10^2 \AA), a differential refractive-index detector and a UV detector ($\lambda = 305 \text{ nm}$). The DMAc GPC system was calibrated based on narrow molecular distribution of poly(methyl methacrylate) standards with molecular weights of 200 to 10^6 g mol^{-1} .

Nuclear Magnetic Resonance (NMR). NMR analysis was performed on a 400 MHz Bruker Advance III instrument installed with SampleXpress operating for ^1H and ^{13}C with CDCl_3 or DMSO-d_6 as solvent. Spectra were reported as chemical shift (δ) in ppm downfield from 0 ppm.

Matrix Assisted Laser Desorption Ionization-Time of Flight Mass Spectrometry (MALDI-TOF MS). MALDI-TOF MS analysis was performed at the University of New South Wales Bioanalytical Mass Spectrometry Facility (UNSW BMSF) on a Bruker ultrafleXtreme mass spectrometer in positive ion, linear mode using MeCN as the solvent.

Density Functional Theory (DFT) Computation. DFT calculations of the electrostatic potential (ESP) surfaces were performed with Gaussian 09 computational chemistry package; post-computational analysis of the obtained ESP results was conducted with Multiwfn software package³ including the qualitative molecular surface analysis module; ESP maps were visualized by the Visual Molecular Dynamics (VMD) package;⁴ post

labelling was conducted with Adobe Creative Cloud Photoshop CC 2019 and Illustrator CC 2019 under a student subscription licence. DFT calculations of optimized molecular geometries and energies were calculated with Gaussian 09 computational chemistry package. DFT calculations of frontier orbital distributions and time-dependent DFT (TD-DFT) calculations of ground/excited state transitions were calculated with Gaussian 09 computational chemistry package; frontier orbital visualization was performed with Multiwfn software package.³ Radiative and non-radiative decay rates were calculated by the Molecular Materials Property Prediction Package (MOMAP) 1.0⁵⁻⁶ with results calculated from Gaussian 09 and Beijing Density Functional (BDF) program package.⁷⁻⁹ For computational details of each part see respective sections below.

- (1) Ferguson, C. J.; Hughes, R. J.; Nguyen, D.; Pham, B. T. T.; Gilbert, R. G.; Serelis, A. K.; Such, C. H.; Hawkett, B. S., *Macromolecules* **2005**, *38*, 2191.
- (2) Sun, W. C.; Gee, K. R.; Klaubert, D. H.; Haugland, R. P., *Journal of Organic Chemistry* **1997**, *62*, 6469.
- (3) Lu, T.; Chen, F., *Journal of Computational Chemistry* **2012**, *33*, 580.
- (4) Humphrey, W.; Dalke, A.; Schulten, K., *J Mol Graph* **1996**, *14*, 33.
- (5) Peng, Q.; Yi, Y.; Shuai, Z.; Shao, J., *Journal of the American Chemical Society* **2007**, *129*, 9333.
- (6) Niu, Y. L.; Li, W. Q.; Peng, Q.; Geng, H.; Yi, Y. P.; Wang, L. J.; Nan, G. J.; Wang, D.; Shuai, Z. G., *Molecular Physics* **2018**, *116*, 1078.
- (7) Li, Z.; Xiao, Y.; Liu, W., *Journal of Chemical Physics* **2014**, *141*, 054111.
- (8) Li, Z.; Xiao, Y.; Liu, W., *Journal of Chemical Physics* **2012**, *137*, 154114.
- (9) Li, Z.; Suo, B.; Zhang, Y.; Xiao, Y.; Liu, W., *Molecular Physics* **2013**, *111*, 3741.